

Disordered Alkali-Niobates for Use as a Sodium-ion Battery Anode Material

Wai Chi (Rachel) Tang

A thesis submitted to the *University of Birmingham* for the degree of
Doctor of Philosophy

Supervisors
Dr Phil Chater
Dr Phoebe Allan

School of Chemistry
College of Engineering and Physical Sciences
University of Birmingham
April 2023

UNIVERSITY OF
BIRMINGHAM

University of Birmingham Research Archive

e-theses repository

This unpublished thesis/dissertation is copyright of the author and/or third parties. The intellectual property rights of the author or third parties in respect of this work are as defined by The Copyright Designs and Patents Act 1988 or as modified by any successor legislation.

Any use made of information contained in this thesis/dissertation must be in accordance with that legislation and must be properly acknowledged. Further distribution or reproduction in any format is prohibited without the permission of the copyright holder.

Dedication

媽咪 阿妹 未婚夫

Acknowledgement

This project would not be possible without the guidance and insights provided by my supervisors Phil Chater and Phoebe Allan. Phil has been a fundamental cornerstone throughout this project, always present and a source of guidance and inspiration throughout. Phoebe has advocated for my growth as a scientist and her curiosity has sparked many discussions. A special thanks to Zoe Schnepp and Joe Hriljac kindly who stepped in as temporary supervisors, offering their time and expertise.

I am grateful to have the pleasure of sharing this journey with Marleen Vetter, Dan Irving, Beatrice Browning, Fanny Costa, Christine Beavers, Javi Castells-Gil, Katie Morton, Aly Abdeldaim, my fiance Callum Dilley and my family who were there during the toughest moments, part of my happiest and everything in between.

I am indebted to Sarah Day, Eamonn Connolly and the I11 team, who have shown wholehearted support, facilitating the experimental work of this study in their labs. Thank you Gavin Stenning and Daniel Nye who graciously opened the doors of their Materials Characterisation Lab, ISIS.

Thank you to Lee Warren, Sarah Gurung, Maria Dias-Lopez, Allan Ross, Finley Belcher and Dom Daisenberger for the corridor discussions and smiles that brighten my day. I profusely thank Iain Wilkinson and the Kristina Penman for their invaluable administrative work that has underpinned this PhD.

Thank you to Emanuela Liberti and Tom Slater offered their expertise in STEM, whilst Brian Pauw and Glen Smales provided SAXS measurements. Annette Kleppe, Sarah Day and Eamonn Connolly provided XRD measurements towards this study, thank you.

This experience would not be the same without my group at I15-1 and the Allan group who have provided many interesting scientific discussions challenging my understanding and they have continuously supported me and my research.

I am honoured have been part of the Crystallography team at Diamond Light Source and also the Materials research at the University of Birmingham. Both outstanding facilities producing world-class research, and for a moment, I was part of it.

It takes a village. Thank you all.

Abstract

Nanostructured and disordered materials have been shown to possess improved and emergent properties which are distinct from the bulk material. Top-down and bottom-up nanostructuring methods of alkali-niobates have been explored in this study. The synthesis of three nanostructured phases is demonstrated, two of which are 2D nanostructured materials showing turbostatic disorder based on the layered structure of KNb_3O_8 and $K_4Nb_6O_{17}$. The third nanostructured niobate shows a very high degree of disorder, posing challenges in characterisation, however was determined to be a corner sharing niobate structure. Solid state structural analysis was carried out using x-ray diffraction (XRD), x-ray pair distribution function (XPDF), microscopy and Raman spectroscopy.

Alkaline-niobates are electronically active, this has mostly been investigated as a lithium-ion anode material, however little is known about their capacbilities as a sodium-ion battery anode material. Due to increasing supply chain risks and our ever depleting lithium resource it is imperative global energy storage systems are diversified to meet the energy demands of our growing populations. Sodium-ion batteries have potential cost, safety and resource-availability advantages over lithium-ion batteries, albeit generally with some loss of energy density, which is not a concern for staitionary battery applications.

KNb_3O_8, HNb_3O_8 and the three aforementioned nanostructured niobates were studied within sodium half cell, coin cells by galvanostatic (dis)charge and cyclic voltammetry (CV). HNb_3O_8 showed the highest capacity (122.0 $mAhg^{-1}$ after 20 cycles at $3mAg^{-1}$) consistent with previous work, theorised to be due to the small interlayer ion H^+. The nanostructured materials showed poorer capacities, however the 2D nanomaterials of KNb_3O_8 and $K_4Nb_6O_{17}$ showed almost no capacity loss when comparing the 20^{th} cycle

capacity at rates of 10 $mAhg^{-1}$ and 40 $mAhg^{-1}$, whilst crystalline KNb_3O_8 showed a capacity loss of over 50 %. Most interestingly, at a rate of 3 $mAhg^{-1}$, coin cells made from KNb_3O_8:C:CMC (7:1.5:1.5) anode coatings were found to show capacity increase from 161 $mAhg^{-1}$ (second cycle) to 200 $mAhg^{-1}$ (15th cycle), an increase of around 25 %. To tbe best of our knowledge, a new phenomena which has not been previously reported. The same coating made with PVDF (Poly(vinylidene fluoride)) binder instead of CMC (sodium carboxymethyl cellulose) binder did not exhibit this behaviour, therefore, this increase in capcity is most likely related to the superior stability of CMC over PVDF in this system.

These results indicate the careful choice of nanostructure and electrode-level fabrication methods (e.g. binder) have the potential to optimise capacity, capacity retention and power capabilities.

Glossary

BVS	Bond valence sum
BF	Bright field
cif	Crystallographic information file
CMC	Sodium carboxymethyl cellulose
CV	Cyclic voltammetry
DI	Deionised
DCC	Differential capacitance curves
DLS	Diamond Light Source
DTA	Differential thermal analysis
FT	Fourier transform
GITT	Galvanostatic intermittent titration technique
HAADF	High-angle annular dark-field
IPA	Iso-propyl alcohol
ICSD	Inorganic Crystal Structure Database
ICDD	International Centre for Diffraction Data
JCPDS	Joint Committee on Powder Diffraction Standards
LIB	Lithium-ion battery
LIBs	Lithium-ion batteries
LINAC	Linear accelerator
LFP	$LiFePO_4$
MAC	Multi-analyser crystal
MOF	Metal–organic framework
NMF	Non-negative matrix factorization
NMR	Nnuclear magnetic resonance
PDF	Pair distribution function
PDF 4+	Powder diffraction file 4+
PSD	Position sensitive detector
PVDF	Polyvinylidene fluoride
PXRD	Powder x-ray diffraction
RMC	Reverse- Monte Carlo
r_{wp}	Weighted profile R-factor
SAXS	Small angle scattering
SEI	Solid electrolyte interphase
SEM	Scanning electron microscopy
SHE	Standard hydrogen electrode

SIB	Sodium-ion battery
SIBs	Sodium-ion batteries
SOC	State of charge
ss	Solid state synthesis
STEM	Scanning transmission electron microscopy
std	Standard deviation
TBAOH	Tetrabutylammonium hydroxide
TEM	Transmission electron microscopy
TGA	Thermogravimetric analysis
TGA-MS	Thermogravimetric analysis-mass spectrometry
XANES	X-ray absorption near edge structure
XPDF	X-ray pair distribution function
XPS	X-ray photoelectron spectroscopy
XRD	X-ray diffraction
XRF	X-ray fluorescence

Contents

Dedictation III

Acknowledgements IV

Glossary VIII

List of Figures XVIII

List of Tables XXVIII

Introduction to this thesis XXXIV

1 Literature review 1

1.1 Introduction to batteries 1

1.1.1 The important role of batteries in society 1

1.1.2 How batteries work: Lithium-ion batteries 2

1.1.3 Beyond lithium-ion batteries 3

1.1.4 Chemistry of sodium vs. lithium 4

1.1.5 Sodium-ion battery anode materials 7

1.1.6 Alloying anodes 8

1.1.7 Conversion anodes 8

1.1.8 Insertion anodes 9

1.1.9 Summary: Anode types 10

1.1.10 Components and features of an anode coating 11

1.2 Battery testing 14

1.2.1 How to calculate theoretical capacity 14

1.2.2 Galvanostatic charge discharge 15

1.3 Innovation through morphology design: anode materials 17
1.3.1 Top-down nanostructuring 18
1.3.2 Bottom-up nanostructuring 19
1.3.3 Nanostructuring aims of this study 20
1.3.4 Characterising nanostructured materials 21
1.4 Niobates as anode materials 23
1.4.1 Introduction 23
1.4.2 Nb-O systems 24
1.4.3 A-Nb-O systems, A = Na, K 26
1.5 MNb_3O_8, where M = H_3O, H, Li, Na and K 28
1.5.1 Synthesis of KNb_3O_8 28
1.5.2 MNb_3O_8 anode material 29
1.5.3 KNb_3O_8 in lithium-ion batteries 32
1.5.4 KNb_3O_8 in sodium-ion batteries 33
1.6 Aims of this study 36

2 Theory and practice of techniques **39**

2.1 Introduction 39
2.2 Crystallography 40
2.2.1 The importance of crystallography 40
2.2.2 Introduction to the unit cell 40
2.2.3 Symmetry within the unit cell 41
2.2.4 Crystallographic information files and databases 43
2.3 X-ray scattering 44
2.3.1 Introduction 44
2.3.2 Powder x-ray diffraction 46
2.3.3 X-ray sources 47
2.3.4 PXRD equipment 48
2.3.5 PXRD methodology 50
2.3.6 PXRD analysis 52

2.3.7 PDF introduction . . . 56
2.3.8 PDF equipment and methodology . . . 56
2.3.9 PDF generation: theory . . . 58
2.3.10 PDF generation: practice . . . 60
2.3.11 PDF analysis . . . 61
2.3.12 Limitations of XRD and PDF . . . 62
2.4 Small angle x-ray scattering . . . 64
2.5 Raman spectroscopy . . . 65
2.5.1 Raman spectroscopy: theory . . . 65
2.5.2 Raman system at I15 . . . 66
2.6 Microscopy . . . 67
2.6.1 Introduction to microscopy . . . 67
2.6.2 Hitachi TM4000 . . . 68
2.6.3 ePSIC at Diamond Light Soruce . . . 68
2.7 Thermogravimetric analysis- mass spectroscopy . . . 69
2.7.1 TGA-MS: theory . . . 69
2.7.2 TGA-MS: method . . . 69
2.8 Electrochemical testing . . . 71
2.8.1 Differential capacitance curves . . . 71
2.8.2 Cyclic voltammetry . . . 72

3 Synthesis and characterisation of KNb_3O_8, HNb_3O_8 and $H_3ONb_3O_8$ 77

3.1 Introduction . . . 77
3.2 Synthesis of KNb_3O_8 . . . 78
3.2.1 Introduction of impurity phases . . . 78
3.2.2 Solid-state synthesis . . . 80
3.3 Molten salt synthesis of KNb_3O_8 . . . 85
3.3.1 Introduction . . . 85
3.3.2 Molten salt synthesis . . . 86
3.3.3 Detailed characterisation of KNb_3O_8 . . . 89

3.3.4 Summary: KNb_3O_8 92
3.4 Synthesis of $H_3ONb_3O_8$ from KNb_3O_8 93
3.4.1 Protonation of KNb_3O_8 using HCl 93
3.4.2 Stacking faults study of $H_3ONb_3O_8$ 97
3.4.3 Summary: $H_3ONb_3O_8$ 100
3.5 Dehydration of $H_3ONb_3O_8$ to HNb_3O_8 102
3.5.1 Structure of $H_3ONb_3O_8$ and HNb_3O_8 102
3.6 Future work: KNb_3O_8, HNb_3O_8 and $H_3ONb_3O_8$ 108
3.7 Summary: KNb_3O_8, HNb_3O_8 and $H_3ONb_3O_8$ 108

4 Synthesis and characterisation of a nanostructured niobate *via* exfoliation of $H_3ONb_3O_8$ 111

4.1 Introduction 111
4.2 Method: exfoliation and restacking of $H_3ONb_3O_8$ 113
4.3 Results: exfoliation and restacking of $H_3ONb_3O_8$ 114
4.4 Summary: Synthesis of restacked niobate 118
4.5 PDF analysis of restacked niobate using TOPAS 119
4.5.1 Introduction 119
4.5.2 Obtaining the XPDF 119
4.5.3 Setting up the refinement: Creating a model 120
4.5.4 Step one: Refinement from 7 Å onwards 124
4.5.5 Step two: Background fitting 126
4.5.6 Step three: Refining atomic positions 128
4.5.7 Step four: Removing potassium and adding restraints 131
4.5.8 Step five: Refinement of the full dataset 135
4.5.9 Step six: Refinement with additional ONb_3O_8 phase 138
4.6 Summary: Structure of restacked niobate 142

5 Synthesis and characterisation of nanostructured niobates *via* hydrothermal synthesis 145

5.1 Introduction . . . 145

5.1.1 Literature established methods . . . 145

5.2 Hydrothermal synthesis method . . . 148

5.3 Hydrothermal synthesis results . . . 149

5.3.1 Characterisation of hydrothermal nanostructured material . . . 154

5.3.2 Summary: Hydrothermal nanostructured . . . 158

5.3.3 Strengths and weaknesses: hydrothermal synthesis . . . 159

6 Synthesis and characterisation of nanostructured niobates *via* Lindqvist ion 161

6.1 Introduction . . . 161

6.1.1 The Lindqvist ion . . . 162

6.1.2 Synthesis of niobates using the Lindqvist salt . . . 163

6.1.3 Reported Lindqvist synthesis product $K_4Nb_6O_{17} \cdot nH_2O$ . . . 164

6.2 Method . . . 166

6.3 Results and discussion . . . 168

6.3.1 Structural characterisation of the Lindqvist salt . . . 168

6.3.2 Variable molarity of KOH . . . 172

6.3.3 Variable pH using HCl . . . 176

6.3.4 Variable heating duration . . . 183

6.3.5 Nanostructured $K_4Nb_6O_{17}$ product . . . 186

6.3.6 Summary: nanostructured $K_4Nb_6O_{17}$ . . . 192

7 Electrochemistry of niobates 195

7.1 Introduction . . . 195

7.1.1 The active materials . . . 195

7.1.2 Literature background . . . 195

7.2 Method . . . 199

7.2.1 Anode coating . . . 199

7.2.2 Coin cell assembly . . . 200
7.2.3 Cell cycling . . . 201
7.2.4 Data analysis . . . 201
7.3 Electrochemical testing . . . 202
7.3.1 KNb_3O_8 . . . 202
7.3.2 HNb_3O_8 . . . 208
7.3.3 Restacked niobate . . . 214
7.3.4 Hydrothermal nanostructured . . . 217
7.3.5 Nanostructured $K_4Nb_6O_{17}$ . . . 220
7.4 Probing the sodiated structure . . . 223
7.4.1 Literature background . . . 223
7.4.2 *Inoperando* XPDF Method . . . 224
7.4.3 KNb_3O_8 results: *inoperando* XPDF . . . 226
7.4.4 Restacked niobate results: *inoperando* XPDF . . . 230
7.5 Summary: Electrochemical testing of niobates . . . 234
7.5.1 Summary: Electrochemical performance . . . 234
7.5.2 Summary: Electrochemical performance and its structure . . . 237

8 Conclusion **241**

9 Future work **247**

10 Appendix: Benchmarking of cells by XRD raster scanning $LiFePO_4$ electrodes 251

10.1 Introduction . . . 251
10.2 Aims . . . 252
10.3 *Inoperando* and *Insitu* testing . . . 253
10.3.1 Air- and moisture-sensitivity . . . 253
10.3.2 Metastable phases . . . 253
10.3.3 Self-consistency . . . 254
10.3.4 $LiFePO_4$ cathode material . . . 255

10.4 Experimental methodology 257
10.4.1 Cell assembly 257
10.4.2 Cell cycling and disassembly 259
10.4.3 X-ray diffraction grid scan 259
10.4.4 Rietveld refinement and visualising the map 260
10.4.5 Rietveld refinement 262
10.5 Results and discussion 263
10.5.1 Weight percent of $FePO_4$ 263
10.5.2 Unit cell parameters of $FePO_4$ 265
10.5.3 Unit cell parameters of $LiFePO_4$ 267
10.6 Conclusion 268
10.6.1 Acknowledgements 268
10.6.2 Limitations and further work 269

Bibliography **270**

List of Figures

1.1 Lithium ion cell diagram. Cathode is made from a layered oxide $LiCoO_2$ whilst the cathode is made from graphite. The green spheres represent Li^+ ions which can move between anode and cathode. Diagram reproduced with permission from Dr Phoebe Allan. 3

1.2 The price of a lithium-ion battery ($LiMnO_2$ battery) vs. a theoretical sodium-ion battery ($NaMnO_2$) with the copper anode collected swapped for aluminium and operating with sodium.The cost is provided in USD and the paper was published in 2018. Image reproduced with permission from C. Vaalma *et al.*[5] 5

1.3 The average energy of anode materials used in SIBs are plotted material against their capacity. $Na_{2/3}Fe_{1/2}Mn_{1/2}O_2$ is used as the cathode material which has a potential of 2.74 V vs. Na^+/Na^0 to determine the average energy shown as blue and grey lines. Diagram reproduced with permission from M. Dahbi *et al.*[23] 7

1.4 1 Schematic showing the alloying process in which sodium moves into the metal lattice. The blue circles indicate metal or metalloid (M), whilst the yellow circles are sodium-ions. Diagram reproduced with permission from M. R. Palacin *et al.*[24] 8

1.5 Schematic showing the insertion process which can be described as homogeneous (solid solution) or heterogeneous (two-phase). The black circles indicate an empty space, whilst the yellow circles are sodium-ions. Diagram reproduced with permission from M. R. Palacin*et al.*[24] 9

1.6 Atomic structure of sodium carboxymethyl cellulose (CMC) as published by Merck.[32] 12

1.7 Schematic of the process of exfoliation and restacking of layered metal oxides. The green layers represent metal oxide layers whilst the red atoms are alkali earth ions. Image adapted from M. A. Tsiatsouri *et al.* (published under open access licence, CC-BY).[19] 18

1.8 a) $NaNb_3O_8$ b) KNb_3O_8. Potassium is shown as purple, sodium in yellow, whilst oxygen is depicted as red spheres. NbO_6 distorted octahedra are shown in green. The unit cell boundary is shown as a grey cuboidal outline. 27

1.9 Figure reproduced with permission from H. Nakayama *et al.*[143] Electrochemical testing results from KNb_3O_8 anode material within a sodium half cell. a) The first and second cycle galvanostatic profiles of KNb_3O_8 cycled at a rate of 3 $mAhg^{-1}$. b) The cyclic voltammetry of KNb_3O_8 collected at a scan rate of 0.05 mV/s from 0.1 V- 2.5 V. 34

2.1 Illustration of the geometric requirements for Bragg's law. 44
2.2 A schematic of how atom to atom distances correspond to peaks in the pair distribution function. Diagram obtained with permission from Yougui Liao.[149] 46
2.3 A schematic of the EH3 room (sample room) of the beamline I15-1 at Diamond Light Source, where the sample and detectors can be found (year: 2002). 57
2.4 Diagram of Stokes, Rayleigh and Anti-Stokes scattering processes. . . . 65
2.5 Example of a differential capacitance curve (DCC) for HNb_3O_8 in a sodium half cell. 71
2.6 Plot showing the change in voltage and current against time in a CV experiment. 73
2.7 Cyclic voltammetry results at sweep rates of 0.1 mV/s, 0.2 mV/s, 0.5 mV/s, 1.0 mV/s, 2.0 mV/s and 5.0 mV/s. 73

3.1 XRD patterns of KNb_3O_8, Nb_2O_5, $K_2Nb_4O_{10}$ and $K_2Nb_8O_{21}$ obtained from the PDF 4+ database ($\lambda = 1.542$ Å). 80
3.2 Unit cells depicted using green NbO_6 units with red spherical vertices representing oxygen and potassium as purple spheres for a) Nb_2O_5 b) $K_2Nb_4O_{10}$. 80
3.3 PXRD pattern of pellet-KNb_3O_8 (black) with the fit obtained from Rietveld refinement (red) and the difference line (blue). Tick marks showing the peak positions found for phases Nb_2O_5, $K_2Nb_4O_{10}$ and KNb_3O_8 obtained from the PDF 4+ database have been added at the bottom. For clarity purposes not all marks from Nb_2O_5 were added, any peaks less than 5 % intensity of the most intense Nb_2O_5 peak are unmarked. . 81
3.4 XRD patterns of samples synthesised using the parameters as outlined in Table 3.2. Tick marks for $K_2Nb_4O_{10}$ have been added at the bottom. 83
3.5 XRD patterns of samples made *via* molten salt synthesis using different molar ratios of K_2CO_3:Nb_2O_5 and KCl. 87
3.6 KNb_3O_8 XRD pattern obtained on I11 ($\lambda = 0.825255$ Å) with the results from Rietveld refinement with the d-spacing values. 88
3.7 Results from structural analysis of KNb_3O_8. a) Pair distribution function b) Raman spectra. 90

3.8 Results from structural analysis of KNb_3O_8. a) SEM b) High resolution STEM-HAADF. 91
3.9 Results from structural analysis of $H_3ONb_3O_8$. a) XRD pattern collected on I11 (λ = 0.825255 Å) and Rietveld refinement with the d-spacing values labelled. b) Pair distribution function c) Raman spectra. 94
3.10 Pawley fitting of $H_3ONb_3O_8$ on XRD pattern collected from I11 beamline (λ = 0.825255 Å) with tick marks in blue to show the expected peak locations. a) in the range 0- 50° 2θ. b) in the range 10- 20° 2θ. 95
3.11 Microscopy of $H_3ONb_3O_8$ a) SEM b) High resolution STEM-HAADF with some electron damage. 96
3.12 a) A schematic of the KNb_3O_8 structure transformed into the *Pmm2* unit cell with the K atoms replaced with O, shown in red; Nb atoms are in green. b) A colour map displaying the effect of changing parameters pa and pb to the r_{wp} values, where pa and pb change in steps of 0.25. . 97
3.13 Colour maps displaying the effect of changing parameters pa and pb to the r_{wp} values, where pa and pb change in steps of 0.02. a) In the range of 0-0.5 b) In the range of 0.5-1.0. 99
3.14 XRD plots of $H_3ONb_3O_8$ collected at I11 (λ = 0.825255 Å) in black with the Rietveld refinement results using the parameters pa and pb. 99
3.15 The PXRD patterns of HNb_3O_8, $H_3ONb_3O_8$ and KNb_3O_8 obtained from the PDF 4+ database (λ = 1.542 Å). 103
3.16 The dehydration of $H_3ONb_3O_8$ using TGA-MS. 104
3.17 Probing the dehydration of $H_3ONb_3O_8$ using VT-PXRD (λ = 1.542 Å) and then cooled to room temperature. With tick marks for HNb_3O_8 and $H_3ONb_3O_8$ as described in the PDF 4+ database. a) between 60 °C and 200 °C. b) between 80 °C and 100 °C. 105
3.18 Probing the dehydration of $H_3ONb_3O_8$ of VT-PXRD at temperatures a) 100 °C using Pawley refinement. b) 88 °C using Pawley refinement c) 80 °C using Pawley refinement. With tick marks for HNb_3O_8 and $H_3ONb_3O_8$. 106

4.1 A schematic diagram of the steps required to synthesise the restacked niobate from KNb_3O_8, with the TBAOH structure displayed explicitly in the lower right corner. 113
4.2 Microscopy images of restacked niobate. a) SEM b) STEM-HAADF. . . 114
4.3 Results from structural analysis of restacked niobate. a) XRD pattern (λ = 1.5406 Å) with the d-spacing values (given in Å) annotated. b) Pair distribution function c) Raman spectra of restacked niobate and $H_3ONb_3O_8$. 116

4.4 small angle scattering (SAXS) data of restacked niobate material. 117
4.5 Atomic model of a niobate layer in an unit cell with a large *b* parameter which exceeds 40 Å. The niobate octahedra are shown in green with red spheres representing oxygen. Purple spheres represent potassium. 120
4.6 A diagram illustrating the `beq_spherical` function given that `beq_low` = 0.1, `beq_high` = 0.5 and `radius` = 10. 123
4.7 Results from step one of small box analysis on the PDF collected from the restacked material. 124
4.8 Results from step two of small box analysis on the PDF collected from the restacked material. 126
4.9 Results from step three of small box analysis on the PDF collected from the restacked material. 128
4.10 Diagram of the refined one layer model obtained from step three of small box analysis of restacked niobate that produced a highly distorted niobate layer with abnormal K-O bond lengths. Niobate octahedra shown as green octahedra. Oxygen is shown as red spheres. 129
4.11 Results from step four of small box analysis on the PDF collected from the restacked material 132
4.12 Diagram of the refined one layer model obtained from step four of small box analysis of restacked niobate. Niobate octahedra shown as green octahedra. Oxygen is shown as red spheres. 132
4.13 Results from step five of small box analysis on the PDF collected from the restacked material. 136
4.14 Results from step six of small box analysis on the PDF collected from the restacked material. 138
4.15 Diagram of the one layer model obtained from small box analysis of the PDF dataset corresponding to the restacked nanostructured material. . 140

5.1 Raman spectra of hydrothermal products, synthesised with variations in the mass of KOH and pH (adjusted using HCl). 149
5.2 X-ray scattering results from I15-1 (λ = 0.161669 Å) of hydrothermal products synthesised with variations in the mass of KOH and pH (adjusted using HCl) a) XRD patterns b) Pair distribution function. 151
5.3 XRD pattern collected on I15-1 (λ = 0.161669 Å) of the product synthesised using 0.5 g KOH at pH 0-1 fit to Nb_2O_5 using Rietveld refinement (weighted profile R-factor (r_{wp}) of 10.75 %). 152
5.4 Results from XRD of hydrothermal nanostructured product, with d-spacing values annotated (λ= 1.54056 Å) 154

5.5 Microscopy images of hydrothermal product which was acidified to pH 2-3. a) Benchtop SEM b,c,d) High resolution STEM 155
5.6 Results from structural analysis of hydrothermal nanostructured product. a) Pair distribution function. b) Raman spectra. 156
5.7 Unit cell of $Nb_{12}O_{29}$ (ICSD: 155015) where the niobate octahedra are shown in green and oxygen are shown as red spheres. a) viewed along [010] b) viewed along [100] 157

6.1 Schematic of the hydrothermal synthesis of alkali niobates *via* Lindqvist intermediate. 162
6.2 Diagram of the Lindqvist ion $[Nb_6O_{19}]^{8-}$ Nb in green and oxygen in red. 162
6.3 Diagram of anhydrous $K_4Nb_6O_{17}$ structure. Distorted niobate octahedra shown in green with oxygen atoms in red whilst potassium ions are shown in purple. ICSD cif file: 35030. a) views along [001] b) viewed along [100].164
6.4 Pair distribution function collected from I15-1 (λ = 0.161669 Å) of the Lindqvist salt product with labelled r values in Å, with a small box refinement against $K_7[HNb_6O_{19}] \cdot 10\,H_2O$. 168
6.5 Results from structural analysis of the Lindqvist salt. a) XRD pattern collected on I15-1 (λ = 0.161669 Å) with a refinement against $K_7[HNb_6O_{19}] \cdot 10\,H_2O$. b) Raman spectra. 170
6.6 Pair distribution functions collected on I15-1 ($\lambda = 0.161669$ Å) of Lindqvist synthesis products made by varying the concentration of KOH. . . . 172
6.7 XRD collected on I15-1 ($\lambda = 0.161669$ Å) of Lindqvist synthesis products made by addition of KOH, Pawley fitted using the starting parameters obtained from $K_4Nb_6O_{17} \cdot 4.5\,H_2O$ (ICSD: 00-021-1297). 173
6.8 X-ray scattering data (collected on I15-1, $\lambda = 0.161669$ Å) from a range of hydrothermally synthesised products which was acidified to a range of pH. a) XRD patterns. b) Pair distribution functions. 177
6.9 Rietveld refinement on x-ray scattering data (collected on I15-1, λ = 0.161669 Å) of the sample synthesised at pH 5.65. a) XRD fitting to $K_4Nb_6O_{17}$ with d-spacing labels b) PDF fitting to $K_4Nb_6O_{17}$. 178
6.10 Rietveld refinement on x-ray scattering data (collected on I15-1, λ = 0.161669 Å) of the sample synthesised at pH 5.21. a) XRD fitting to KNb_3O_8 b) PDF fitting to KNb_3O_8. 179
6.11 Hypothesised mechanism regarding the phase transformation from KNb_3O_8 to $K_4Nb_6O_{17}$. 180
6.12 Hypothesised mechanism regarding the phase transformation from $K_4Nb_6O_{17}$ to KNb_3O_8. 181

6.13 X-ray scattering data collected on I15-1 ($\lambda = 0.161669$ Å) from a range of hydrothermally synthesised products form *via* the Lindqvist intermediate which was acidified to pH 5-6 and heated for 1-12 hrs. a) XRD patterns. b) Pair distribution functions. 184

6.14 A single layer of $K_4Nb_6O_{17}$ which is 20 units long in the *a* and *c* direction, and 0.25 unit cells high in *b*. The [NbO_6] unit in green tetrahedra with red vertices and K ions in purple. The grey box shows the outline of one unit cell. 186

6.15 XRD pattern of nanostructured $K_4Nb_6O_{17}$ (λ= 1.54056 Å). 187

6.16 Pair distribution function with the small box refinement results of nanostructured $K_4Nb_6O_{17}$. 188

6.17 Raman spectra of nanostructured $K_4Nb_6O_{17}$. 189

6.18 Microscopy images of nanostructured $K_4Nb_6O_{17}$ using a) Benchtop SEM b.c.d) High resolution STEM. 190

6.19 SAXS of nanostructured $K_4Nb_6O_{17}$. 191

7.1 Charge and discharge capacities of aged NMC pouch cells stored open circuit for 300 hrs at various SOC in 40 °C. Diagram reproduced from open access journal, originally produced by B. Gyenes *et al.*[218] 198

7.2 Electrochemical cell testing of KNb_3O_8. Cells cycled at 3 mAg^{-1} (left) and cells cycled at variable current or voltage (right) a) At 3 mAg^{-1} b) 5th charge and discharge cycle when cycled at rates of 3 mAg^{-1}, 10 mAg^{-1}, 20 mAg^{-1}, 40 mAg^{-1} and 100 mAg^{-1}. c) Capacity of each cycle at 3 mAg^{-1} d) Cell cycled at 10 mAg^{-1}, 20 mAg^{-1}, 50 mAg^{-1}, 100 mAg^{-1} and 200 mAg^{-1} for 5 cycles each e) dQ/dV plot of cell cycled at 3 mAg^{-1} f) Cyclic voltammetry at sweep rates of 0.1 mV/s, 0.2 mV/s, 0.5 mV/s, 2.0 mV/s and 5.0 mV/s. 203

7.3 Electrochemical cell testing of KNb_3O_8 using PVDF binder cycled at 3 mAg^{-1}. 205

7.4 The charge and discharge capacities of KNb_3O_8 with PVDF shown in red and blue, respectively, and the Coulombic capacity in green. The charge and discharge capacities of KNb_3O_8 with CMC are shown in orange and black, respectively. Both cells cycled at a rate of 3 mAg^{-1}. 206

7.5 Electrochemical cell testing of HNb_3O_8. Cells cycled at 3 mAg^{-1} (left) and cells cycled at variable current or voltage (right) a) At 3 mAg^{-1} b) 5^{th} charge and discharge cycle when cycled at rates of 3 mAg^{-1}, 10 mAg^{-1}, 20 mAg^{-1}, 40 mAg^{-1} and 100 mAg^{-1}. c) Capacity of each cycle at 3 mAg^{-1} d) Cell cycled at 10 mAg^{-1}, 20 mAg^{-1}, 50 mAg^{-1}, 100 mAg^{-1} and 200 mAg^{-1} for 5 cycles each e) dQ/dV plot of cell cycled at 3 mAg^{-1} f) Cyclic voltammetry at sweep rates of 0.1 mV/s, 0.2 mV/s, 0.5 mV/s, 2.0 mV/s and 5.0 mV/s. 209

7.6 Capacity and Coulombic efficiency of each cycle for HNb_3O_8 anode coating made using CMC binder in a sodium half cell cycled at 40 mAg^{-1}. . 211

7.7 Galvonostatic curves of HNb_3O_8 anode coating made using CMC binder in a sodium half cell cycled 40 mAg^{-1}. 212

7.8 Differential capacitance curve from galvanostatic cyling of HNb_3O_8 using CMC binder cycled at 40 mAg^{-1}. 213

7.9 Electrochemical cell testing of restacked niobate. Cells cycled at 3 mAg^{-1} (left) and cells cycled at variable current or voltage (right) a) At 3 mAg^{-1} b) 5^{th} charge and discharge cycle when cycled at rates of 3 mAg^{-1}, 10 mAg^{-1}, 20 mAg^{-1}, 40 mAg^{-1} and 100 mAg^{-1}. c) Capacity of each cycle at 3 mAg^{-1} d) Cell cycled at 10 mAg^{-1}, 20 mAg^{-1}, 50 mAg^{-1}, 100 mAg^{-1} and 200 mAg^{-1} for 5 cycles each e) dQ/dV plot of cell cycled at 3 mAg^{-1} f) Cyclic voltammetry at sweep rates of 0.1 mV/s, 0.2 mV/s, 0.5 mV/s, 2.0 mV/s and 5.0 mV/s. 215

7.10 Electrochemical cell testing of hydrothermal nanostructured. Cells cycled at 3 mAg^{-1} (left) and cells cycled at variable current or voltage (right) a) At 3 mAg^{-1} b) 5^{th} charge and discharge cycle when cycled at rates of 3 mAg^{-1}, 10 mAg^{-1}, 20 mAg^{-1}, 40 mAg^{-1} and 100 $mAhg^{-1}$. c) Capacity of each cycle at 3 mAg^{-1} d) Cell cycled at 10 mAg^{-1}, 20 mAg^{-1}, 50 mAg^{-1}, 100 mAg^{-1} and 200 mAg^{-1} for 5 cycles each e) dQ/dV plot of cell cycled at 3 mAg^{-1} f) Cyclic voltammetry at sweep rates of 0.1 mV/s, 0.2 mV/s, 0.5 mV/s, 2.0 mV/s and 5.0 mV/s. 218

7.11 The log of peak current against the log of sweep rate for CV sweep rates between 0.2 mV/s - 5 mV/s for nanostructured $K_4Nb_6O_{17}$. 220

7.12 Electrochemical cell testing of nanostructured $K_4Nb_6O_{17}$. Cells cycled at 3 mAg^{-1} (left) and cells cycled at variable current or voltage (right) a) At 3 mAg^{-1} b) 5^{th} charge and discharge cycle when cycled at rates of 3 mAg^{-1}, 10 mAg^{-1}, 20 mAg^{-1}, 40 mAg^{-1} and 100 mAg^{-1}. c) Capacity of each cycle at 3 mAg^{-1} d) Cell cycled at 10 mAg^{-1}, 20 mAg^{-1}, 50 mAg^{-1}, 100 mAg^{-1} and 200 mAg^{-1} for 5 cycles each e) dQ/dV plot of cell cycled at 3 mAg^{-1} f) Cyclic voltammetry at sweep rates of 0.1 mV/s, 0.2 mV/s, 0.5 mV/s, 2.0 mV/s and 5.0 mV/s. 221

7.13 a) The result from BVS mapping of KNb_3O_8. b) and c) both show $NaNb_3O_8$ structure using green octahedra with red vertices to represent $[NbO_6]$ units with purple Na atoms. The lithium intercalation sites x, y and z (shown in cyan, yellow and neon green, respectively) and a new sodium-ion site shown in blue-grey as described by K. McColl[131] and diagram recreated in VESTA for this study. b) Along [001] axis c) Along [010] axis 224

7.14 A cell specially designed for *inoperando* PDF collections on I15-1.[226] . 225

7.15 PDFs obtained during cell cycling of KNb_3O_8 plotted alongside the voltage profile. 226

7.16 XPDF pattern from the *inoperando* study of KNb_3O_8. a) The first pattern collected. b) The last pattern collected. 227

7.17 NMF results of *inoperando* XPDF cell testing of KNb_3O_8. a) Shows the change in weighting with XPDF scan number. A blue vertical dotted line indicates where two scans were removed due to a lack of x-rays at the synchrotron. b) The two components plotted between the range 0- 30 Å. c) The two components plotted between the range 0- 10 Å, with peak position labels for component one. d) The two components plotted between the range 0- 10 Å, with peak position labels for component two. 228

7.18 PDFs obtained during cell cycling of restacked niobate plotted alongside the voltage profile. 230

7.19 XPDF pattern from the *inoperando* study of restacked niobate. a) The first pattern collected b) The last pattern collected. 231

7.20 NMF results of *inoperando* XPDF cell testing of restacked niobate. a) Shows the change in weighting with XPDF scan number. A blue vertical dotted line indicates where two scans were removed due to a lack of x-rays at the synchrotron. b) The two components plotted between the range 0- 30 Å. c) The two components plotted between the range 0- 10 Å, with peak position labels for component one. d) The two components plotted between the range 0- 10 Å, with peak position labels for component two. 232

10.1 A diagram of $LiFePO_4$ unit cell. The FeO_6 units are shown in blue whilst PO_4 units are shown in pink. The oxygen atoms are shown as red sphere and the lithium atoms are shown as green spheres. a) As viewed along [021] direction. b) As viewed along the [001] direction. 256
10.2 A diagram of $FePO_4$ unit cell. The FeO_6 units are shown in blue whilst PO_4 units are shown in pink. The oxygen atoms are shown as red sphere. a) As viewed along [021] direction. b) As viewed along the [001] direction. 256
10.3 a) An image of a 1/8 inch PFA Swagelok tube fitting. b) A schematic of an *insitu* swagelock cell which is adapted for the I15-1 beamline c) The commercial cell (ECC-Opto-Std) used for *insitu* laboratory PXRD. *Images a, b and c obtained from Swagelock, P.K. Allan and EL-CELL respectively.* 258
10.4 A graph to show voltage over time as the labXRD cell was discharged. . 259
10.5 The colour map plot of the grid scans displaying the weight percent of $LiFePO_4$ which was used to generate a mask for different cells: a) Spring b) w/oSpring c) labXRD d) S-Swagelock. 261
10.6 The experimental XRD pattern (black) is shown alongside the calculated XRD pattern from Rietveld refinement (red) with the different line below (blue) for the 620th data point for each sample. a) Spring b) w/oSpring c) labXRD d) S-Swagelock. 262
10.7 The calculated weight percent of $FePO_4$ for each cell: a) Spring b) w/oSpring c) labXRD d) S-Swagelock. 264
10.8 The calculated unit cell volume of $FePO_4$ in units of $Å^3$: a) Spring b) w/oSpring c) labXRD d) S-Swagelock. 266
10.9 The error associated with each calculated unit cell volume of $FePO_4$: a) Spring b) w/oSpring c) labXRD d) S-Swagelock. 266

List of Tables

1.1 Definitions, symbols and units of the parameters used in a the calculation of maximum theoretical capacity. 15
1.2 Metal oxides that have been nanostructured and tested for their respective properties and applications. Table adapted and updated from S. Laurent *et al.*[39] 17
1.3 Nb, NbO and NbO_2 phases and their applications. 24
1.4 Crystal structure information for $ANbO_3$ and ANb_3O_8 phases. 26
1.5 Literature reports of MNb_3O_8 cell cycling capacities. 31
1.6 MNb_3O_8 phases tested within a sodium half cell between 0.1 V- 2.5 V at a rate of 3 mAg^{-1}. Table reproduced from the US patent submitted by the Toyota corporation regarding.[140] 35

2.1 Names of crystal system and the rules regarding unit cell parameters. . 41
2.2 Lattice system and their corresponding lattice points. Table reproduced from C. Giacovazzo.[146] 42
2.3 Information about the Wykoff position for space group *Pnma*, 62. Information obtaind from Bilbao Crystallographic Server.[144] 42
2.4 Properties of an XRD pattern and the sample information that can be derived from the property. 52
2.5 The properties observed in a Pair distribution function and the information that can be interpreted by analysing the property. 56
2.6 Definitions, symbols and units of the parameters used in a Nernst equation, adapted for Nb. 72
2.7 Properties of an XRD pattern and the sample information that can be derived from the property. 74

3.1 Crystallographic information for Nb_2O_5 $K_2Nb_4O_{10}$ and $K_2Nb_8O_{21}$. . . . 79
3.2 Various heating methods and their corresponding sample names. 83
3.3 Calculated weight percentages from Rietveld refinement. 84
3.4 Proportion of KCl, K_2CO_3 and Nb_2O_5 used as a reagent in the molten salt synthesis of KNb_3O_8 86
3.5 Rietveld refinement results from molten salt synthesis. 87
3.6 Peaks identified in the D(r) matched to the known atomic distances of KNb_3O_8. 89
3.7 A table of results from χ^2 minimisation analysis methods to study KNb_3O_8. 89

3.8 Peaks identified in the Raman spectra for KNb_3O_8 obtained from this study compared against the reported wavenumbers for KNb_3O_8 have been obtained from J.K D. de Souza *et al.*[177] whilst the assignment was made using B. Yu *et al.* reports on KNb_3O_8.[186] 91
3.9 The implications of probability parameters pa and pb on the structure of the material, liked to the phases KNb_3O_8 and $NaNb_3O_8$, but the interlayer ions are oxygen (instead of K or Na) in the model. 98
3.10 The phases HNb_3O_8 and $H_3ONb_3O_8$ and its information, obtained from the PDF 4+ database. 103
3.11 Crystallographic information obtained from the Pawley refinement of the dehydration of $H_3ONb_3O_8$ at 80 °C, 88 °C and 100 °C. 107

4.1 Wykoff position information for the space group *Amam* belonging to KNb_3O_8. 120
4.2 KNb_3O_8 atomic sites obtained from ICSD code: 31994. 121
4.3 Table of parameters used to define the atomic sites of a single layer of KNb_3O_8 in a *P1* unit cell. 121
4.4 Table of parameters used to define the atomic sites of a single layer of KNb_3O_8 in a *P1* unit cell. 122
4.5 Table summarising the results from step one of small box refinement on the XPDF of restacked niobate. 125
4.6 Table summarising the results from step two of small box refinement on the XPDF of restacked niobate. 127
4.7 Table summarising the results from step three of small box refinement on the XPDF of restacked niobate. 130
4.8 Table of parameters used to define the atomic sites of a single layer of KNb_3O_8 in a *P1* unit cell, before and after refinement. Values without errors have not been refined. 130
4.9 Table summarising the results from step four of small box refinement on the XPDF of restacked niobate. 132
4.10 Results from step four of the refinement: the distance restraints placed between atoms in the one layer structure with a tolerance of 0.1 Å and a penalty of 1. 133
4.11 Results from step four of the refinement: the angle restraints placed between atoms in the one layer structure with a tolerance of 5 ° and a penalty of 1. 133
4.12 Table of parameters used to define the atomic sites of a single layer of KNb_3O_8 in a *P1* unit cell, before and after refinement. Values without errors have not been refined. 134

4.13 Table summarising the results from step five of small box refinement on the XPDF of restacked niobate. 135
4.14 Table of parameters used to define the atomic sites of a single layer of KNb_3O_8 in a *P1* unit cell, before and after refinement. Values without errors have not been refined. 136
4.15 Results from step five of the refinement: the distance restraints placed between atoms in the one layer structure with a tolerance of 0.1 and a penalty of 1. 137
4.16 Results from step five of the refinement: the angle restraints placed between atoms in the one layer structure with a tolerance of 5 ° and a penalty of 1. 137
4.17 Table summarising the results from step six of small box refinement on the XPDF of restacked niobate. 139
4.18 Table of parameters used to define the atomic sites of a single layer of KNb_3O_8 in a *P1* unit cell, before and after refinement. Values without errors have not been refined. 140
4.19 Results from step six of the refinement: the distance restraints placed between atoms in the one layer structure with a tolerance of 0.1 and a penalty of 1. 141
4.20 Results from the angle restraints placed between atoms in the one layer structure with a tolerance of 5 ° and a penalty of 1. 141

5.1 Bands identified in the Raman specta for sample 1g KOH// pH 5-6 compared to those reported by B. Balachahdean *et al.*[199] for Nb_2O_5. . 150
5.2 Table summarising the results from refinement of 0.5 g KOH at pH 0-1 fitted to literature reported structure of Nb_2O_5 (space group *P2/m*, ICSD: 29) 152
5.3 Table of results from small box fitting of hydrothermal nanostructured PDF to known phases obtained from the ICSD database. 157

6.1 The unit cell parameters for $K_4Nb_6O_{17}$ and its reported hydrated forms. 165
6.2 Synthesis conditions used in part two of the Lindqvist synthesis study. 167
6.3 Peaks identified in the XPDF of Lindqvist salt of this study and their assignment based on the reported structure of $K_7[HNb_6O_{19}] \cdot 10\,H_2O$ (ICSD: 391372), compared to the assignments made by O.G. Grendal *et al.*[214] based on their XPDF of Lindqvist salt containing NH_4^+ ions. 168
6.4 Refinement results of Lindquist salt compared to tthe reported structure of $K_7[HNb_6O_{19}] \cdot 10\,H_2O$ (ICSD: 391372). 169
6.5 Peaks identified in the Raman specta compared to the Raman spectra of $Na_7(HNb_6O_{19}) \cdot 15\,H_2O$ as identified by H. Tong of *et al.*[201] 171

6.6 Synthesis conditions . . . 172
6.7 Results of Pawley fitting the XRD patterns collected from products synthesised *via* the Lindqvist ion to $K_4Nb_6O_{17} \cdot 4.5\,H_2O$ (00-021-1297). . . . 174
6.8 Synthesis conditions . . . 176
6.9 Results of small box refinements performed on the XRD and PDF data collected on samples synthesised at pH 5.21 and pH 5.65. . . . 179
6.10 Synthesis conditions . . . 183
6.11 Peaks identified in the XRD pattern of samples synthesised at pH 5-6 for a varied duration given as d-spacings in units of Å. The three most intense peaks have been written in bold font. . . . 185
6.12 Table summarising the results from small box refinement on the XPDF of nanostructured $K_4Nb_6O_{17}$, using a one layered model based on $K_4Nb_6O_{17}$. 188
6.13 Bands identified in the Raman specta for $K_4Nb_6O_{17}$ by M. Maczka *et al.*[184] compared to the Raman spectra of nanoctructured $K_4Nb_6O_{17}$ collected in this study. . . . 190

7.1 Table reproduced from J. Guo *et al.*[219] of various reported mechanisms that could cause an observed increase in cell capacity. . . . 197
7.2 Calculated capacities of each active material at the end of cycle one, two and 20th cycle capacity at various rates. . . . 219
7.3 Table matching the peak locations as obtained by non-negative matrix factorization (NMF) analysis and known atomic distances of KNb_3O_8 to study *inoperando* changes to the local atomic structure. . . . 229
7.4 Table matching the peak locations as obtained by NMF analysis and known atomic distances of restacked nanostructured to study *inoperando* changes to the local atomic structure. . . . 231
7.5 Discharge capacities of each niobate-based active material at the end of cycle one, two and the 20th cycle when cycled at of 3 mAg^{-1}, 10mAg^{-1}, 20mAg^{-1}, 40 mAg^{-1} and 100 mAg^{-1} in a sodium half cell. . . . 234
7.6 Table of peaks observed in the dQ/dV sodiation curves for niobate samples given in units of V. . . . 236
7.7 Table of peaks observed in the dQ/dV desodiation curves for niobate samples given in units of V. . . . 236
7.8 The interlayer distance for each material. . . . 238

10.1 The four various types of cells investigated in this benchmarking study . 259
10.2 The dimensions of the grid scans obtained for each cathode sample . . . 260
10.3 The minimum, maximum, mean and standard deviation of weight percent of $FePO_4$ values observed in the insert grid scans presented in Figure 10.7 for each cell. . . . 264

10.4 The unit cell properties of $FePO_4$.[231] 265
10.5 The minimum, maximum, mean and standard deviations of the unit cell volume of $FePO_4$. 265
10.6 The unit cell properties of $LiFePO_4$.[231] 267
10.7 The minimum, maximum, mean and standard deviations of unit cell volume of $LiFePO_4$. 267

Introduction to this thesis

This thesis begins with a Literature review in Chapter One which outlines the aims of this study; to characterise disordered niobates to understand their electrochemcial properties within a sodium-ion cell. This Chapter also presents relevant concepts such as battery chemistry and niobate chemistry and the current state of research, at the time of this work.

Chapter Two presents the theory and practices of analytical techniques used throughout this thesis, such as x-ray diffraction (XRD), x-ray pair distribution function (XPDF), microscopy and Raman spectroscopy.

Chapter Three begins with the synthesis of crystalline KNb_3O_8 *via* conventional solid state synthesis and molten salt methods. The KNb_3O_8 ion-exchanged product, $H_3ONb_3O_8$ and its subsequent dehydrated form HNb_3O_8 is also studied. The products, KNb_3O_8, $H_3ONb_3O_8$ and HNb_3O_8, are all characterised using conventional solid state methods.

Chapter Four utilises $H_3ONb_3O_8$ as a reagent to synthesise a disordered restacked niobate, this was achieved by the established "top down" method, known as exfoliation and restacking. The product, restacked nioabte, was characterised using a novel one layer model in the small box refinement of XPDF data.

Chapter Five details a "bottom up", hydrothermal synthesis method to form disordered niobates. This was attempted as it decreased synthesis time, and utilises a greener synthesis method compared to solid state heating methods. This method yielded a product known as hydrothermal nanostructured, a niobate phase formed from corner shared NbO_6 units. Unfortunately, the low solubility of Nb_2O_5 reagent was not ideal,

therefore an more soluble niobate source was studied in the following Chapter.

Chapter Six outlines the hydrothermal synthesis of the Lindqvist ion, a superoctahedraon of niobate octahedra with superior solubility in water. Using the Lindqvist ion, nanostructured $K_4Nb_6O_{17}$ was synthesised, a turbostatically disordered layered material, in which the connectivity within the layer is the same as that of bulk $K_4Nb_6O_{17}$.

Chapter Seven discusses the aforementioned characterised materials (KNb_3O_8, HNb_3O_8, restacked niobate, hydrothermal nanostructured and nanostructured $K_4Nb_6O_{17}$) which are then tested for applications as an anode active material within a sodium-ion half cell, to probe the electrochemical characteristics. Additionally, *in-operando* XPDF was used to understand the structural changes of these phases upon discharging and charging.

The Conclusion is presented in Chapter Eight and Further work is presented in Chapter Nine, to summarise the work presented.

The Appendix includes a short, separate case study of $LiFePO_4$ within various types of batteries.

1 Literature review

1.1 Introduction to batteries

1.1.1 The important role of batteries in society

Decreasing greenhouse gas emissions is imperative to maintaining the delicately balanced ecosystems which allow us to thrive. Therefore UK has committed to achieving net zero emissions by 2050, which involves fully decarbonising the power system by 2035.[1] This ambitious aim is backed by £26 billion of government capital investment. Furthermore, UK Research and Innovation (UKRI) and the National Academy are funding research towards achieving national energy security, with an initial £1 billion of investment (2023/24 Financial Year) towards this endeavour.[1]

Decarbonisation poses a new challenge, as previously fossil fuel could be instantly burnt to generate more electricity to meet demand. However renewable energy is an unpredictable method of generating energy and often the energy supply does not match the demand. Therefore, during times of surplus, excess energy needs to be stored and then released when demand increases. This requires high-power grid energy storage which can accommodate irregular charging cycles whilst being safe and cost effective.

Batteries are well-established within our society due to their ability to store energy chemically which can be released as electricity. Lithium-ion batteries were first commercialised by Sony in 1991, and it is still undergoing constant innovation to meet our increasing energy demands, for example within electric vehicles.[2,3] Lithium-ion batteries have dominated the mobile energy sector due to their high gravimetric density

(high energy capacity per unit weight). However, lithium-ion battery technology is facing a similar fate to crude oil, as scientists are now predicting when the world's lithium supply will be exhausted.[4] Furthermore, political monopolies and rising prices of raw materials required for battery manufacture pushes the government, industry and scientists to look for new solutions.[5] One line of research focuses on developing sodium-ion batteries as an alternative in applications where the importance of cost, cyclability and fast charging rates outweighs the importance of high gravimetric energy,[6,7] such as stationary batteries.

1.1.2 How batteries work: Lithium-ion batteries

There are three main components of a cell; the anode (negative electrode), cathode (positive electrode) and electrolyte. The anode is the material which undergoes oxidation under cell discharge (e.g. graphite), whilst the cathode is the material which undergoes reduction during cell discharge (e.g. $LiCoO_2$ or $LiFePO_4$). There is also the charge carrier which is lithium in a lithium-ion battery (LIB), or sodium in a sodium-ion battery (SIB).

During cell charging (Figure 1.1), lithium-ions move out of the cathode (delithiation) and into the anode (lithiation) whilst electrons move similarly from the cathode to anode, but *via* the external circuit. This is because the electrolyte (usually a mixture of alkylcarbonates and a lithium salt, such as $LiPF_6$) is a good ionic conductor whilst being a poor electronic conductor which forces the electrons to move separately to the lithium-ions.[8] This process requires an external source of energy e.g. electricity from a wall socket. During cell discharge the lithium-ions and electrons move from the anode, back into the cathode *via* the same medium. As the electrons move *via* the external circuit, it can perform work e.g. the bulb lights up. Due to the shuttling of lithium-ions and electrons back and forth within the cell it is sometimes termed a rocking chair battery.

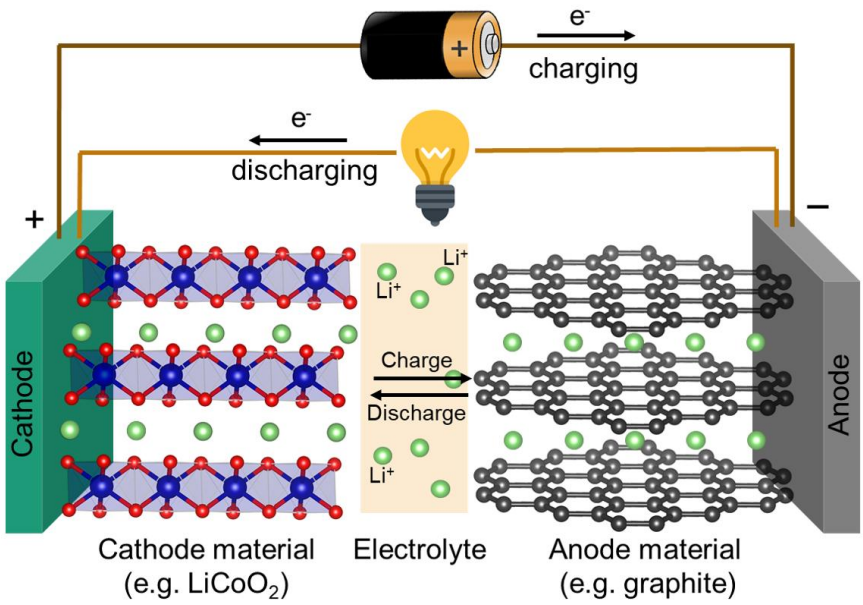


Figure 1.1: Lithium ion cell diagram. Cathode is made from a layered oxide $LiCoO_2$ whilst the cathode is made from graphite. The green spheres represent Li^+ ions which can move between anode and cathode. Diagram reproduced with permission from Dr Phoebe Allan.

1.1.3 Beyond lithium-ion batteries

Sodium-ion batteries (SIBs) is attracting attention due to the many issues related to lithium-ion batteries (LIBs) such as the supply chain concerns, with most of the lithium reserves being located outside of Europe. The importance of securing a reliable supply chain has only been highlighted by the shortages caused by Russian-Ukraine war and by the recent semi-conductor chip shortage.[9,10,11] There are other concerns such as the use of child labor in cobalt mining (commonly used in LIB cathodes) and the dangerous chemicals used within batteries which hinders a circular economy, thereby straining the supply of lithium further, as a result, alternatives are required.[7,12,13]

Sodium is widely accessible in the form of salt from seawater, or from rocks. Therefore, the UK has access to a direct source, whereas lithium brine reserves are

not found anywhere in Europe.[14] Sodium is also one of the most abundant elements on Earth. Due to the higher supply of sodium than lithium, sodium is cheaper. As a result, sodium-ion batteries (SIBs) could be a cheaper, more ethical alternative to lithium.

1.1.4 Chemistry of sodium vs. lithium

There are key differences between lithium-ion battery technology and its sodium-ion counterpart:

1. Sodium does not intercalate into graphite

Graphite is the anode of choice within LIBs however it is incompatible with sodium showing negligible sodium intercalation (approximately NaC_{186}).[15] One of the biggest bottlenecks in the widespread commercialisation of SIBs is the lack of appropriate anode materials.

2. Sodium is significantly heavier than lithium

The mass of sodium and lithium are 22.99 g mol^{-1} and 6.94 g mol^{-1}, respectively. Therefore, sodium-ion batteries are expected to provide poorer gravimetric capacity than its LIBs counterpart, if analogous materials are used. Consequently, sodium-ion batteries are not expected to match lithium-ion batteries in terms of volumetric or gravimetric energy density (about 30-50 % lower energy density expected).[16] However, sodium-ion batteries are expected to be a cheap alternative to lithium-ion batteries with raw materials such as Na_2CO_3 costing 0.11 EUR per kg whilst Li_2CO_3 costing 6.93 EUR per kg (average price from 2007-2017).[17] As a result, sodium-ion batteries are predicted to complement the use of LIBs.[12,18,19]

3. Sodium possess a higher redox potential than lithium

Sodium (-2.71 V vs standard hydrogen electrode (SHE)) has a slightly higher redox potential than lithium (-3.05 V vs. SHE), this decreases the achievable energy density

of sodium cells compared to lithium.[20] This has implications for the materials that can be used as current collectors. LIBs requires aluminium and copper as current collectors on the cathode and anode, respectively. On the other hand, SIBs can operate using aluminium for both its current collectors as aluminium does not alloy with sodium at low voltages.[21] The cost of a theoretical, comparable SIBs and LIBs was calculated and SIBs were predicted to be 12.5 % cheaper than LIBs (Figure 1.2).[21] Moreover, the use of copper in LIBs forces the battery to be transported with a 5- 30% state of charge to prevent copper dendrite formation as aluminium alloys with lithium below 0.1 V.[21] SIBs can be transported fully discharged which is much safer.[5] However, this modification from copper to aluminium increases the size of sodium-ion batteries as the volume of aluminium current collector required is larger than the volume of copper.[21] This provides poorer volumetric capacity of the overall cell. S. Roberts *et al.*[21] modelled a standard cell to contain current collector thicknesses of: 10 μm for copper and 20 μm for aluminium. However, copper is over 3 times heavier per cm^3 and therefore a swap to aluminium current collectors could also potentially improve gravimetric capacity.

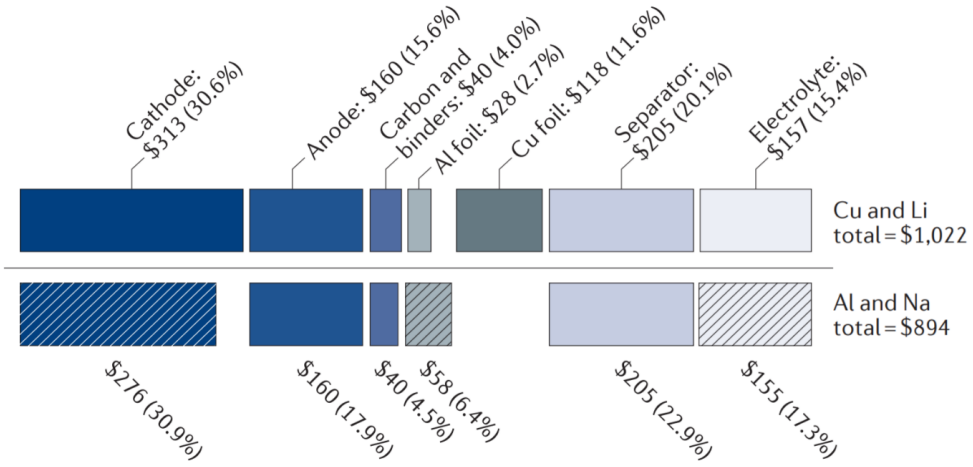


Figure 1.2: The price of a lithium-ion battery ($LiMnO_2$ battery) vs. a theoretical sodium-ion battery ($NaMnO_2$) with the copper anode collected swapped for aluminium and operating with sodium.The cost is provided in USD and the paper was published in 2018. Image reproduced with permission from C. Vaalma *et al.*[5]

4. Sodium is larger than lithium

Sodium-ions are larger than lithium-ions, therefore greater electrode volume changes on cycling are expected within SIBs, as the ions move in and out of the electrode. This leads to cracking of the active material particles, increasing solid electrolyte interphase (SEI) and can cause electrical isolation from the current collector. This can also cause problems with the battery housing if the volume changes are large.

For example, a study comparing Li^+ and Na^+ insertion into $FePO_4$ it was determined Na^+ diffused slower than Li^+ and the volume change upon insertion was greater for Na^+ than Li^+ (17 % and 10 % respectively), both negative side effects of using a larger charge carrier.[22]

1.1.5 Sodium-ion battery anode materials

A major issue with sodium-ion batteries is the lack of anode materials which possess both high capacity and a high coulombic efficiency. One obvious material is to study graphite as it has proven effective for lithium-ion batteries with a capacity of 372 $mAhg^{-1}$. However it has proven ineffective in SIB with negligible sodium intercalation (approximately NaC_{186}).[15]

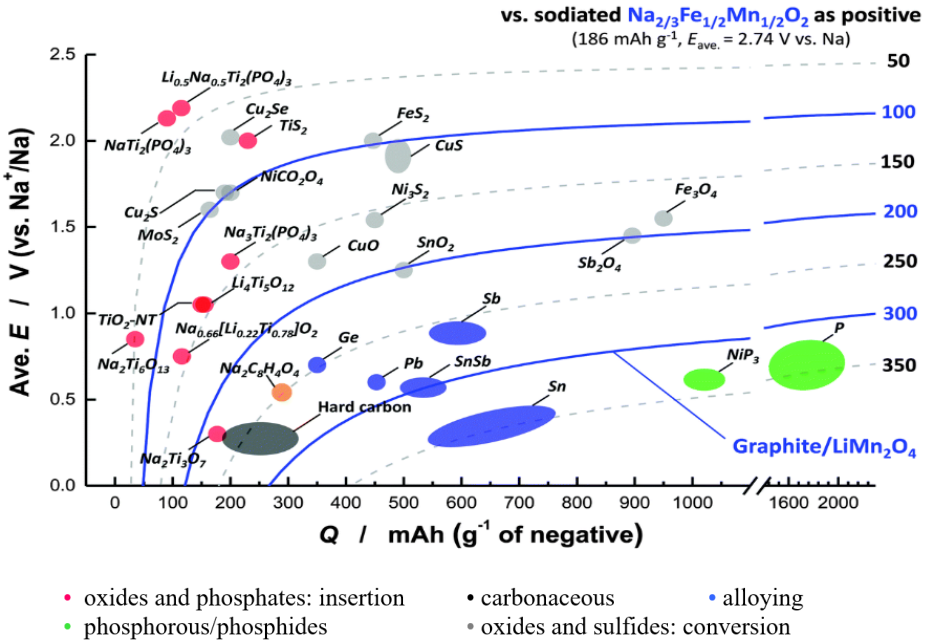


Figure 1.3: The average energy of anode materials used in SIBs are plotted material against their capacity. $Na_{2/3}Fe_{1/2}Mn_{1/2}O_2$ is used as the cathode material which has a potential of 2.74 V vs. Na^+/Na^0 to determine the average energy shown as blue and grey lines. Diagram reproduced with permission from M. Dahbi *et al.*[23]

There are a variety of anode materials being explored for use for SIBs. These anode materials can be classified into three main categories: insertion, alloying and conversion, depending on its mechanism (Figure 1.3).

1.1.6 Alloying anodes

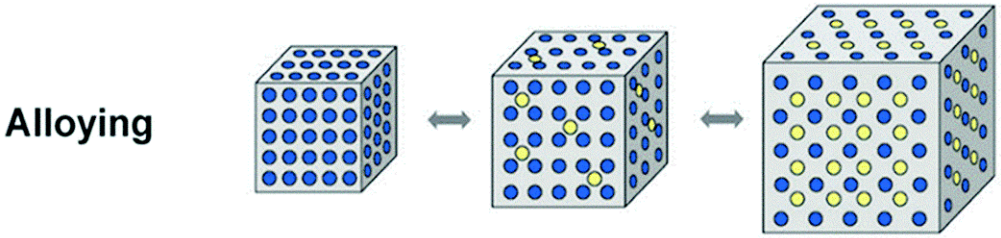


Figure 1.4: 1 Schematic showing the alloying process in which sodium moves into the metal lattice. The blue circles indicate metal or metalloid (M), whilst the yellow circles are sodium-ions. Diagram reproduced with permission from M. R. Palacin *et al.*[24]

The process of alloying involves the metal/metalloid with sodium to form an alloy (Na_zM) as shown in in Figure 1.4. This involves breaking M-M bonds. Group 14 and 15 are metals typically undergo alloying with sodium (e.g. tin).[25]

This mechanism involves more than one electron per one metal or metalloid atom (M) and therefore many sodium-ions can be alloyed to one M (Equation 1.1). This provides excellent capacity, however alloying also causes huge volume expansion which leads to more rapid capacity fade and shorter lifetimes as electrode materials self-pulverize and delaminate over cycling (Figure 1.4).[25]

$$M + z\mathrm{Na}^+ + z\mathrm{e}^- \rightleftharpoons Na_zM \tag{1.1}$$

1.1.7 Conversion anodes

A transition metal system, represented by MX where M is a transition metal and X is an oxygen, chalcogen (e.g., S, Se, and Te) or halogen, can host sodium-ions (Equation 1.2).[25,26] For example, in CuO, the oxidation of copper oxide to decrease to form Cu^0 whilst forming Na_2O. There is a change in the oxidation state of the transition metal (M) to zero. Conversion allows for high theoretical and experimental capacities but

still suffers from large volume expansion problems, although to a lesser degree than alloying anodes.

$$M_aX_b + (b)Na^+ + (b)e^- \rightleftharpoons aM^0 + (b)Na_cX \tag{1.2}$$

1.1.8 Insertion anodes

The mechanism by which lithium is inserted into a graphite anode or sodium into a layered metal oxide material is known as insertion. The insertion process can be homogeneous (i.e. solid-solution) or heterogeneous (i.e. two-phase process) as outlined in Figure 1.5.

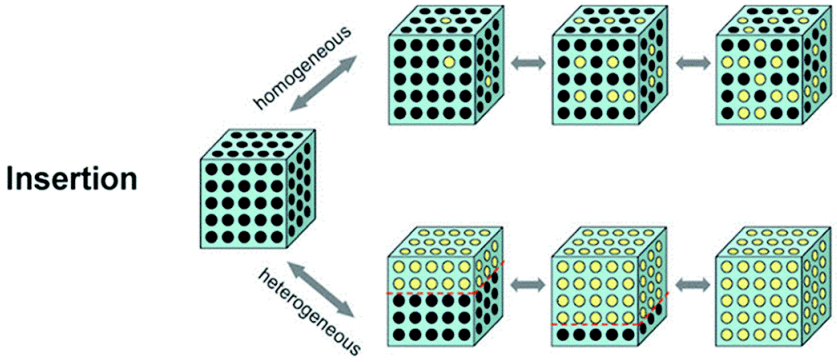


Figure 1.5: Schematic showing the insertion process which can be described as homogeneous (solid solution) or heterogeneous (two-phase). The black circles indicate an empty space, whilst the yellow circles are sodium-ions. Diagram reproduced with permission from M. R. Palacin *et al.* [24]

Insertion is limited to one electron transfer per metal redox couple which leads to its lower theoretical capacity, compared to alloying and conversion type anodes. [25] In practice, it is also limited by the number of intercalation sites, diffusion and kinetic behaviour and the potential of insertion, as at 0 V vs Na^+/Na sodium plating can take place. Nevertheless, materials typically undergo small volume changes unlike alloying and conversion mechanism materials. Therefore, insertion materials tend to be more stable over many cycles despite possessing a lower theoretical capacity.

Insertion is typically observed in carbonaceous, oxide and phosphate based anode ma-

terials. Generally layered materials which allow for 2D diffusion between the layers (e.g. lithium diffusion in and out of graphite) has proven to be an effective structure.

1.1.9 Summary: Anode types

A high-power energy grid storage anode requires an anode material which remains stable throughout many irregular charge and discharge cycles. Secondly the weight density of the material is of little importance as the battery will remain stationary throughout its use. Despite the high capacity of alloying and conversion anode materials, its tendency to self-pulverise means its poorly suited to the long term demands of a high-power energy grid anode material. Ideally, an open and layered structure which can facilitate diffusion is favoured for insertion anode materials. [27]

1.1.10 Components and features of an anode coating

The active material is the redox active material, for example $LiFePO_4$ as a cathode material and graphite for an andoe material. The active material is often a loose powder, with less than ideal electron conductivity. Therefore to improve this, carbon black is added. To hold this powder matrix together during repetitive cycling, a binder is used, often a polymer based material due to its flexibility and adhesive properties.

Therefore the anode active material is often mixed in with a binder and carbon alongside a solvent to create a slurry which is cast onto a metal current collector. As the solvent evaporates, a thin, homogeneous anode coating remains which is flexible to volume changes and is electrically conductive. This singular cohesive coating cast on a metal current collector can be easily assembled into a cell.

Role of the carbon black

Although alternatives are sometimes used to improve conductivity, carbon black is the most commonly used additive. Carbon black is a good electron conductor and therefore mixing in carbon black with the active material improves its electrical conductivity, which improves battery performance. Carbon black used in an electrode applications, possess a high surface area and is ground into an extremely fine powder, is then handled in a powder handling unit throughout this project.

Adding carbon to the active material has is most simply achieved by grinding them together, although more complex processes has been explored such as adding carbon to an autoclave during synthesis of the active material.[28] Additionally, alternative forms of carbon such as carbon nanotubes have also been explored.[29]

Role of the binder

Due to the volume changes which occur during cell cycling, the binder has to be flexible and able to withstand many cell cycles, therefore these are often made from polymer-based materials. Polymers are flexible and adhesive which minimises electrical isolation

due to volume changes. One common binder is polyvinylidene fluoride (PVDF), which is formed from the polymerisation of CH_2CF_2 and is now widely used as a binder in electrode coatings and is the most commonly reported binder in sodium-ion battery papers.[30] PVDF itself is an electron insulator and therefore requires additional conductive matrix such as carbon black to be added into the coating formulation. However there are reports regarding PVDF which indicate alternative binders maybe more suitable in some systems; for example sodium carboxymethyl cellulose (CMC).

CMC (Figure 1.6) is a linear polymer with two functional groups. Firstly, the carboxylate anion with the β-linked glucopyranose residues that makes it water soluble. Secondly, the hydroxyl (–OH) groups give favorable adhesive strength and uniform active material dispersion in water to form a gel-like substance.[31]

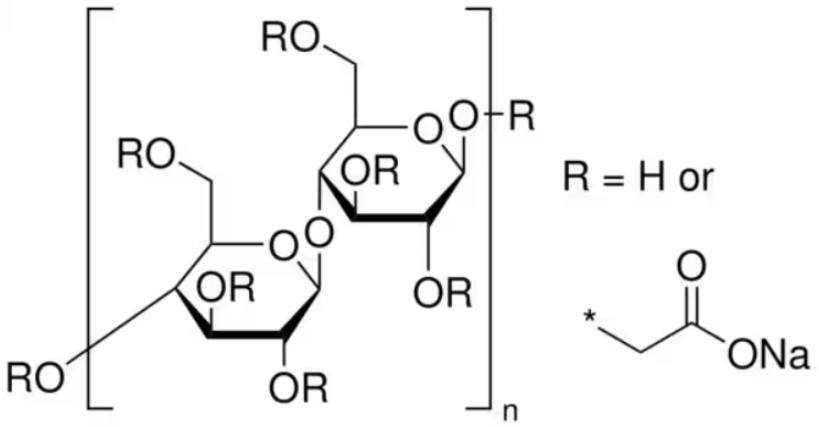


Figure 1.6: Atomic structure of sodium carboxymethyl cellulose (CMC) as published by Merck.[32]

CMC is a water soluble binder and therefore dangerous solvents are not required, unlike when utilising PVDF which is often paired with N-Methylformamide (often abbreviated to NMF)* which is highly toxic, volatile and flammable.[31] CMC is also significantly cheaper than PVDF (1-2 EUR per kg and 15-18 EUR per kg respectively), which will contribute to lower battery costs.[31]

*NMF in this thesis stands for non-negative matrix factorisation

A paper published by C. Wang *et al.*[33] compares the two binders, they reported CMC possessed superior stability compared to PVDF, as CMC is more stable at low voltages. Furthermore defluorination of PVDF leads to changes in the adhesive property of the binder which causes cracking. When PVDF and CMC were cycled with TiO_2 nanoparticles, PVDF showed cracking whilst CMC did not.[33] There is also further evidence that the formation of a passive protective layer protects the electrode and also prevents the electrode from cracking, improving the Coulombic efficiency.[30] Additionally, CMC has been shown to bind more strongly (4 Newton) than PVDF (2 Newtons), a desired characteristic.[30] Enhanced cycling stability and capacity retention have been reported for a range of electrodes (antimony electrodes and sodium titanate electrodes) in a SIB when using CMC compared to PVDF.[34,35]

However, CMC-based electrodes can be prone to brittleness due to its inelasticity in some formulations (overall lower Young's modulus and tensile strength) and therefore may not always show superior performance compared to PVDF.[31]

1.2 Battery testing

It is important to quantify the properties of a battery so that their electrochemical behaviour can be critically compared. These concepts will be introduced in this section to enable a more detailed discussion about SIB anode materials.

Half-cell

Typically when studying the feasibility of an anode or cathode material, a half-cell is used as this allows for the testing of anode or cathode, independent of the effects caused by the opposite electrode. A half cell consists of the electrode of interest alongside a pure metal electrode, corresponding to the charge carrier of the battery. Therefore there is always an abundance of the charge carrier within the system. Detailed methodology regarding cell assembly can be found in the Chapter 7, this section will focus on the theory behind established electrochemical testing techniques.

1.2.1 How to calculate theoretical capacity

Theoretical capacity (Equation 1.3) is commonly used to indicate the maximum capacity that is possible by identifying the number of electrons partaking in redox reactions in one gram of material. In KNb_3O_8, if you consider that each Nb can provide one electron *via* the single redox couple: Nb^{5+}/Nb^{4+}, then $n = 3$ which provides a theoretical capacity of 180.36 $mAhg^{-1}$.

$$Q_{theoretical} = \frac{1000 \times nF}{3600 \times M_W} \tag{1.3}$$

In Equation 1.3, the 1000 is used to convert A into mA and the 3600 is used to convert s into hrs.

Table 1.1: Definitions, symbols and units of the parameters used in a the calculation of maximum theoretical capacity.

Symbol	Information	Units
$Q_{theoretical}$	Capacity	$mAhg^{-1}$
n	Number of electrons	a.u.
F	Faraday constant	sA/mol
M_W	Molecular weight	g/mol

1.2.2 Galvanostatic charge discharge

In galvanostatic charge/discharge experiments, a current is applied to the cell, this is often given either as a C rate or as mAg^{-1}. This experiment charges and discharges the cell in a controlled method to determine its capacity.

Anode studies

In the study of anode materials, the cell is first discharged and the voltage drops by applying a negative current. In a SIB, this causes the sodium to intercalate into the anode material (sodiation), and during cell charging, sodium moves out of the anode (desodiation). This is different for cathode material studies, in which the first charging step is a desodation step.

C rate calculations

Applying a current at a rate of 0.1 C (equal to a rate of C/10) would apply the current required to fully charge/ discharge the cell in 10 hours, whilst a rate of 2 C corresponds to full charge in 0.5 hrs (Equation 1.4). Therefore large C rates indicate fast charging (i.e. 2 C) whilst small C rates indicate slow charging (i.e. 0.1 C). The C rate is dependent on the active material's theoretical capacity and also the mass of the active material in the cell.

$$\frac{1}{Number\ of\ hours} = C\ rate \tag{1.4}$$

Alternative to using C rate

An alternative method is to apply a set number of amps, per gram of active material

present in the cell (mAg^{-1}). This has the benefit of not requiring a maximum theoretical capacity in the calculation as this value is not always obtainable, for example in the instance of a novel disordered material.

Coulombic Efficiency

The capacity of the cell can be calculated from a known rate (C rate or mAg^{-1}) which is given in units of $mAhg^{-1}$, the larger the value the greater the capacity. This can be calculated for both charge and discharge cycles, and the relationship between these values is known as Coulombic efficiency.

The Coulombic Efficiency of an anode is calculated using Equation 1.5, which describes the ratio between sodiation and desodiation. Ideally a Coulombic Efficiency of 100 % is observed, which implies all the sodium inserted into the anode is removed during the subsequent charge cycle.

$$\frac{Discharge\ capacity}{Charge\ capacity} = \frac{Sodiation\ capacity}{Desodiation\ capacity} = Coulombic\ Efficiency \tag{1.5}$$

Further analysis can be performed on the galvanostatic charge discharge datasets by plotting the dQ/dV against V, this is also known as differential capacity analysis.

Solid electrolyte interphase (SEI)

The SEI is formed by the reduction of salt anions to form insoluble and partially soluble species such as NaF, Na_2O and Na_2CO_3 on the anode. This occurs when the alkali metal (i.e. Li or Na) comes into contact with the electrolyte and grows during sodiation (when a negative current is applied).[36,37]

The effects of SEI formation is most noticeable through a capacity loss between the first and second cycle. This is because during the first cycle, the formation of SEI is most prominent and contributes significantly to the observed capacity. The degree of SEI formation is significantly reduced on the second cycle, and the capacity is more representative of the reversible cell capacity.

1.3 Innovation through morphology design: anode materials

Emergent and tunable properties have been linked to nanostructuring and therefore this has been explored for many different oxides and applications (Table 1.2).[38] Nanostructuring implies a structure on the length scale of nanometers, this can be achieved by forming a nanomaterial, or by forming a disordered structure with local range order on the length scale of several nanometers.

Table 1.2: Metal oxides that have been nanostructured and tested for their respective properties and applications. Table adapted and updated from S. Laurent *et al.*[39]

Oxide	Properties	Applications	Ref
Ba_2O_3	Optoelectric, semiconductor, photocatalyst.	Water treatment	[40]
Co_3O_4	Optical, magnetic, electrochemical	Energy storage	[41,42]
CuO, Cu_2O	Optical, electronic	Antimicrobial agent	[43]
Fe_2O_3, Fe_3O_4	Magnetic	Biomedical	[44]
Sb_2O_3	Semiconductor	Chemical catalysis	[45]
SiO_2	Biocompatible	Biomedical applications, cosmetic	[46,47]
TiO_2	Electronic properties	Environmental, biomedical applications, photocatalysis	[48]
CeO_2	Electronic properties	Antioxidant effects, biomedical application	[49]
UO_2	Electronic properties	Nuclear application	[50]
ZnO	Electronic properties	Decontamination of hydrogen sulfide	[51]
ZrO_2	Electro-optical, piezoelectric, and dielectric material	Catalysis application	[52]
SnO_2	Optical and electronic properties	Biomedical applications	[53]

Intercalaction materials are often layered to facilitate diffusion of the charge carrier throughout the structure. Therefore this discussion will focus on 2D nanomaterials and their applications as an electrode material.

Nanostructuring approaches can be categorised into one of two routes: "top-down" or "bottom-up". A "top-down" approach would be to synthesise the bulk material and then nanosize, whilst a "bottom-up" approach would synthesise the nanomaterial from smaller components, using routes such as hydrothermal synthesis, or thin film deposition.

1.3.1 Top-down nanostructuring

One well established "top-down" synthesis methods for bulk layered materials is *via* liquid exfoliation. By synthesising the bulk material first, the atomic level connectivity has already been established.

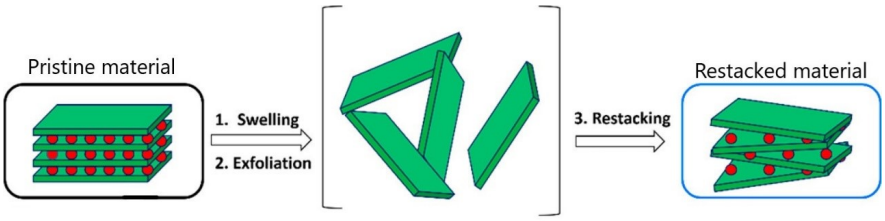


Figure 1.7: Schematic of the process of exfoliation and restacking of layered metal oxides. The green layers represent metal oxide layers whilst the red atoms are alkali earth ions. Image adapted from M. A. Tsiatsouri *et al.* (published under open access licence, CC-BY).[19]

The most common method of creating 2D nanosheets of a layered material, from bulk crystalline material is by liquid exfoliation. This is achieved by delaminiating the layers (forming 2D nanomaterials) in a colloidal solution. If the layered material possesses low charge density then in some cases it is possible to exfoliate the layers using facile methods such as mechanical stirring or sonication.[54,55] Once the layers have been

exfoliated, they can be restacked/ aggregated to form a solid state material (Figure 1.7), which have a significantly higher specific surface area than the bulk material.[56]

Nanostructuring has improved the electrode behaviour within batteries,[55,57,58] and different thicknesses of these nanosheets have shown to possess new properties. For example, ultrathin $Na_2Ti_3O_7$ was found to show capacitance behaviour whilst thicker nanoplatelets undergoes a diffusion controlled redox reactions.[59] Nanostructuring has also improved capacities, 110 $mAhg^{-1}$ after 300 cycles at a rate of 5 C, with high Coulombic efficiencies (95 %), which has been attributed to the shorter diffusion path of the charge carrier into the nanostructured material.

Further examples of 2D nanomaterials being explored for applications as electrode materials in batteries include: V_2O_5 nanosheets as lithium-ion battery cathode materials have shown high capacities (117 $mAhg^{-1}$) at high rates (50 C).[60] Whilst NiO nanosheets[61] are capable of high capacities of 1574.7 $mAhg^{-1}$ at a current density of 200 mAg^{-1}.

Therefore 2D nanomaterials shows great promise in electrochemical applications. However, J. Mei *et al.*[58] comments that the effect of utilising 2D nanomaterials on lithium battery electrodes is more thoroughly researched than sodium-ion batteries. Therefore there is a gap in the literature: the study of 2D nanomaterials for applications in sodium-ion batteries, which this study aims to contribute towards.

1.3.2 Bottom-up nanostructuring

Bottom-up synthesis refers to building a nanostructured material from smaller components, often from dissolved molecules. This can be achieved by methods such as precipitation, hydrothermal synthesis and electro-deposition. In this method, control of the synthesis conditions will determine the morphology and size of the nanostructured material. "Bottom-up" nanostructuring has shown improvements in the field of

anode materials.

Hydrothermally synthesised $Li_4Ti_5O_{12}$ nanorods[62] maintained a capacity of 155 $mAhg^{-1}$ after 200 cycles at 1 C in LIBs, and a capacity of 132 $mAhg^{-1}$ was achieved in SIBs after 100 cycles at a slower rate of 0.1 C. This was attributed to shorter diffusion lengths.[63]

TiO_2 nanospheres were synthesised by hydrothermal synthesis, after 100 cycles at 50 mAg^{-1} in a SIB, 208 $mAhg^{-1}$ discharge capacity was retained.[64] This was attributed to the many active sites on its large surface area and porous structure, in addition to rapid diffusion through the structure.[64]

High surface area of an active material leads to increased SEI formation, thereby often diminishing cell performance. However, a high surface area could be beneficial, contributing to the capacity, if surface processes occur. For example, in $Na_2Ti_3O_7$ nanotubes,[63] the surface processes accounted for 47 % of the capacity with a 95 % Coulombic efficiency at a sweep rate of 0.5 mVs^{-1}.

1.3.3 Nanostructuring aims of this study

Both top-down and bottom-up methods have proven success with improving anode properties, therefore both methods of nanostructuring will be explored in this study using layered materials for the study of sodium-ion intercalaction anodes.

1.3.4 Characterising nanostructured materials

Characterising nanostructured materials is non-trivial as one of the most powerful solid state characterisation methods, x-ray diffraction (XRD), is less comprehensive due to the lack of Bragg peaks due to a lack of long range order in nanostructured materials.[65] However, the addition of x-ray pair distribution function (XPDF) alongside XRD data has shown extensive promise in this field.[66] The theory and practice of XPDF is discussed in detail in Section 2.2, this section will focus on literature case studies demonstrating its use.

Pair distribution function (PDF) has been used on a multitude of systems, from small organics, metal–organic frameworks (MOFs), non-graphitic carbons, polymers, biological compounds, layered materials, covalent organic frameworks, nano-materials and glasses.[67,68] These materials can be crystallographically challenging, producing broad Bragg peaks, therefore XPDF can aid characterisation and analysis.

XPDF for disordered layered oxides

V. Petkov *et al.*[69] demonstrated the power of XPDF in studying exfoliated and restacked, layered 2H-WS_2 using Rietveld refinement of XPDF data, they disproved previous theories of turbostatic disorder and determined there are observable atomic correlations between the layers. The process of exfoliating and restacking caused the metal atom coordination to change from trigonal-prismatic to distorted octahedral. Shorter W-W bonds within the layer were also observed. These changes explain why 2H-WS_2 changes from semiconducting to a p-type metal. This understanding was achieved by small box least squares refinement of the XPDF with a suitable model, a technique that will be employed in this study too.[69]

M. Terban *et al.*[70] probed disordered hybridzirconium(IV) phosphonate-phosphate UMOFs, and used a single layer model with periodic boundaries in x and y to achieve a

good small box refinement result. They successfully provided evidence for turbostatic stacking using Diffpy-CMI and PDFgui.

There are only a few case studies of this nature, using small box modelling of XPDF data to understand disordered 2D materials, therefore there is an opportunity to establish a new method to characterise disordered niobate materials.

XPDF for battery materials

M. Leesmith *et al.*[71] obtained *exsitu* and *inoperando* XPDFs for β-MnO_2 and α-Mn_2O_3 anode during its lithiation and delithiation stages to identify the phases formed. XPDF is ideal in this situation as the electrode shows a high degree of disorder due to the local distortions that arise due to the uptake of lithium-ions into the structure. The large datasets were analysed using NMF and small box refinement to identify several intermediate disordered rock salt phases, however further work was required for a more complete understanding.[71] X. Wang *et al.*[72] has collated many further examples of XPDF analysis aiding electrode characterisation. These examples demonstrates the suitability of using XPDF to understand disordered electrode materials.

Summary

There are a substantial collection of published methods by which XPDF has proven beneficial in the characterisation of battery electrode materials. However, more complex characterisation and modelling of disordered layered oxide materials are not common, and therefore there is an opportunity to establish a new methodology.

1.4 Niobates as anode materials

1.4.1 Introduction

The element niobium was first documented in 1867 but the first pure niobium sample was made in 1907.[73] Since then, many properties of niobium-based phases have been understood, many of which appeals to this study:

Sodium insertion voltage

Niobates have a suitable sodium insertion voltage (below 1 V vs Na^+/Na) to be used as an anode. It has also been shown to be electrochemically active and if both Nb redox couples are active (Nb^{5+}/Nb^{4+} and Nb^{4+}/Nb^{3+}), then the material would possess a large maximum theoretical capacity of 360 $mAhg^{-1}$.

Layered structure

Niobate based materials can form a range of layered structures depending on the synthetic conditions from which structure-property relationships can be probed.

Commercialisation promise

Nyobolt† and Echion‡ are companies that are committed to providing fast charging LIBs using niobium-based anodes. Nyobolt has raised 50 million GBP to build a battery manufacturing plant in 2023.[74] Niobium has shown promise with LIB, however its compatibility within SIBs are not well understood.

†https://nyobolt.com/
‡https://www.echiontech.com/

1.4.2 Nb-O systems

The most stable oxidation state of Nb is +5, although can also possess a 0, +2 and +4 oxidation state.[73,75] Therefore the most common and stable form of niobium oxide is Nb_2O_5, which has at least 10 polymorphs: T (orthorhombic), B (monoclinic), H (mono-clinic), N (monoclinic), Z (monoclinic), R (monoclinic), M (tetragonal), P (tetragonal), TT (pseudohexagonal or monoclinic) and amorphous.[75] Applications and properties of Nb_2O_5 extend from wide band gap semiconductor,[76] pseudocapcitance,[77] capacitors,[78] catalyst,[79] lithium-ion battery anode material,[80] and sensor based applications.[81]

In addition to Nb_2O_5, other niobium oxides such as NbO_2 and NbO have been reported (Table 1.3) in addition to a homologous series of $Nb_{3n+1}O_{8n-2}$ where n = 5, 6, 7, and 8. However even this does not cover the full range of niobates reported, as niobates are known to contain point defects and ordered defects leading to the prevalence of non-stoichiometric niobates such as $Nb_{12}O_{19}$, $Nb_{12}O_{29}$, $Nb_{22}O_{52}$, $Nb_{25}O_{62}$, $Nb_{47}O_{116}$ and $Nb_{53}O_{13}$.[75,82] Therefore there is an extremely large range of niobate structures and connectivity, depite this, they are all built from [NbO_6] octahdera which can form linkages by edge or corner sharing.

Table 1.3: Nb, NbO and NbO_2 phases and their applications.

Form	Crystal system	Property	Industrial application
Nb	Cubic	Superconductivity	High strength steel-alloys
NbO	Cubic	Superconductivity	Capacitor†
NbO_2	Tetragonal	Semiconductor	Biosensor, electrocatalyst

† Proposed future application.

Although there has been significant progress in the study of niobate systems since the 1960s, there is still significant difficulty in determining accurate stoichiometries due to the challenge of identifying precise oxygen quantities.[75,83] For example, in 2017 H. T. Kreissl *et al.*[84] proposed the structure and formation of oxygen defects within niobate octahedra but were not able to quantitatively determine the degree of defects

present. Another example is G. H. M Gomes *et al.*[85] recent paper in 2022 assigning TT-Nb_2O_5 to a pseudohexagonal unit cell. TT-Nb_2O_5 has been previously published to be monoclinic, hexagonal, pseudohexagonal, orthorhombic or even not a distinct phase.[85] This further proves the understanding of niobates is still incomplete, partly due to its tendency to form vacancies[75] which can be occupied by impurities such as Cl and OH^-. This problem is not limited to the Nb-O system, the K-Nb-O system also has any inconsistencies throughout literature, for example: $K_4Nb_6O_{17}$ and $K_2Nb_8O_{21}$.§

The Nb-O system have been shown to possess interesting electrochemical properties such as the capability for high rate charging. For example, the polymorph H$-Nb_2O$ was formed into nanowires that exhibited reversible capacities of 120mAhg^{-1}, 100mAhg^{-1} and 80 mAhg^{-1} at 5 C, 10 C and 20 C, respectively.[86] Alternatively, hydrothermally synthesised Nb_2O_6 (PDF 4+: 07-0061) produced "urchin-like" morphology[87] which is capable of 131 mAhg^{-1} after 1000 cycles at 1 Ag^{-1}.

Niobates also show good capacities within SIBs as T$-Nb_2O_5$ shows 131 mAhg^{-1} after 500 cycles at a rate of 5 Ag^{-1} alongside a known sodium-diffusion pathway.[88] The use of Nb-O systems for anode materials is well studied, in addition to the use of nanostructuring techniques, many of which have been summarised by Q. Deng *et al.*[89] therefore alternative systems were explored.

§Discussed in more detail in other chapters

1.4.3 A-Nb-O systems, A = Na, K

Introduction to A-Nb-O systems, A = Na, K

Niobium typically occupies an octahedral site within A-Nb-O systems, surrounded by six oxygen atoms with a tendency for distortion from a perfect octahedron. These [NbO_6] units can either corner-share or edge-share with each other to form the niobate structure. The A cations can occupy sites between the [NbO_6], which can form channels or layers. $ANbO_3$ and ANb_3O_8 are two common types of alkali metal niobate which will be discussed in more detail (Table 1.4).

Table 1.4: Crystal structure information for $ANbO_3$ and ANb_3O_8 phases.

Property	$NaNbO_3$	$KNbO_3$	$NaNb_3O_8$	KNb_3O_8
Space group	*Pbcm*†	*Amm2*	*Pmnm*	*Amam*
a / Å	5.506	3.971	8.771	8.903
b / Å	5.566	5.697	10.160	21.160
c / Å	15.52	5.723	3.784	3.799
Unit cell volume / Å^3	475.63	129.47	337.20	715.68
ICSD cif code		39869	202400	31994
PDF 4+ code	73-0803	71–2171		

† Cubic pervoskite *Pm3m* structure at high temperature (>913 K), PDF 4+ = 075-2102.[90]

$ANbO_3$ phases, A = Na, K

$KNbO_3$ is synthesised by solid state synthesis,[91] hydrothermal,[92] microwave,[93] and sol-gel -methods.[94] $NaNbO_3$ has also been synthesised *via* many routes such as solid state,[95] molten salt,[96] hydrothermal,[97] high-pressure synthesis,[98] microwave[99] and mechanochemical synthesis.[100]

Changing synthesis method and parameters such as temperature and duration can induce difference size, morphology and atomic structure of crystals. N. Kouichi *et al.*[101,102] also explored the effect of using different solvent systems which utilises the difference in solubility of Nb in different solvents.[103,104] The mechanism of formation of $ANbO_3$ has been proposed by L. Bai*et al.*[92] in the following Equations:

$$3\,Nb_2O_5 + 8\,OH^- \rightarrow {Nb_6O_{19}}^{8-} + 4\,H_2O \tag{1.6}$$

$$Nb_6O_{19}{}^{8-} + 6\,A^+ + H_2O \rightarrow 6\,ANbO_3 + 2\,OH^- \quad (1.7)$$

$KNbO_3$ has properties such as luminescence,[105], ferroelectricity,[106] ferromagnetism[107] and has a high Curie temperature.[108] Whilst $NaNb_3O_8$ has shown some similar properties of: luminescence,[109] ferroelectricity,[110] photocatalysis,[111] and semiconductivity.[109]

ANb_3O_8 phases, A = Na, K

ANb_3O_8 is a layered metal oxide material with an orthorhombic structure which is formed from edge and corner sharing distorted NbO_6 octahedra sheets held together by potassium or sodium atoms (Table 1.4 and Figure 1.8). In this structure there are two niobium sites, one potassium site and five oxygen sites. KNb_3O_8 is related to $NaNb_3O_8$ by a 0.5 shift in *c* every alternate, Nb and K layer.

KNb_3O_8 has been of interest for its photocatalysis for many reactions such as the production of H_2, a property shared with $H_3ONb_3O_8$.[112,113] It can also photocatalyse dye degradation of acid red G[114,115] and rhodamine B.[104]

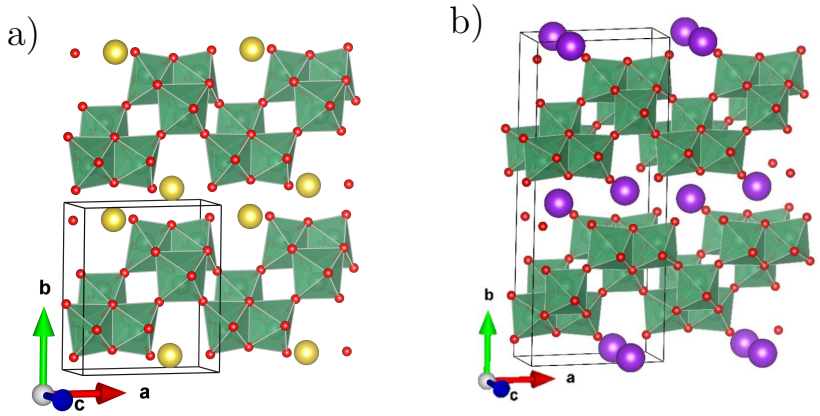


Figure 1.8: a) $NaNb_3O_8$ b) KNb_3O_8. Potassium is shown as purple, sodium in yellow, whilst oxygen is depicted as red spheres. NbO_6 distorted octahedra are shown in green. The unit cell boundary is shown as a grey cuboidal outline.

Although it is interesting to discuss ANb_3O_8 (A = Na, K), a fuller and more rounded discussion can be achieved by discussing MNb_3O_8, where M = H_3O, H, Li, Na and K.

1.5 MNb_3O_8, where M = H_3O, H, Li, Na and K

The MNb_3O_8 materials where M = H_3O, H, Li, Na and K are layered niobates that have mostly been studied for catalysis applications.[116,117,118] With the majority of papers focusing on HNb_3O_8 or $H_3ONb_3O_8$ phases for the photocatalysis of carbon dioxide and water to produce hydrogen and methane.[117,119] There are also many reports of improved characteristics, such as higher surface area and higher catalytic activity due to the formation of HNb_3O_8 or $H_3ONb_3O_8$ nanosheets, which can be synthesised by exfoliation.[113,120,121] MNb_3O_8 nanosheets have also shown improvements in other applications,[56,118,122,123,124,125] proving the interest in exfoliated structures and its effect on a wide range of applications.

1.5.1 Synthesis of KNb_3O_8

Synthesis of MNb_3O_8 is often approached *via* ion-exchange of KNb_3O_8 (unless M = potassium). The synthesis of KNb_3O_8 has been achieved by solid state synthesis, by mixing reagents K_2CO_3 with Nb_2O_5 followed by heating in a furnace. In some cases, excess K_2CO_3 was added to combat the volatization of potassium at high temperatures. A range of heating times have been reported (10- 24 hrs) in addition to a range of heating temperatures (900- 1200 °C).[57,115,119,126,127,128] However, many of these papers also report impurity phases.[57,115,119]

A slight modification is the use of KCl as a molten salt to aid mixing at high temperatures has also been reported.[129,130,131] This has also been widely reported, with a range of heating times (2- 6 hrs) and temperatures (800- 1000 °C).

Hydrothermal synthesis has also been explored as an alternative synthesis route with superior morphology control.[28,115,132] This is achieved by mixing Nb_2O_5, KOH and water into a homogeneous solution which is then placed in an autoclave and heated in an oven, which is then acidified and heated again in an autoclave. This has also

been widely reported, with a range of heating times (3- 72 hrs) and temperatures (200-800 °C).

Additional alternative methods to the synthesis of KNb_3O_8 include electrospinning to form KNb_3O_8 nanowires[133], pulsed laser deposition to form a thin film[134] or grown on glass[135]

1.5.2 MNb_3O_8 anode material

Since 2011,[136] MNb_3O_8 phases have been studied as anode materials, showing great promise with high capacities and high Coulombic efficiencies. Different morphologies have been studied such as nanowires,[133,137] nanocomposites,[138] hollow-structured,[139] and the crystalline material.[136,140] Many studies have been performed to study the electrochemical behaviour of MNb_3O_8 (Table 1.5).

To the best of our knowledge, Table 1.5 is a conclusive list of the results from galvanostatic testing performed on MNb_3O_8 type materials, with the first paper published in 2011,[136] therefore this is a relatively novel area of study. There are some additional papers that studied the electrochemical properties using other methods like cyclic voltammetry.[132,141] and therefore have not been added to Table 1.5.

Generally, but not in all instances, the capacities of sodium-ion anodes are lower than the lithium-ion counterparts (Table 1.5), which indicates there is scope for improvement with SIBs. This is further supported by the lack of research for sodium-ion systems.

In both LIB and SIB (Table 1.5), HNb_3O_8 shows the highest capacities with a general trend of decreasing capacities as you increase the molecular mass of the alkali metal. However are are very few studies on HNb_3O_8, despite its promising results. C. Huang *et al.*[128] hypothesised the larger interlayer space facilitated diffusion leading to a higher capacity. This maybe true for $H_3ONb_3O_8$ (interlayer distance 11.24(2) Å), however after drying for 12 hrs at 120 °C in a vacuum oven prior to cell assembly, a

dehydration phase transition occurs[124] to form HNb_3O_8 which involves a compression in *b*, decreasing the interlayer distance to 9.31(4) Å, which is less than the interlayer distance of KNb_3O_8 (10.58(2) Å). Therefore this does not support their hypothesis. As a result, the reason behind the high capacity of HNb_3O_8 is unknown.

KNb_3O_8 within LIBs show a decrease in capacity as rate increases from 3 mAg^{-1} to 400 $mAhg^{-1}$, as expected (Table 1.5). KNb_3O_8 is also the most commonly studied MNb_3O_8 phase as an anode material, this is most likely because it can be synthesised directly, whilst other MNb_3O_8 phases are synthesised by ion-exchange of KNb_3O_8.

Therefore in this study, KNb_3O_8 was studied as a benchmark against HNb_3O_8. Enabling a direct comparison of the impact the interlayer ion causes to electrochemical behaviour, this should yield meaningful structure-electrochemical understanding.

Table 1.5: Literature reports of MNb_3O_8 cell cycling capacities.

$-Nb_3O_8$	Charge carrier	Binder	Rate	1st cycle capacity $mAhg^{-1}$	2nd cycle capacity $mAhg^{-1}$	Settled capacity $mAhg^{-1}$	Ref
HNb_3O_8	Li	PVDF	0.1 C	1295	-	427	[128]
$LiNb_3O_8$	Li	none	0.05 C	250	153	-	[136]
$LiNb_3O_8$	Li	PVDF	0.1 C	241	-	170	[137]
$LiNb_3O_8$	Li	PVDF	0.1 C	-	-	224	[128]
$LiNb_3O_8$	Li	PVDF	0.1 C	285	-	78	[139]
$LiNb_3O_8$	Li	PVDF	0.5 C	250	-	40	[139]
$LiNb_3O_8$	Li	PVDF	0.5 C	231	-	142	[137]
$LiNb_3O_8$	Li	PVDF	1 C	-	217	119	[137]
$LiNb_3O_8$	Li	PVDF	1 C	228	-	29	[139]
$NaNb_3O_8$	Li	none	C/180	350	160	130	[131]
$NaNb_3O_8$	Li	PVDF	3 mAg^{-1}	200	-	-	[140]
$NaNb_3O_8$	Li	PVDF	0.1 C	-	-	351	[128]
KNb_3O_8	Li	PVDF	0.1 C	-	-	252	[128]
KNb_3O_8	Li	none	C/180	380	200	140	[131]
KNb_3O_8	Li	PVDF	3 mAg^{-1}	137	-	-	[140]
KNb_3O_8	Li	PVDF	10 mAg^{-1}	350	270	219	[142]
KNb_3O_8	Li	PVDF	50 mAg^{-1}	552	-	219	[133]
KNb_3O_8	Li	PVDF	50 mAg^{-1}	293	-	-	[133]†
KNb_3O_8	Li	PVDF	50 mAg^{-1}	253	-	-	[133]†
KNb_3O_8	Li	PVDF	100 mAg^{-1}	212	-	-	[133]†
KNb_3O_8	Li	PVDF	200 mAg^{-1}	182	-	-	[133]†
KNb_3O_8	Li	PVDF	300 mAg^{-1}	160	-	-	[133]†
KNb_3O_8	Li	PVDF	400 mAg^{-1}	142	-	-	[133]†
HNb_3O_8	Na	PVDF	3 mAg^{-1}	295	-	-	[140]
$LiNb_3O_8$‡	Na	PVDF	3 mAg^{-1}	249	-	-	[140]
$LiNb_3O_8$*	Na	PVDF	3 mAg^{-1}	156	-	-	[140]
$NaNb_3O_8$	Na	PVDF	3 mAg^{-1}	200	-	-	[140]
KNb_3O_8	Na	PVDF	3 mAg^{-1}	166	-	104	[143]
KNb_3O_8	Na	PVDF	3 mAg^{-1}	172	-	-	[140]

† Values obtained from sequential cell cycling of one cell. ‡ Orthorhombic crystal form of $LiNb_3O_8$. * Monoclinic crystal form of $LiNb_3O_8$.

1.5.3 KNb_3O_8 in lithium-ion batteries

KNb_3O_8 has been studied for use as an anode material within LIBs and SIBs.[28,131,133] Within a LIB, most of the capacity is located at 1.65 V (vs Li^+/Li) and both redox couples were in use (Nb^{5+}/Nb^{4+} and Nb^{4+}/Nb^{3+}).[131,136]

When morphology has not been optimised, second cycle KNb_3O_8 capacity is 200 $mAhg^{-1}$ when cycled slowly (approximately C/180),[131] However modifying the morphology to nanowires has shown considerable improvement. Z. Chen *et al.*[133] reported KNb_3O_8 nanowires to have a first cycle charge and discharge capacity of 325.2 $mAhg^{-1}$ and 551.8 $mAhg^{-1}$ respectively (at a rate of 50 mAg^{-1}). This occurred with a low Coulombic efficiency of 58.0 % after the first cycle, due to the formation of the SEI layer, which is expected due to the high surface area of nano-materials. After 150 cycles at 50 mAg^{-1}, the capacity was 218.8 $mAhg^{-1}$, which is very high.[133] At an even faster rate of 500 mAg^{-1} current density, after 750 cycles the capacity remains at 100 $mAhg^{-1}$ which is 64.1% of the first cycle capacity (155.9 $mAhg^{-1}$).[133]

KNb_3O_8 nanosheets coated with carbonized polydopamine were studied at even higher rates of cycling. It was found to display a very high degree of capacity retention,[28] after 3000 cycles at a current density of 2 Ag^{-1}, 95 % of its capacity was retained. The process improved its capacity compared to pristine KNb_3O_8 within LIBs.[28]

In summary, nanostructuring of KNb_3O_8 has shown significant electrochemical improvement in LIBs, with higher capacities obtained at significantly faster cycle rates with a high degree of capacity retention. Therefore this supports the study of nanostructured niobates within SIBs.

1.5.4 KNb_3O_8 in sodium-ion batteries

To the best of our knowledge, there are only two reports[140,143] of MNb_3O_8 materials used in a sodium-ion battery, both lead by H. Nakayama from Toyota motor-corporation. In 2015 his team published a paper: *Electrochemical reactions of layered niobate material as novel anode for sodium ion batteries*,[143] which primarily focused on KNb_3O_8. In 2016, they submitted a patent request detailing brief information regarding KNb_3O_8, HNb_3O_8, $NaNb_3O_8$, $LiNb_3O_8$ (orthorombic) and $LiNb_3O_8$ (monoclinic) as a sodium-ion battery anode material.

In 2015, H. Nakayama *et al.*[143] reported KNb_3O_8 has a reversible capacity of 104 $mAhg^{-1}$ corresponding to 1.7 Na^+ inserted per formulae unit of KNb_3O_8 at at 3 mAg^{-1}, similar to that reported for Li^+ intercalation. Most of the capacity was located at around 1 V (vs Na/Na^+) and x-ray absorption near edge structure (XANES) revealed activity of only one redox couple (Nb^{5+}/Nb^{4+}), whereas within lithium-ion batteries, both redox couples are active (Nb^{5+}/Nb^{4+} and Nb^{4+}/Nb^{3+}), highlighting fundamental differences in behaviour.

Galvanostatic charge and discharge at a rate of 3 mAg^{-1} revealed two plateaus at 0.8 V and 0.6 V during sodiation, whilst plateaus were observed at 0.9 and 1.5 V during desodiation (Figure 1.9.a.). First cycle capacity achieved 166 $mAhg^{-1}$ with a Coulombic efficiency of 62.7 %. Another coin cell was tested at 7 different currents between 3 mAg^{-1}- 3000 mAg^{-1} for 10 cycles each, provided initial capacity of 140 $mAhg^{-1}$ and ended at 25 $mAhg^{-1}$.

The cyclic voltammetry (CV) (Figure 1.9.b.) shows peaks in the sodiation curve at 0.9 V, 0.8 V and 0.6 V, and peaks in the desodiation curve at 0.9 V, 1.0 V and 1.5 V.

From *inoperando* XRD patterns, sodiation initially causes peaks shifts, indicating a 3 % contraction in b and a 3 % expansion in c, then at 10 mV peak splitting is observed. This indicates the sodiation mechanism occurs *via* a solid solution and then a two phase process.

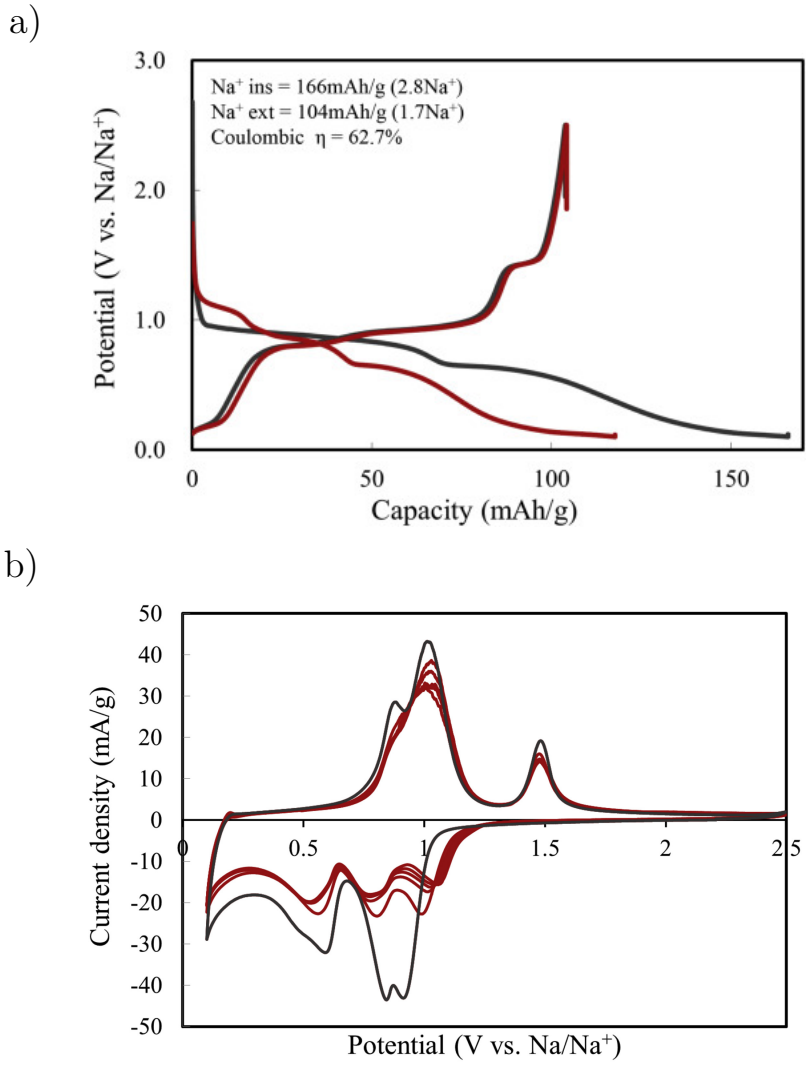


Figure 1.9: Figure reproduced with permission from H. Nakayama *et al.*[143] Electrochemical testing results from KNb_3O_8 anode material within a sodium half cell. a) The first and second cycle galvanostatic profiles of KNb_3O_8 cycled at a rate of 3 $mAhg^{-1}$. b) The cyclic voltammetry of KNb_3O_8 collected at a scan rate of 0.05 mV/s from 0.1 V- 2.5 V.

Unfortunately the sites in which sodium-ions intercalates into are unknown, and therefore the mechanism of diffusion is also not known for KNb_3O_8.[143] However, the number

of sites has been theorised to be a limiting factor in performance.[28,143]

Similar findings were later reported in a patent submitted by Toyota motor-corporation with H. Nakayama and J. Yoshida as named inventors (Figure 1.6).[140] which found the sodiaution and desodiation capacities of KNb_3O_8 to be 172 $mAhg^{-1}$ and 96 $mAhg^{-1}$ respectively at a current value of 3 mAg^{-1} from 0.1- 2.5 V and a reversible capacity of 89 $mAhg^{-1}$, similar to the values reported a year prior.

This is the only study of HNb_3O_8 in sodium-ion batteries, unfortunately only first cycle galvanostatic cycling results were included. Therefore not much is understood about its capabilities as a SIB anode material.

Table 1.6: MNb_3O_8 phases tested within a sodium half cell between 0.1 V- 2.5 V at a rate of 3 mAg^{-1}. Table reproduced from the US patent submitted by the Toyota corporation regarding.[140]

Phase	Crystal system	Sodiation capacity / $mAhg^{-1}$	Desodiation capacity / $mAhg^{-1}$
KNb_3O_8	Orthorhombic	172	96
HNb_3O_8	Orthorhombic	295	162
$NaNb_3O_8$	Orthorhombic	100	117
$LiNb_3O_8$	Orthorhombic	249	121

In this paper they also studied KNb_3O_8 in LIB and reported a reversible capacity of 137 $mAhg^{-1}$ at rates of 3 mAg^{-1}, corresponding to 2.3 Li^+ per formulae unit, with a plateau at 1.5 V. The reversible capacity of KNb_3O_8 in a LIB is significantly higher the SIB counterpart.

1.6 Aims of this study

The suitable voltage, promising high capacity and layered structure of KNb_3O_8 makes it an ideal candidate for optimising through nanostructuring. Therefore, this study aims to study KNb_3O_8, the liquid exfoliated product as well as "bottom up"-synthesised nanostructured niobates as potential sodium-ion battery anode materials.

The techniques to study crystalline materials are well established by many experts worldwide. However understanding nanomaterials is a significantly more recent scientific advancement with scope for improvement. Understanding the disorder within 2D nanomaterials is non-trivial and therefore this study aims to utilise techniques such as pair distribution function (PDF) towards this goal. The intial models for PDF analysis will be constrained by information from complementary techniques such as XRD, Raman and microscopy. This study will also contribute towards the lack of 2D nanomaterials studied for sodium-ion batteries.

Although this study does not hope to encourage the prolific use of niobium, hopefully by characterising 2D nanomaterials, a little more can be understood about how nanostructuring can improve electrochemical properties. In the future, hopefully the methods and techniques used in this study can be applied to other systems, and maybe even other applications.

2 Theory and practice of techniques

2.1 Introduction

This Chapter outlines the techniques and analysis methods that are used throughout this study and provides a brief introduction to the theory behind these practices. This Chapter also provides detailed information about the methods and equipment used in the following Chapters.

2.2 Crystallography

2.2.1 The importance of crystallography

Crystallography is the study of crystalline structures and underpins solid state chemistry. It is only by first understanding a structure that we can then relate its structure to its properties, and then ultimately design a new material with the desired characteristics. This section will highlight the power of x-ray scattering techniques to probe the atomic structure.

2.2.2 Introduction to the unit cell

A perfect crystal is formed from a repeating lattice of atoms in 3D space. The unit cell is the smallest volume which is representative of the whole crystal through translational symmetry alone. When the unit cell is tessellated (without mirroring or inverting the unit cell), it reproduces the atomic structure for the whole crystal.

Unit cell parameters describe the dimensions and angles of the unit cell. Parameters a, b and c are the lengths of the unit cell edges, and the angles between them are denoted α, β and γ; where α is the angle between b and c, β is the angle between a and c and γ is the angle between a and c.

The locations of atoms within a unit cell are given as a fractional coordinates relative to the unit cell parameter, these are defined as x, y and z which correspond to the a, b and c axes of the unit cell parameters respectively. For example, $x = 0.5$ would indicate the site is positioned halfway along the a direction, similarly the y and z values can be described to provide atomic sites relative to the unit cell.

2.2.3 Symmetry within the unit cell

The relationships between the unit cell parameters define the crystal system of the unit cell (Table 2.7). There 7 lattice types: P (Primitive), R (Rhombohedral), I (Body centered), F (All-faces centered), A (A face centered), B (B face centered) and C (C face centered). Combining the crystal systems with lattice types, where symmetry permits, provides 14 Bravias lattices. These in turn combined with the 32 crystallographic point groups, where symmetry permits, produces 230 space groups, each identifiable by number or by the Hermann–Mauguin notation.[144,145]

Table 2.1: Names of crystal system and the rules regarding unit cell parameters.

Crystal system	Lengths	Angles
Cubic	a = b = c	$\alpha = \beta = \gamma = 90°$
Tetragonal	a = b ≠ c	$\alpha = \beta = \gamma = 90°$
Orthorhombic	a ≠ b ≠ c	$\alpha = \beta = \gamma = 90°$
Rhombohedral (Trigonal)	a = b = c	$\alpha = \beta = \gamma \neq 90°$
Hexagonal	a = b ≠ c	$\alpha = \beta = 90°$ and $\gamma = 120°$
Monoclinic	a ≠ b ≠ c	$\alpha = \beta = 90°$ and $\gamma \neq 90°$
Triclinic	a ≠ b ≠ c	$\alpha \neq \beta \neq \gamma$

All structures possess lattice points at the vertices of the unit cell, with additional lattice points which are determined by the lattice types (Table 2.2).[146]

The atomic positions within a unit cell are defined using Wykoff positions, which groups symmetry related atomic positions together. For example for space group *Pnma* (Table 2.3) an atom occupying the 8d Wykoff position (8 = multiplicity, d = Wykoff letter), will have eight atoms within the unit cell, with the same chemical environment (i.e. bond distances, bond number etc).[144] The coordinates (Table 2.3) outline how the eight atomic sites are generated whilst the site symmetry provides symmetry information using the Hermann–Mauguin notation.

Table 2.2: Lattice system and their corresponding lattice points. Table reproduced from C. Giacovazzo.[146]

Symbol	Type	Positions of additional lattice points	Number of lattice points per cell
P	Primitive	-	1
I	Body-centered	(1/2,1/2,1/2)	2
A	A face centered	(0,1/2,1/2)	2
B	B face centered	(1/2,0,1/2)	2
C	C face centered	(1/2,1/2,0)	2
F	All faces centered	(0,1/2,1/2) (1/2,0,1/2) (1/2,1/2,0)	4
R	Rhombohedrally centered	(1/3,2/3,2/3) (2/3,1/3,1/3	3

Table 2.3: Information about the Wykoff position for space group *Pnma*, 62. Information obtaind from Bilbao Crystallographic Server.[144]

Multiplicity	Wyckoff letter	Site symmetry	Coordinates
8	d	1	(x,y,z) (-x+1/2,-y,z+1/2) (-x,y+1/2,-z) (x+1/2,-y+1/2,-z+1/2) (-x,-y,-z) (x+1/2,y,-z+1/2) (x,-y+1/2,z) (-x+1/2,y+1/2,z+1/2)
4	c	.m.	(x,1/4,z) (-x+1/2,3/4,z+1/2) (-x,3/4,-z) (x+1/2,1/4,-z+1/2)
4	b	-1	(0,0,1/2) (1/2,0,0) (0,1/2,1/2) (1/2,1/2,0)
4	a	-1	(0,0,0) (1/2,0,1/2) (0,1/2,0) (1/2,1/2,1/2)

2.2.4 Crystallographic information files and databases

The digital storage of crystal structure information in a way which is readily accessible and searchable is fundamental to modern crystallography. A digital file containing structural information such as a unit cell and the atomic coordinates can be saved as a crystallographic information file (cif) which can then be interpreted by data analysis or plotting software.

The Inorganic Crystal Structure Database (ICSD) provides a large searchable database of structures which can be uniquely identified by an ICSD code and downloaded in cif format. The JCPDS-ICDD (Joint Committee on Powder Diffraction Standards- International Centre for Diffraction Data) also provides an alternative searchable structural database known as powder diffraction file 4+ (PDF 4+) which has its own unique codes for identifying each unique structure. Both of these databases have been used in this work to identify suitable structural candidates for the materials produced. Where structures from databases are used, they are referenced using the unique identifier provided by the database.

VESTA software

VESTA (https://jp-minerals.org/vesta/en/) is a piece of software that is designed to handle crystallographic information file (cif) files, manipulate structures, creating models and also for crystal structure visualisation. All the ball and stick structures displayed in this thesis have been generated using VESTA.

2.3 X-ray scattering

2.3.1 Introduction

X-ray scattering is a powerful mechanism that can be used to probe the atomic structure of solid state materials due to the interactions between the x-rays and the electrons within the structure. This has lead to the development of XRD and PDF. Although this study focuses on the use of x-rays, neutron-XRD and neutron-PDF are also established techniques.

X-rays are part of the electromagnetic spectrum and therefore can be described as both a wave and a photon. As a wave, x-rays can constructively and destructively interfere with each other to provide a gain or loss in amplitude, respectively. The electric field component of x-ray waves can interact with the electrons of an atom and cause the x-ray to be scattered elastically; to change direction without a change in energy. The ability of an atom to scatter an x-ray increases with its number of electrons and is known as its atomic cross section.

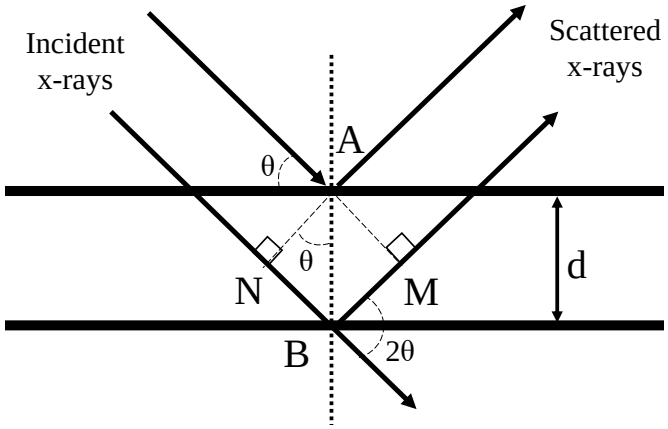


Figure 2.1: Illustration of the geometric requirements for Bragg's law.

Coherent x-ray scattering (Bragg scattering) of x-rays occurs when x-rays interacts with a regular array of atoms. Constructive and destructive interference arising from

the interaction of x-rays with a crystal gives rise to a diffraction pattern which contains information on the structure of that crystal.

The Bragg condition expresses a geometric constraint, where the distance Δ = NB + BM (Figure 2.1) is a multiple of the wavelength by a factor n, where n is a positive integer (Equation 2.1). This mathematical criteria has to be satisfied for coherent scattering to occur, which subsequently can be observed as a peak in an XRD pattern (Equation 2.2).

$$\Delta = n\lambda \tag{2.1}$$

$$n\lambda = 2d_{\mathrm{hkl}}sin\theta \tag{2.2}$$

n = multiplicity

λ = wavelength of x-rays

d = spacing between lattice planes

θ = half the scattering angle (2θ)

2θ is dependent on λ, which varies depending on x-ray source. Sometimes it is preferable to use a parameter which is not λ dependent, for example Q. Where Q is the scattering vector given in units of Å^{-1} which is related to θ through Equation 2.3.[145]

$$Q = \frac{4\pi sin\theta}{\lambda} \tag{2.3}$$

Q = magnitude of the scattering vector

θ = half the scattering angle (2θ is the scattering angle)

λ = wavelength of x-rays

Bragg peaks obtained from Bragg scattering as defined by Bragg's law is used in XRD crystallography to understand the structure of crystalline materials. On the other hand, total scattering makes use of both Bragg intensity and also the intensity between the Bragg peaks (diffuse scattering), and therefore contains information on

both the long- and short-range ordering in a material. By analysing the total scattering data, and its associated pair distribution function (PDF), it is possible to understand the structure of amorphous and disordered materials.[147,148] The PDF is obtained by the fourier transform (FT) of the total scattering data. The pair distribution function (PDF) denotes the probability of finding an atom at a given distance r from any arbitrary atom in the system (Figure 2.2).

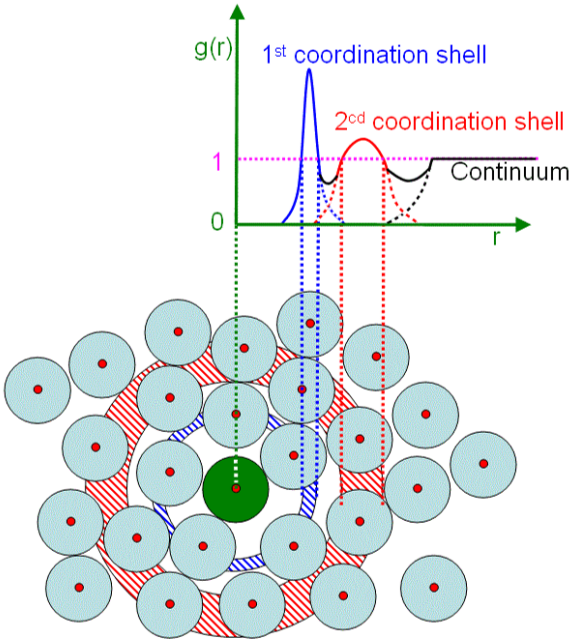


Figure 2.2: A schematic of how atom to atom distances correspond to peaks in the pair distribution function. Diagram obtained with permission from Yougui Liao.[149]

2.3.2 Powder x-ray diffraction

Single crystal x-ray diffraction provides a pattern of dots, generated by the reciprocal lattice of the single crystal. However in a powder (a poly-crystalline sample), as orientation of the crystals are completely random, the dots are smeared out into a cone known as Debye-Scherrer rings. An x-ray diffraction (XRD) pattern is obtained by taking a cross section to obtain the 1D data of intensity vs. 2θ.

2.3.3 X-ray sources

The most common x-ray source is an x-ray tube. Electrons are accelerated and collided with a metal anode target inside a vacuum tube. The high energy electrons induce electronic transitions in the atoms of the target. Upon relaxation, electronic transitions within the atoms lead to the emission of radiation of characteristic wavelengths. The most common metal target is copper, which generates Cu K_α ($\lambda = 1.542$ Å) and Cu K_β ($\lambda = 1.392$ Å), typically a filter is used to remove the K_β leaving an almost monochromatic Cu K_α for use. Alternative wavelengths can be used by using a different metal target, commonly Mo and Ag are used to perform laboratory based PDF experiments due to the higher energy x-rays they produce.

Alternatively synchrotrons are used to generate high energy, high flux, highly monochromatic and small beamsize x-rays, amongst other interesting characteristics which are not possible using lab sources. Combined with complex sample environments and superior detectors, this enables new types of experiments which are not possible with a lab source, and typically also provides improved data quality too.

Synchrotrons

Every synchrotron shares the same skeletal structure which is necessary to generate the x-rays. Firstly, the electron gun generates electrons which are accelerated and guided by magnets through the linear accelerator (linac) into the booster synchrotron, followed by the storage ring where the electrons will remain until they are dumped.

The storage ring itself is formed of many straight sections joined together using bending magnets until a ring is formed. When electrons pass through a bending magnet, or an insertion device (undulators and wriggler magnets), photons are emitted. The photons enter the beamline whilst the electrons continue along the storage ring.

A beamline itself consists of 3 parts: the optics hutch, the sample room and

also the control room. The photons will first enter the optics hutch which house the mirrors, monochromators, lenses and filters. This will alter the photon beam according to the needs of the beamline.

The x-rays pass into the sample room which contains the sample and the detector, and a few additional optical elements such as slits. In some cases, the sample environment is a simple capillary at room temperature whereas in other situations, it could be a high pressure gas loaded diamond anvil cell with a Raman system attached. Beamlines allow for unique *inoperando* and *insitu* experiments, the high flux allows for high time resolution experiments in addition to intensive experiments such as raster scanning or tomography. The multitude of possible sample environments allows for creativity when designing an experimental set up.

There are many synchrotons around the world, most notably are: Super Photon ring-8 GeV (SPring-8) in Sayo, Japan; National Synchrotron Light Source in Brookhaven, USA, Advanced Photon Source (APS) in Oakridge, USA; European Synchrotron Radiation Facility (ESRF) in Grenoble, France; Deutsches Elektronen Synchrotron (DESY) in Hamburg, Germany and Diamond Light Source (DLS) in Oxford, UK.

2.3.4 PXRD equipment

There are several components that are often used to describe a PXRD set-up, these include the geometry, mirrors, monochromators, filters, sample holder, rotation and detector. These will all impact the XRD pattern produced and therefore are important to understand.

Geometry

There are two main geometries possible, reflection (Bragg-Brentano) and transmission. Reflection geometry is often used with a flat sample plate in which a divergent x-ray bean is reflected by the sample and converges at the detector. Alternatively, in

transmission geometry, the x-ray, sample and detector are placed in a line.

Mirror

Mirrors are more commonly found at synchrotons than lab sources and are used to reflect the x-rays, whilst curved mirrors can be used collimate or focus x-rays. They can also be used to filter out high energy x-rays.

Filter

A filter utilises the absorption edge of a material (i.e. Ni K edge $\lambda = 1.542$ Å) to filter out wavelengths of x-rays.[145] Typically Cu x-ray sources use a Ni filter to significantly reduce the intensity of the Cu K_β.

Monochromator

A monochromator is highly selective towards a specific wavelength of x-rays and is used to monochromate the beam, however this decreases the flux significantly and therefore sometimes a filter is used instead. Typically silicon, germanium and quartz are used for this purpose.

Sample holder

In reflection geometry, samples are typically packed as a disk with a smooth upper surface, typically on a plastic or on a silicon crystal which contributes little to the XRD pattern. Alternatively, in transmission geometry, samples are loaded into a capillary, typically borosilicate although quartz or kapton can be used depending on sample requirements.

Rotation

Rotating the sample improves the Debye-Scherrer cone, by reducing the prevalence of incomplete or spotty rings.

Detector

Most lab XRD machines are fitted with a position sensitive detector (PSD) which extends over 5-10 degrees 2θ, therefore collection is slower as the PSD has to move

across the full collection range. A standard lab collection takes between 20- 60 minutes depending on the quality required. For synchrotrons, area detectors are typically used which can detect whole sections of the Debye-Scherrer cone. This increases collection speed and coupled with the high flux, XRDs can take just seconds at synchrotrons.

2.3.5 PXRD methodology

Most XRD patterns were collected using either a Brucker D8, Siemens D5005 or a Rigaku Miniflex; these diffractometers are equipped with a Cu source x-ray tube (λ= 1.54056 Å). XRD patterns collected on synchrotron beamlines use a different wavelength of x-rays, which will be explicitly stated in the figure caption and in addition, outlined below.

Siemens D5005

A Siemens D5005 diffractometer was equipped with a copper x-ray tube with a nickel filter in front of the detector. Cu Kα_1 (λ= 1.54056 Å) and Kα_2 (λ= 1.54439 Å) respectively are utilised. A Braun position sensitive detector (PSD) detector was used in a θ/θ reflection geometry. Samples were static during data collection.

Bruker D8

A Bruker D8 diffractometer was used with a copper source and nickel filter as above, Cu Kα_1 (λ= 1.54056 Å) and Kα_2 (λ= 1.54439 Å). The detector is a solid-state LynxEye PSD with the instrument working in a $\theta/2\theta$ reflection geometry. In most cases the sample was rotated at 15 rpm during data collection. However, if a "low background" sample holder was used rotation was not possible as the sample would be prone to moving out of the beam position during collection. A heated Al_2O_3 flat sample holder was also used for variable temperature-XRD (VT-XRD) data collections.

Rigaku Miniflex

A Rigaku Miniflex was equipped with a fixed copper source and a graphite monochromator, supplying just Cu Kα_1 radiation (λ= 1.54056 Å). The sample holder tilts and the detector move during data collection. A silicon low background sample holder was used and the sample was typically rotated at 10 rpm during data collection; however rotation was not used if the sample was prone to sliding off the sample holder.

I11 beamline

The I11 beamline is a high resolution x-ray diffraction beamline at Diamond Light Source, UK. It is optimised for the highest possible resolution, high flux and quick collection times. The beamline is equipped with two detectors; PSD and a multi-analyser crystal (MAC) detector. The PSD detector can collect whole diffraction patterns in just a few seconds. The MAC detector uses diffraction from an array of secondary crystal analysers to provide the very high resolution; this is ideal for samples with low symmetry or complex microstructures. X-rays with wavelength of 0.825255 Å was used at this beamline. The samples were packed within a borosilicate capillary with an external diameter of 0.5 mm and spun perpendicular to the beam, during data collections.

I15-1 XPDF beamline

The I15-1 beamline at Diamond Light Source, UK, is optimised for XPDF and is capable of collecting XRD patterns, however the beamline is optimised to collect data to a high Q range and therefore the XRD patterns produce are of lower resolution than lab diffractometers, therefore this was only used as a last resort. X-rays of 0.161669 Å were used to collect XRD data in transmission mode. Two flat 2D area detectors were used; one placed close to the sample (200 mm) for PDF data and one further from the sample (850 mm) for Bragg data. The samples were packed inside a borosilicate capillary with an outer diameter of 1 mm and spun perpendicular to the beam during data collection.

I15 XRD beamline

The I15 beamline is the Extreme Conditions XRD beamline at Diamond Light Source, UK. It it optimised for focused x-rays of energies from 20- 80 keV. Further details are given in the appendix.

2.3.6 PXRD analysis

Each crystal structure produces a unique XRD pattern (Table 2.4). Fingerprinting exploits this property, allowing experimentally obtained XRD patterns to be matched to XRDs from a database with of known structures that can be used for phase identification purposes. This is one of the most basic methods of analysing an XRD pattern and is highly effective and ideal for materials which are well described. In instances where a suitable XRD pattern match can not be found, then modelling (e.g. Rietveld refinement) can provide a better description of the material by comparing the experimentally obtained XRD pattern to a simulated XRD pattern generated from a user defined structure.

Table 2.4: Properties of an XRD pattern and the sample information that can be derived from the property.

Property	Information
Peak location	Relates to the hkl values and can be used to determine the unit cell lattice parameters and crystal system.
Peak intensity	Relates to atomic positions and thermal vibrations, and phase fractions.
Peak shape	Relates to microstructure such as stress and strain in the crystal. This may be isotropic (affecting all peaks equally) or anisotropic (affecting peaks depending on their hkl values)

There are two popular types of small box modelling analysis; Pawley fitting and Rietveld refinement and both of these methods utilises the least-squares (χ^2) fitting method to minimise the difference between the simulated XRD pattern to the experimentally obtained XRD pattern. The r_{wp} value is often used to quantify how closely the model fits the data (Equation 2.4).[150]

$$r_{wp} = \frac{(G_{exp} - G_{cal})^2}{(G_{exp})^2} \tag{2.4}$$

TOPAS software

TOPAS is a software program developed by Coelho Software[151] and is used throughout this study (TOPAS-academic-64 V6). The software is able to perform small box analysis on XRD and PDF data.[152] It is also able to calculate values such as weight percentage.

Pawley fitting

A Pawley fit involves fitting an experimental XRD pattern to unit cell parameters and a space group, with a disregard to peak intensities. This is often used as the first step in small box modelling if there is a degree of uncertainty about the sample/ model. This is especially useful if there is no known structure to work with as there are no atomic sites to model, therefore there are only a few refineable parameters which makes this technique faster and more easily accessible than Rietveld refinement which will model peak intensities though the occupation of defined atomic sites.

Rietveld refinement

A Rietveld refinement, unlike a Pawley fit, can refine atomic positions and is affected by the peak intensity. This is one of the most rigorous methods of analysing XRD patterns. When there is a good fit, the parameters (i.e. atomic positions) and therefore the model, can be taken as a description of the system.

There are many programs available to perform Rietveld refinements such as: Fullprof, TOPAS and GSAS. They vary in price, ease of use and also in their flexibility to adapt to the experimental needs. As all Rietveld refinement analysis has been performed using TOPAS, discussions about Rietveld refinement will be provided in the context of TOPAS.

Rietveld refinement generates a crystal lattice by defining a few atomic positions and then expanding these atomic positions according to the space group symmetry operation. In TOPAS, in addition to the space group, the user has to also input other parameters to describe the x-ray source, other phases in the sample, peak shape description, refinement range, background function etc. A thermal parameter is also associated with each site, known as a `beq` value in TOPAS, which is used to model changes in the XRD due vibrations of the atom. These parameters enables the program to simulate the XRD pattern for the model. As the model is computer generated, it is highly flexible and functions such as Stephens anisotropic peak shape function [153] mathematically modifies the simulated XRD pattern by applying hkl-dependent contributions to the peak shape which is able to model different size/strain along different crystallographic directions in the sample. Therefore, a large variety of models and their XRD patterns can be generated and compared to the experimentally obtained XRD pattern.

Some parameters such as unit cell parameters, thermal parameters, background function etc. are allowed to refine whilst others such as x-ray wavelength are not. Least-squares fitting aims to minimise the difference, between the experimental XRD pattern and the model, by changing the refineable parameters to obtain the set of parameters which provide the global minima r_{wp}, in an ideal situation.

Debyer

Rietveld and Pawley refinements are limited to modelling infinite crystals by defining a unit cell. When studying disordered or nanostructured structures, sometimes it is desirable to generate XRD patterns of finite length scales. This is achieved by using Debyer software, (website: http://debyer.readthedocs.org/ and Github: wojdyr/debyer).

The program Debyer utilises Debye's scattering equation [154] to generate a diffraction pattern. The Debye scattering equation (Equation 2.5), r_{ij} is the distance between

atoms i and j whilst f_i and f_j is the atomic scattering factor for atoms atoms i and j respectively.

$$I(Q) = \sum_i \sum_j f_i f_j \frac{sin(Qr_{ij})}{Qr_{ij}} \tag{2.5}$$

2.3.7 PDF introduction

Pair distribution function (PDF) is a powerful technique in probing materials with short range coherence, and a lack of long range order. PDF can be used to probe the local structure, as each atom to atom distance produces a peak (Figure 2.2), which contains information beyond atomic distances (Table 2.7). Using the understanding of how a PDF changes due to changes in the structure, it is possible to create a model and match it to the PDF, similarly to XRD.

Table 2.5: The properties observed in a Pair distribution function and the information that can be interpreted by analysing the property.

Property	Information
Peak position	Atom to atom distance in sample
Integrated peak intensity	Scattering power and abundance of that particular pair correlation
Peak width	Relates to the amount of disorder in the system in addition to thermal parameters.
Damping	Particle size/ scattering coherence length

At high r (around 30 Å), the PDF of a disordered material will eventually become flat and featureless indicating there are no more atom to atom correlations at that distance.

2.3.8 PDF equipment and methodology

For good quality PDF data, collection of scattering data to a high $Q_{\max}$ is crucial to minimise termination ripples (arising from convolution with the sinc function) and to produce a PDF with sufficient real-space resolution to perform structural refinement. Achieving a high Q range can be achieved by utilising a synchrotron source.

Pair distribution function is typically performed at a synchrotron, such as at Diamond Light Source, Oxford, UK. This is because of the high $Q_{\max}$ range of measurements required, therefore requiring a high energy x-ray beam which is best achieved at a synchrotron. For comparison, the energy of Cu Kα source is 8.04 keV (1.5406 Å),

however the I15-1 PDF beamline typically operates at 76.69 keV.

I15-1 beamline utilises a monochromatic beam without any bremstrallugg. During this study, the beamline used two flat 2D area detectors, a Perkin Elmer XRD 1611 CP3 (4096 x 4096 pixels with 100 μm pixel size) Perkin Elmer XRD 4343 CT (2880 x 2880 pixels with 150 μm pixel size). This has since been upgraded to a bespoke new detector.

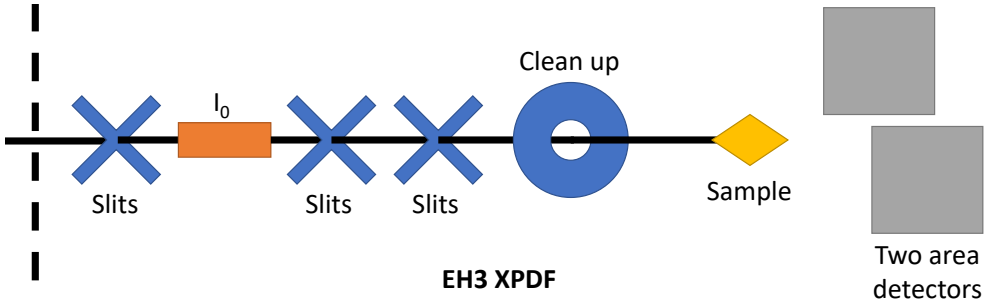


Figure 2.3: A schematic of the EH3 room (sample room) of the beamline I15-1 at Diamond Light Source, where the sample and detectors can be found (year: 2002).

2.3.9 PDF generation: theory

This technique has been utilised by various feilds of science from glasses, nano-particles and disordered materials.[67] As a result, different conventions and forms of the pair distribution function have been developed by various scientific communities. However, they are all representations of the same function, just with different scaling applied, these comparisons have been reviewed by D. A. Keen.[155]

The total coherent scattering, $I(Q)$, is collected by the detector to a high Q range. This data needs to be corrected for contributions due to the sample environment (i.e. capillary), background (empty scan), Compton scattering, absorption, polarisation and scattering due to multiple scattering events (Equation 2.6).[156]

$$S(Q) - 1 = \frac{I(Q) - C(Q)}{\langle f^2(Q) \rangle} \tag{2.6}$$

Where $C(Q)$ is the sum of all the corrections required. $S(Q)$, the normalised total scattering intensity (in absolute units of scattering-per-atom) which is achieved by normalising by the average form factor, $\langle f^2(Q) \rangle$ to remove Q dependence.[156,157] The Fourier transform of $S(Q)$ provides the D(r) which is one form of a pair distribution function (Equation 2.7), where ρ is the atomic number density.[157]

$$G(r) - 1 = \frac{1}{2\pi^2 r\rho} \int_{Qmin}^{Qmax} Q\,[S(Q) - 1]\, sin(Qr) dQ \tag{2.7}$$

There are two forms most commonly seen in materials chemistry; $G(r)$ and $D(r)$. $G(r)$ oscillates around 0 and possesses a flat background indicating zero probability of an atom-atom interaction.[157] $D(r)$ (Equation 2.8) is scaled as a function of r and therefore high r contributions are more evident in the $D(r)$ than the $G(r)$.[147,157] In order to emphasise the analysis of mid-range correlations (20- 40 Å), the $D(r)$ form of PDF is utilised thoughout this work.

$$D(r) = 4\pi r\rho G(r) \tag{2.8}$$

In an ideal scenario to obtain the highest resolution PDF, FT would be performed between the limits Q_0 to Q_∞. However, due to experimental limitations, only a limited Q range is accessible. Realistically, to generate a good quality PDF, collection of scattering data to a high $Q_{\max}$ is crucial to minimise termination ripples (arising from convolution with the sinc function) and to produce a PDF with sufficient real-space resolution to perform structural refinement. Achieving a high Q range can be achieved by increasing θ and/or by minimising λ (Equation 2.3).[147,157] The scattering angle 2θ is fundamentally limited to a maximum of 180° due to geometric constraints. Therefore, to achieve a $Q_{\max}$ in excess of 25 Å^{-1}, which is often necessary for the study of semi-crystalline materials, short λ x-rays are needed which typically requires the use of a synchrotron. Although PDFs can be collected by silver x-ray tubes within a laboratory, these datasets have a lower resolution. Alternatively, neutrons with a suitable wavelength can also be used generate PDFs.

2.3.10 PDF generation: practice

There are a variety of programs used to convert the raw x-ray scattering data into a pair distribution function, for example: GudrunX and PDFgetX3. All the PDFs have been generated using GudrunX, unless otherwise specified.

GudrunX

The 1D total-scattering pattern is processed within GudrunX to produce $D(r)$. Firstly container (i.e. empty capillary), then a calibration factor is applied to the raw data so that the intensity of the peaks of the PDF can be interpreted. Then the data is corrected for fluorescence when needed and the x-ray attenuation (due to the polarisation of the beam). The $S(Q)$ is then obtained by subtracting single atom scattering, then dividing by the form factor (obtained from coherent single atom scattering). To remove a possible slowly varying Q background, a Top Hat convolution is applied to the data. Finally, $S(Q)$ is Fourier Transformed into $G(r)$ which is multiplied by $4\pi r\rho$ to obtain $D(r)$.

PDFgetX3

PDFgetX3 is also able to generate PDFs[158] by modifying 5 parameters: background scale, $Q_{max-inst}$, Q_{max}, R-poly and Q_{min}. PDFgetX3 also allows large raw datasets to be converted into PDFs easily.

2.3.11 PDF analysis

Through pair distribution function analysis, a large range of information can be accessed (Table 2.7), which can be used to fit a model of the system. Big box modelling utilises a large quantity of atoms, not limited to a unit cell to model the data, the most popular technique is RMC (reverse Monte Carlo simulation). However the complexity of the result can be difficult to understand. Both big and small box modelling methods allow for the characterisation of disordered/ nanosized solids which lack long range order, yet possess a degree of local order.

The most simplistic method of using a PDF is matching the low r peak locations to atomic distances within the proposed structure. This can easily identify structures that do not fit the PDF obtained.

Small box refinement

Small box refinement of XPDF are used extensively in this study, this method utilises χ^2 minimisation to reduce the difference between modelled and experimental PDF, similar to the technique Rietveld refinement which is applied to XRD patterns. In TOPAS, structural parameters, thermal (`beq`) parameters, scale and spherical damping are allowed to refine.[159] PDFs can also be refined in combination with XRD data of the sample.

Spherical damping is a function that models the loss of coherence observed when the coherence range is short within the sample, this is achieved by decreasing the intensity of the PDF with increasing r.

Non-negative matrix factorization

Non-negative matrix factorization (NMF) is a mathematical method by which models changes in PDF over time (or over any other vector) by utilising a set of linear components that are combined with a weighting factor which changes as a function of time

(or the vector of choice). This deconvolutes the PDF dataset into n number of components, the components may show similarities to PDF of individual components that are within the structure.[160] Individual components maybe easier to analyse compared to the original PDFs which is the power of NMF. Furthermore changes in the weighting of the components can indicate the growth or destruction of a phase.

2.3.12 Limitations of XRD and PDF

1. Unrealistic values

From the program's perspective, its goal is to minimise the difference by altering the refinebale parameters. Unless restrictions are put in place in the code, the values could refine to unrealistic values, or example an atomic site with a negative occupation parameter or atomic sites that are overlaid. Therefore it is the researcher's job to critically evaluate the refinement, not just by using the r_{wp}.

2. Calculating errors

The errors associated with each parameter are calculated by TOPAS. At times, these errors are very large and therefore it would be unwise to trust the calculated value completely in these instances.

3. Microabsorption error

The atomic cross section increases as z increases, where z is the number of electrons possessed by an atom. Therefore a heavier atom i.e. niobium will scatter more strongly than a lighter element i.e. sodium. Therefore it is important to understand that niobium will have a much larger contribution to the refinement and the XRD pattern than lighter atoms.

4. Weight percent

Accurate weight percentage values calculated from Rietveld refinement of PXRD

measurements can only be achieved through the use of Al_2O_3 scans or by producing a calibration curve. Weight percentage values obtained from a Rietveld refinement is obtained by the scale factor of that phase. However the scale factor is affected by variables other than just the weight percent of a phase. Secondly, phases which are present in the sample but were omitted in the refinement model will not be accounted for. The total weight percent of accounted refinement phases always equals 100 %, therefore the omission of phases will lead to artificially inflated weight percent of all accounted phases.

5. Amorphous and disordered samples

XRD depends on the long range ordering of atoms to produce Bragg peaks for analysis. Therefore if a phase does not possess long range order, these domains do not contribute to any Bragg peaks, instead produce broad peaks which are sometimes interpreted as background. As a result, it is not possible to fully characterise amorphous or disordered domains using only Bragg peaks.

2.4 Small angle x-ray scattering

Small angle x-ray scattering (SAXS) studies the x-ray scattering at small angles to probe in very low Q space, which can be used to understand the structure of the sample in the range 1 nm up to around 300 nm, such as nanopore and nanoparticle with attributes such as shape and size and aspect ratio.[161]

The Guinier relationship is used to determine the presence and the shape of macro features.[162] To extract information about features such as nanopores, the shape and size of the nanopore has to be consistent to be detected by SAXS as a feature in the curve, else a smooth curve is observed.

Method

Small angle x-ray scattering was performed in collaboration with Brian Pauw (ORCiD: 0000-0002-8605-838X)* and Glen Smales (ORCiD: 0000-0002-8654-9867) at BAM, Berlin with the SAXS instrument MOUSE, as detailed further in their paper: *The MOUSE project: a meticulous approach for obtaining traceable, wide-range X-ray scattering information.*[163]

*https://lookingatnothing.com/

2.5 Raman spectroscopy

2.5.1 Raman spectroscopy: theory

Raman spectroscopy is a form of vibrational spectroscopy in which changes in the incident and scattered photons can be used to probe the molecular structure given the presence of polarizable bonds.

Rayleigh scattering on the other hand is essentially elastic scattering. A photon interacts with the molecule or crystal, polarising the electron cloud and exciting it to a virtual state, which relaxes down to the original v level, emitting a photon. The energy of the incident photon is the same as the scattered photon, and therefore these are not observed in Raman scattering, unlike Stokes and Anti-Stokes scattering which causes a change in photon energy (inelastic scattering).

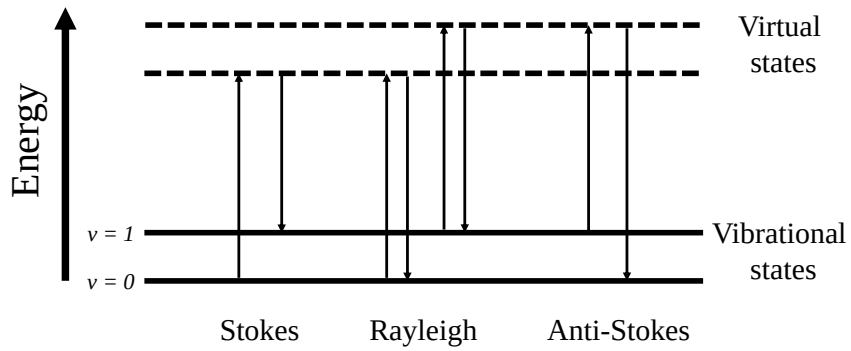


Figure 2.4: Diagram of Stokes, Rayleigh and Anti-Stokes scattering processes.

Inelactic Stokes scattering occurs when a photon excites the molecule or crystal from the vibrational ground state ($v = 0$) to a virtual state, and then the molecule or crystal relaxes down to a higher vibtational state (i.e. $v = 1$), emitting a photon of lower energy, longer wavelength than original (Figure 2.4). In Anti-Stokes scattering, the emitted photon is of higher energy, shorter wavelength than the incident photon.

At room temperature the intensity of the Stokes lines out weight that of the anti-Stokes as the population of the ground state energy level ($n = 0$) is higher than that of $n = 1$. Therefore typically only the Stokes lines are presented in the Raman spectra.

2.5.2 Raman system at I15

At Diamond Light Source, I15 own a LabRam HR800 from Horiba with an mpc 3000 laser (532-nm, green). At the beginning of each use, silicon is used to calibrate the machine. After calibration, scans are performed from 200-1000 cm^{-1}, five 30 s scans are aggregated together to produce the Raman spectra. A few locations are studied for each sample to ensure a true representation of the sample as the spectra is only collected from the a small local area of the sample which could possess local irregularities which are not representative of the whole sample.

2.6 Microscopy

2.6.1 Introduction to microscopy

Microscopy is a phenomenally powerful technique which enables easy to understand visual images of the particles to determine morphology and atoms to determine morphology. This technique has been used throughout this study for the aforementioned purposes.

The most basic microscope are light microscopes that uses a series of lenses and mirrors to magnify the image of the sample. This is archived by focusing light onto the sample and then passing the light through a convex lens, for magnification. Although sample preparation for light microscopy is easy, the resolution (around 0.2 μm) and magnification (typically x400) is not ideal.[164]

Higher resolution and magnification can be achieved by using electrons accelerated by a voltage, which has a significantly shorter wavelength than visible light. Now the optical lenses are replaces with electromagnetic lenses which modify the electron path. Furthermore the sample is placed within a vacuum chamber so that air does not interfere with the electron path. Electron microscopy can be further subdivided into Transmission Electron Microscopy (TEM), Scanning Electron Microscopy (SEM) and Scanning Transmission Electron Microscopy (STEM).[165] TEM uses a parallel beam to probe the sample in transmission mode, this is often used to study the deeper structural features of the sample. On the other hand SEM uses a convergent beam of electrons to scan the sample and uses secondary electrons or back scattered to form an image. STEM utilises a convergent beam to scan over the sample whilst in transmission mode, which produces high-angle annular dark-field (HAADF) and bright-field (BF) images.[149,165,166,167] The highest resolution microscopes in the world are aberration-correction and enables atomic resolution images.

2.6.2 Hitachi TM4000

This is a tabletop scanning electron microscope which enables the option of detecting back scattering or secondary electrons which highlights more structural features or surface details respectively. Electrons can be accelerated at 20 keV, 15 keV, 10 keV and 5 keV. These parameters were optimised prior to collecting each image.

The sample is lightly scattered over adhesive carbon tape and then attached to the sample holder and placed under vacuum during analysis.

2.6.3 ePSIC at Diamond Light Soruce

Electron Physical Science Imaging Centre (ePSIC) is located at Diamond Light Source, Oxford and serves as a national facility which provides aberration corrected electron microscopy services through its two microscopes:

E01: a JEOL ARM200CF optimised for atomic resolution spectroscopy

E02: a JEOL ARM300CF optimised for high resolution imaging

E01 was accessed via a rapid access proposal during the Covid-19 pandemic, therefore we were not permitted to be at the microscope. Therefore images were taken through collaboration with the microscopy scientists: Emanuela Liberti and Tom Slater through two different sessions. The samples were passed onto them and ethanol was used to disperse the samples on a copper grid. In both sessions, microscope E01 was mostly operated in HAADF and BF mode at 200 kV. The microscopy images were studied using DigitalMicrograph Software by Gatan which enables distances to be measures on the image and also the fast Fourier transformed version too.

2.7 Thermogravimetric analysis- mass spectroscopy

2.7.1 TGA-MS: theory

Thermogravimetric analysis (TGA) is an intuitive study in which heat and gravity are used in combination to study the sample.[168] A sample is placed in a crucible on very sensitive scales and the weight of the sample is recorded as it is heated or cooled, when mass loss is observed this indicates the formation of gaseous species from the sample. This could be water moving out of pores, into the gaseous phase or a decomposition process to form carbon dioxide gas. Usually a TGA plot also contains a Differential Thermal Analysis (DTA) curve which is the temperature difference between a reference crucible and the sample, this is used to indicate exothermic and endothermic reactions as a function of temperature or time.[169]

If the crucibles and scales were placed in an inert gas atmosphere in a mostly sealed chamber with the exception of gas inlet and outlet flow, any gaseous species evolved can be analysed by analysing the outlet gas. In this study a mass spectrometer was attached to the TGA which enables us to plot the relative intensity of a m/z (mass/charge) signal as a function of temperature or time. By plotting the TGA, DTA and the mass spectroscopy measurements it is possible to deduce the range of temperatures between which a gas with a known mass is evolved. This is typically used to identify water, as surface water and water held in the pores or framework can be released during heating. Carbon dioxide can also be easily identified and is formed during the decomposition of carbonates.

2.7.2 TGA-MS: method

In this study a NETZSCH STA 449F1 TGA machine was used with the 403 Aëolos® Quadro quadrupole mass spectrometer. Nitrogen was used as the inert gas and Al_2O_3

crucibles with lids were used as the reference and also sample holder. Calibration was performed by running the heating program with the empty crucible and lid. Then the same heating program is used with the same crucible and lid, in addition to a small quantity of sample to collect the TGA, DTA and mass spectrometry data which is then plotted.

2.8 Electrochemical testing

2.8.1 Differential capacitance curves

Differential capacitance curves (DCC) (Figure 2.5) are generated by the collection of galvanostatic charge discharge data, however instead of plotting voltage against capacity, the differential of the capacity (dQ) is divided by the differential of the voltage (dV), plotted against the voltage (V).[†]

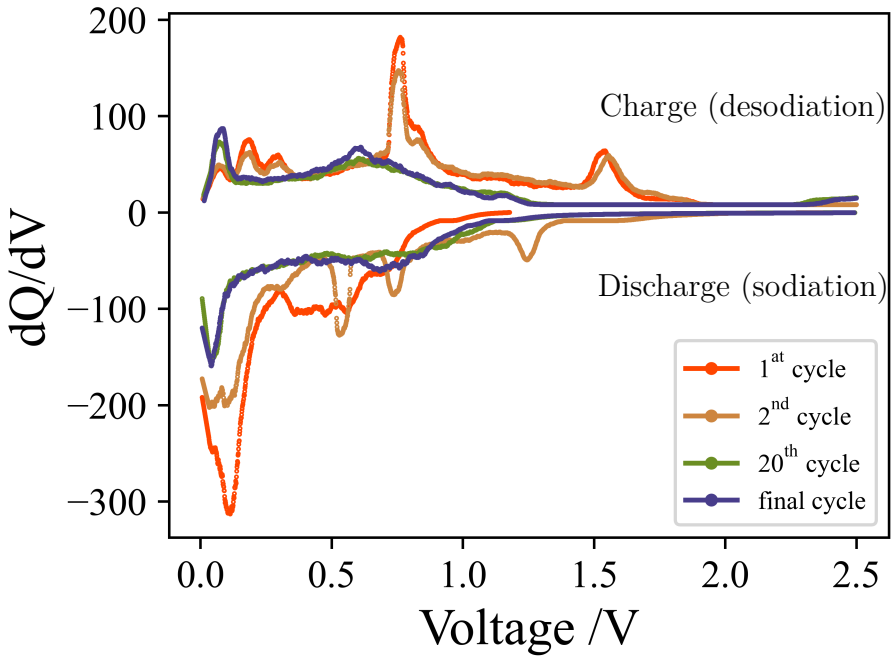


Figure 2.5: Example of a differential capacitance curve (DCC) for HNb_3O_8 in a sodium half cell.

Peaks observed in the differential capacitance curves are related to the voltages at which intercalation occurs. ΔV (units of V) is the difference between the sodiation and desodiation peaks. Typically ΔV will increase as cell cycling progresses due to the formation of SEI over cell cycles which increases the resistance within the cells, increasing the overpotential, and as a result reduces the capacity of the cell. Therefore

[†]A Savitzky–Golay filter is used to smooth the curves.[170]

differential capacitance curves provides additional information about the cell which is not easily obvious in the galvanostatic charge discharge curves.

2.8.2 Cyclic voltammetry

Cyclic voltammetry (CV) is used to probe the potential at which oxidation and reduction occurs. In CV experiments, the voltage is swept between two voltage limits at increasingly faster scan rates as demonstrated by the increasingly steep voltage lines Figure 2.6. Scan rates are typically given in units of mV/s.

$$Nb^{5+} + e^{-} \rightleftharpoons Nb^{4+} \tag{2.9}$$

When considering a simple system containing only Nb^{5+} and Nb^{4+} as the redox active species (Equation 2.9), the Nernst equation can be applied (Equation 2.10).[171] By changing the voltage, this alters the Nb^{5+}:Nb^{4+} ratio.

$$E = E^{0} + \frac{RT}{F} ln \frac{[Nb^{5+}]}{[Nb^{4+}]} \tag{2.10}$$

Table 2.6: Definitions, symbols and units of the parameters used in a Nernst equation, adapted for Nb.

Symbol	Information
E	Potential
E^{0}	Standard potential
R	Universal gas constant
T	Temperature
F	Faraday constant
$[Nb^{5+}]$	Concentration of Nb^{5+}
$[Nb^{4+}]$	Concentration of Nb^{4+}

Figure 2.6 shows a CV experiment swept at 0.1, 0.2 and 0.5 mV/s between the limits 2.5 V and 0.005 V and back, whilst the current is being recorded (Figure 2.6). Cyclic voltammetry results are typically presented with the current plotted against voltage

(Figure 2.7). The bottom curve shows desodiation characteristics whilst the upper curve shows sodiation characteristics.

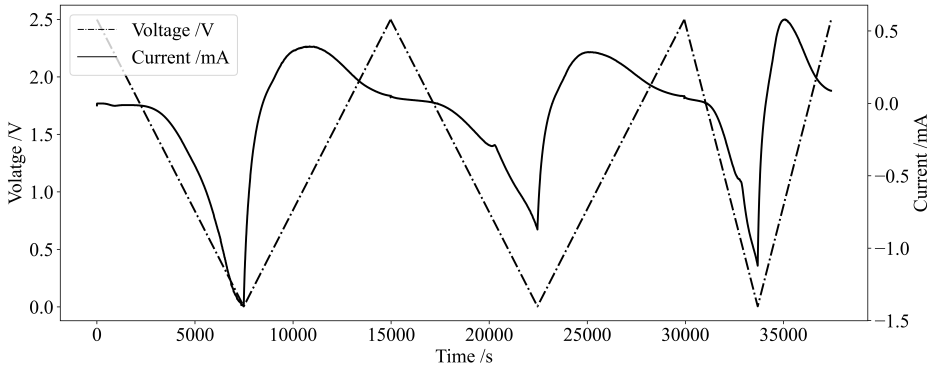


Figure 2.6: Plot showing the change in voltage and current against time in a CV experiment.

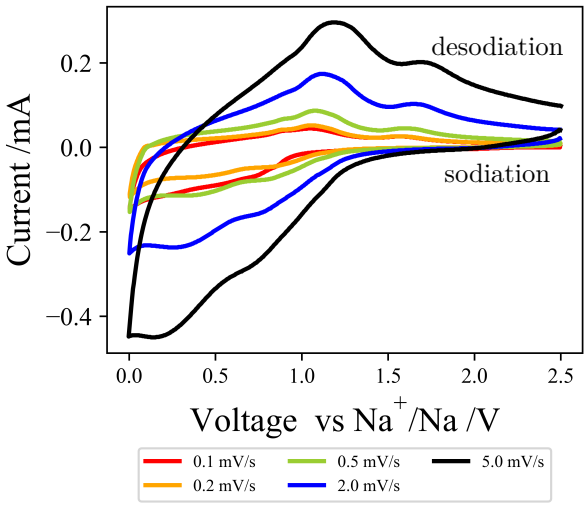


Figure 2.7: Cyclic voltammetry results at sweep rates of 0.1 mV/s, 0.2 mV/s, 0.5 mV/s, 1.0 mV/s, 2.0 mV/s and 5.0 mV/s.

Initially the system begins with 100 % Nb^{5+} and as the potential is swept from high to low potentials (sodiation), at a threshold potential Nb^{5+} concentration drops as it is converted to Nb^{4+}, correlated to sodium intercalation and an electron is released. The electron creates a Faradaic current which is detected and creates a peak in the cyclic voltammagram. This peak corresponds to the voltage a which the fastest rate

of reduction occurs. As the voltage is swept from low to high, the opposite it true and Nb^{4+} is oxidised and also creates a peak. The difference in voltage between these two peaks[171] is called the peak-to-peak separation (ΔE_p).

The aforementioned one electron system (Equation 2.9) is an oversimplification of a battery as there can be multiple redox reactions, irreversible reactions (i.e. SEI formation) and also diffusion or energy barrier dependent features.[171] For example a high energy barrier will cause an increase in ΔE_p.

The CV can be further processed by applying the Randles Sevcik equation (Equation 2.11), for fully reversible redox systems, obtained from N. Elgrishi *et al.*[171]

$$i_p = 0.446nFAC^0 \left(\frac{nFvD_o}{RT}\right)^{0.5} \tag{2.11}$$

Which can be simplified, where $b = 0.5$ and a is a constant:

$$i_p = av^b \tag{2.12}$$

Table 2.7: Properties of an XRD pattern and the sample information that can be derived from the property.

Symbol	Information
i_p	peak current
n	the number of electrons transferred in the redox event
F	Faraday constant
A	electrode surface area
C^0	bulk concentration of the analyte
v	scan rate
D_o	diffusion coefficient of the oxidized analyte

For a fully reversible redox reaction, with the charge carrier freely diffusing through the active material, i_p and $v^{0.5}$ should show a linear relationship. Deviation from this can be caused by two different reasons:

1. Electrochemical quasi-reversibility
2. Reaction occurs via a surface adsorbed species

These can be differentiated by studying the peaks in the CV. If the capacity is reversible, the sodiation and desodaition peaks show little peak separation (small ΔE_p). Conversely, an irreversible capacity occurs at the extremes of voltages, causing a large peak separation (large ΔE_p). Between these two limits are known as quasi-reversible reactions, and the peak changes varies with sweep rate. Whereas the peak separation of reactions that occurs via a surface adsorbed species do not change with sweep rates.[77,171]

Alternatively if the relationship between i_p and v is linear (b equals 1 in Equation 2.12), this also indicates that the reaction is surface-controlled.[77]

3 Synthesis and characterisation of KNb_3O_8, HNb_3O_8 and $H_3ONb_3O_8$

3.1 Introduction

KNb_3O_8 and HNb_3O_8 (sometimes reported as $H_3ONb_3O_8$) have shown some promise as anode materials, especially within lithium-ion batteries.[131,140,172] However little is understood about their capabilities within a sodium-ion battery.[143]

KNb_3O_8 is a well-studied structure with known atomic coordinates and a cif file, however this is not the case for $H_3ONb_3O_8$ and its dehydrated counterpart HNb_3O_8. The protonated structures are not fully understood, however these structures have also shown superior capacities compared to KNb_3O_8. Synthesis of KNb_3O_8 and HNb_3O_8 ($H_3ONb_3O_8$) are also the first steps in the synthesis of exfoliated and restacked $[Nb_3O_8]$ sheets, which we would also like to study as a nanostructured 2D anode material.

This Chapter outlines the synthesis and characterisation of KNb_3O_8, HNb_3O_8 and $H_3ONb_3O_8$. The following Chapter discusses the "top down" synthesis of nanostructured niobate from $H_3ONb_3O_8$ and its structure. Chapters 5 and 6 utilises "bottom up" approaches to form layered nanostructured niobates, which are also characterised. Finally, these materials will be tested as sodium-ion anode materials in Chapter 7, acting as important benchmarks for the electrochemical behaviour of the nanostructured niobates.

3.2 Synthesis of KNb_3O_8

Synthesis of KNb_3O_8 has been reported *via* a range of methods: solid-state,[84,131,143] molten-salt,[129] hydrothermal[28,135] and *via* organic gel.[173] The most commonly reported method is solid-state synthesis, which was therefore the first method tested. The method used in this study closely follows the methods reported by H. Nakayama and M. Nose *et al.*[143] which is discussed in more detail in the methods section.

This Chapter then explores the use of ball milling to improve homogeneity in the reagent mixture prior to heating, this has been explored with niobate systems[174] and is an established method for inorganic synthesis of oxide materials and also KNb_3O_9[174]. Commonly, an excess of K_2CO_3 is added to combat potassium-ion volatility.[175] Furthermore to improve the synthesis, molten salt method[129,130] was trialled by adding KCl to act as a liquid solvent at high temperatures. This has been reported within KNb_3O_8 systems by F. Madaro *et al.*[129] and then refined to the appropriate quantities.

Finally, mixing the reagents in a wet mixture was explored, a little similar to[174] who used a K_2CO_3 solution whilst this study utilised the solvent iso-propyl alcohol (IPA), in addition to the use KCl, a novel method which has not been reported elsewhere. The aforementioned methods all lead to the synthesis of KNb_3O_8[114,128,129,131] although at times an impurity phase was reported, such as $K_{2.6}Nb_{11.6}O_{30}$[176], $K_2Nb_4O_{11}$[177] and $K_2Nb_8O_{21}$[130] whilst some papers did not name the impurity.[115]

3.2.1 Introduction of impurity phases

Ideally synthesis leads to a phase pure sample, however this is often not the case. Generally synthesis procedures are optimised to minimise impurities and this requires the identification of impurities.

Table 3.1: Crystallographic information for Nb_2O_5 $K_2Nb_4O_{10}$ and $K_2Nb_8O_{21}$.

Property	Nb_2O_5,	$K_2Nb_4O_{10}$	$K_2Nb_8O_{21}$
Space group	*P2/m*	*P /mbm*	*Pmam*
a / Å	21.153	12.577	37.509
b / Å	3.8233	12.577	12.494
c / Å	19.356	3.983	3.9701
β / °	119.8	90	90
Known atomic positions	yes	proposed†	no
ICSD cif code	29	193496	-
PDF 4+	-	01-083-6139	00-031-1060

† ICSD entry for $K_2Nb_4O_{10}$ reports that the stoichiometry is not precise, due to large errors.

The impurity phases relevant to this discussion are: Nb_2O_5, $K_{2.05}Nb_{3.74}O_{9.81}$ and $K_2Nb_8O_{21}$ (Table 3.1). In this study the structure $K_{2.05}Nb_{3.74}O_{9.81}$ (PDF 4+: 00-031-1059, ICSD: 193496) will be discussed as $K_2Nb_8O_{21}$ for simplicity and clarity during discussion. The ICSD entry 193496 has several warnings associated with it, particularly due to the refinement of atomic occupancies against relatively poor data. Therefore, the stoichiometry of this phase is not well known, and although this structure could potentially be used as a secondary phase in Rietveld refinements, these results would not be robust. The structural information for these impurity phases were obtained from ICSD and PDF 4+ databases (Table 3.1). The phases Nb_2O_5 and $K_2Nb_4O_{10}$ have known atomic positions and reported cif files (Figure 3.2) and therefore can be used for Rietveld refinement, unlike $K_2Nb_8O_{21}$.

Interestingly the $K_2Nb_4O_{10}$ and $K_2Nb_8O_{21}$ phases appear to be related, with similar b and c unit cell parameters and a factor of three difference in a. Furthermore the reported XRD patterns are very similar too (Figure 3.1). Therefore XRD patterns can be matched to either $K_2Nb_4O_{10}$ or $K_2Nb_8O_{21}$, it is not possible to differentiate between the two using XRD. Nb_2O_5 on the other hand is a thoroughly studied material. Any refinements performed in reference to Nb_2O_5 and $K_2Nb_4O_{10}$ begins with the parameters stated in Table 3.1.

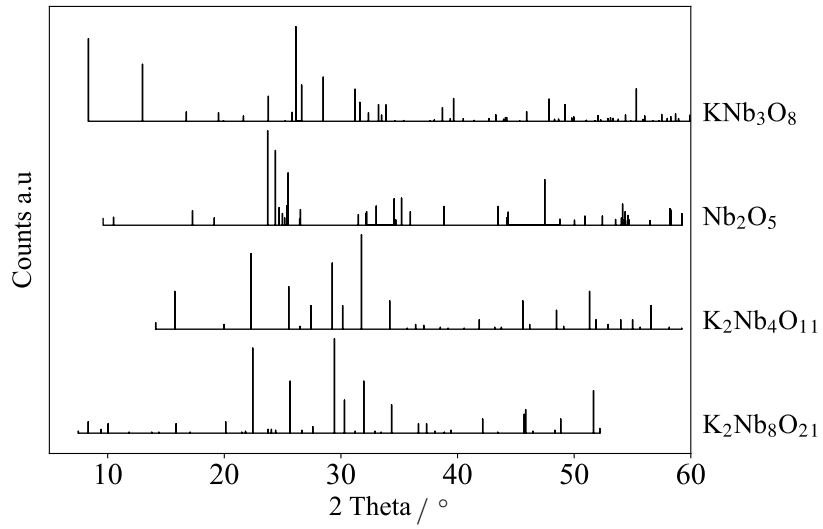


Figure 3.1: XRD patterns of KNb_3O_8, Nb_2O_5, $K_2Nb_4O_{10}$ and $K_2Nb_8O_{21}$ obtained from the PDF 4+ database ($\lambda = 1.542$ Å).

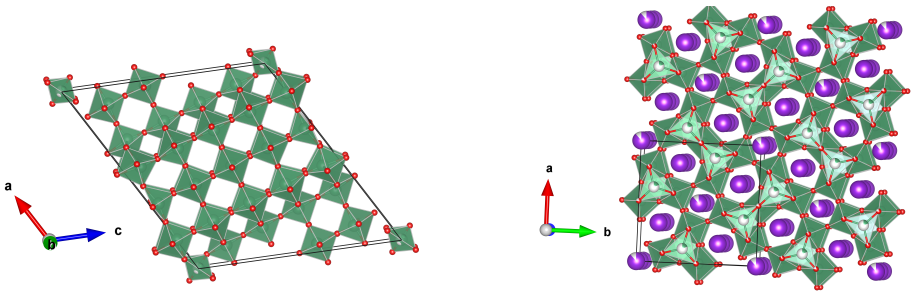


Figure 3.2: Unit cells depicted using green NbO_6 units with red spherical vertices representing oxygen and potassium as purple spheres for a) Nb_2O_5 b) $K_2Nb_4O_{10}$.

3.2.2 Solid-state synthesis

Synthesis method

KNb_3O_8 was synthesised following the method reported by H. Nakayama *et al.*[143] by mixing reagents K_2CO_3 (99+ %, ACS reagent, anhydrous, Thermo Scientific Chemicals) and Nb_2O_5 (99.9 % metals basis, Thermo Scientific Chemicals) in a stoichiometric molar ratio of 1:3 using a pestle and mortar (Equation 3.1). 0.7 g of the ground powder

was formed into a pressed pellet (13 mm diameter) and was placed in an open Al_2O_3 crucible. The pellet was heated to 800 °C at a heating ramp rate of 10 °C per min and annealed for 40 hrs using a Carbolite CSF 1200 muffle furnace. The white pellet (pellet-KNb_3O_8) was cooled naturally within the furnace to room temperature, ground using a pestle and mortar, and analysed using powder x-ray diffraction (PXRD) (Figure 3.3).

$$K_2CO_{3(s)} + 3\,Nb_2O_{5(s)} \rightarrow 2\,KNb_3O_{8(s)} + CO_{2(g)} \tag{3.1}$$

Results

The PXRD pattern showed some reflections which could be indexed to KNb_3O_8. However, there were also additional reflections indicative of an impurity phase. Impurities of both Nb_2O_5 and reflections due to either $K_2Nb_8O_{21}$ or $K_2Nb_4O_{10}$ were identified.

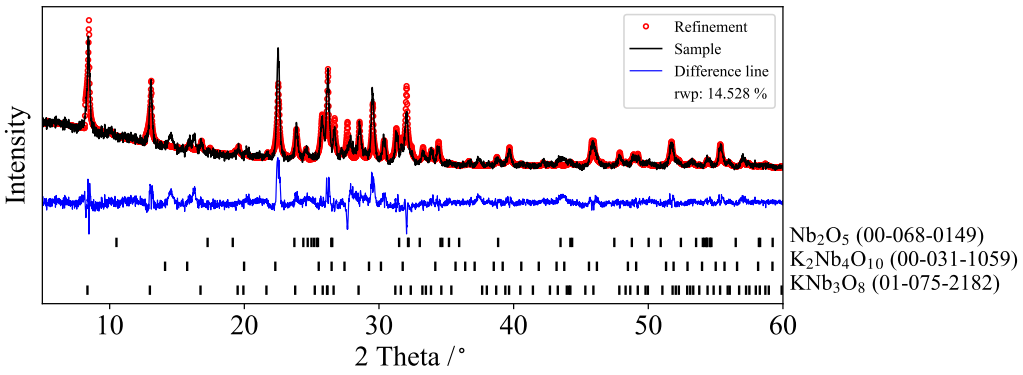


Figure 3.3: PXRD pattern of pellet-KNb_3O_8 (black) with the fit obtained from Rietveld refinement (red) and the difference line (blue). Tick marks showing the peak positions found for phases Nb_2O_5, $K_2Nb_4O_{10}$ and KNb_3O_8 obtained from the PDF 4+ database have been added at the bottom. For clarity purposes not all marks from Nb_2O_5 were added, any peaks less than 5 % intensity of the most intense Nb_2O_5 peak are unmarked.

$K_2Nb_8O_{21}$ is potassium rich whilst $K_2Nb_4O_{10}$ is potassium deficient compared to KNb_3O_8, and due to the inability to indisputably assign the impurity phase to a chemical formula, this impurity phase could not be used to indicate whether the system was potassium rich or potassium deficient. However, the persistence of Nb_2O_5, from the

starting material, either indicated a lack of K_2CO_3 in the system, which is possible due to the known high temperature volatility of K or a localised deficit of K which is due to inhomogeneity during reagent mixing.

R.L. Lehman *et al.*[178] reported heating K_2CO_3 and observing mass loss when heating K_2CO_3 between 850- 1000 °C using TGA due to the volatility of K_2CO_3 or its decomposition products. As a result, it is common practice[174,179,180,181,182] to increase the K_2CO_3 content, beyond the stoichiometric ratio within the reagent mixture to counteract this phenomena.

As a result, above stoichiometric amounts of potassium were added and a ball mill was used to improve the homogeneity of the reagent mixture.

Figure 3.3 shows the Rietveld refinement containing the phases KNb_3O_8, Nb_2O_5 and $K_2Nb_4O_{10}$ with 33.77 %, 10.06 % and 56.16 % weight percent respectively. Note that $K_2Nb_4O_{10}$ was used for the Rieveld refinement instead of $K_2Nb_8O_{21}$ because no structure is available for this other phase. This shows a suitable fit with an r_{wp} of 14.528 %, therefore, this supports the results from DIFFRAC.EVA software.

Ball mill method

A 1.2:3 molar ratio of K_2CO_3:Nb_2O_5* respectively were milled in a ball mill (Pulverisette 7 Planetary Micro Mill) was used to improve homogenisation. Samples were milled for 30 minutes at 500 rpm with two Al_2O_3 balls with a intermediate pause at 15 minutes to reverse milling direction. Both wet (denoted W-) and dry (denoted D-) milling were tested in order to determine how to most effectively form a homogeneous mixture and the impact on the yield of KNb_3O_8. IPA (Certified AR for Analysis, Fisher Chemical) was added to the regent mixture for wet milled samples and dried at 60 °C prior to annealing to evaporate the IPA. The implementation of an intermediate grinding step during annealing was also tested with the aim of improving the purity of KNb_3O_8.

*(99+ %, ACS reagent, anhydrous, Thermo Scientific Chemicals) and (99.9 % metals basis, Thermo Scientific Chemicals) respectively

Table 3.2: Various heating methods and their corresponding sample names.

Sample name	Heating pattern	Reference
W-HeatA	800 °C for 40 hrs	[143]
W-HeatC	600 °C for 2 hrs and then 900 °C for 3 hrs	[56]
D-HeatA	800 °C for 40 hrs	[143]
D-HeatB	800 °C for 20 hrs, twice*	n/a†

* Includes an intermediate grinding step at rt with a pestle and mortar.
† This is a novel heating pattern.

All heating was performed at a ramp rate of 10 °C per min. The milled powders were heated in an alumina crucible fitted with an alumina lid in an attempt to mitigate the loss of K. Different heating patterns were tested as a variety was reported in literature (Table 3.2).

Ball mill results

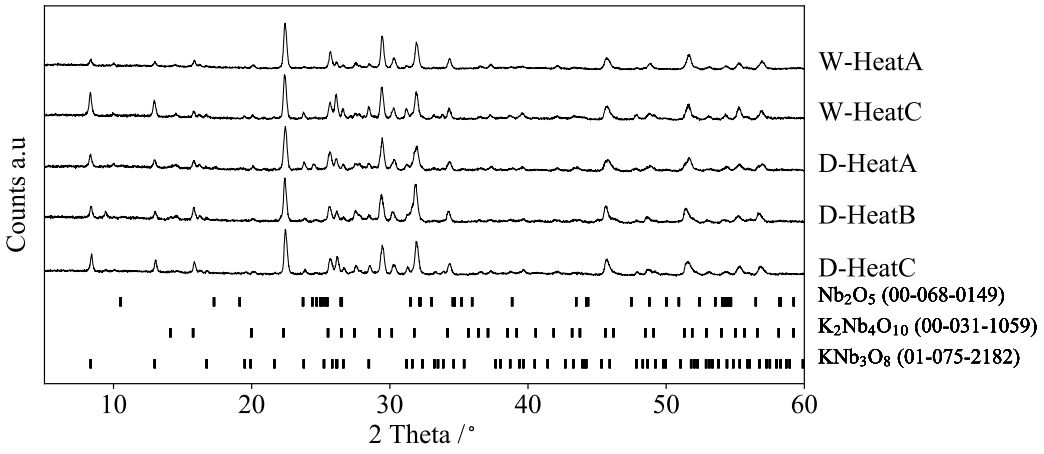


Figure 3.4: XRD patterns of samples synthesised using the parameters as outlined in Table 3.2. Tick marks for $K_2Nb_4O_{10}$ have been added at the bottom.

Despite different heating patterns and improved mixing by using a ball-milling step, this formed even more impure samples of KNb_3O_8 (Figure 3.2 and Table 3.3). Despite the introduction of a ball mill, there are still significant problems with the homogeneity

of the mixture and possibly potassium content, therefore molten salt synthesis was explored.

Table 3.3: Calculated weight percentages from Rietveld refinement.

Sample name	r_{wp} %	Weight percentage of phases fitted %		
		KNb_3O_8	Nb_2O_5	$K_2Nb_4O_{10}$
pellet-KNb_3O_8	14.47	33.23	10.19	56.6
W-HeatA	18.71	9.14	17.0	73.9
W-HeatC	19.57	28.9	6.94	64.2
D-HeatA	17.10	10.8	21.4	67.7
D-HeatB	14.28	13.4	10.1	76.5
D-HeatC	17.24	20.3	12.7	66.9

3.3 Molten salt synthesis of KNb_3O_8

3.3.1 Introduction

Above 770 °C, KCl melts and acts as a solvent to facilitate mixing of K_2CO_3 and Nb_2O_5 during calcination. This, in theory, encourages the synthesis of one single pure product. However, the introduction of KCl into the reagent mixture can cause the formation of the $K_2Nb_8O_{21}$ phase (Equation 3.2), therefore this reaction will invariably compete with the synthesis of KNb_3O_8 (Equation 3.1) during calcination. Despite this, the molten salt method is widely reported for KNb_3O_8 [129,130,183] and commonly used as an alternative to conventional solid-state synthesis.

$$8\,Nb_2O_5 + 4\,KCl + O_2 \rightarrow 2\,K_2Nb_8O_{21} + 2\,Cl_2 \tag{3.2}$$

Madaro *et al.* reported significantly higher mass loss due to the evaporation of the salt flux, [129] when heating at 1000 °C compared to 800 °C. Therefore the the heating pattern was modified by reducing the synthesis duration from 20 hrs to 3 hrs at 800 °C. Lastly to thoroughly ensure a homogeneous mixture, the duration of ball milling was increased from 30 mins to 2 hrs.

3.3.2 Molten salt synthesis

Molten salt synthesis method

Four samples were made to identify the effect of further addition (increase from 10 wt. % to 15 wt. %) of KCl (Sigma- Aldrich, >99.0 %) coupled with increase the ratio between K_2CO_3:Nb_2O_5 from 1:3 to 1.1:3. Therefore, four samples in total, as outlined in Table 3.4. The desired quantities of K_2CO_3 (99+ %, ACS reagent, anhydrous, Thermo Scientific Chemicals), Nb_2O_5 (99.9 % metals basis, Thermo Scientific Chemicals) and KCl (99 %, Thermo Scientific Chemicals) were ball milled at 500 rpm for 2 hrs. The mixture was heated for 3 hrs at 800 °C and then cooled naturally to room temperature. The sample was then ground using a pestle and mortar and washed with deionised water to remove KCl from the insoluble product. The product was dried overnight at 60 °C and then analysed by PXRD.

Table 3.4: Proportion of KCl, K_2CO_3 and Nb_2O_5 used as a reagent in the molten salt synthesis of KNb_3O_8

Excess KCl by wt. %	Molar ratio of K_2CO_3:Nb_2O_5
15	1.1:3
10	1.1:3
15	1.0:3
10	1.0:3

Molten salt synthesis results

The molten-salt synthesis route has shown significant improvement to conventional solid-state synthesis (Table 3.5 and Figure 3.5) with a significant increase in the weight percentage of the target KNb_3O_8 in the product. A change in the proportion of KCl from 10 to 15 wt. % caused little effect on the product, however changing the ratio of K in the regent mixture has a significant effect. Phase factions determined through Rietveld refinement shows the highest yields when using a molar ratio of 1.1:3, this also corresponds to the most ideal K:Nb ratio obtained in this study so far, however these results are significantly different from those reported by F. Madaro[129] and Z. Zhan,[114] who reported high phase purity.

Table 3.5: Rietveld refinement results from molten salt synthesis.

Sample name	r_{wp} %	Weight percentage of phases fitted %		
		KNb_3O_8	Nb_2O_5	$K_2Nb_4O_{10}$
15 % KCl, 1.1:3 ratio	11.93	75.45	0.03	24.52
10 % KCl, 1.1:3 ratio	12.47	76.72	0.17	23.11
15 % KCl, 1:3 ratio	15.92	61.23	1.78	36.99
10 % KCl, 1:3 ratio	15.08	57.31	0.00	42.69

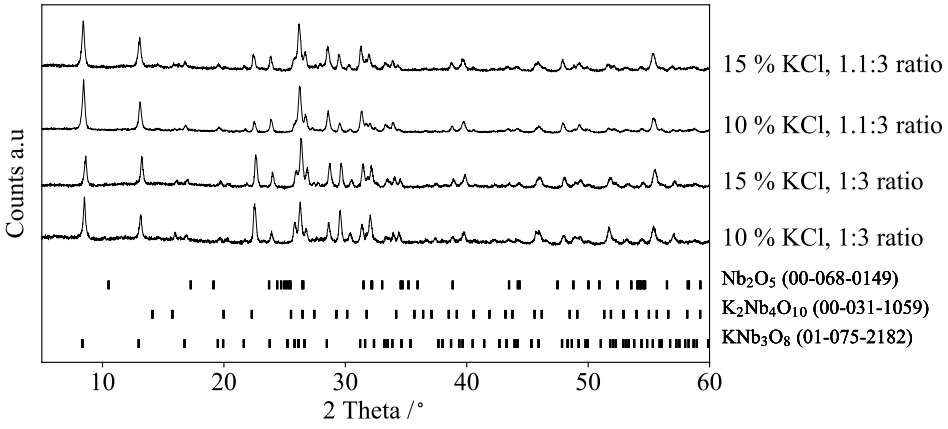


Figure 3.5: XRD patterns of samples made *via* molten salt synthesis using different molar ratios of K_2CO_3:Nb_2O_5 and KCl.

Adapted method at Diamond Light Source

During my PhD, I relocated from the University of Birmingham to Diamond Light Source in which access to a ball mill was not possible and an alternative synthesis method was developed did not require a ball mill. Therefore to achieve a high degree of mixing, K_2CO_3 (99+ %, ACS reagent, anhydrous, Thermo Scientific Chemicals), Nb_2O_5(99.9 % metals basis, Thermo Scientific Chemicals), KCl (99 %, Thermo Scientific Chemicals) in a 1:3 stoichiometric ratio, with the addition of 10 % by weight was stirred in IPA (Certified AR for Analysis, Fisher Chemical) for 20 mins and then poured into a Al_2O_3 crucible and left at room temperature overnight to allow for the IPA to evaporate. This leaves a pellet-like solid in the crucible which is then heated to 800 °C for 2 hrs and then cooled naturally to room temperature. The product is washed with deionised water using a Buchner funnel to remove excess KCl and then dried and analysed by powder x-ray diffraction (PXRD) (Table 3.5).

Results following adapted method at Diamond Light Source

The purity was first assessed using PXRD, the single phase Rietveld refinement of the PXRD pattern (Figure 3.6) provided a good fit using KNb_3O_8 with a Stephens Orthorhombic function to model anisotropy (r_{wp} 7.54 %). Indicating a peak broadening of reflections containing h and k contributions, whilst reflections containing l contributions sharpened. This suggests the rods grow along the [001] direction. This is consistent with the refinement methods used by K. McColl *et al.*[131] for KNb_3O_8. The position (020) reflection indicates an interlayer spacing of 10.61 Å.

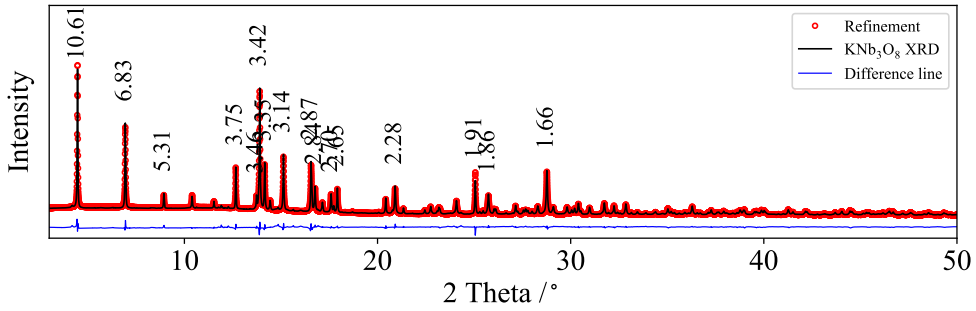


Figure 3.6: KNb_3O_8 XRD pattern obtained on I11 (λ = 0.825255 Å) with the results from Rietveld refinement with the d-spacing values.

Although the improvement in phase purity could be attributed to the change in methodology, this could also be attributed to the use of new, uncontaminated chemicals. This would also explain the discrepancy between reported successful synthesis of KNb_3O_8 via solid state and molten salt methods which were not reproduced in the aforementioned studies. Although it would be interesting to determine the cause of this observed improved phase purity, this is beyond the aims of this study which focuses on the synthesis of exfoliated and restacked [Nb_3O_8] layers. As a reproducible, reliable method of synthesising KNb_3O_8 with a high phase purity has been established, this was used throughout this study.

3.3.3 Detailed characterisation of KNb_3O_8

Table 3.6: Peaks identified in the D(r) matched to the known atomic distances of KNb_3O_8.

r /Å	Assignment	Reported r /Å*
1.99	Nb-O	2.067
3.42	Edge sharing Nb-Nb	3.446
3.81	Corner shared Nb-Nb and K-K	3.844 and 3.799
4.17	K-Nb	4.155
4.91	K-K	4.4996
5.43	Nb-Nb distance	5.455

*Information obtained from KNb_3O_8 cif file, ICSD code: 31994. There are also variation between bond lengths from atoms occupying various sites and therefore these values are only used as a representation.

The PDF for KNb_3O_8 (Figure 3.7.a.) was fitted to the known structure of KNb_3O_8 using small box modelling (Table 3.7), providing results consistent from Rietveld refinement of PXRD. Low r peaks, shorter atomic distances observed in the PDF have been assigned to known atomic distances obtained from the cif file (Table 3.6) and show a good agreement. The PDF (Figure 3.7.a.) shows medium range coherence as there are peaks still present at 40 Å, this supports the observation of strong Bragg peaks in the PXRD and is expected of crystalline materials. Using x-ray scattering techniques we have deduced the structure to be consistent with the known structure of KNb_3O_8 locally, and in the long range.

Table 3.7: A table of results from χ^2 minimisation analysis methods to study KNb_3O_8.

Unit cell parameters	Rietveld refinement of PXRD	Small box refinement of PDF	ICSD values
a / Å	8.91748(8)	8.9324(18)	8.90300
b / Å	21.2026(2)	21.240(4)	21.16000
c / Å	3.80465(3)	3.8138(7)	3.79900
r_{wp} / %	7.54	29.69	-

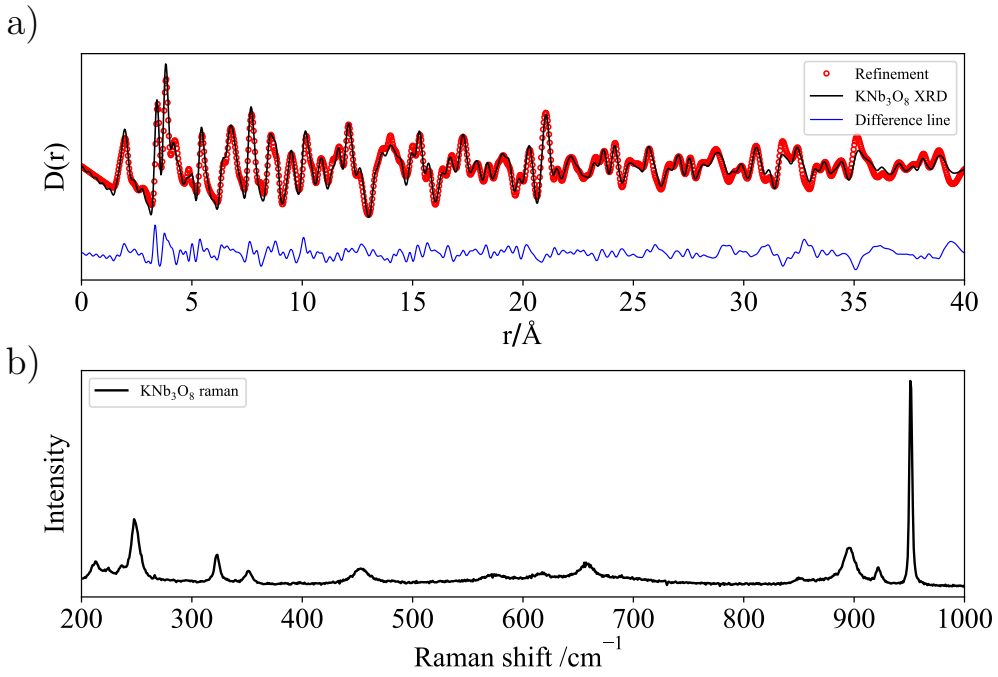


Figure 3.7: Results from structural analysis of KNb_3O_8. a) Pair distribution function b) Raman spectra.

Peaks between 850-1000 cm^{-1} in the Raman spectra (Figure 3.7.b.) have been assigned to the short Nb=O bond vibration in a highly distorted NbO_6 unit, whilst peaks between 500-700 cm^{-1} have been assigned to Nb-O vibrations within the framework which are expected in layered niobates like KNb_3O_8.[184,185] Finally the 200- 300 cm^{-1} region has been assigned to Nb-O-Nb vibrations.[128,185] Raman spectra were consistent with literature and the expected peaks are observed (Figure 3.7.b. and Table 3.8).

SEM images (Figure 3.8) show particles with needle-like morphology, which supports literature reports.[129] Fouier Transform of HDAAFF STEM shows a spacing of 10.56 Å between the atom lattice then which supports the d-spacing value of 10.61 Å as determined through Rietveld analysis of the PXRD data.

By comparing the results from a range of characterisation techniques and known literature reports, we are confident that KNb_3O_8 has been successfully synthesised. This is crucial as this is the precursor to $H_3ONb_3O_8$ and also the restacked niobate phases.

Table 3.8: Peaks identified in the Raman spectra for KNb_3O_8 obtained from this study compared against the reported wavenumbers for KNb_3O_8 have been obtained from J.K D. de Souza *et al.*[177] whilst the assignment was made using B. Yu *et al.* reports on KNb_3O_8.[186]

Band cm^{-1}	Intensity	Reported band cm^{-1}	Reported assignment
213	weak	-	Nb–O framework
248	medium	249	Nb–O framework
323	medium	323	E mode: deformation in the NbO_6 framework
351	weak	352	E mode: deformation in the NbO_6 framework
453	weak	453	E mode: Nb–O–Nb bending modes
617	weak	618	E mode: antisymmetric stretching of NbO_6 octahedra
657	weak	660	E mode: antisymmetric stretching of NbO_6 octahedra
852	weak	851	Stretching of short Nb=O bond
895	medium	896	Stretching of short Nb=O bond
922	weak	924	Stretching of short Nb=O bond
951	strong	952	Stretching of short Nb=O bond

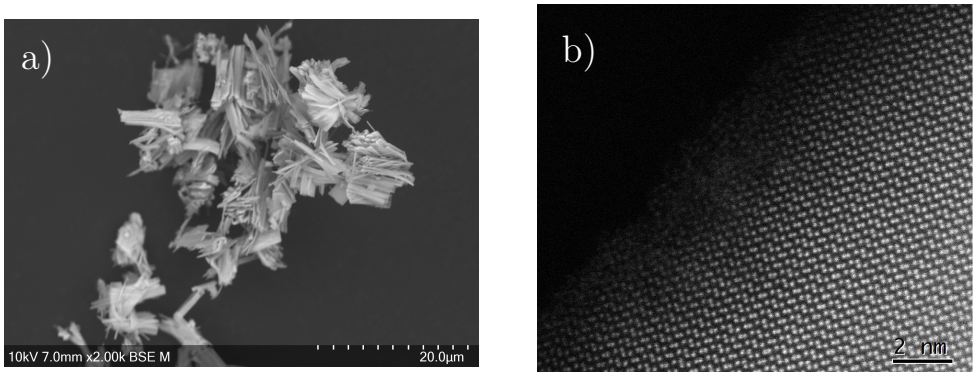


Figure 3.8: Results from structural analysis of KNb_3O_8. a) SEM b) High resolution STEM-HAADF.

3.3.4 Summary: KNb_3O_8

There are many successful reports of conventional solid state synthesis of KNb_3O_8, which could not be replicated in this study. This could be due to impurities in the regents used, and on moving to Diamond Light Source and the use of new reagents, enabled the synthesis of high purity KNb_3O_8. Further studies on the purity of each reagent was not carried out as the study focuses on synthesising a pure sample of KNb_3O_8.

Nonetheless, changing reagent ratios, heating duration and modifying the method of mixing the regents were all tested and optimised. Synthesis of KNb_3O_8 was found to produce impurities such as Nb_2O_5 and $K_2Nb_4O_{10}$.

This study found that the highest purity KNb_3O_8 phase was produced by the adapted molten salt method. All subsequent synthesis was carried out at Diamond Light Source using the novel molten salt method, a new synthesis method that has previously never been reported.

3.4 Synthesis of $H_3ONb_3O_8$ from KNb_3O_8

Protonation is a crucial step in exfoliating KNb_3O_8 as the ion-exchange increases the interlayer spacing in -Nb_3O_8 systems.[55] The larger interlayer spacing weakens the forces of attraction between the niobate layers. This weaker attraction facilitates the delamination of the niobate layers, which is not possible directly from KNb_3O_8.[55,179,179,187]

$$KNb_3O_{8(s)} + H_3O^+{}_{(aq)} \rightleftharpoons H_3ONb_3O_{8(s)} + K^+{}_{(aq)} \tag{3.3}$$

Direct synthesis of $H_3ONb_3O_8$ has not been reported, and is synthesised via KNb_3O_8, by adding aqueous HCl to KNb_3O_8 to produce $H_3ONb_3O_8$ (Equation 3.3).[56,119,124] Cation exchange is achieved by adding HCl of various concentrations to KNb_3O_8 for periods of several days.[56]

3.4.1 Protonation of KNb_3O_8 using HCl

Method

Following established methods,[56] ground powder of KNb_3O_8 was added to 6 M HCl[†] (75 mL/g) and stirred for one week. The solution was then filtered using a Buchner funnel, washed with deionised (DI) water and then dried at 60 °C overnight. The white powder was ground by hand using a pestle and mortar and then analysed.

[†]Thermo Scientific Chemicals

Results

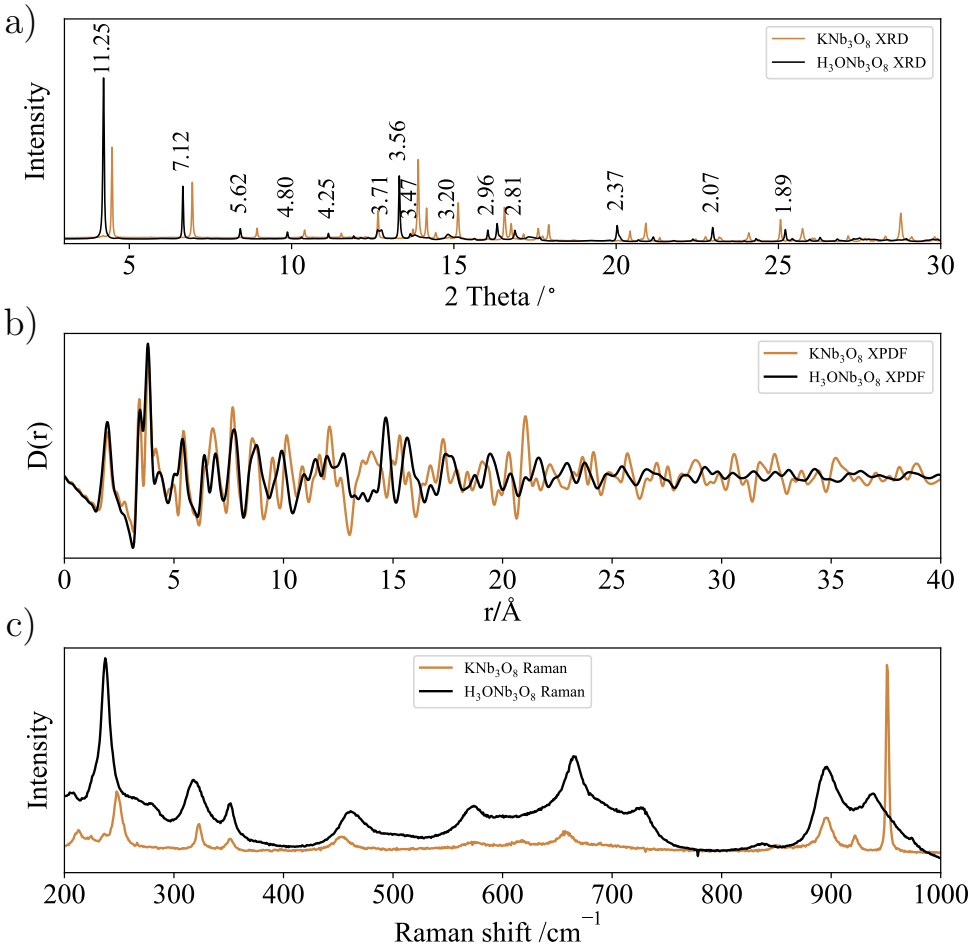


Figure 3.9: Results from structural analysis of $H_3ONb_3O_8$. a) XRD pattern collected on I11 ($\lambda = 0.825255$ Å) and Rietveld refinement with the d-spacing values labelled. b) Pair distribution function c) Raman spectra.

The PXRD pattern (Figure 3.9.a.) shows a shift in most peaks to lower 2θ values which indicated successful ion-exchange due to the expansion in the b direction. An exception can be observed in the (002) peak at 1.89 Å in which the peak shifts to a higher two theta. The (020) reflection showed an increase in the interlayer spacing from 10.61 Å in KNb_3O_8 to 11.25 Å in $H_3ONb_3O_8$. C. Huang *et al.*[128] reported the interlayer space of KNb_3O_8 and $H_3ONb_3O_8$ to be 10.5 Å and 11.1 Å respectively which supports the findings of this study.

The PXRD pattern for $H_3ONb_3O_8$ was studied further by Pawley refinement using space group *Amam* and lattice parameters as adopted from KNb_3O_8 in preparation for further Rietveld analysis work (Figure 3.10). The Pawley fit showed interesting inconsistencies in the peak shape especially between 13- 18° 2θ. The majority of the peaks are very sharp, but in some regions the peaks became very broad, but not smooth. This change in peak shape within one sample lead us to explore the presence of stacking faults within the sample, which is discussed further in Section 3.4.2.

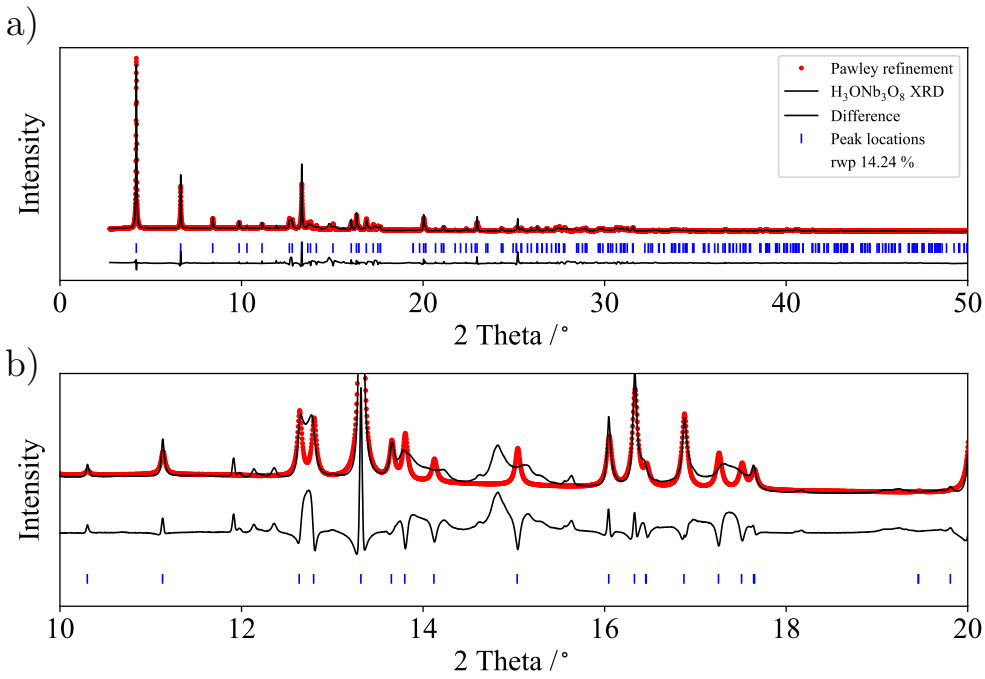


Figure 3.10: Pawley fitting of $H_3ONb_3O_8$ on XRD pattern collected from I11 beamline (λ = 0.825255 Å) with tick marks in blue to show the expected peak locations. a) in the range 0- 50° 2θ. b) in the range 10- 20° 2θ.

The ion exchanged sample still shows significant long range order (Figure 3.9.a. and b.), although to a lesser degree than KNb_3O_8 which is expected due to the process of ion-exchange. ICP-MS results reveal that K is still present (2.96 wt. %) of the total sample, which is a reduction from KNb_3O_8 (7.88 wt. %), but not completely exchanged and therefore we would expect some inconsistency in the interlayer distance. This is supported by the PDF pattern which indicates that the short range structure (0 Å$< r <$ 6 Å) remains similar to KNb_3O_8, although there are significant differences beyond

10 Å which is probably due to differences in correlation distances between atoms of different niobate layers. The process of ion-exchange reduced the overall crystallinity of the structure, as observed in the PDF data (Figure 3.9.b.) which damps more rapidly as a function of r in $H_3ONb_3O_8$ due to the shorter coherence range of the sample.

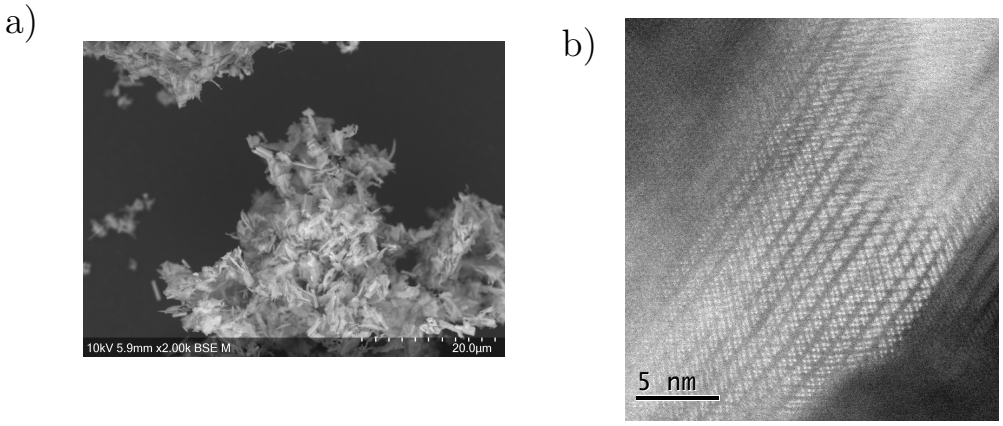


Figure 3.11: Microscopy of $H_3ONb_3O_8$ a) SEM b) High resolution STEM-HAADF with some electron damage.

SEM (Figure 3.11.a.) shows the retention of needle morphology as inherited from KNb_3O_8, whilst STEM-HAADF (Scanning Transmission Electron Microscopy- High Angle Annular Dark Field) (Figure 3.11.b.) shows the presence of layered ordered atoms which is expected of a crystalline material. The group of three atoms in a triangle within the layers is similar to the niobate arrangement found in KNb_3O_8.

A comparison of the Raman spectra of $H_3ONb_3O_8$ and KNb_3O_8 is shown in Figure 3.9.c. The decrease in the intensity of the band at around 950 cm^{-1} upon protonation of KNb_3O_8 has also been observed by A. Kudo *et al.*[181] They assigned the band at 950 cm^{-1} to the short Nb-O bond which protrudes into the interlayer. Furthermore the bands have shifted to a lower wavenumber on ion exchange, as expected due to H-bonding to the interlayer H_3O^+ ion which decreases the Nb-O bond order.[181] This peak shift was also observed in the study performed by C. Huang *et al.*[128]

3.4.2 Stacking faults study of $H_3ONb_3O_8$

The crystal structure of $H_3ONb_3O_8$ was investigated using high resolution powder XRD collected on the I11 beamline ($\lambda = 0.825255$ Å).

The structure of $H_3ONb_3O_8$ is not known and therefore this study has utilised the structure of KNb_3O_8 as a starting point. The interlayer K was replaced with an O atom in the modelled structure; H-atoms were neglected as this stage due to their negligible scattering.

Within TOPAS, stacking faults are probed by describing a structure as a series of layers, where different transitions between layers can have different probabilities.[‡] Layers are generated according to user defined probabilities for stack transitions, and add up to form a stack containing a user defined number of layers. Then by generating a large number of stacks and using these to generate an XRD pattern, we are able to model a structure with stacking faults by describing the probability of transitioning from one layer to the next.

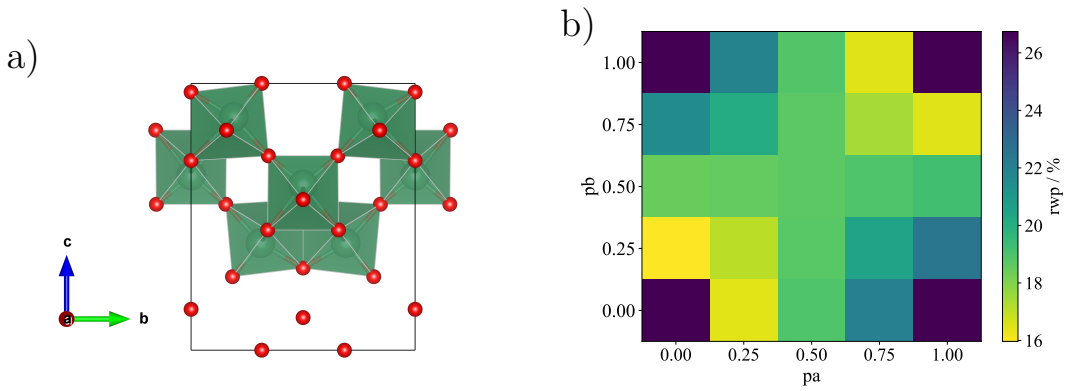


Figure 3.12: a) A schematic of the KNb_3O_8 structure transformed into the *Pmm2* unit cell with the K atoms replaced with O, shown in red; Nb atoms are in green. b) A colour map displaying the effect of changing parameters pa and pb to the r_{wp} values, where pa and pb change in steps of 0.25.

[‡]For more information refer to this tutorial:
https : //topas.webspace.durham.ac.uk/tutorial_stacking_faults/

TOPAS only allows the stacks to be generated in the *c* direction and therefore the unit cell had to be reassigned to the *Pmm2* space group from *Amam* so that the stacking direction is in *c* (Figure 3.12.a.).[144] The unit cell was also halved so that it only contained one of each layer type; one niobate layer and one interlayer. The relative alignment of these two layers is then handled within the stacking faults code.

The new *Pmm2* based structure (Figure 3.12.a.) was written in the format required by the stacking faults code in TOPAS, all niobate layers would transition to oxygen layers and vice versa. The transition from the niobate layer to the oxygen layer either proceeded *via* a shift of $a + 0.5$ (probability of pa) or no shift (probability of 1 - pa), where pa is a user determined parameter. Similarly, the transition from the oxygen layer to niobate layer *via* a shift of $a + 0.5$ (probability of 1 - pb) or no shift (probability of pb), where pb is a user determined parameter. The parameters were written this way because when pa = 0 and pb = 0, the structure is analogous to KNb_3O_8 (Table 3.9). The $NaNb_3O_8$ structure is similar to KNb_3O_8, however the niobate layers do not shift by 0.5.§

Table 3.9: The implications of probability parameters pa and pb on the structure of the material, liked to the phases KNb_3O_8 and $NaNb_3O_8$, but the interlayer ions are oxygen (instead of K or Na) in the model.

		pa value	
		0	1
pb value	0	KNb_3O_8	$NaNb_3O_8$ but K atoms are in a shifted site*
	1	$NaNb_3O_8$	KNb_3O_8 but the K atoms are in a shifted site*

*The K atoms possess a 0.5 unit cell shift out of their ideal positions in *a*.

TOPAS generates 100 stacks, each stack containing 100 layers, and the XRD pattern of these 100 stacks are used to model the structure, the PXRD patterns were simulated and averaged and refined to the experimental PXRD data. The nature of these stacks are determined by the probability parameters pa and pb. Only peak shapes and thermal parameters were allowed to refine as lattice parameters were previously optimised.

§Diagram of KNb_3O_8 and $NaNb_3O_8$ can be found in the Section *A-Nb-O systems, A = Na, K*

A broad study was performed by varying pa and pb by a step-size of 0.25 from 0 to 1. A symmetrical pattern was found when looking at the r_{wp} and the top left and bottom right quadrants (Figure 3.12.b.) showed the lowest r_{wp} values and was investigated further using narrower step-sizes of 0.02 (Figure 3.13).

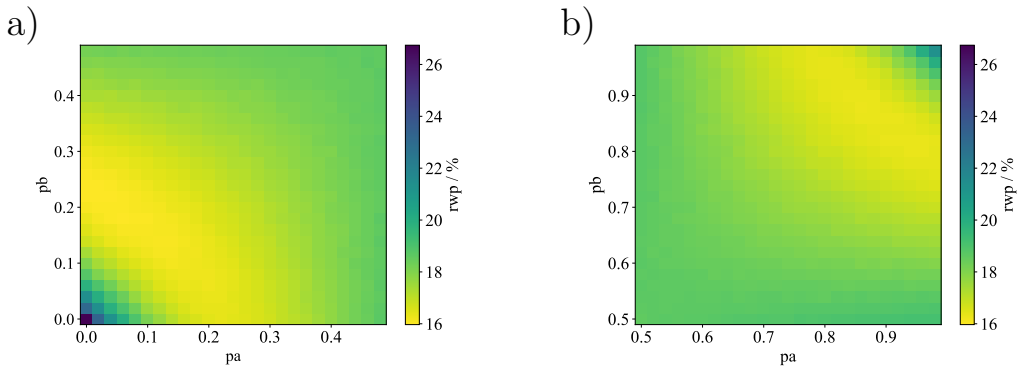


Figure 3.13: Colour maps displaying the effect of changing parameters pa and pb to the r_{wp} values, where pa and pb change in steps of 0.02. a) In the range of 0-0.5 b) In the range of 0.5-1.0.

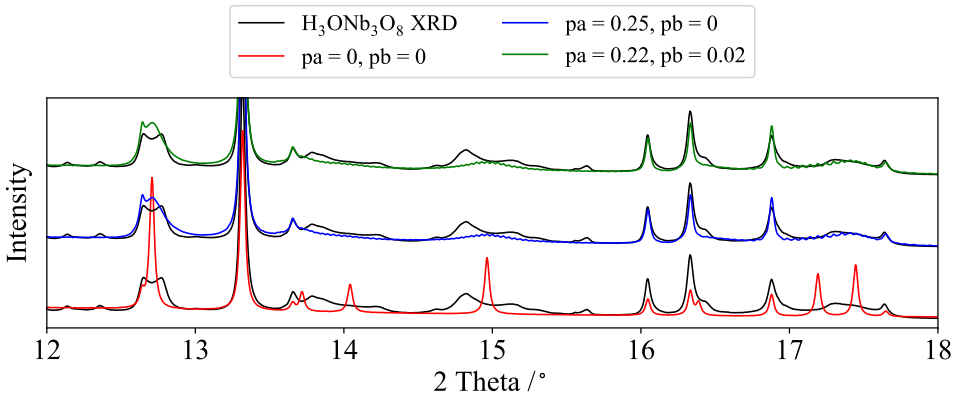


Figure 3.14: XRD plots of $H_3ONb_3O_8$ collected at I11 (λ = 0.825255 Å) in black with the Rietveld refinement results using the parameters pa and pb.

This study identified the lowest r_{wp} values for pa = 0.25 pb = 0 from Figure 3.12.b. and pa = 0.022 and pb = 0.02 from Figure 3.13. The XRD refinement has been plotted (Figure 3.14) against pa = 0 and pb = 0 which is equivalent to the KNb_3O_8 structure with no stacking faults. Significant improvement in the modelling of the double peak at 12.8 ° 2θ is achieved with including stacking faults, in addition to broad peak centered at around 17.4° 2θ. Additionally the peak at 13.7° 2θ fits much better, although there are areas for improvement such as the anisotropic peak around 15° 2θ.

Comparing the results pa = 0.022 and pb = 0.02 and pa = 0.25 pb = 0, there is very minimal change (Figure 3.14). This is because the improvement r_{wp} is not particularly significant. From our studies there are a broad range of suitable pa and pb values to model $H_3ONb_3O_8$ (Figure 3.13).

The best description of $H_3ONb_3O_8$ is that is is structurally similar to KNb_3O_8 with 10- 20 % occurrence of stacking faults in the *a* direction, by a displacement of 0.5 unit cell. The presence of two low r_{wp} regions in Figure 3.13 suggests an insensitivity to the interlayer ions. X-rays are known to be more sensitive to heavier atoms and therefore the lack of counts in the PXRD regarding interlayer ion location, unsurprisingly makes PXRD stacking faults study also an insensitive method to the interlayer ions.

Limitations and future work

Unfortunately there are limitations to this XRD study as the structure of $H_3ONb_3O_8$ is still not fully resolved as the atomic positions of the protons have not been identified. Although a neutron scattering experiment was performed (POLARIS at ISIS) on $H_3ONb_3O_8$, the noise from the protons made the data difficult to analyse and therefore has not been presented as part of this study. To successfully resolve the structure of $H_3ONb_3O_8$, a fully deuterated form should be synthesised ($D_3ONb_3O_8$) for neutron scattering.

3.4.3 Summary: $H_3ONb_3O_8$

As determined using x-ray scattering techniques, $H_3ONb_3O_8$ is structurally similar to KNb_3O_8 and HNb_3O_8 (Table 3.10) with similar local structure at low *r* distances as determined by similariles in the XPDF. The refined unit cell parameters from the XRD, support known literature reported values.[128] Therefore protonation of KNb_3O_8 was achieved successfully, following known methods.

Further understanding of the structure was acquired by Rietveld refinement of $H_3ONb_3O_8$ which shows approximately 20 % stacking faults, a stacking shift of 0.5 unit cells as determined using Rietveld refinement analysis. To best of our knowledge, the stacking fault defects have not been studied in this material until now.

3.5 Dehydration of $H_3ONb_3O_8$ to HNb_3O_8

It is crucial to clearly differentiate between $H_3ONb_3O_8$ and HNb_3O_8 as they are structurally distinct. However $H_3ONb_3O_8$ is often incorrectly referred to as HNb_3O_8 in the literature,[113,128] despite R. Nedjar *et al.* explicitly discussing the differences between the two phases in 1985.[124] Furthermore, the PDF 4+ also have separate entries for $H_3ONb_3O_8$ and HNb_3O_8 with distinct unit cell parameters and XRD patterns (Figure 3.15 and Table 3.10).

Therefore the shifting of XRD peaks observed in the PXRD patterns of samples has been used to differentiate KNb_3O_8, $H_3ONb_3O_8$ and HNb_3O_8. The first study on this was performed in 1985 by R. Nedjar *et al.*[124] who observed that dehydration began at 80 °C with a maximum at 150 °C in their TGA, whilst H. T. Kreissl *et al.*[84] heated $H_3ONb_3O_8$ for 3 hrs at 150 °C to form HNb_3O_8.

It is crucial to udnerstand the phase transition that occurs, as battery coatings are dried vigorously in a vacuum oven to remove water, therefore by understanding the structure of HNb_3O_8, will lead to an understanding of its characteristics as an anode material.

3.5.1 Structure of $H_3ONb_3O_8$ and HNb_3O_8

The crystal structure of $H_3ONb_3O_8$ is not yet known, but HNb_3O_8 is most likely based on the ion-exchanged form of KNb_3O_8, which has been presented by T. Kreissl *et al.*[84] Unit cell determinations of $H_3ONb_3O_8$ and HNb_3O_8 have been reported and are recorded in the PDF 4+ database; details of these determinations are given in Table 3.10 and the reference XRD peak locations and intensities are presented in Figure 3.15. The PXRD data obtained from the PDF 4+ database (Figure 3.15) show that HNb_3O_8 shows a shift to higher 2θ relative to KNb_3O_8, whilst $H_3ONb_3O_8$ shifts to lower 2θ

values. This is as expected as the size of $H^+ < K^+ < H_3O^+$ (-0.38 Å, 0.99 Å and 1.38 Å Shannon radii, respectively).[188,189,190]

Table 3.10: The phases HNb_3O_8 and $H_3ONb_3O_8$ and its information, obtained from the PDF 4+ database.

Chemical formula	Ref*	System	Space group	a/Å	b/Å	c/Å
HNb_3O_8	00-037-0833	Orthorhombic	*P*nb*	8.811	18.462	3.788
$H_3ONb_3O_8$	00-044-0672	Orthorhombic	*Pnn**	9.183	22.470	3.775

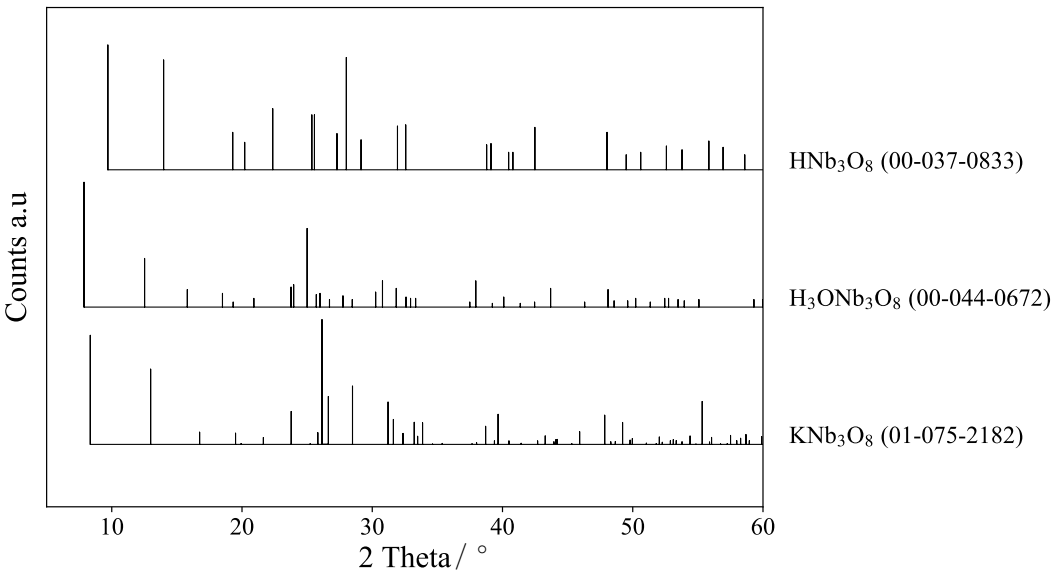


Figure 3.15: The PXRD patterns of HNb_3O_8, $H_3ONb_3O_8$ and KNb_3O_8 obtained from the PDF 4+ database ($\lambda = 1.542$ Å).

Method

$H_3ONb_3O_8$ was heated within a Bruker D8 PXRD machine with an Anton Parr heating chamber attached. This allowed the collection of *insitu* PXRD data during dehydration of $H_3ONb_3O_8$. Two variable temperature data collections were performed; one broad range collection between 60 °C and 200 °C followed by a narrow range collection between 80 °C and 100 °C each ending with an XRD collection at room temperature. Each XRD pattern took approximately 30 mins to collect. Thermogravimetric analysis-mass spectrometry (TGA-MS) was used to study any evolved gaseous species.

Using the information about $H_3ONb_3O_8$ and HNb_3O_8 obtained from the PDF 4+ database as a starting point for Pawley refinement, a range of possible space groups were tested against the XRD patterns collected at 80 °C and 100 °C respectively. The space groups tested for $H_3ONb_3O_8$ were: *Pnnm, Pmnn and Pnmn* (reported *Pnn**), whilst the space groups tested for HNb_3O_8 were: *Pnma, Pmnb, Pbnb, Pcmn, Pmcn and Pnam* (reported *P*nb*, but all settings for space group 62 were tested). The space groups that provided the best fit were then which were then combined to Pawley fit the XRD data collected at 88 °C (Figure 3.18).

Results

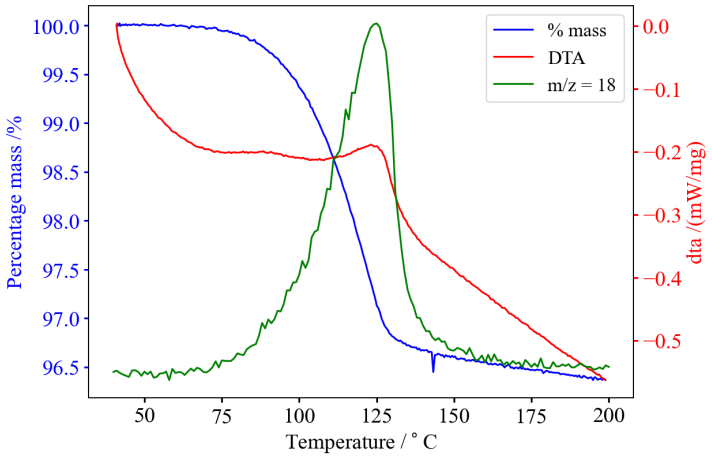


Figure 3.16: The dehydration of $H_3ONb_3O_8$ using TGA-MS.

The PXRD of $H_3ONb_3O_8$ (Figure 3.18) shows the dehydration process begins at 86 °C which is consistent between the TGA-MS (Figure 3.16) and VT-XRD and also consistent with the study performed by R. Nedjar *et al.*[124] The TGA-MS shows weight loss of 3.7 % which coincides perfectly with the detection of water by the mass spectrometer. The mass of HNb_3O_8 is 95.7 % of $H_3ONb_3O_8$ (407.7 g mol^{-1} and 425.7 g mol^{-1} respectively) and therefore a theoretical mass loss of 4.3 % is expected for this process. The observed lower than expected mass loss can be attributed to incomplete ion-exchange in the synthesis of $H_3ONb_3O_8$. ICP-MS showed that $H_3ONb_3O_8$ showed to contain on average 2.9 % by weight of K in $H_3ONb_3O_8$.

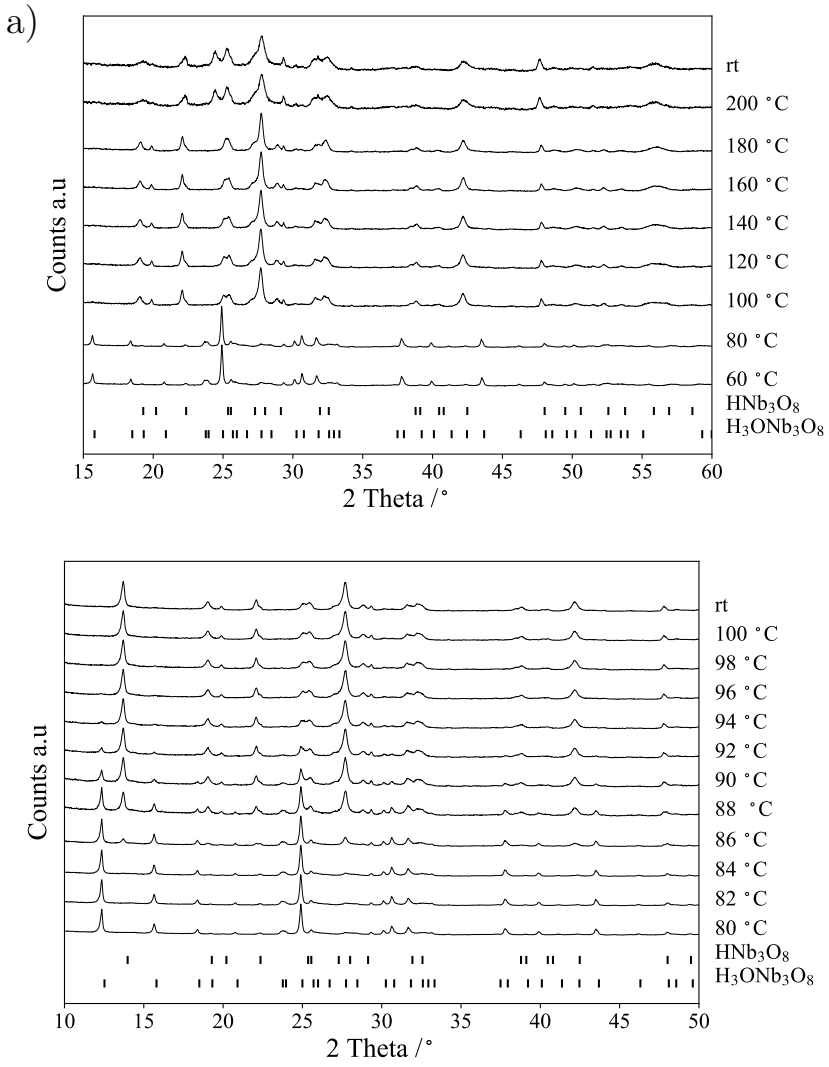


Figure 3.17: Probing the dehydration of $H_3ONb_3O_8$ using VT-PXRD (λ = 1.542 Å) and then cooled to room temperature. With tick marks for HNb_3O_8 and $H_3ONb_3O_8$ as described in the PDF 4+ database. a) between 60 °C and 200 °C. b) between 80 °C and 100 °C.

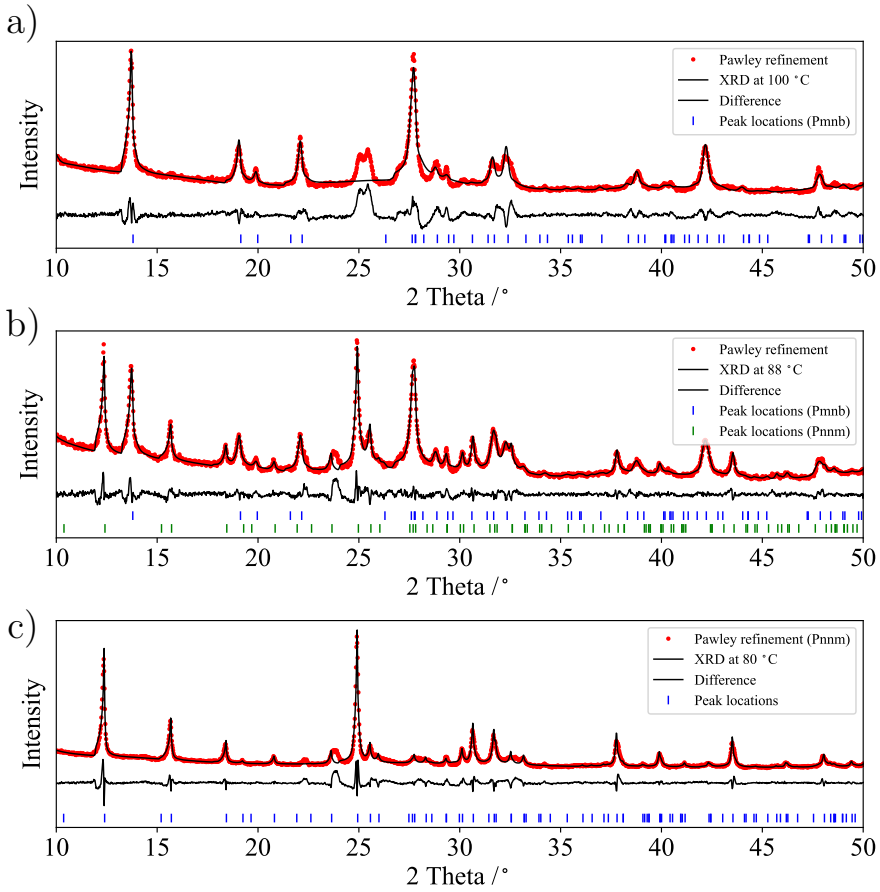


Figure 3.18: Probing the dehydration of $H_3ONb_3O_8$ of VT-PXRD at temperatures a) 100 °C using Pawley refinement. b) 88 °C using Pawley refinement c) 80 °C using Pawley refinement. With tick marks for HNb_3O_8 and $H_3ONb_3O_8$.

The PXRD confirms the phase change at around 88 °C which occurs *via* a distinct two-phase process (Figure 3.18). At temperatures above 180 °C, the peaks broaden, which indicates increased disorder, or a reduction in particle size (Figure 3.17). A Pawley refinement using the space group *Pmnb* and *Pnnm* gave a good fit to the XRD patterns (Table 3.11) and obtaining lattice parameters similar to the values published in the PDF 4+ database. The interlayer distance was determined using the d_{040} at 4.63 Å and therefore the d_{020} would be at 9.26 Å corresponding to the interlayer distance.

The refined phases (Table 3.11) are in agreement with the results reported by R. Nedjar *et al.*[124] who reported $H_3ONb_3O_8$ unit cell parameters of 9.173(7), 22.47(2) and

3.743(3) Å respectively for a, b and c, whilst HNb_3O_8 values were 8.87(1), 18.61(4) and 3,848(8) Å respectively for a, b and c.

Table 3.11: Crystallographic information obtained from the Pawley refinement of the dehydration of $H_3ONb_3O_8$ at 80 °C, 88 °C and 100 °C.

Property	80 °C	88 °C		100 °C
$\mathbf{r_{wp}}$**/ %**	11.9	7.53		13.6
Space group	*Pnnm*	*Pnnm*	*Pnmb*	*Pnmb*
a / Å	9.2124(6)	9.1960(14)	8.887(2)	8.878(2)
b / Å	22.5546(16)	22.539(3)	18.542(4)	18.527(4)
c / Å	3.4650(6)	3.4592(10)	3.4449(16)	3.4392(17)

3.6 Future work: KNb_3O_8, HNb_3O_8 and $H_3ONb_3O_8$

The structure of KNb_3O_8 is well documented with various synthesis routes, unlike HNb_3O_8 and $H_3ONb_3O_8$. Resolving the structure of HNb_3O_8 and $H_3ONb_3O_8$ can be achieved by the ion-exchange of KNb_3O_8 with DCl (deuterated HCl) for neutron XRD and PDF, ideally variable temperature to probe the phase transition from $H_3ONb_3O_8$ to HNb_3O_8. The sensitivity of neutrons to deuterium will enable structure elucidation of the interlayer H and O which is not possible with XRD.

Although this was attempted with undeuterated $H_3ONb_2O_8$ for neutron-PDF, the noise from the H_3O made the corrections difficult and therefore a suitable quality PDF could not be generated.

3.7 Summary: KNb_3O_8, HNb_3O_8 and $H_3ONb_3O_8$

KNb_3O_8, HNb_3O_8 and $H_3ONb_3O_8$ have been reported in literature and we have successfully synthesised these products *via* modified synthesis methods. They have been analysed using conventional solid-state methods such as XRD, XPDF, Raman and microscopy. KNb_3O_8 has been characterised and matched literature reports.

The XRD pattern of $H_3ONb_3O_8$ shows the presence of stacking faults whilst the dehydration behaviour have been further understood to form HNb_3O_8, alongside a transition from *Pnnm* to *Pnmb* and a compression in a and b at around 88 °C.

4 Synthesis and characterisation of a nanostructured niobate *via* exfoliation of $H_3ONb_3O_8$

4.1 Introduction

Nanostructuring is known to change the physical properties of materials, for example KNb_3O_8 nanosheets coated with carbonized polydopamine in a LIB [28] showed an enhanced capacity of above 200 $mAhg^{-1}$ after 3000 cycles at high rate of 2 Ag^{-1}.

Nanostructuring can be achieved by exfoliation, if the material is layered. This method causes the layers within the material to delaminate forming nanosheets in a colloidal solution. [55] When these sheets are aggregated, a disordered, nanostructured layered material is produced.

This Chapter explores exfoliation and restacking of $H_3ONb_3O_8$ to obtain a restacked niobate and to understand its disorder. Furthermore, it can be hypothesised that the larger interlayer spaces available may lead to an improvement in its electrochemical characteristics, such as faster charging and higher capacity.

Due to the strong ionic interactions between the niobate layers and potassium-ions, a more complicated method, beyond simple agitation, is required: *ion-intercalation*. This is a commonly used method applicable to a variety of solid state materials, such as: transition metal dichalcogenides, metal halides, transition metal oxides and pervoskites for exfoliation. [55]

The exfoliation and restacking process has been established for many materials, including niobium oxides.[55,56] The steps are outlined in Figure 4.1 and summarised in the following three steps:

Step 1: Swelling of the layers

Increasing the interlayer distance can be achieved by ion-exchanging the interlayer cation for a bulky amine e.g. tetrabutylammonium hydroxide (TBAOH). In the case of KNb_3O_8, the potassium cannot be directly ion-exchanged for TBAOH and must progress *via* the protonated form $H_3ONb_3O_8$.[56] It should be noted that for other systems such as titanates, different intercalating ions are used to swell the layers have been used such as propylamine and methylamine.[55]

Step 2: Exfoliation

This involves mechanical agitation of the system, typically by utilising an ultrasonic bath or stirring to form a colloidal mixture. KNb_3O_8 forms $[Nb_3O_8]^-$ nanosheet layers in a stable colloidal solution.[191]

Step 3: Restacking

Adding acid into the colloidal solution, will cause the $[Nb_3O_8]^-$ colloidal layers to aggregate.[56,192] The restacked material can be collected by filtration, sometimes coupled with centrifuging.

The nanostructured product, restacked niobate material, was characterised using a combination of techniques: XRD, XPDF, Raman, microscopy and SAXS.

4.2 Method: exfoliation and restacking of $H_3ONb_3O_8$

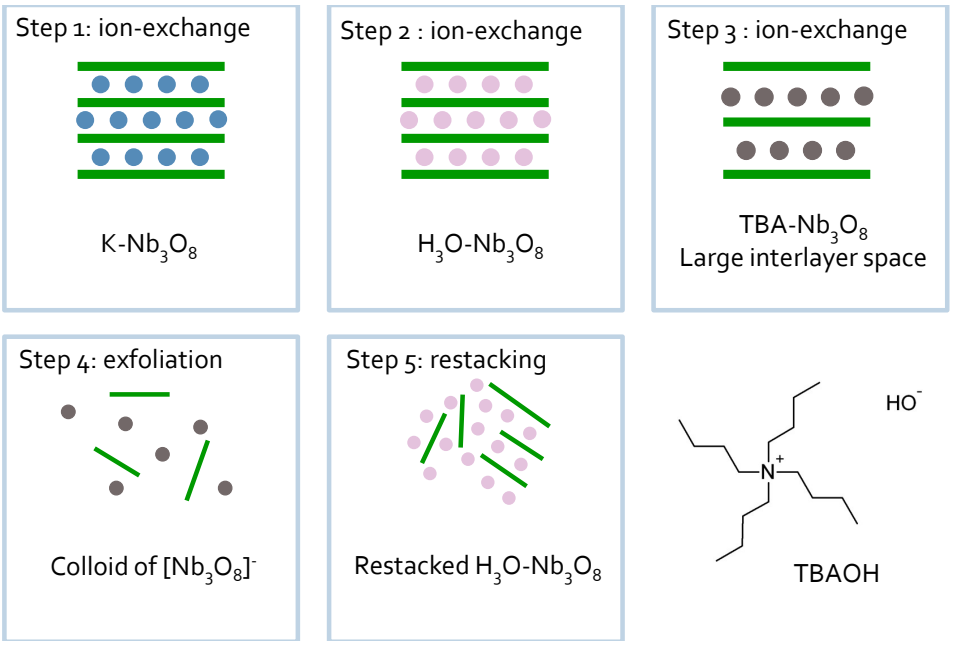


Figure 4.1: A schematic diagram of the steps required to synthesise the restacked niobate from KNb_3O_8, with the TBAOH structure displayed explicitly in the lower right corner.

A. S. Dias *et al.*[56] reported the exfoliation methodology for a range of titanates; niobates and titanoniobates, their exfoliation method (Figure 4.1) has been adapted in this study, $H_3ONb_3O_8$ was added to deionised water and stirred whilst adding tetra(n-butylammonium) hydroxide (TBAOH, 15 wt% with water, Sigma-Aldrich) dropwise until a pH of 9.5-11.5 was reached, this solution was stirred slowly at around 250 rpm for several weeks at room temperature. Non-exfoliated particles were separated from the colloidal sheets by centrifugation at 4.4×10^4 rpm for a total of 30 min (centrifuged for 10 mins, three times), then the supernatant poured into a beaker and separated from the residue. 4 M nitric acid was added to the supernatant solution until no further aggregation was observed. The mixture was left to rest for several minutes and then filtered using a Buchner funnel whilst taking care to keep the gel hydrated at all times, to prevent the force of the vacuum from compressing the gel. The gel was dried overnight at 60 °C and formed a white solid.

4.3 Results: exfoliation and restacking of $H_3ONb_3O_8$

Although exfoliated and restacked $H_3ONb_3O_8$ has been synthesised previously, it has not been thoroughly characterised to this depth. Typically only an XRD is presented, with a lack of in depth discussion.

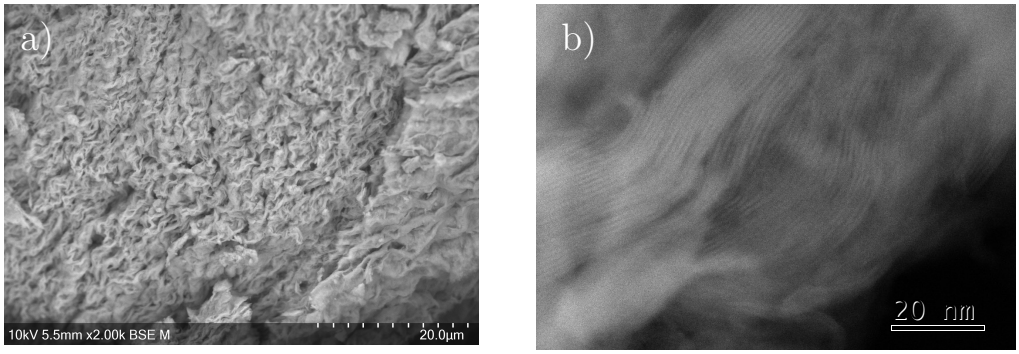


Figure 4.2: Microscopy images of restacked niobate. a) SEM b) STEM-HAADF.

SEM and STEM-HAADF

The SEM image (Figure 4.2.a.) shows a the tissue-paper like morphology with some voids, built from very crinkled features. Figure 4.2.b. shows bending of layers, in addition to early termination and limited stacking range.

XRD

The XRD pattern (Figure 4.3.a.) shows peaks at 13.08 Å, 3.72 Å, 3.47 Å and 1.90 Å which corresponds to the (020), (011), (311) and (002) peaks respectively. The (002) peak is significantly sharper than the other peaks in the XRD pattern because the restacked material possesses significantly longer range order within the layer than along the stacking direction. Comparing the (020) peaks of KNb_3O_8 and $H_3ONb_3O_8$ (at 10.42 Å and 11.25 Å respectively), the restacked niobate shows a peak shift to even lower 2θ, corresponding to an increase in d-spacing (13.08 Å) which indicates an increase in the average interlayer distance (Figure 4.3.a.). The broad nature of the (020) peak indicates a significant variation in the interlayer distance which is to be expected of a restacked material.

The XRD pattern is supported by Y. Zhou *et al.*[182] who studied the photocatalytic activity of Nb_3O_8 nanosheets and produced similar XRD pattern by exfoliation and restacking methods.

High resolution STEM (Figure 4.2.b.) shows stacks of layers. These layers, assumed to be niobate layers based on the sharp (002) peak present in the XRD. The niobate layers bend and curve Figure 4.2.b.). Some termination of the layers can also be observed, resulting in a limited correlation length.

There are regions where stacking of the layers can be observed. Figure 4.2.b.) reveals, up to 20 layers are observed to stack, but there are also areas where little or no stacking is observed. Therefore, a range of local environments are present. This range of stacking environments is consistent with the broad (020) peak observed at 13.08 Å in the XRD (Figure 4.3.a.).

XPDF

The PDF (Figure 4.3.b.) shows very low intensity peaks beyond 35 Å, in contrast to its crystalline precursors. This shows that the material has a limited correlation length. However, there are peaks in the mid-r region (5 Å- 35 Å), which indicates that the material has not been fully amorphized during the exfoliation and restacking.

A comparison of the PDFs for KNb_3O_8 and the restacked material show similar peak position and intensity at low r. This indicates that the immediate Nb-O and Nb-Nb connectivity is similar in the two materials. This is preliminary evidence that the in-layer structure of the niobate is retained throughout exfoliation and restacking. The PDF was studied and refined in detail in Section 4.5.

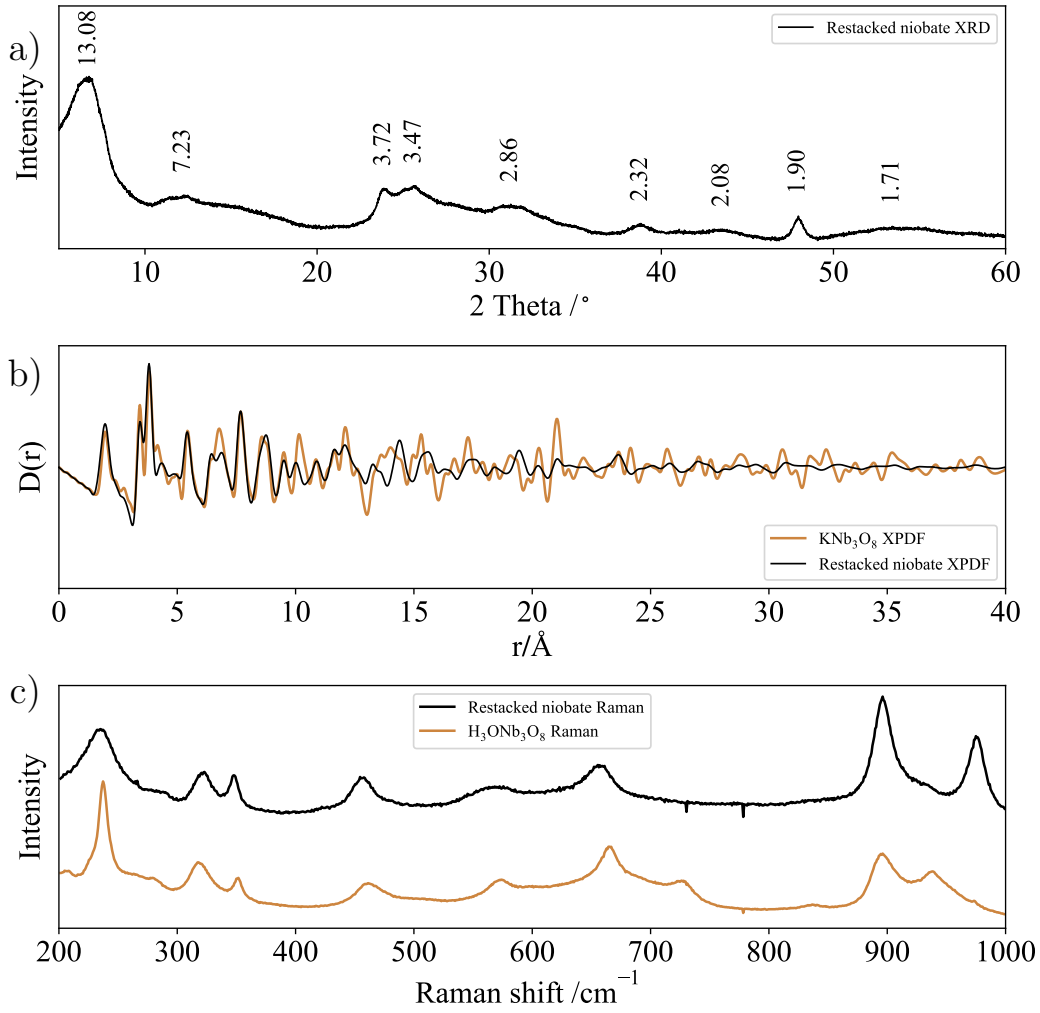


Figure 4.3: Results from structural analysis of restacked niobate. a) XRD pattern (λ = 1.5406 Å) with the d-spacing values (given in Å) annotated. b) Pair distribution function c) Raman spectra of restacked niobate and $H_3ONb_3O_8$.

Raman

The Raman spectrum of restacked niobate (Figure 4.3.c.) shows bands at 320 cm^{-1}, 437 cm^{-1}, 457 cm^{-1}, 563 cm^{-1}, 659 cm^{-1}, 896 cm^{-1} and 976 cm^{-1}. J. Xiong *et al.*[113] published Raman spectrum for an ultrathin HNb_3O_8 nanosheet which shows a similar XRD and Raman spectrum to the results of this study for our restacked niobate.

J. Xiong observed a shift in the band at 932 cm^{-1} to 976 cm^{-1}, whilst in this study, a

similar shift was observed from 938 cm^{-1} to 976 cm^{-1}. This band is typically assigned to Nb-O terminal bonds at the surface. Peak shift to a higher wavenumber is indicative of a shorter Nb-O bond, indicating that the interaction between the niobate layer and the interlayer ions is weaker than in $H_3ONb_3O_8$.

The retention of Raman bands from $H_3ONb_3O_8$ precursor was also observed by J. Xiong *et al.*[113], for example the band at 896 cm^{-1}, and the same behaviour is observed in this study. Visually, the Raman spectrum from this study and of J. Xiong *et al.* is the same as in this study, unfortunately they did not present the peak values and therefore the exact peak locations could not be compared.

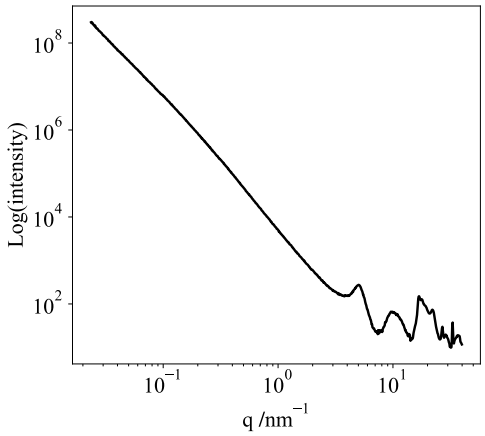


Figure 4.4: SAXS data of restacked niobate material.

SAXS

SAXS (Figure 4.4) was used to probe larger features in the sample. The SAXS data is the linear region of below 10 nm^{-1} which indicates that there are no pores or particles of a consistent size and shape at sizes above 0.628 Å.

4.4 Summary: Synthesis of restacked niobate

$H_3ONb_3O_8$ was successfully exfoliated and restacked to form a nanostructured material, following a slightly adapted synthesis method that is reported in literature. This phase has been synthesised previously, but this study furthers our understanding by analysing XRD and XPDF datasets in detail.

The restacked niobate possesses short range order, as determined by the lack of Bragg peaks in the XRD pattern. However the type of disorder in the material is not understood, therefore further small box refinements of XPDF are required to model this. Restacked niobate has also been studied for the photocataysis of hydrogen production[182] and therefore understanding this structure will also contribute to understanding its enhanced behaviour compared to $H_3ONb_3O_8$ precursor.

4.5 PDF analysis of restacked niobate using TOPAS

4.5.1 Introduction

The pair distribution function (PDF) was analysed in more detail to further understand the local structure of the restacked material and its disorder. Small box refinement using TOPAS software was used for analysis. This is a novel method, which has not been published before, and the results at each stage will be discussed in the subsequent subsections.

4.5.2 Obtaining the XPDF

The sample was ground using a pestle and mortar and loaded into a 1 mm borosilicate capillary and placed on the I15-1 beamline at Diamond Light Source. The XPDF was generated using GudrunX and then analysed using TOPAS v6. All the TOPAS functions/ macros used in this XPDF study are either part of the standard TOPAS package or they can be found here: *https://github.com/pachater/topas/blob/master/pdf.inc*.

4.5.3 Setting up the refinement: Creating a model

Creating a model

Typically, an atomic structure model consists of a unit cell which tessellates to form a crystal with long range order. However this is not the case in this restacked-material. From the XRD pattern we understand that the interlayer distance shows significant variation and probably shows poor atom to atom correlation in the stacking direction [020], however the [002] contains longer range order evident as a sharper reflection in the XRD pattern indicating the retention of niobate layers. Therefore we attempted to model the PXRD pattern using a single niobate layer (Figure 4.5). To avoid correlations between niobate layers. a unit cell was generated with a very large b parameter (around 211 Å) with only one niobate layer in empty space. The a and c are taken from KNb_3O_8 (8.862 Å and 3.818 Å, respectively).

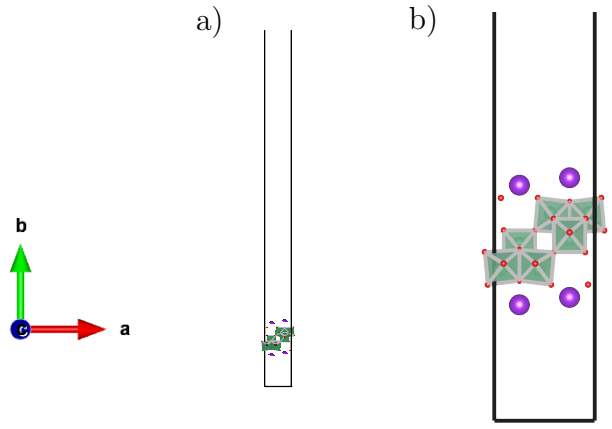


Figure 4.5: Atomic model of a niobate layer in an unit cell with a large b parameter which exceeds 40 Å. The niobate octahedra are shown in green with red spheres representing oxygen. Purple spheres represent potassium.

Table 4.1: Wykoff position information for the space group *Amam* belonging to KNb_3O_8.

Multiplicity	Wykoff letter	Symmetry	Coordinates (0,0,0) + (0, 1/2, 1/2)
8	f	m..	(-z,y,0), (-z+1/2,-y,0), (z+1/2,y,0), (z,-y,0)
4	c	m2m	(3/4,y,0), (1/4,-y,0)

The generation of the model was achieved by using atomic site information of KNb_3O_8 obtained from the cif file (ICSD: 31994) (Table 4.2) and the known Wykoff positions for space group *Amam* (Table 4.1).[144] The unit cell as outlined in Figure 4.5 has a *P1* symmetry, however the symmetry is retained within the layer has been maintained by manually defining equations to generate the atomic positions (Table 4.8 and 4.4). Therefore the niobate layer retains a *Amam* space group symmetry. This is a novel method of modelling a single layer against XPDF data in TOPAS.

Table 4.2: KNb_3O_8 atomic sites obtained from ICSD code: 31994.

	x	y	z	Multiplicity	Wykoff letter	Symmetry
Nb1	0.9403	0.3682	0	8	f	m..
Nb2	0.25	0.2416	0	4	c	m2m
K1	0.25	0.9845	0	4	c	m2m
O1	0.408	0.1565	0	8	f	m..
O2	0.0654	0.4311	0	8	f	m..
O3	0.0951	0.2954	0	8	f	m..
O4	0.25	0.7134	0	4	c	m2m
O5	0.25	0.5851	0	4	c	m2m

Table 4.3: Table of parameters used to define the atomic sites of a single layer of KNb_3O_8 in a *P1* unit cell.

Parameter name	Parameter value	Parameter name	Parameter value
xNb1a	0.0597	yNb1a	0.3682
xNb2	0	yNb2a	0.7584
xK1a	0	yK1a	0.0155
xO1a	0.592	yO1a	0.1565
xO2a	0.9346	yO2a	0.4311
xO3a	0.9049	yO3a	0.2954
xO4a	0	yO4a	0.2866
xO5a	0	yO5a	0.4149
xNb1b	0.0597	yNb1b	0.8682
xNb2b	0	yNb2b	0.2584
xK1b	0	yK1b	0.5155
xO1b	0.592	yO1b	0.6565
xO2b	0.9346	yO2b	0.9311
xO3b	0.9049	yO3b	0.7954
xO4b	0	yO4b	0.7866
xO5b	0	yO5b	0.9149

Table 4.4: Table of parameters used to define the atomic sites of a single layer of KNb_3O_8 in a *P1* unit cell.

Site name	x position	y position	z position
Nb1_2a	-xNb1a+0.5	(1-yNb1a)/divisor	0
Nb1_4a	xNb1a	(1-yNb1a)/divisor	0
Nb2_1a	0.75	yNb2a/divisor	0
K1_1a	0.75	(1-yK1a)/divisor	0
K1_2a	0.25	(1-yK1a)/divisor	0
O1_2a	1-xO1a+0.5	(1-yO1a)/divisor	0
O1_4a	xO1a	(1-yO1a)/divisor	0
O2_2a	1-xO2a+0.5	(1-yO2a)/divisor	0
O2_4a	xO2a	(1-yO2a)/divisor	0
O3_2a	1-xO3a+0.5	(1-yO3a)/divisor	0
O3_4a	xO3a	(1-yO3a)/divisor	0
O4_2a	0.25	(1-yO4a)/divisor	0
O5_2a	0.25	(1-yO5a)/divisor	0
Nb1_1b	1-xNb1b	yNb1b/divisor	0.5
Nb1_3b	xNb1b+0.5	yNb1b/divisor	0.5
Nb2_2b	0.25	(1-yNb2b)/divisor	0.5
K1_1b	0.75	yK1b/divisor	0.5
K1_2b	0.25	(1-yK1b)/divisor	0.5
O1_1b	1-xO1b	yO1b/divisor	0.5
O1_3b	xO1b+0.5-1	yO1b/divisor	0.5
O2_1b	1-xO2b	yO2b/divisor	0.5
O2_3b	xO2b+0.5-1	yO2b/divisor	0.5
O3_1b	1-xO3b	yO3b/divisor	0.5
O3_3b	xO3b+0.5-1	yO3b/divisor	0.5
O4_1b	0.75	yO4b/divisor	0.5
O5_1b	0.75	yO5b/divisor	0.5

Where the divisor = 10 because b was defined as 211.60001 Å (10 times the unit cell length of KNb_3O_8.

Thermal parameters

Several thermal functions were tested and `beq_spherical` (uses three variables) showed a better fit then `beq_cut` (uses two variables) whilst more complex functions with more variable parameters did not show an improved fit. Therefore `beq_spherical` was used in this study. Further information about these functions can be found in the TOPAS technical reference manual.*

*http://www.topas-academic.net/

beq_spherical utilises three parameters: beq_low, beq_high and radius given starting parameters of 2, 5 and 10, respectively, for all atoms. Each atomic site shares a beq_low and beq_high parameter value with other sites occupied by the same element, value whilst radius is a global parameter shared by all elements (and therefore all sites). The function starts at 0 Å at a value equal to beq_low and increases to the beq_high at a distance equal to twice the radius. The starting parameters for beq_low, beq_high and radius were 2, 6 and 10 respectively.

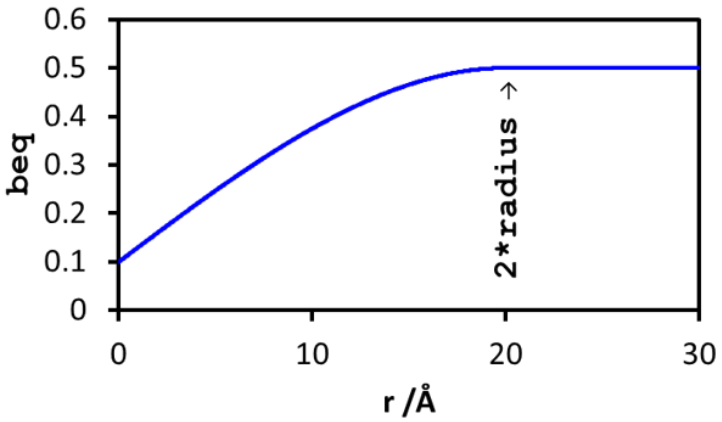


Figure 4.6: A diagram illustrating the beq_spherical function given that beq_low = 0.1, beq_high = 0.5 and radius = 10.

4.5.4 Step one: Refinement from 7 Å onwards

Method

Initially, only a few parameters were allowed to refine: thermal parameters and the Chebyshev background function and the lattice parameters a and c. Additionally, the refinement began at 7 Å, as the low r data has a tendency to outweigh the high r data and therefore intricacies in the high r data can easily be overshadowed.

Results

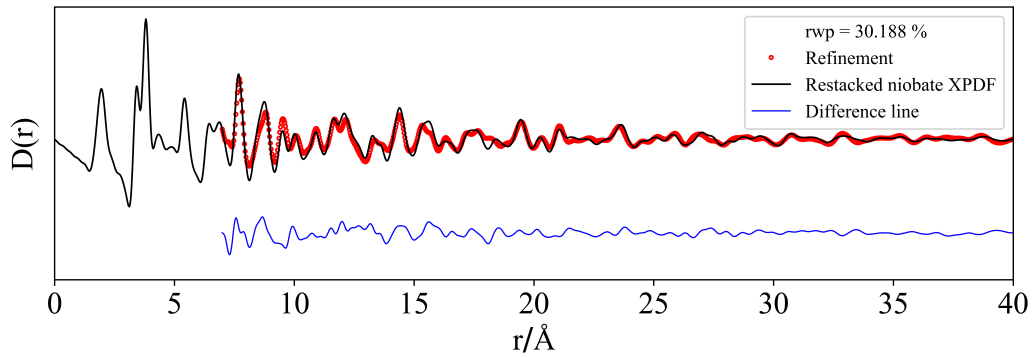


Figure 4.7: Results from step one of small box analysis on the PDF collected from the restacked material.

Figure 4.7 shows that the one layer model is a resonable fit to the PDF at this preliminary stage with a respectable r_{wp} of 30.188 %, even without refining atomic positions. Therefore the peaks at high r can be attributed to atom to atom correlations within the layer. The a and c lattice parameters in KNb_3O_8 are 8.903(3) Å and 3.799(2) Å respectively and they have been refined to 8.858(3) Å and 3.8227(16) Å. Therefore, a contraction in a and expansion in c by approximately 0.1 Å in each direction (Table 4.5). The change was not too large and the errors were low, and therefore these values were accepted for subsequent refinements.

Table 4.5: Table summarising the results from step one of small box refinement on the XPDF of restacked niobate.

Parameter	Refined value
r_{wp} / %	30.188
One layer model a / Å	8.858(3)
One layer model c / Å	3.8227(16)
Nb `beq_low`	0.00(3)
Nb `beq_high`	2(8)
K `beq_low`	10(10)
K `beq_high`	100(320)
O `beq_low`	2.9(6)
O `beq_high`	6(9)
`radius`	35(132)

The thermal parameters for K are significantly higher than Nb and O, this suggests that the K sites are much more poorly defined. A `radius` value of 35, implies the thermal parameters reach their respective high values at 70 Å, therefore the thermal functions in the region of our XPDF, follow an almost linear relationship.

4.5.5 Step two: Background fitting

Method

Although this one layer model allows the study of atomic correlations between atoms limited to a single niobate layer, this is achieved by creating large areas of empty space in the unit cell. This causes an artificially low average density (ρ) in the model which has implications on the PDF generated. The lower than expected ρ value has to be accounted for in the modelling by introducing a function that compensated for the effect of the missing density. This effect has been studied by K. Kodama *et al.*[193] and in this study a simplistic version was created and introduced to the refinement using two linear lines.

Results

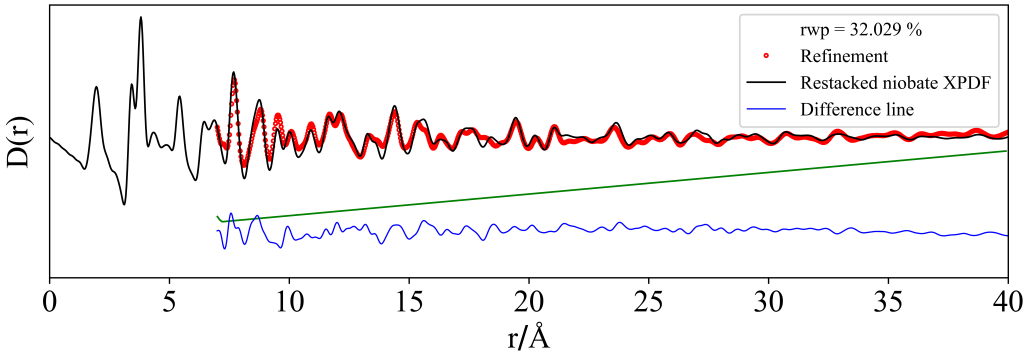


Figure 4.8: Results from step two of small box analysis on the PDF collected from the restacked material.

The background provided two linear lines that meet at the refined *background intersect* value of 7.07949 Å with refined gradient values of -2.51541 and 0.09103 for low r and high r regions respectively (Figure 4.8). The new r_{wp} of 32.029 % is unfortunately poorer than the original fit, however the background now has chemical meaning.

The lattice parameters and thermal parameters show minimal difference to the previous refinement (Table 4.6). The new background function is not significantly impacting the

Table 4.6: Table summarising the results from step two of small box refinement on the XPDF of restacked niobate.

Parameter	Previous value	New refined value
r_{wp} / %	30.188	32.029
One layer model a / Å	8.858(3)	8.856(4)
One layer model c / Å	3.8227(16)	3.8226(17)
Background intersect / Å	-	7.16(9)
Low r background gradient	-	-1.4(8)
High r background gradient	-	0.0922(7)
Nb `beq_low`	0.00(3)	0.00(3)
Nb `beq_high`	2(8)	2(5)
K `beq_low`	10(10)	10(13)
K `beq_high`	100(320)	100(218)
O `beq_low`	2.9(6)	2.5(6)
O `beq_high`	6(9)	6(7)
`radius`	35(132)	29(78)

refinement when compared to the Chebyshev background function. Therefore the new background function was retained for future refinements, and the the parameters, the intersect and the two gradient values were allowed to refine. The new background function utilises two lines that intersect, as the refined intersect (7.1 Å) is around the start of the refined dataset, therefore the background appears as a linear function in Figure 4.8. The error associated with the low r background gradient is significantly higher than the value for high r, this is because the low r gradient is being fit to 0.1 Å worth of data points. The limited number of data points available to fit a parameter increases the uncertainty in the refined value, leading to larger errors.

Although the thermal parameters are still higher than ideal, these are expected to decrease once the information rich low r data is included into the refinement. However, prior to that, the high and mid r data should be fitted to the best of our abilities, to prevent low r data from overshadowing the high r information.

4.5.6 Step three: Refining atomic positions

Method

The atomic positions were allowed to refine by allowing the parameters outlined in Table 4.8 to refine, except for those on lattice points and the parameters for xNb1a and yNb1a. This is to prevent the whole layer refining up and down the unit cell, by forming an anchor point around which all the values refine around.

Additionally a `spherical_damping` function was added to model the loss of intensity at high r due to particle size, to determine whether this would improve the fit.

Results

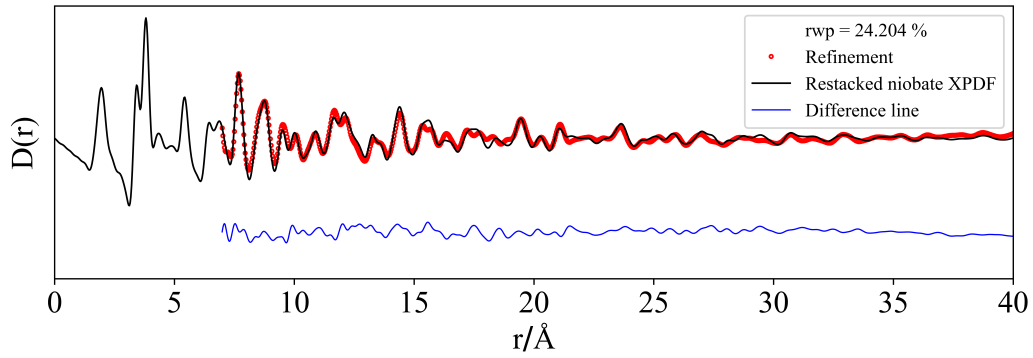


Figure 4.9: Results from step three of small box analysis on the PDF collected from the restacked material.

Allowing atomic positions to refine improved the refinement (Table 4.8) and fit by the observed lowering of r_{wp} to 24.204 % (Figure 4.9). However studying the structure more closely, the atoms have shifted to an extremely distorted niobate octahedra (Figure 4.10). The distorted octahedra of $K_4Nb_6O_{17}$ have been studied and bond lengths are reported to be between 1.7815 Å and 2.4756 Å using DFT (density functional theory).[194] However bond lengths of 3.0 Å are observed in this structure which is chemically unrealistic. Therefore bond restraints and angle restraints were introduced, so that penalties were applied outside set tolerances.

Furthermore the K^+ ions have migrated, with K-O bond lengths ranging from 2.0 Å to

3.8 Å (original bond length is 2.75 Å). The thermal parameters associated with K also persistently have a high degree of error. This is likely due to: (a) the low quantities of K present in the restacked material which has undergone protonation and ion-exchange prior to acid restacking; (b) the relatively weak contribution of K (and other interlayer ions) to the PDF and (c) the possible occupation of different interlayer sites enabled by the larger interlayer spaces. Therefore, the K^+ ions were removed from subsequent refinements.

The `spherical_damping` function refined a value of 52(2) Å, which is substantially beyond the limit of the XPDF, consequently the `spherical_damping` function was removed from subsequent refinements as it did not improve the fit.

The lattice parameters, thermal parameters and also background parameters have all shown very little change since the previous refinement (Table 4.7).

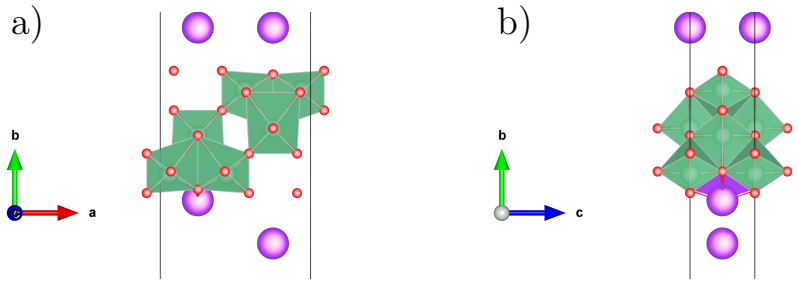


Figure 4.10: Diagram of the refined one layer model obtained from step three of small box analysis of restacked niobate that produced a highly distorted niobate layer with abnormal K-O bond lengths. Niobate octahedra shown as green octahedra. Oxygen is shown as red spheres.

Table 4.7: Table summarising the results from step three of small box refinement on the XPDF of restacked niobate.

Parameter	Previous value	New refined value
r_{wp} / %	32.029	24.204
One layer model a / Å	8.856(4)	8.888(4)
One layer model c / Å	3.8226(17)	3.8189(17)
Background intersect / Å	7.16(9)	7.10(8)
Low r background gradient	-1.4(8)	-2(2)
High r background gradient	0.0922(7)	0.092(3)
Nb `beq_low`	0.00(3)	0.00(6)
Nb `beq_high`	2(5)	1.1(7)
K `beq_low`	10(13)	0(37)
K `beq_high`	100(218)	100(74)
O `beq_low`	2.5(6)	0(6)
O `beq_high`	6(7)	4(2)
`radius`	29(78)	17(12)
`spherical_damping` / Å	-	52(2)

Table 4.8: Table of parameters used to define the atomic sites of a single layer of KNb_3O_8 in a *P1* unit cell, before and after refinement. Values without errors have not been refined.

Parameter name	Original value	Refined value	Parameter name	Original value	Refined value
xNb1a	0.0597	0.0597	yNb1a	0.3682	0.3682
xNb2	0	0	yNb2a	0.7584	0.76(4)
xK1a	0	0	yK1a	0.0155	-0.039(2)
xO1a	0.592	0.57(13)	yO1a	0.1565	0.14(10)
xO2a	0.9346	0.91(12)	yO2a	0.4311	0.42(9)
xO3a	0.9049	0.91(7)	yO3a	0.2954	0.31(7)
xO4a	0	0	yO4a	0.2866	0.26(14)
xO5a	0	0	yO5a	0.4149	0.41(15)
xNb1b	0.0597	0.061(11)	yNb1b	0.8682	0.867(14)
xNb2b	0	0	yNb2b	0.2584	0.26(5)
xK1b	0	0	yK1b	0.5155	0.44(4)
xO1b	0.592	0.57(12)	yO1b	0.6565	0.64(10)
xO2b	0.9346	0.91(12)	yO2b	0.9311	0.92(9)
xO3b	0.9049	0.91(8)	yO3b	0.7954	0.81(7)
xO4b	0	0	yO4b	0.7866	0.76(15)
xO5b	0	0	yO5b	0.9149	0.91(16)

4.5.7 Step four: Removing potassium and adding restraints

Method

Distance and angle restraints were put in place to prevent the unrealistic distortion of niobate octahedra. `Distance_Restrain` function adds a penalty to the refinement if the bond distance refines to a value beyond the permitted tolerance away from the *acceptable distance*. The tolerance and penalty used in this study are 0.1 Å and 1, respectively. The `Angle_Restrain` function operates in a similar fashion, the tolerance and penalty used in this study are 5°and 1, respectively.

Furthermore K^+ ions were removed from the refinements due to suspected insufficient information in the XPDF pattern to deduce accurate sites, due to the poor x-ray scattering cross-section of the interlayer-ions.

The `spherical_damping` function was also removed due to lack of contribution to the refinement.

Results

The r_{wp} increased to 29.588 % (Figure 4.11), an increase is expected because the restrains have prevented a lower χ^2 structure to be accessed due to its unrealistic chemistry. The Nb-O bonds are now within 1.7 Å and 2.7 Å (Figure 4.12) which is much closer to being within the reported[194] 1.7815 Å and 2.4756 Å. By introducing the low r data, the Nb-O bond lengths may naturally refine to within reported limits.

The removal of K and introduction of restraints (Table 4.10 and 4.11) has had minimal impact on the lattice parameters (Table 4.9). The parameters which dictate the atomic positions have also undergone minor changes (Table 4.12).

Although the thermal parameters and atomic position parameters have higher than ideal errors associated with them, these should decrease once the low r XPDF is introduced into the analysis.

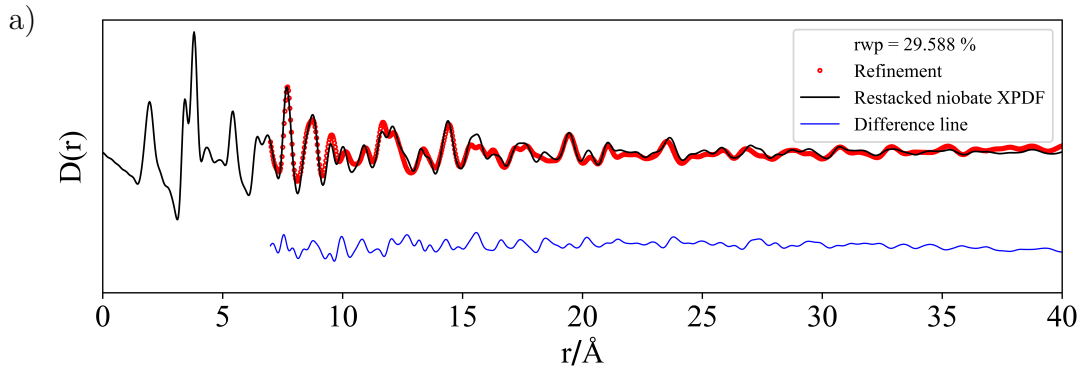


Figure 4.11: Results from step four of small box analysis on the PDF collected from the restacked material

Table 4.9: Table summarising the results from step four of small box refinement on the XPDF of restacked niobate.

Parameter	Previous value	New refined value
r_{wp} / %	24.204	29.588
One layer model a / Å	8.888(4)	8.857(4)
One layer model c / Å	3.8189(17)	3.8238(16)
Background intersect / Å	7.10(8)	6.7(6)
Low r background gradient	-2(2)	0.7852(3)
High r background gradient	0.092(3)	0.09(2)
Nb `beq_low`	0.00(6)	0.02(5)
Nb `beq_high`	1.1(7)	2(5)
O `beq_low`	0(6)	0(1)
O `beq_high`	4(2)	8(4)
`radius`	17(12)	30(66)

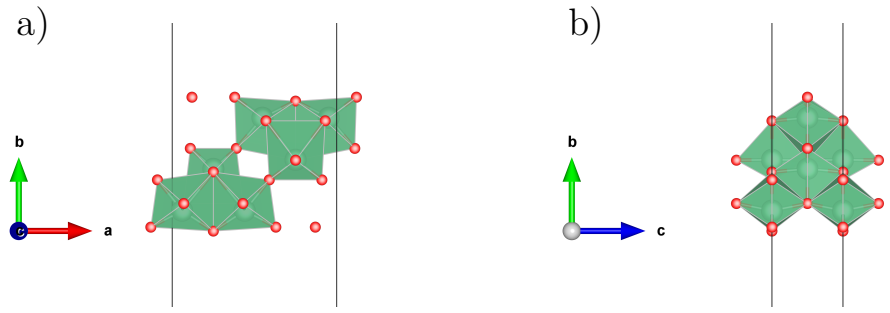


Figure 4.12: Diagram of the refined one layer model obtained from step four of small box analysis of restacked niobate. Niobate octahedra shown as green octahedra. Oxygen is shown as red spheres.

The distance restraints and angle restraints has maintained the niobate layer. The O1_4a to Nb2_1a and O1_2a to Nb2_1a atom distances show the highest error and interestingly these are also the longest Nb-O bond distances (Table 4.10). The angle restraint (Table 4.11) shows that the bond angles are not being pushed outside the limits. Although a lower χ^2 would be reached without these restraints, it would be chemically unrealistic. Furthermore the errors should decrease once the low r data is refined.

Table 4.10: Results from step four of the refinement: the distance restraints placed between atoms in the one layer structure with a tolerance of 0.1 Å and a penalty of 1.

Atom one	Atom two	Acceptable distance / Å	Refined distance / Å
O3_1b	Nb2_2b	1.62	1.61(18)
O4_2a	Nb2_2b	1.92	1.915(17)
O3_3b	Nb2_2b	1.62	1.62(18)
O3_2a	Nb2_1a	1.64	1.73(17)
O4_1b	Nb2_1a	1.91	1.912(7)
O3_4a	Nb2_1a	1.63	1.73(17)
O1_4a	Nb2_1a	2.55	2.6(8)
O1_2a	Nb2_1a	2.55	2.6(8)

Table 4.11: Results from step four of the refinement: the angle restraints placed between atoms in the one layer structure with a tolerance of 5 ° and a penalty of 1.

Atom one	Atom two	Atom three	Acceptable angle / °	Refined angle / °
O4_2a	Nb2_2b	O4_2a	173	173(16)
Nb2_1a	O4_1b	Nb2_1a	177	176(16)
O1_4a	Nb1_3b	O1_4a	161	161(18)
Nb1_2a	O1_1b	Nb1_2a	160	160(19)
Nb1_4a	O1_3b	Nb1_4a	160	160(19)

Table 4.12: Table of parameters used to define the atomic sites of a single layer of KNb_3O_8 in a *P1* unit cell, before and after refinement. Values without errors have not been refined.

Parameter name	Original value	Refined value	Parameter name	Original value	Refined value
xNb1a	0.0597	0.0597	yNb1a	0.3682	0.3682
xNb2	0	0	yNb2a	0.7584	0.761(4)
xO1a	0.592	0.57(4)	yO1a	0.1565	0.14(5)
xO2a	0.9346	0.87(5)	yO2a	0.4311	0.41(4)
xO3a	0.9049	0.91(5)	yO3a	0.2954	0.28(4)
xO4a	0	0	yO4a	0.2866	0.27(8)
xO5a	0	0	yO5a	0.4149	0.42(5)
xNb1b	0.0597	0.048(1)	yNb1b	0.8682	0.8679(12)
xNb2b	0	0	yNb2b	0.2584	0.262(4)
xO1b	0.592	0.57(5)	yO1b	0.6565	0.65(5)
xO2b	0.9346	0.88(5)	yO2b	0.9311	0.92(4)
xO3b	0.9049	0.89(5)	yO3b	0.7954	0.79(4)
xO4b	0	0	yO4b	0.7866	0.76(8)
xO5b	0	0	yO5b	0.9149	0.91(6)

4.5.8 Step five: Refinement of the full dataset

Method

Now the mid and high r region have been fitted suitably using the one layer model, the low r region can be introduced.

Results

Table 4.13: Table summarising the results from step five of small box refinement on the XPDF of restacked niobate.

Parameter	Previous value	New refined value
r_{wp} / %	29.588	35.157
One layer model a / Å	8.857(4)	8.863(4)
One layer model c / Å	3.8238(16)	3.8211(18)
Background intersect / Å	6.7(6)	4.75(5)
Low r background gradient	0.7852(3)	-0.682(15)
High r background gradient	0.09(2)	0.078(15)
Nb `beq_low`	0.02(5)	0.06(5)
Nb `beq_high`	2(5)	2(4)
O `beq_low`	0(1)	0.0(3)
O `beq_high`	18(34)	12(20)
`radius`	30(66)	35(63)

As expected when introducing more information to the refinement, the atomic positions can be modelled with more certainty (Table 4.14). In the previous refinement, the errors associated with oxygen sites, were in the second decimal place, and now they are all in the third decimal place, showing an approximate 10 fold increase in certainty. This is because the low r data shows atom to atom bond distances, and is very information rich for determining atomic positions.

The lattice parameters, thermal parameters and background parameters have not changed significantly with the exception of the low r background gradient, which is expected due to the introduction of low r data.

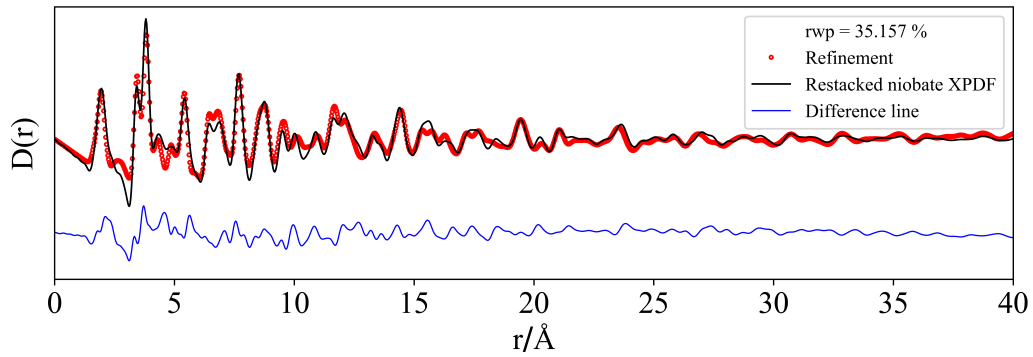


Figure 4.13: Results from step five of small box analysis on the PDF collected from the restacked material.

Table 4.14: Table of parameters used to define the atomic sites of a single layer of KNb_3O_8 in a *P1* unit cell, before and after refinement. Values without errors have not been refined.

Parameter name	Original value	Refined value	Parameter name	Original value	Refined value
xNb1a	0.0597	0.0597	yNb1a	0.3682	0.3682
xNb2	0	0	yNb2a	0.7584	0.7605(11)
xO1a	0.592	0.573(17)	yO1a	0.1565	0.145(6)
xO2a	0.9346	0.869(18)	yO2a	0.4311	0.414(7)
xO3a	0.9049	0.904(15)	yO3a	0.2954	0.289(6)
xO4a	0	0	yO4a	0.2866	0.267(9)
xO5a	0	0	yO5a	0.4149	0.418(13)
xNb1b	0.0597	0.048(1)	yNb1b	0.8682	0.868(4)
xNb2b	0	0	yNb2b	0.2584	0.26148(94)
xO1b	0.592	0.569(15)	yO1b	0.6565	0.650(7)
xO2b	0.9346	0.877(19)	yO2b	0.9311	0.917(7)
xO3b	0.9049	0.893(14)	yO3b	0.7954	0.788(6)
xO4b	0	0	yO4b	0.7866	0.787(8)
xO5b	0	0	yO5b	0.9149	0.915(12)

The r_{wp} however increased (Table 4.13), this appears to be caused by an intensity mismatch at low r. From the microscopy images of restacked niobate, the layers are often a few sheets thick and therefore short range coherence along the [010] direction maybe present. Therefore to model this, a second phase, with the KNb_3O_8 structure was used.

Previously the O1_2a to Nb2_1a and O1_4a to Nb2_1a bond distances (Table 4.10 and 4.15) were refining to unrealistically large values, however they have also now shown a decrease in refined distance from 2.6(8) Å to 2.54(14) Å, which similar to the

longest Nb-O bond lengths observed by J.K.D. Souza *et al.* (2.4756 Å).[194] The angle restraints have shown little change apart from a decrease in error (Table 4.16).

Table 4.15: Results from step five of the refinement: the distance restraints placed between atoms in the one layer structure with a tolerance of 0.1 and a penalty of 1.

Atom one	Atom two	Acceptable distance / Å	Refined distance / Å
O3_1b	Nb2_2b	1.62	1.65(12)
O4_2a	Nb2_2b	1.92	1.914(11)
O3_3b	Nb2_2b	1.62	1.62(12)
O3_2a	Nb2_1a	1.64	1.73(13)
O4_1b	Nb2_1a	1.91	1.912(5)
O3_4a	Nb2_1a	1.63	1.73(13)
O1_4a	Nb2_1a	2.55	2.54(14)
O1_2a	Nb2_1a	2.55	2.54(14)

Table 4.16: Results from step five of the refinement: the angle restraints placed between atoms in the one layer structure with a tolerance of 5 ° and a penalty of 1.

Atom one	Atom two	Atom three	Acceptable angle / °	Refined angle / °
O4_2a	Nb2_2b	O4_2a	173	173(11)
Nb2_1a	O4_1b	Nb2_1a	177	176(10)
O1_4a	Nb1_3b	O1_4a	161	159(8)
Nb1_2a	O1_1b	Nb1_2a	160	157(9)
Nb1_4a	O1_3b	Nb1_4a	160	157(9)

4.5.9 Step six: Refinement with additional ONb_3O_8 phase

Method

The r_{wp} however increased from step 4 to 5 (Table 4.13), this appears to be caused by an intensity mismatch at low r. From the microscopy images of restacked niobate, the layers are often a few sheets thick and therefore short range coherence along the [010] direction maybe present. Therefore a crystalline ONb_3O_8 phase as added, based on the structure of KNb_3O_8 with the interlayer K^+ replaced with O to model the suspected structure of $H_3ONb_3O_8$. This additional phase was with a function (`shortrange_erf`) which allows the intensity contributions from ONb_3O_8 to gently fade out to mimic the gradual loss of atomic correlation with increasing r. Lattice parameters of ONb_3O_8 were allowed to refine, but not the atomic positions and a singular thermal parameter was given to each element.

Results

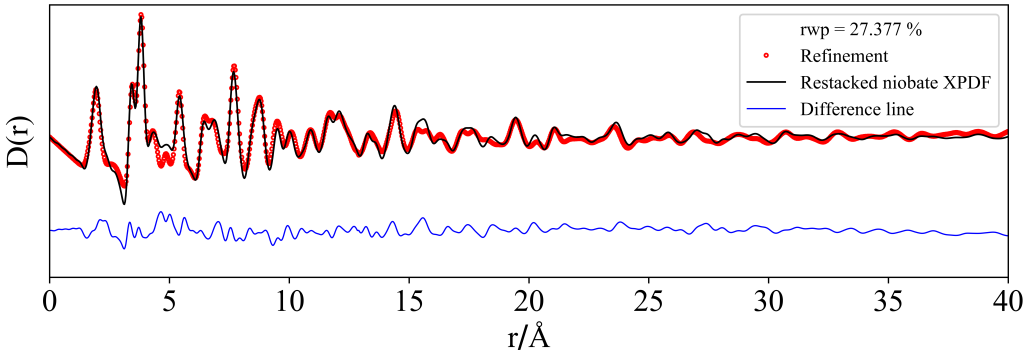


Figure 4.14: Results from step six of small box analysis on the PDF collected from the restacked material.

The ratio of the two scales (one layer model and ONb_3O_8) can be used as molar ratio between the two phases, 1.00(2):0.36(3) which indicates that only a minority of layers experience atom to atom correlations between layers ([020] direction).

The thermal parameters (Table 4.17) show an almost linear increase as determined by

Table 4.17: Table summarising the results from step six of small box refinement on the XPDF of restacked niobate.

Parameter	Previous value	New refined value
r_{wp} / %	35.157	27.377
One layer model a / Å	8.863(4)	8.864(3)
One layer model c / Å	3.8211(18)	3.8198(17)
One layer model scale	1.006(17)	1.00(2)
ONb_3O_8 a / Å	-	10.15(2)
ONb_3O_8 b / Å	-	23.28(4)
ONb_3O_8 c / Å	-	3.786(9)
ONb_3O_8 `beq` N	-	0.9(5)
ONb_3O_8 `beq` O	-	3.3(1.1)
ONb_3O_8 scale	-	0.36(3)
`shortrange_erf` / Å	-	12.84(4)
Background intersect / Å	4.75(5)	4.75(4)
Low r background gradient	-0.682(15)	-0.683(15)
High r background gradient	0.078(15)	0.0780(17)
Nb `beq_low`	0.06(5)	0.08(4)
Nb `beq_high`	2(4)	3(3)
O `beq_low`	0.0(3)	0.0(3)
O `beq_high`	12(20)	13(16)
`radius`	35(63)	33(45)

the large `radius`. The `beq_high` values are significantly higher for O than Nb which is expected as O is lighter and will therefore vibrate more.

The ONb_3O_8 lattice parameters can be compared to the reported KNb_3O_8 values of, 8.903 Å, 23.44 Å and 3.799 Å for a, b and c respectively which show an expansion in a with little change in b and c. The lattice parameters for the one layer model have not changed significantly from KNb_3O_8, unlike ONb_3O_8. This is further supported by the parameters used to dictate atomic positions, outlines in Table 4.18 which also, have not altered drastically and the niobate layer structure remains, although the octahedra are significantly more distorted than previous (Figure 4.15).

The O1_2a to Nb2_1a and O1_4a to Nb2_1a bond distance has remained at 2.54(15) Å, similar to the previous refinement. Compared to the corresponding bond distance in the original KNb_3O_8 (Nb2-O1), it is 2.285(5) Å, which is significantly shorter. The bond lengths are more extreme in the restacked niobate than the KNb_3O_8,

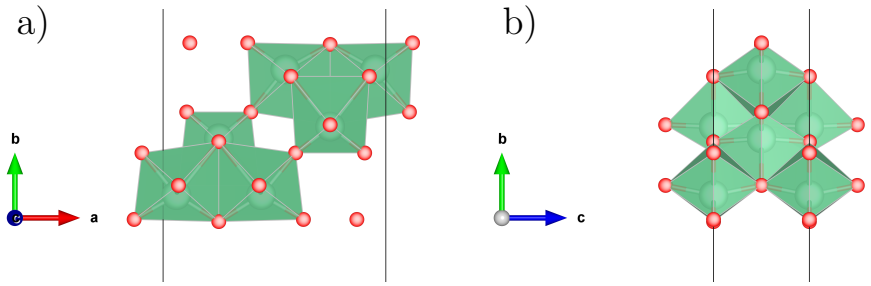


Figure 4.15: Diagram of the one layer model obtained from small box analysis of the PDF dataset corresponding to the restacked nanostructured material.

Table 4.18: Table of parameters used to define the atomic sites of a single layer of KNb_3O_8 in a *P1* unit cell, before and after refinement. Values without errors have not been refined.

Parameter name	Original value	Refined value	Parameter name	Original value	Refined value
xNb1a	0.0597	0.0597	yNb1a	0.3682	0.3682
xNb2	0	0	yNb2a	0.7584	0.761(11)
xO1a	0.592	0.574(19)	yO1a	0.1565	0.145(6)
xO2a	0.9346	0.870(19)	yO2a	0.4311	0.414(7)
xO3a	0.9049	0.904(15)	yO3a	0.2954	0.289(6)
xO4a	0	0	yO4a	0.2866	0.267(8)
xO5a	0	0	yO5a	0.4149	0.418(14)
xNb1b	0.0597	0.04831(9)	yNb1b	0.8682	0.8680(4)
xNb2b	0	0	yNb2b	0.2584	0.2615(9)
xO1b	0.592	0.569(15)	yO1b	0.6565	0.650(7)
xO2b	0.9346	0.877(19)	yO2b	0.9311	0.917(7)
xO3b	0.9049	0.893(13)	yO3b	0.7954	0.788(6)
xO4b	0	0	yO4b	0.7866	0.764(7)
xO5b	0	0	yO5b	0.9149	0.915(12)

leading to a more distorted octahedra in the one layer model (Figure 4.15). The other angle and distance restraints have shown little change compared to previous (Table 4.19 and 4.20).

The introduction of the ONb_3O_8 phase has improved the refinement as determined by the decrease in r_{wp} from 35.157 % to 27.377 %. The intensities of the modelled data is matching the experimental data better in the low r region (Figure 4.15).

The interlayer distance of the restacked niobate determined by XRD is 13.08 Å, which is higher than the interlayer distance of ONb_3O_8 (d_{020} = 11.64 Å). This discrepancy is

due to the `shortrange_erf` (12.84(4) Å) which has removed this phase from being modelled against the high r data, therefore the lattice parameter b as refined from the PDF is not very meaningful.

Table 4.19: Results from step six of the refinement: the distance restraints placed between atoms in the one layer structure with a tolerance of 0.1 and a penalty of 1.

Atom one	Atom two	Acceptable distance / Å	Refined distance / Å
O3_1b	Nb2_2b	1.62	1.65(12)
O4_2a	Nb2_2b	1.92	1.91(11)
O3_3b	Nb2_2b	1.62	1.65(12)
O3_2a	Nb2_1a	1.64	1.73(13)
O4_1b	Nb2_1a	1.91	1.911(5)
O3_4a	Nb2_1a	1.63	1.73(13)
O1_4a	Nb2_1a	2.55	2.54(14)
O1_2a	Nb2_1a	2.55	2.54(14)

Table 4.20: Results from the angle restraints placed between atoms in the one layer structure with a tolerance of 5 ° and a penalty of 1.

Atom one	Atom two	Atom three	Acceptable angle / °	Refined angle / °
O4_2a	Nb2_2b	O4_2a	173	173(11)
Nb2_1a	O4_1b	Nb2_1a	177	176(9)
O1_4a	Nb1_3b	O1_4a	161	159(8)
Nb1_2a	O1_1b	Nb1_2a	160	157(8)
Nb1_4a	O1_3b	Nb1_4a	160	157(8)

4.6 Summary: Structure of restacked niobate

The structure of restacked niobate can be described as a single niobate layer with the same connectivity as found in KNb_3O_8, however the niobate octahedra are highly distorted, with some long Nb-O bonds of 2.54(14) Å.

The average interlayer distance of restacked niobate is 13.08 Å, as determined by XRD. Microscopy shows evidence of some stacked layers, but with significant disorder caused by layer curvature, termination and limited stacking. From Raman spectroscopy, the local structure appears to be similar to the parent material, but with a shift of the peak corresponding to the terminal Nb=O bonding implying that the association with the interlayer ions may be weaker.

From XPDF, there is evidence of atomic correlations between layers as modelled using ONb_3O_8 crystalline phase with a refined `shortrange_erf` value of 12.84(4) Å, however this is less than the average interlayer distance. Therefore although there are some interlayer correlations, the majority are stacked turbostatically. The molar ratio of single layer: ONb_3O_8 of 1.00:0.36 indicates the majority of niobate layers do not show have interlayer correlations.

The occupancy and nature of the interlayer space is not well characterised in this study, largely due to the small x-ray scattering cross section of K, H and O. Understanding of this structure can be improved by obtaining neutron-PDF data on deuterated restacked niobate, however due to the small yield, long synthesis times and large quantities of H_2O and HCl used in synthesis, this experiment was not possible within the timeframe of this thesis.

This restacked niobate has a larger interlayer space which could be beneficial to the sodium-ion diffusion kinetics during cycling, this would lead to an anode material capable of faster charging. The disordered nature of the material also impacts the sodium-intercalation sites which are more loosely defined and therefore sodium-ion insertion is

more likely to occur *via* a solid-solution mechanism.

The capacity could benefit from larger interlayer spacing making more sites accessible, however the disorder may have also negatively affected many sites, therefore it is difficult to predict the impact of this structure on its capacity. It is also not known how stable this disordered materials is to cycling and may succumb to capacity fade at a faster rate than its crystalline counterpart.

Understanding this structure will also benefit the field of photocatalysis who study this material for its ability to catalyse hydrogen production.

5 Synthesis and characterisation of nanostructured niobates *via* hydrothermal synthesis

5.1 Introduction

"Top-down" nanostructuring has been achieved by the synthesis of restacked niobate, however this synthesis requires a long time (5 weeks) with multiple steps. The formation of nanostructured alkali niobates using hydrothermal synthesis would also result in faster synthesis time and lower temperature use, which would be favoured by industry and would result in a more environmentally friendly energy use.

Hydrothermal synthesis has previously been successfully employed to produce various morphologies such as nanosheets, belts and hexagonal plates. It is widely accepted that hydrothermal synthesis allows for the improved morphology control and, in some systems, allows for the formation of phases that are inaccessible by solid state synthesis. Hence, this study aims to synthesise and characterise disordered niobate phases by hydrothermal methods.

5.1.1 Literature established methods

Hydrothermal synthesis of potassium niobates involves a mixture of Nb_2O_5, KOH and water, which is heated in an autoclave.[195,196,197] KOH acts as both a potassium source and aid the dissolution of Nb_2O_5.[103]

J. F. Liu *et al.*[197] provides important insight into how by varying KOH concentration affects the niobate product ($KNbO_3$, KNb_3O_8 and $K_4Nb_6O_{17}$) through Equations 5.1, 5.2 and 5.3. They also reported a one step hydrothermal synthesis of $KNbO_3$ requiring 6-10 M KOH whilst $K_4Nb_6O_{17}$ requires 0.5-1 M KOH solution. On the other hand synthesis of KNb_3O_8 occurs as a two step process, it firstly requires 1-4 M KOH solution to produce a colourless solution which is then acidified using HCl to pH 4-5.

$$\text{Stongly alkaline: } 3\,Nb_2O_5 + 6\,OH^- \rightarrow 6\,NbO_3{}^- + 3\,H_2O \tag{5.1}$$

$$\text{Medium alkaline: } 3\,Nb_2O_5 + 4\,OH^- \rightarrow Nb_6O_{17}{}^{4-} + 2\,H_2O \tag{5.2}$$

$$\text{Slightly alkaline: } 3\,Nb_2O_5 + 2\,OH^- \rightarrow 2\,Nb_3O_8{}^- + H_2O \tag{5.3}$$

As pH decreases, the Nb:O ratio also increases (from 25 % in $NbO_3{}^-$ to 27 % in $Nb_3O_8{}^-$). Therefore the control of pH is crucial in niobate oxide design.

G. Zhang *et al.*[114] hydrothermally synthesised KNb_3O_8 in a two step process. Firstly, G. Zhang *et al.* heated a solution of KOH and Nb_2O_5 in an autoclave for 200 °C for 4 hrs, which were then acidified dropwise using HCl to the desired pH, then the autoclave was then heated again at 200 °C. The product was washed and dried and analysed by XRD. A range of pH was studied from pH 9-2. At pH 5.5, the XRD pattern revealed KNb_3O_8 was synthesised. The XRD patterns from the other samples, with a few peaks, were not assigned in detail.

In many of these hydrothermal syntheses, amorphous or disordered products are disregarded, often their XRD patterns are not even presented.[104,114,197] Additionally, the products synthesised from a two-step hydrothermal synthesis at pH 0-5 and pH 5-14, reported by G. Zhang *et al.*[114], have not been characterised.

X. Liu *et al.*[104] performed a systematic study by varying the concentration of KOH (0.595-6.54 M corresponding to 1 - 11 g KOH in 30 mL H_2O). KOH concentrations between 3.5-6.5 M (6-11 g KOH) produced pure KNb_3O_8 when acidified to pH 5-6. In

this study, the solutions were acidified to pH 5-6 and beyond (pH 0-1, 2-3 and 5-6), to determine its effects.

X. Liu *et al.*[104] reported that at a very low KOH concentration of 0.595 M (1 g KOH), the XRD pattern shows nanostructured features of interest, therefore low KOH concentration synthesis was also explored, more specifically 0.29 M and 0.60 M.

To the best of our knowledge, there are no attempts to characterise hydrothermally synthesised disordered KNb_3O_8 phases, a gap this project aims to contribute towards.

Typically 1-4 M of KOH is used in the synthesis of KNb_3O_8, this study aims to broaden this pH range to determine its effects (0.6-6.5 M). By varying the concentration of reactants, temperature and duration, the synthesis of a self-assembly disordered KNb_3O_8 product was attempted.

5.2 Hydrothermal synthesis method

A broader range of KOH concentrations and quantity of HCl were explored in this study, to discover new disordered phases.

For a 45 mL autoclave, 0.5 g or 1 g of KOH (Extra Pure, Pellets, Fisher Chemical) was added to 30 mL of stirring H_2O to form a 0.29 M or 0.60 M KOH solution respectively, then 0.3 g of Nb_2O_5 (99.9 %, Thermo Scientific Chemicals) was added and stirred for 20 mins. The mixture was poured into a teflon lined autoclave and heated for 2 days at 180 °C. The solution was then acidified using 6 M HCl (Thermo Scientific Chemicals) under stirring conditions until the chosen pH was in the desired pH range, either 0-1, 2-3, or 5-6. The mixture was returned to the autoclave and heated at 180 °C for a further 4 days. All weight and volume measures were scaled up for a 125 mL autoclave.

5.3 Hydrothermal synthesis results

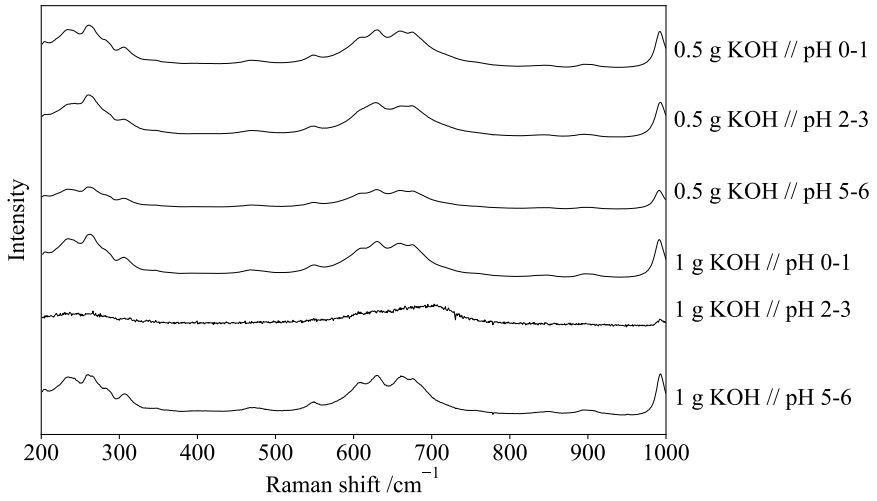


Figure 5.1: Raman spectra of hydrothermal products, synthesised with variations in the mass of KOH and pH (adjusted using HCl).

The sample 1g KOH// pH 2-3 shows a marked difference in the Raman spectrum compared to others (Figure 5.1), the bands are significantly broader. This is most likely due to the an increase in disorder within the sample. This is supported by the rapid damping observed in the PDF (Figure 5.2).

The Raman spectra of the other products (Figure 5.1); the bands at lower Raman shift are not sharp, indicative of a disordered or amorphous material. The band at 993 cm^{-1} which is indicative of the Nb=O short bond vibrations. The bands at around 650 cm^{-1} is the characteristic band for the structure consisting of corner shared NbO_6 octahdera.[198] Whilst the band at around 250 cm^{-1} is the Nb-O-Nb bending mode.[185,198] These bands suggest the presence of Nb_2O_5 which is supported by the similarities between the Raman spectra (Table 5.1) in peak position and intensity.

Table 5.1: Bands identified in the Raman specta for sample 1g KOH// pH 5-6 compared to those reported by B. Balachahdean *et al.*[199] for Nb_2O_5.

This study		B. Balachahdean *et al.*[199]	
Wavenumber cm^{-1}	Intensity	Wavenumber cm^{-1}	Intensity*
205	medium	207	medium
234	strong	235	strong
260	strong	261	strong
306	medium	305	medium
468	weak	571	weak
549	weak	550	weak
608	strong	-	-
629	strong	632	strong
660	strong	659	strong
676	strong	674	strong
850	weak	846	weak
893	weak	897	weak
993	strong	992	strong

* Intensity interpreted by Rachel (Wai Chi) Tang, author of this study.

X. Liu *et al.*[104] performed an analogous experiment using 1g KOH, acidified to pH 5.61, akin to the reported 1g KOH//pH 5-6 sample in this study (Figure 5.2.a.). X. Liu *et al.* reported an XRD pattern showing a mixture of broad and sharp peaks, similar to this study, however the sharp peaks were significantly different, indicating a different crystalline phase was synthesised. Unfortunately, X. Liu *et al.* did not identify the disordered phase, however it shows significant resemblance to the XRD pattern obtained from the exfoliation and restacking of KNb_3O_8. Further XPDF based studies are required to establish this fact.

The XRD patterns (Figure 5.2.a.) of the samples 1 g KOH//pH 2-3 and 1 g KOH//pH 5-6 do possess a higher, undulating background indicative of an amorphous phase. All samples show the same set of peaks, indicating the same phase has been formed. The Rietveld refinement of the 0.5 g KOH//pH 0.1 XRD pattern (Figure 5.3 and Table 5.2) revealed the main product to be Nb_2O_5, a reagent of the reaction. The refinement provided lattice parameters with a low degree of error, which also supports the literature reported values.

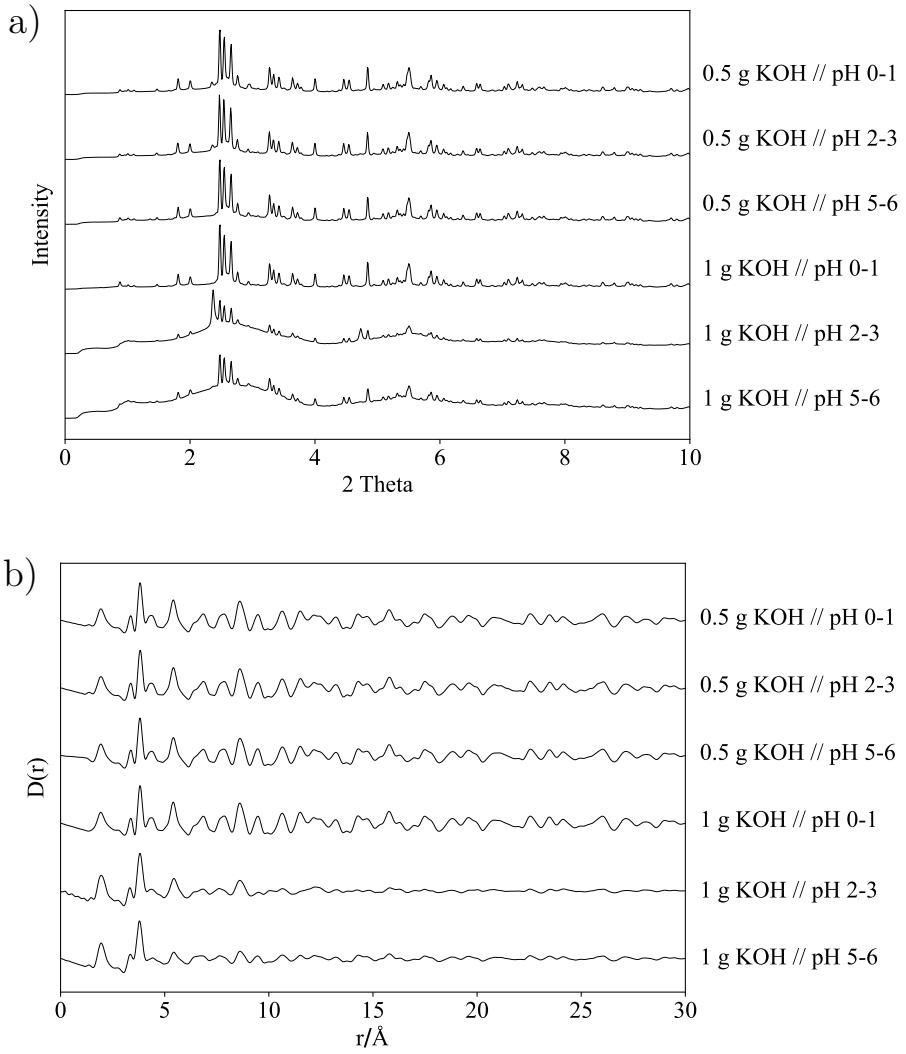


Figure 5.2: X-ray scattering results from I15-1 (λ = 0.161669 Å) of hydrothermal products synthesised with variations in the mass of KOH and pH (adjusted using HCl) a) XRD patterns b) Pair distribution function.

A crucial experimental difference between our approach and that of X. Liu *et al.*[104] was their use of a stirred autoclave whilst heating. This was unfortunately not available for this study and thus, instead of obtaining a clear solution after the first heating step, a clear solution and sediment was obtained instead. Therefore, we can conclude that the Nb_2O_5 starting material had not been fully digested by the KOH prior to being acidified.

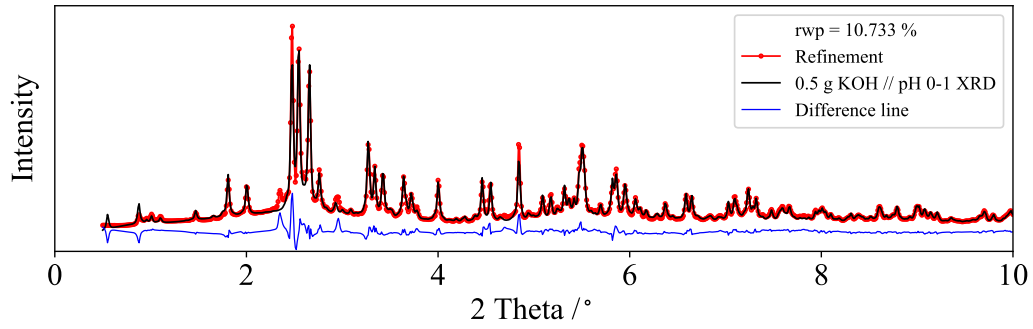


Figure 5.3: XRD pattern collected on I15-1 ($\lambda = 0.161669$ Å) of the product synthesised using 0.5 g KOH at pH 0-1 fit to Nb_2O_5 using Rietveld refinement (r_{wp} of 10.75 %).

Table 5.2: Table summarising the results from refinement of 0.5 g KOH at pH 0-1 fitted to literature reported structure of Nb_2O_5 (space group *P2/m*, ICSD: 29)

Parameter	Refined value	Reported values
r_{wp} / %	10.75	-
Nb_2O_5 *a* / Å	21.1595(16)	21.153(7)
Nb_2O_5 *b* / Å	3.8253(3)	3.8233(5)
Nb_2O_5 *c* / Å	19.3513(14)	19.3560(50)
Nb_2O_5 β	119.816(8)	119.80(2)
Nb_2O_5 beq	0.38(8)	

Before further investigating the disorder found in two of the samples, the method was first optimised to remove the impurity phase Nb_2O_5, which was found to be present unchanged in all previous synthesis products. Therefore, a filtration step was introduced after the first heating step. This is designed to filter out the undissolved Nb_2O_5 sediment, whilst retaining the solution of dissolved Nb_2O_5. To this solution, 6 M HCl was added to induce precipitation followed by the second heating step.

From the XPDF, the sample: 1g KOH//pH 2-3 possesses significant disorder due to the

rapid damping of peaks in the PDF, which can also be seen in the high background of the observed XRD pattern of the same sample (Figure 5.2,a,b.). Similar characteristics, although to a lesser extent were also observed with the 1 g KOH//pH 5-6 sample. Hence, these two samples were selected for further study.

5.3.1 Characterisation of hydrothermal nanostructured material

A sample was synthesised using the modified method for 1g KOH// pH 2-3, a set of synthesis conditions that had previously never been tested. The product of which has been named hydrothermal nanostructured material for ease of discussion.

XRD

The XRD pattern (Figure 5.4) shows two sharp peaks at 3.91 Å and 1.96 Å d-spacing. 3.91 Å is approximately double 1.96 Å which leads to the suspicion that these reflections are related. An additional weaker and broader peak at 8.52 Å which tends to indicate the interlayer spacing. The large width of this peak would indicate that a range of interlayer distances are present, which suggests turbostatically stacked layers. The combination of very sharp and broad peaks in the same XRD pattern suggests that there is either two phases or anisotropy which is observed as hkl dependent peak shapes.

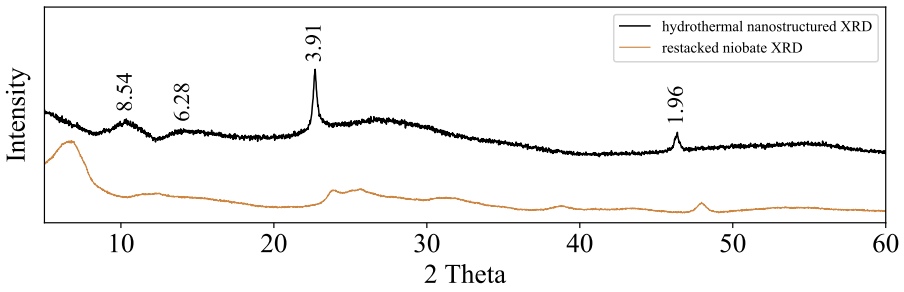


Figure 5.4: Results from XRD of hydrothermal nanostructured product, with d-spacing values annotated (λ= 1.54056 Å)

Microscopy

The hypothesis that there are two phases is supported by microscopy (Figure 5.5), which shows crystal needles with a high aspect ratio and the presence of globular, porous amorphous material. Figure 5.5.d. shows a layered arrangement of atoms. These layers however are not consistent throughout, and their morphology changes along its length. The rods show a high aspect ratio with a diameter of 25 nm and

length of around 0.5 μm. The Fourier transform of Figure 1.4.d, shows weaker repeats at 8.01 Å and stronger repeats at 4.05 Å, tentatively supporting the d-spacings observed using XRD.

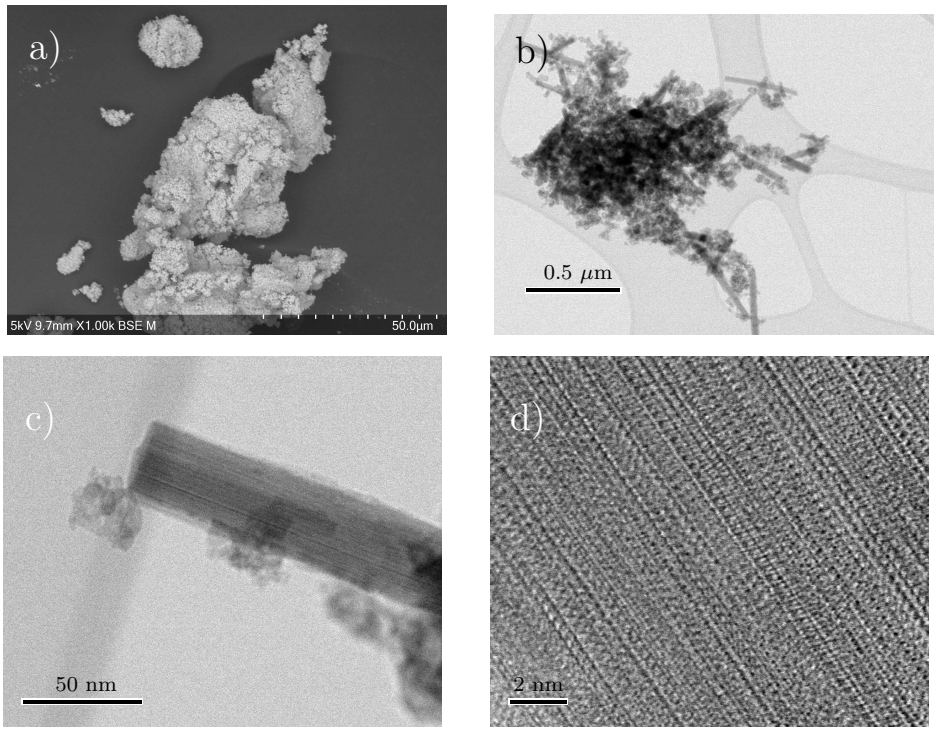


Figure 5.5: Microscopy images of hydrothermal product which was acidified to pH 2-3. a) Benchtop SEM b,c,d) High resolution STEM

Raman

The Raman spectrum of the hydrothermal nanostructured product show a single broad feature centered at around 700 cm^{-1} (Figure 5.6.b.), a feature which is also observed in Nb_2O_5 amorphous type structures.[183] This is supported by a similar Raman spectrum presented by R. Brayner *et al.*[200] during his studies of disordered Nb_2O_5.

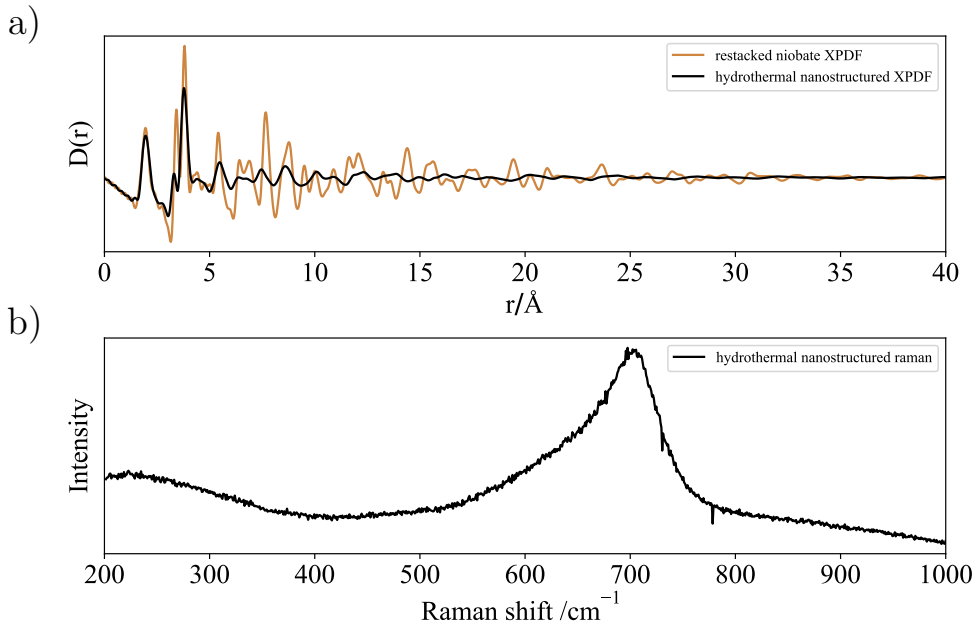


Figure 5.6: Results from structural analysis of hydrothermal nanostructured product. a) Pair distribution function. b) Raman spectra.

PDF

The irregularity in the layers (Figure 5.5) contributes to the the rapid damping observed in the PDF, with a lack of coherence beyond 1 nm (Figure 5.6.a.). When compared to the PDF data above 5 Å of the restacked niobate sample, the peaks are shifted and therefore it may be hypothesised that the niobate connectivity is significantly different to that of the restacked niobate, which is based on KNb_3O_8.

Below 5 Å, the PDF pattern shows peaks at 1.96 Å, 3.34 Å and 3.79 Å corresponding to Nb-O; edge shared Nb-Nb and lastly an overlap of atom distances for corner shared Nb-Nb and K-K distances. The Nb-Nb edge sharing peak intensity (3.34 Å) is significantly lower than the intensity of corner sharing Nb (3.79 Å), a significant difference compared to the ratios observed in restacked niobate. This suggests that the structure contains significant corner sharing niobate octahedra.

Table 5.3: Table of results from small box fitting of hydrothermal nanostructured PDF to known phases obtained from the ICSD database.

Phase name	ICSD code	r_{wp} / %		spherical damping value / Å
		without spherical damping	with spherical damping	
$Nb_{12}O_{29}$	155015	67.5	45.3	6.1(2)
$Nb_{12}O_{29}$	24089	65.7	45.9	6.3(2)
Nb_2O_5	29	67.2	46.1	6.4(2)
NbO_2	35181	74.9	49.1	2.84(4)
NbO_2	95729	80.3	49.7	3.69(7)
KNb_5O_{13}	170693	67.0	55.6	2.83(9)
$K_4Nb_6O_{17}$	35030	72.9	58.1	3.80(9)
NbO_2	75198	81.3	58.9	3.13(8)
$Nb_{168}O_{42}$	1840	80.5	59.8	6.4(2)
$K_3Nb_7O_{19}$	201721	78.7	61.3	4.10(12)
$Nb_{26}Nb_{116}O_{30}$	54960	70.3	63.7	17.7(1.2)
KNb_3O_8	31994	86.3	65.5	4.14(18)
Nb_2O_5	71317	79.8	65.9	2.74(6)
$K_3Nb_7O_{19}$	62550	86.5	71.0	3.12(7)
$KNbO_3$	39869	93.5	72.7	3.23(8)
NbO_2	96	90.2	75.2	3.41(15)
NbO_2	28500	91.3	76.1	3.21(13)
NbO_2	8244	91.5	76.8	3.25(14)
NbO_2	61543	97.3	97.4	1(9)
NbO_2	237585	97.3	97.4	3.69(7)

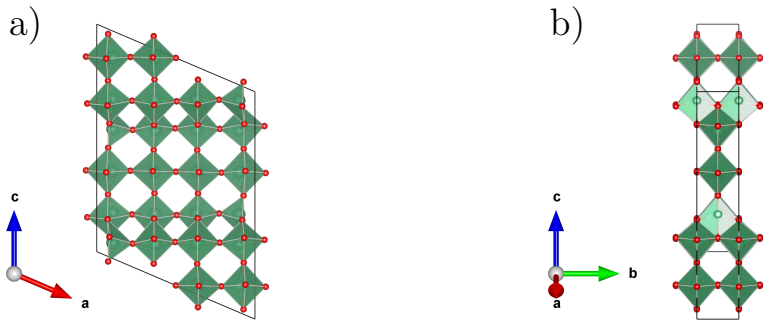


Figure 5.7: Unit cell of $Nb_{12}O_{29}$ (ICSD: 155015) where the niobate octahedra are shown in green and oxygen are shown as red spheres. a) viewed along [010] b) viewed along [100]

An attempt was made to find similarities between the hydrothermal nanostructured and other known niobates and potassium niobates using the PDF, shown in Table 5.3. Many were able to fit the peaks below 5 Å, as niobates are mostly formed of

NbO_6 units. However often spherical damping would begin between 3-6 Å, removing all higher intensities in the model. Without spherical damping, the fit was even poorer. Many structures were refined against our model, none showing a suitable fit which is reflected in the high r_{wp}. The most promising structure identified is $Nb_{12}O_{29}$ (Figure 5.7), which is formed of mostly corner shared NbO_6 units, with some edge sharing present too, which supports our hypothesis regarding the higher ratio of corner shared niobates compared to edge shared due to the height of the 3.34 Å and 3.79 Å peaks.

5.3.2 Summary: Hydrothermal nanostructured

This novel material is highly disordered niobate material with very few features in the XRD, PDF and Raman which has proved extremely challenging for structural characterisation. Microscopy shows the presence of two phases, a rod with highly irregular layered structure alongside an amorphous globular structure. The PDF does not fit many of the known niobates outlined in Table 5.3 however from the PDF it suggests the structure likely contains a high degree of corner sharing niobate compared to edge sharing niobate, simialr to the local structure akin to $Nb_{12}O_{29}$ and a secondary amorphous niobate phase.

This study shows how difficult disordered structures can be to characterise due tot he information poor results from solid state characterisation techniques. Nonetheless XPDF has proven beneficial and provided important clues to its structure.

5.3.3 Strengths and weaknesses: hydrothermal synthesis

There are some weaknesses in regards to the hydrothermal synthesis performed in this Chapter:

1. The poor solubility[103] of Nb_2O_5 hinders synthesis as there is undissolved Nb_2O_5 which is removed by an intermediate filtration step, which is then subsequently discarded. This is a waste as Nb_2O_5 is one of the more expensive chemical reagents. This hinders the yield and economic viability of this synthesis route.

2. Sediment was observed after two days of heating. This may be due to the fact that a stirring autoclave was not available in this study as used in X. Liu *et al.*[104]

3. KOH has been shown to help dissolve Nb_2O_5. However, KOH determines the pH of the solution and is also a reagent and and its quantity determines the niobate phase formed. It would be ideal if these two functions could be decoupled.

6 Synthesis and characterisation of nanostructured niobates *via* Lindqvist ion

6.1 Introduction

Previous hydrothermal work was hindered by the limited solubility of Nb_2O_5 in low concentrations of KOH in short time frames.[201] Given, that low concentrations of OH^- are required to form the Nb_3O_8 unit (Equation 5.3), and to form nanostructured, rather than crystalline layered materials, methods to decouple of the dissolution of Nb_2O_5 and the pH were necessary. Therefore, this Chapter explores the use of a Lindqvist ion intermediate ($[Nb_6O_{19}]^{-8}$) to synthesise a disordered material using "bottom up" hydrothermal synthesis in two stages (Figure 6.1). The first stage produces the more soluble Lindqvist salt of the Lindqvist ion, and the second stage is the synthesis of the disordered structure.

Synthesis *via* a Lindqvist ion intermediate decouples the quantity of KOH required to solvate/ dissolve Nb_2O_5 and the pH of synthesis by forming the more soluble Lindqvist ion which is an established synthesis route for many niobates.[202]

The first step is well established, however the second step is typically used to synthesise crystalline structures. Therefore the second synthesis step requires some adjustments to produce nanostructured niobates.

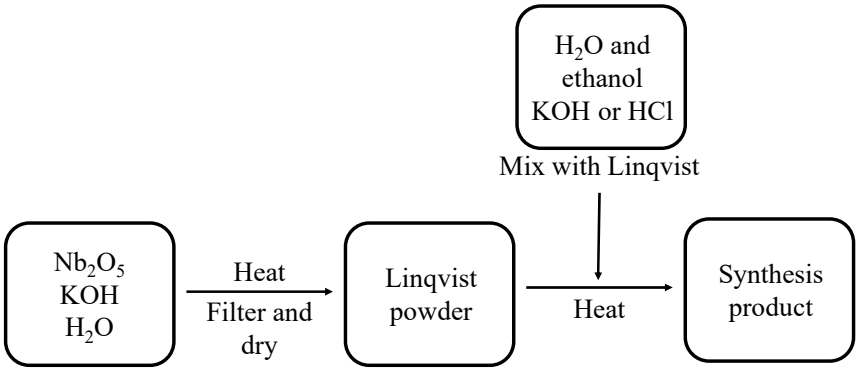


Figure 6.1: Schematic of the hydrothermal synthesis of alkali niobates *via* Lindqvist intermediate.

6.1.1 The Lindqvist ion

The Lindqvist hexaniobate ion $[Nb_6O_{19}]^{8-}$ is a a super-octahedron, formed from edge sharing $[NbO_6]$ units (Figure 6.2). It has been reported to form salts with K, Rb and Cs.[203]

Lindqvist hexaniobate ions can crystallise with with potassium as the counter ion, multiple salts are known, including $K_7[HNb_6O_{19}] \cdot 10\,H_2O$ or $K_8[Nb_6O_{19}] \cdot 16\,H_2O$ (ICSD: 391372 and 391371 respectively), however M. Nyman *et al.*[203] also noted that many different stoichiometries are also possible. The salt has a higher solubility than Nb_2O_5, making it an ideal reagent for synthesis of potassium niobates.[201] A second implication of the excellent solubility is that a second solvent (e.g. ethanol) is required to initiate salt crystallisation.

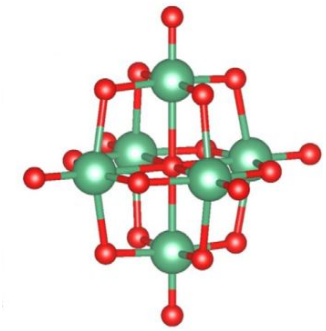


Figure 6.2: Diagram of the Lindqvist ion $[Nb_6O_{19}]^{8-}$ Nb in green and oxygen in red.

6.1.2 Synthesis of niobates using the Lindqvist salt

Lindqvist hexaniobate ions have been reported for the synthesis of various oxide materials such as $YNbO_4$ and $LaNbO_4$, in addition to potassium oxide materials such as $KNbO_3$, $K_2Nb_2O_6 \cdot H_2O$, KNb_3O_8 and $K_4Nb_6O_{17} \cdot nH_2O$.[202] The formation mechanism is understood for some phases, such as $KNbO_3$, a pervoskite based structure. Firstly Nb_2O_5 dissolves to form the Lindqvist ion ($[Nb_6O_{19}]^{8-}$) which in turn breaks into $[NbO_6]^-$ units that react in concentrated KOH to form $KNbO_3$.[202] The reaction mechanisms for the formation of KNb_3O_8 and $K_4Nb_6O_{17} \cdot nH_2O$ from Nb_2O_5 are still unknown.

X. Kong *et al.*[202] investigated the effect of various KOH concentrations, when using Nb_2O_5 in a 1:1 H_2O:ethanol solvent mixture, heated to 230 °C for 12 hrs. Using 3 M KOH, $KNbO_3$ was synthesised. At 1 M KOH; $K_2Nb_2O_6 \cdot H_2O$ was synthesised and at even lower concentrations of 0.3 M, $K_4Nb_6O_{17}$ was produced. The products collected at concentrations below 0.3 M were not assigned, but showed interesting undulating backgrounds in the XRD pattern with a few peaks, indicative of a disordered phase. Therefore this was investigated further (Table 6.2).

X. Kong *et al.*[202] also synthesised KNb_3O_8 using slightly different conditions, by using Nb_2O_5 in a 1:2 H_2O:ethanol solvent mixture, acidifed using HCl to a pH of 5.5 and then heated to 230 °C for 12 hrs. The pH is similar to that reported in conventional hydrothermal synthesis, or pH 4-5 to produce KNb_3O_8. By changing the pH range and also the heating duration, it was hoped a disordered KNb_3O_8 would be produced (Table 6.2).

6.1.3 Reported Lindqvist synthesis product $K_4Nb_6O_{17} \cdot nH_2O$

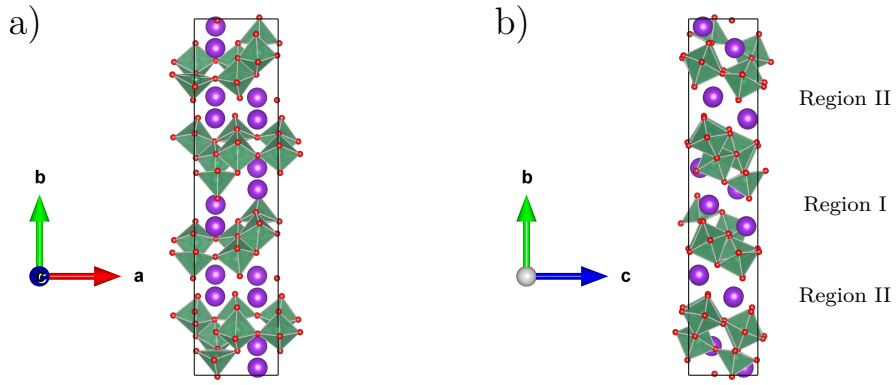


Figure 6.3: Diagram of anhydrous $K_4Nb_6O_{17}$ structure. Distorted niobate octahedra shown in green with oxygen atoms in red whilst potassium ions are shown in purple. ICSD cif file: 35030. a) views along [001] b) viewed along [100].

Anhydrous $K_4Nb_6O_{17}$ (Figure 6.3) is a layered niobate with two distinct potassium layers denoted as region I and II.[194,204,205] Region I is hydrophilic whilst region II is hydrophobic, therefore water intercalates into region I preferentially. Intercalated water forms: $K_4Nb_6O_{17} \cdot 3\,H_2O$ and $K_4Nb_6O_{17} \cdot 4.5\,H_2O$, the former being the more stable phase at room temperature and pressure.[204,206] M. A. Bizeto *et al.*[207] also reported that it is possible to replace the K^+ ions (in region I) to form $H_2Nb_6O_{17} \cdot 2\,H_2O$. Unfortunately for all hydrated forms of $K_4Nb_6O_{17}$, no crystal structure has been presented, most likely due to the difficulty in probing accurate O and H positions. The niobate layers in anhydrous $K_4Nb_6O_{17}$ are formed from $[NbO_6]$ octahedra which are highly distorted to varying degrees over the six distinct Nb sites. Their distortions have been studied to further understand its capabilities as a photocatalyst and as an alkali-metal ion exchange material.[194] $K_4Nb_6O_{17}$ has also shown to be electrochemically active with Li and K charge carriers.[208,209]

Table 6.1: The unit cell parameters for $K_4Nb_6O_{17}$ and its reported hydrated forms.

Properties	$K_4Nb_6O_{17}$	$K_4Nb_6O_{17} \cdot 3\,H_2O$	$K_4Nb_6O_{17} \cdot 4.5\,H_2O$
Crystal system	Orthorhombic	Orthorhombic	Orthorhombic
Space group	*P21nb*	$P22_12_1$ (or $P22_12$)	$P22_12_1$ (or $P22_12$)
a / Å	7.83(3)	7.85(1)	7.82(1)
b / Å	33.21(10)	37.67(10)	41.09(10)
c / Å	6.46(3)	6.46(1)	6.42(1)
ICSD cif code	35035	-	-
Reference	[210]	[211]	[211]

Discrepancies in literature regarding $K_4Nb_6O_{17}$

Anhydrous $K_4Nb_6O_{17}$ has been referenced many times in literature with various XRD patterns, the XRD patterns uploaded to the PDF 4+ database also show significant variation (00-014-0287, 00-031-1064, 00-031-1064,0-053-0780, 04-009-6408 and 00-021-1295). Unfortunately this has created a situation in which a range of XRD patterns have been assigned to one structure ($K_4Nb_6O_{17}$), often without acknowledgement of other reported $K_4Nb_6O_{17}$ phases, which often exhibit similarities in the XRD pattern. Furthermore, the XRD pattern used to confirm the phase of the product is not explicitly stated in many publications.[195,206,212] There is a cif for $K_4Nb_6O_{17}$ (ICSD cif code: 35030) which has been widely accepted within the community, however care should be taken when reading papers about $K_4Nb_6O_{17}$ to study the XRD patterns presented.

6.2 Method

The two-step synthesis was adapted from X. Kong *et al.*[202] the first step produces a Lindqvist salt, and the second step produces a potassium niobate. There are also many alternative methods of synthesis *via* Lindqvist salt that has been reported.[201,213]

Step 1 of Lindqvist synthesis:

2.5 g of Nb_2O_5 (99.9 %, Thermo Scientific Chemicals) was added to 15 mL KOH solution (3 mol L^{-1}, Extra Pure, Pellets, Fisher Chemical) and stirred for 30 mins. The slurry was then poured into a Teflon-lined autoclave with an internal volume of 45 mL, and heated 230 °C for 2 h. The mixture was filtered and the clear filtrate was added to 200 mL ethanol under stirring conditions to form a white precipitate. The potassium hexaniobate precipitate was filtered, washed with ethanol (95 % v/v, Extra Pure, SLR, Fisher Chemical), and then dried overnight at room temperature and pressure.[195,202]

Step 2 of Lindqvist synthesis:

Under constant stirring, 0.25 g of potassium hexaniobate salt and 15 mL of the water-ethanol mixed solvent were combined. The pH of the mixture was adjusted to a desired pH value with a 1.0 mol HCl solution (Thermo Scientific Chemicals), or KOH was added into the solution to adjust to a desired KOH concentration. After adjusting the pH or KOH concentration, the mixture was poured into a Teflon-lined autoclave with an internal volume of 45 mL and heated to either 200 °C or 230 °C for variable time periods. The synthesis procedure was also scaled up when using an autoclave with an internal volume of 125 mL. After heating, the product was filtered and dried overnight at room temperature and pressure.[202]

Varying synthesis conditions

Various synthesis conditions were tested in this study which are outlined in Table 6.2. The temperature and heating duration has a large impact on the species formed, and

can be used to probe intermediates or to form a more crystalline material. The water and ethanol affects the degree of solvation of the niobium containing species. The pH affects the degree of potassium available as a reagent and also was found to affect crystallinity.

Table 6.2: Synthesis conditions used in part two of the Lindqvist synthesis study.

Variable	Experiment One	Experiment Two	Experiment Three
Ratio of H_2O:ethanol by volume	1:1	1:2	1:2
Temperature /°C	200	230	230
Heating duration /hrs	12	12	1-12
Addition of KOH or HCl	KOH (0.1-0.3 M)	HCl (pH 2-6)	HCl (pH 5-6)

6.3 Results and discussion

6.3.1 Structural characterisation of the Lindqvist salt

XPDF

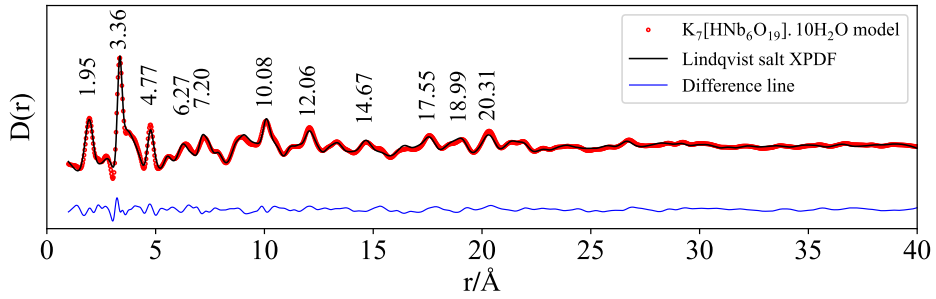


Figure 6.4: Pair distribution function collected from I15-1 (λ = 0.161669 Å) of the Lindqvist salt product with labelled r values in Å, with a small box refinement against $K_7[HNb_6O_{19}] \cdot 10\,H_2O$.

Table 6.3: Peaks identified in the XPDF of Lindqvist salt of this study and their assignment based on the reported structure of $K_7[HNb_6O_{19}] \cdot 10\,H_2O$ (ICSD: 391372), compared to the assignments made by O.G. Grendal *et al.*[214] based on their XPDF of Lindqvist salt containing NH_4^+ ions.

Assignment by this study			O.G. Grendal *et al.*[214]	
Peak location / Å	Reported distance / Å	Assignment	Peak location / Å	Assignment
1.94	2.01	direct Nb to O bond	1.9	Nb-O
3.36	3.35	Edge sharing Nb-Nb	3.3	Edge sharing Nb-Nb
3.74	3.88	O to O distance	3.7	Edge sharing Nb-Nb
4.77	4.77	Corner sharing Nb - Nb	4.7	Corner sharing Nb-Nb
6.39	6.55	Nb to O†	-	-
7.23	7.10	Nb-Nb distance*	-	-
10.08	10.02	Nb-Nb distance*	-	-

† Nb to furthest oxygen in a line: Nb-O-Nb-O where Nb are corner shared i.e. Nb5-O14. *between different niobium clusters

The PDF of the Lindqvist salt collected in this study is consistent with the study by O.G. Grendal *et al.*[214] on a Lindqvist salt containing NH_4^+ ions (Table 6.3).

Both studies report similar peak locations that matches the reported structure of $K_7[HNb_6O_{19}] \cdot 10\,H_2O$ (ICSD: 391372) (Table 6.3 and Figure 6.4). They also reported no correlation beyond 8 Å, however in this study this occurred at 25 Å and beyond, indicating that the synthesised Lindqvist salt has a longer range order than the phase synthesised by O.G. Grendal *et al.*[214] but shorter range order than the reported crystalline $K_7[HNb_6O_{19}] \cdot 10\,H_2O$. Therefore the local structure is consistent with the presence of the Lindqvist ion.

This is further supported by XPDF refinement of the Lindqvist salt of this study modelled using $K_7[HNb_6O_{19}] \cdot 10\,H_2O$ (ICSD: 391372) (Figure 6.4). This results are summarised in Table 6.4 which shows a good agreement with the reported values of $K_7[HNb_6O_{19}] \cdot 10\,H_2O$.

Table 6.4: Refinement results of Lindquist salt compared to tthe reported structure of $K_7[HNb_6O_{19}] \cdot 10\,H_2O$ (ICSD: 391372).

Parameter	$K_7[HNb_6O_{19}] \cdot 10\,H_2O$ ICSD: 391372	Small box XPDF	Rietveld XRD
r_{wp} / %	-	20.13	10.51
a / Å	17.300(2)	17.390(9)	17.349(12)
b / Å	10.1263(14)	10.151(6)	10.049(7)
c / Å	35.203(5)	35.20(2)	35.14(3)
β / °	103.676(2)	103.78(6)	103.73(7)
`spherical_damp`	-	37.7(8)	-

XRD

The XRD pattern (Figure 6.5.a.) shows a good fit to $K_7[HNb_6O_{19}] \cdot 10\,H_2O$ (ICSD: 391372, space group *C2/c*) in Figure 6.5.b. and provided a r_{wp} of 10.51 %. The high intensity peak at 1.08 2θ ($\lambda = 0.161669$) corresponds to d_{040} of 8.57 Å. The refined parameters are in good agreement with the reported values.

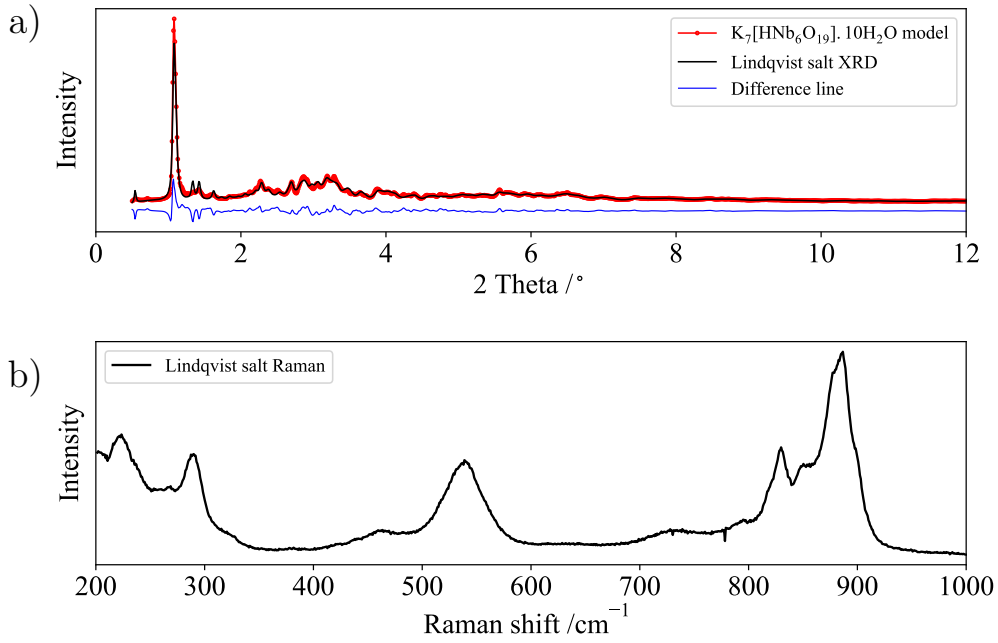


Figure 6.5: Results from structural analysis of the Lindqvist salt. a) XRD pattern collected on I15-1 (λ = 0.161669 Å) with a refinement against $K_7[HNb_6O_{19}] \cdot 10\,H_2O$. b) Raman spectra.

Raman

The Raman spectrum (Figure 6.5.b.) shows broad bands indicating poorly defined environments. The Raman spectra of potassium Lindqvist salts has not been previously reported in the literature. However, the band positions and intensities mostly match those reported by H. Tong *et al.*[201] (Table 6.5) of another Lindqvist salt $Na_7(HNb_6O_{19}) \cdot 15\,H_2O$, with the exception of bands at 776 cm^{-1} and 830 cm^{-1} which which are stronger in this study and corresponds to the short Nb-O bond in NbO_6 octahedra units.[177] H. Tong *et al.*[201] who observed a band at 902 cm^{-1} which is shifted to 982 cm^{-1}, this increase in wavenumber indicates the short Nb=O bond that protrudes into the interlayer is shorter and therefore the octahedra are more distorted. The difference in wavenumber can be attributed to the difference in interlayer ions of H. Tong *et al.* and of this study (Na and K, respectively).

Table 6.5: Peaks identified in the Raman specta compared to the Raman spectra of $Na_7(HNb_6O_{19}) \cdot 15\,H_2O$ as identified by H. Tong of *et al.*[201]

This study		H. Tong *et al.*[201]		
Band / cm^{-1}	Intensity	Band / cm^{-1}	Intensity*	Species
224	medium	214	medium	T2g
290	medium	280	medium	A1g
464	weak	460	very weak	T2g
-	-	492	very weak	A1g
539	medium	531	weak	Eg
776	strong	766	very weak	Eg
830	strong	832	weak	Eg
987	strong	902	strong	A1g

* Intensity interpreted by Rachel (Wai Chi) Tang, author of this study, from their Raman spectrum.

Summary

In summary, the Lindqvist salt synthesised is a match to the reported phase $K_7[HNb_6O_{19}] \cdot 10\,H_2O$ (ICSD: 391372) as determined by XRD and XPDF by a low r_{wp} and refined lattice parameters that are in agreement with the reported values. Raman and XPDF comparisons with other Lindqvist salt studies also support this.

6.3.2 Variable molarity of KOH

Method

The second step of Lindqvist synthesis was performed using the aforementioned Lindqvist salt. The concentration of KOH was varied from 0.1 M to 0.3 M alongside the conditions outlined in Table.6.6. X. Kong *et al.*[202] did not attempt to characterise these phases which showed interesting XRD patterns with broad background and a few sharp peaks.

Table 6.6: Synthesis conditions

Variable	Conditions used
Ratio of H_2O:ethanol by volume	1:1
Temperature /°C	200
Heating duration /hrs	12
Addition of KOH or HCl	KOH (0.1-0.3 M)

Results

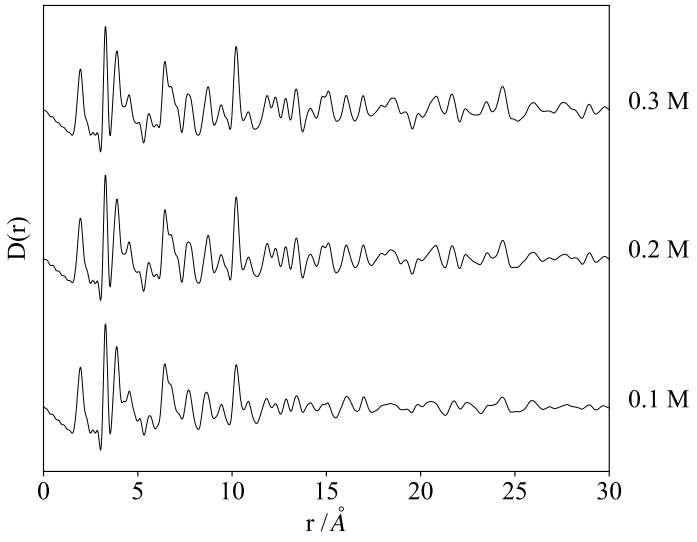


Figure 6.6: Pair distribution functions collected on I15-1 ($\lambda = 0.161669$ Å) of Lindqvist synthesis products made by varying the concentration of KOH.

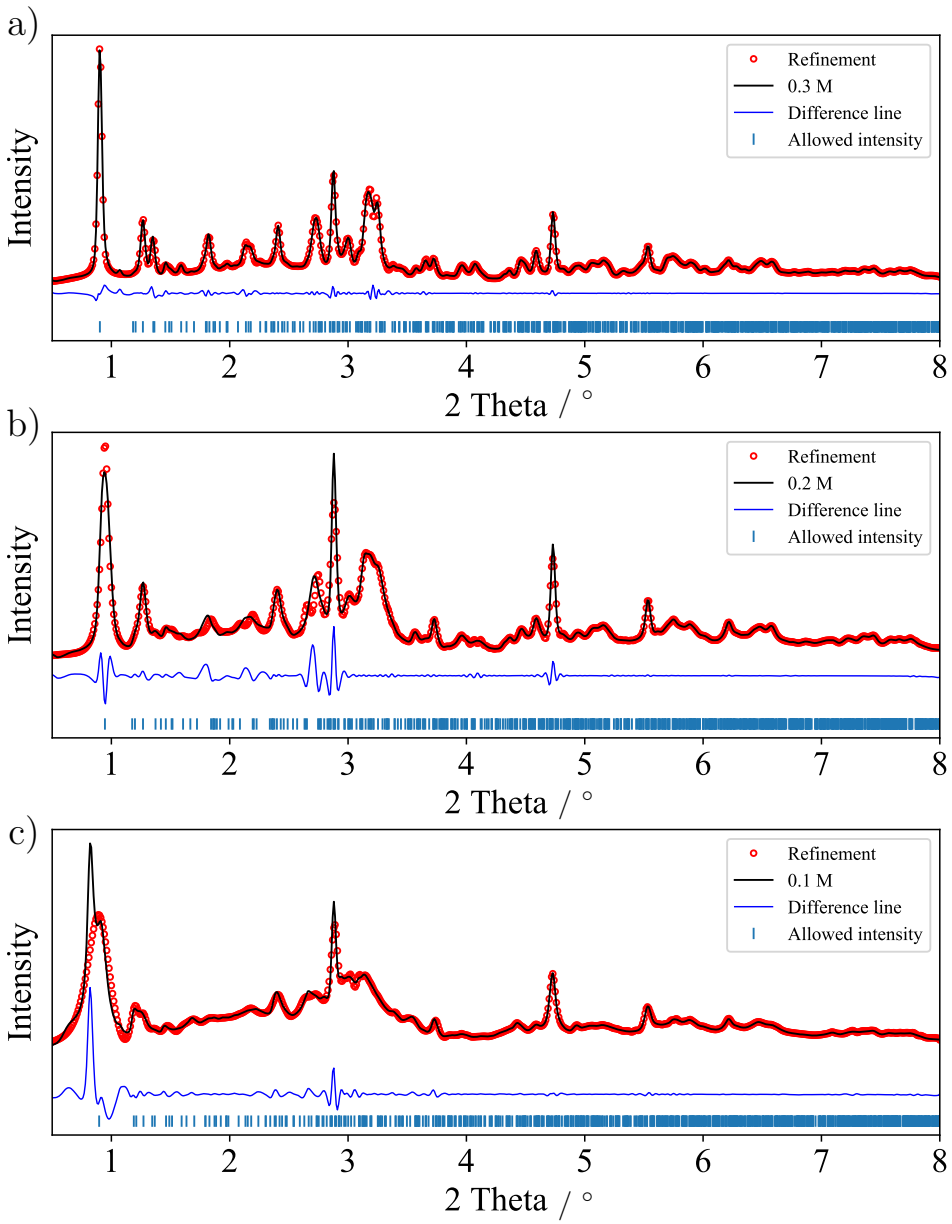


Figure 6.7: XRD collected on I15-1 (λ = 0.161669 Å) of Lindqvist synthesis products made by addition of KOH, Pawley fitted using the starting parameters obtained from $K_4Nb_6O_{17} \cdot 4.5\,H_2O$ (ICSD: 00-021-1297).

The peaks in the PDF show very similar peak positions, which indicate similar local connectivity. At low r, the peak intensities are also similar, although a slight reduction for the 0.1 M, this largely indicates there is a similar degree of local order. At high r, differences in damping become apparent and as the concentration of KOH decreases, the crystallinity of the structure also decreases (Figure 6.6). This loss of crystallinity can also be deduced from the broader peak widths in the XRD (Figure 6.7).

The XRD pattern shows more peaks than the XRD patterns reported by X. Kong *et al.*[202] This could be due to a different sized autoclave being used or the presence of an unidentified impurity phase.

Table 6.7 shows the results from the Pawley refinement (Figure 6.7) performed using the reported parameters of $K_4Nb_6O_{17} \cdot 4.5\,H_2O$ as the starting parameters. The calculated lattice parameter b is determined by the position of the d_{040} peak (at $< 1\,^\circ$ 2θ) (Figure 6.7). The d_{040} appears at 10.30 Å (0.3 M) and then shifts to 9.84 Å (0.2 M). The 0.1 M sample shows two peaks in that region, one at 10.30 Å and 11.26 Å. Therefore, the 0.1 M product could contain two distinct phases, one of which is the same phase as that synthesised using 0.3 M as deduced by the same d_{040} peak and similar XRD pattern.

Table 6.7: Results of Pawley fitting the XRD patterns collected from products synthesised *via* the Lindqvist ion to $K_4Nb_6O_{17} \cdot 4.5\,H_2O$ (00-021-1297).

Properties	0.1 M	0.2 M	0.3 M	$K_4Nb_6O_{17} \cdot 4.5\,H_2O$
r_{wp}/ %	9.42	6.75	3.26	-
Space group	*P22$_1$2$_1$*	*P22$_1$2$_1$*	*P22$_1$2$_1$*	*P22$_1$2$_1$*
a / Å	7.79(6)	7.88	7.83(8)	7.82(11)
b / Å	41.27†	39.185(5)	41.05(4)	41.09(6)
c / Å	6.42	6.47(10)	6.44(10)	6.42(13)
d_{040} / Å	10.30†	9.84	10.30	-

† larger b parameter (i.e. 44.101886 Å) is obtained if the refinement fit the sharper peak on the left at $d_{spacing}$ of 11.26 Å.

The 0.3 M phase shows a high agreement to the reported powder pattern for $K_4Nb_6O_{17} \cdot 4.5\,H_2O$. It is also very similar to the PXRD pattern presented by Y.

Ma *et al.*[215] which was also assigned to $K_4Nb_6O_{17} \cdot 4.5\,H_2O$. M. Bizeto *et al.*[204,206] reports the d_{040} of $K_4Nb_6O_{17} \cdot 4.5\,H_2O$, $K_4Nb_6O_{17} \cdot 3\,H_2O$ and anhydrous $K_4Nb_6O_{17}$ to be 10.27 Å, 9.48 Å and 8.08 Å respectively. This supports the assignment of $K_4Nb_6O_{17} \cdot 4.5\,H_2O$ for 0.3 M and suggests a $K_4Nb_6O_{17} \cdot nH_2O$ where $3 < n < 4.5$ for the product synthesised using 0.2 M KOH. However, the very sharp peak observed in the 0.1 M product at $d_{040} = 11.26$ Å is even larger than the expected d_{040} for $K_4Nb_6O_{17} \cdot 4.5\,H_2O$, therefore the phase of this structure is not clear. Yet, the presence of a peak at 10.30 Å could suggest the presence of $K_4Nb_6O_{17} \cdot 4.5\,H_2O$-like phase.

Unfortunately the structures of $K_4Nb_6O_{17} \cdot 4.5\,H_2O$ and $K_4Nb_6O_{17} \cdot 3\,H_2O$ are not known and therefore further Rietveld refinement, or small box analysis using PDF is not possible without significant work to solve the atomic positions.

Changing the concentration of KOH, lead to little change in the product produced. This could be due to the excess of K within the salt $K_7[HNb_6O_{19}] \cdot 10\,H_2O$, and therefore further addition minor changes in KOH concentration does not significantly alter the stoichiometry of K and Nb in solution. Therefore, the increase in the d_{040} spacing as you increase KOH concentration is theorised to be caused by a change in pH of the solution, affecting the arrangement of the cations, K^+ and/ or H^+.

From this study, it is clear that lowering the pH leads to decreased crystallinity in the sample. Therefore, the addition of HCl, as opposed to KOH, was explored.

6.3.3 Variable pH using HCl

Method

To further probe the effect of pH, HCl was added to obtain pH values between 2-6, (Table 6.8). In addition to pH, the water:ethanol ratio, and temperature we also varied: Kong et al,[202] reported the synthesis of KNb_3O_8 in the conditions: 1:2 ratio of H_2O:ethanol, pH 5.5 at 230 °C. The synthesis of nanostructured KNb_3O_8 *via* a "bottom up" process is an interesting comparison to the exfoliated/restacked material outlined in Chapter 4.

Table 6.8: Synthesis conditions

Variable	Conditions used
Ratio of H_2O:ethanol by volume	1:2
Temperature /°C	230
Heating duration /hrs	12
Addition of KOH or HCl	HCl (pH 2-6)

Results

Decreasing the pH decreases the crystallinity of the product (Figure 6.8) as determined by the absence of Bragg peaks in the XRD at low pH and also damping in the PDF. Therefore in this HCl system, pH can be used to control the coherence length of structure. At low pH, no Bragg peaks are observed, consistent with an amorphous product. This means the structures are unlikely to have defined within-layer correlations and may contain a range of Nb connectivities and structures. This result also shows the tunability of this system which can aid future material design.

The products made at pH 5.21 and 5.65 have Bragg peaks. Some of these, at 0.947 °, 2.88 ° and 4.73 ° 2θ (Q = 9.77 Å, 3.22 Å and 1.95 Å respectively) are relatively sharp, similar to what was observed for the exfoliated/restacked materials. Given this promising XRD pattern, these materials were studied in more detail.

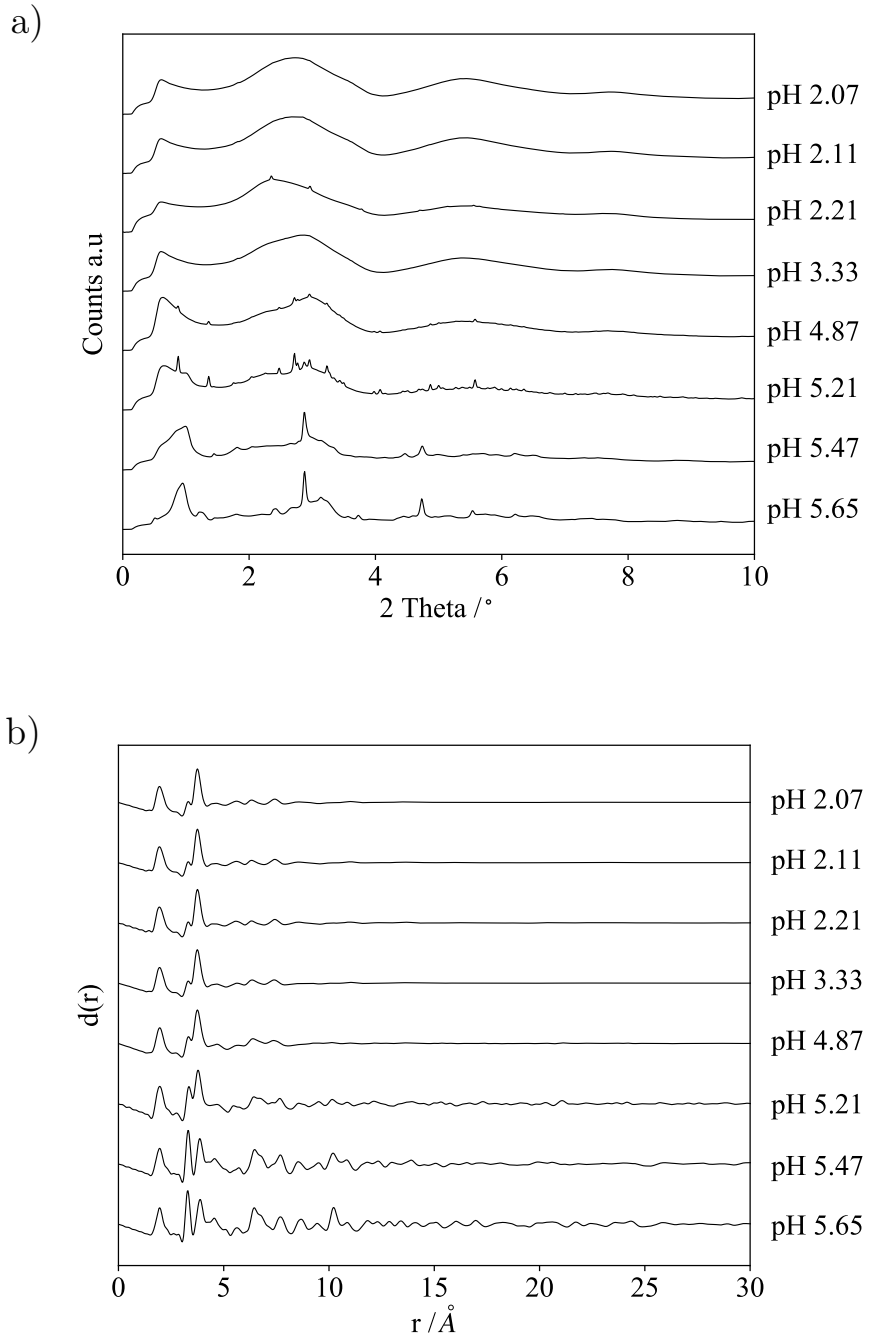


Figure 6.8: X-ray scattering data (collected on I15-1, $\lambda = 0.161669$ Å) from a range of hydrothermally synthesised products which was acidified to a range of pH. a) XRD patterns. b) Pair distribution functions.

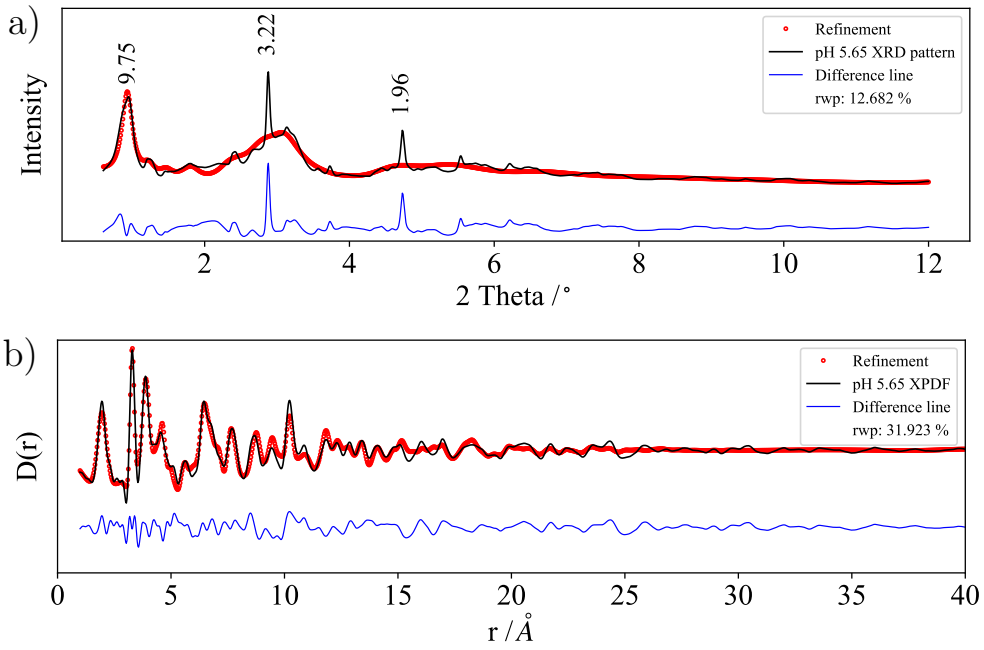


Figure 6.9: Rietveld refinement on x-ray scattering data (collected on I15-1, λ = 0.161669 Å) of the sample synthesised at pH 5.65. a) XRD fitting to $K_4Nb_6O_{17}$ with d-spacing labels b) PDF fitting to $K_4Nb_6O_{17}$.

The product synthesised at pH 5.65 shows a local connectivity similar to $K_4Nb_6O_{17}$ as shown by XPDF Rietveld refinement (Figure 6.9.b.) up to around 20 Å. The Rietveld refinement of the product synthesised at pH 5.65 against $K_4Nb_6O_{17}$ (*P21nb*, ICSD: 35030) gave a poor result, considerably due the discrepancy in intensity at 3.22 Å and 1.96 Å. Therefore this product is similar to $K_4Nb_6O_{17}$ at a local scale, however shows significantly different long range order than expected.

The presence of both sharp and broad peaks is suggestive of a disordered layer structure, especially as the first peak corresponds to the d_{040}, indicative of the interlayer distance in the stacking direction. Due to the similarities in the XRD pattern and XPDF, in addition to synthesis conditions, the material produced at pH 5.65 is theorised to be nanostructured $K_4Nb_6O_{17}$ which is characterised further in Section 6.3.5.

Table 6.9: Results of small box refinements performed on the XRD and PDF data collected on samples synthesised at pH 5.21 and pH 5.65.

Parameter	pH 5.21		pH 5.65	
	PDF	XRD	PDF	XRD
Model	KNb_3O_8	KNb_3O_8	$K_4Nb_6O_{17}$	$K_4Nb_6O_{17}$
r_{wp}/ %	39.55	3.02	31.92	12.68
a / Å	8.731(18)	8.919(2)	7.863(5)	8.13(3)
b / Å	20.52(4)	21.1670(6)	32.85(3)	39.77(9)
c / Å	3.825(6)	3.8060(9)	6.473(5)	5.94(2)
`spherical_damp`	7.63(16)		16.2(3)	

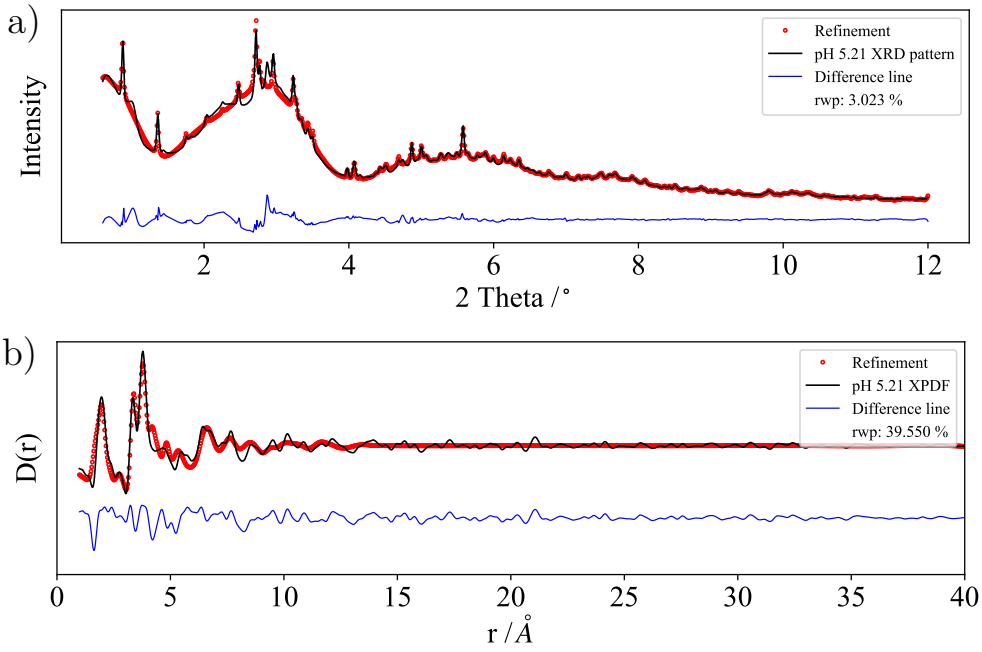


Figure 6.10: Rietveld refinement on x-ray scattering data (collected on I15-1, λ = 0.161669 Å) of the sample synthesised at pH 5.21. a) XRD fitting to KNb_3O_8 b) PDF fitting to KNb_3O_8.

The product synthesised at pH 5.21 shows a good fit to KNb_3O_8 in the Bragg data (Figure 6.10.a. and Table 6.9), albeit on a significantly high background, which suggests the significant presence of an amorphous material in addition to the crystalline KNb_3O_8 (Figure 6.10.a). There also appears to be the presence of a minor impurity phase as peaks at 1.00 °, 2.87 °, 4.74 ° 2θ (corresponding to 1.95 Å, 3.23 Å and 9.28 Å).

The XPDF showed a suitable fit to KNb_3O_8 at low r, indicating local connectivity similar to KNb_3O_8. However at high r the intensities do not match, this could be

due to the presence of the impurity phase. Therefore this sample is most likely a sample containing highly disordered amorphous phase, small nanoparticle sized regions of crystalline KNb_3O_8 and a minor impurity phase.

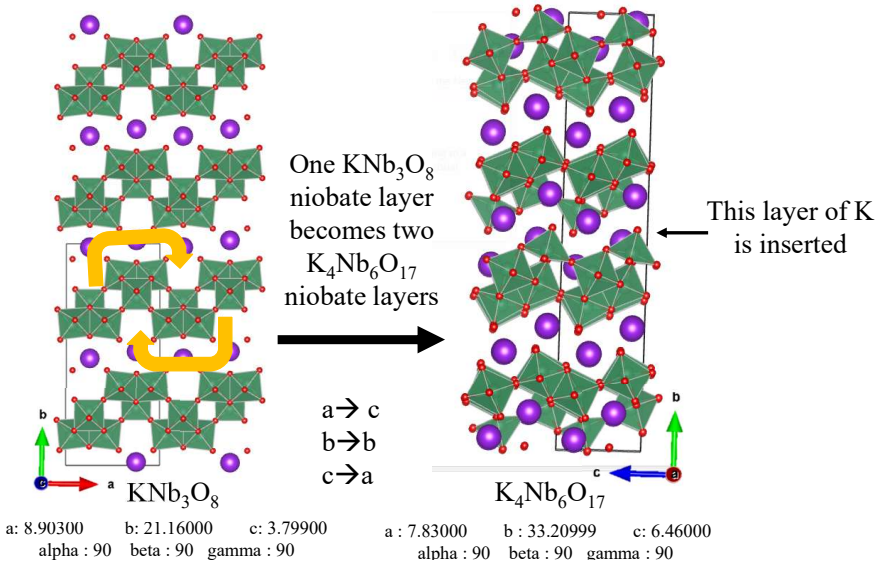


Figure 6.11: Hypothesised mechanism regarding the phase transformation from KNb_3O_8 to $K_4Nb_6O_{17}$.

During this study, the synthesis of KNb_3O_8 is delicately intertwined with $K_4Nb_6O_{17}$ with a slight change of pH. In the Lindqvist synthesis, a precipitate is observed immediately after adding HCl which at high alkalinity redissolves. However under acidic conditions, the precipitates are stable and then heated. As the pH of synthesis for KNb_3O_8 requires more HCl than $K_4Nb_6O_{17}$, it can be assumed the precipitate precursor for $K_4Nb_6O_{17}$ is able to convert into the KNb_3O_8. This study proposes a phase change mechanism between these two phases in Figure 6.11, the $[NbO_6]$ octahedra rotate along the [001] axis (in KNb_3O_8), coupled with the insertion of an additional interlayer cation layer, splitting a single KNb_3O_8 layer into two $K_4Nb_6O_{17}$ layers. This requires additional potassium and oxygen ions to form $K_4Nb_6O_{17}$ from KNb_3O_8. However, when viewed along the [100], it is not obvious how the niobate atoms rearrange, and therefore more work is required to visualise this phase transformation.

An alternative method of understanding this relationship is to view the phase trans-

formation in reverse, this might be easier to understand and therefore has been included in this thesis (Figure 6.12).

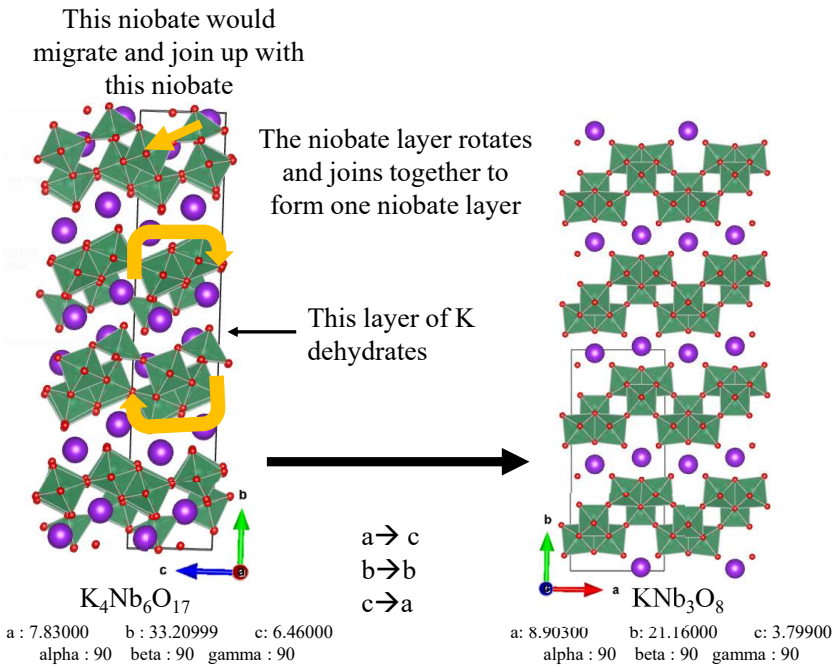


Figure 6.12: Hypothesised mechanism regarding the phase transformation from $K_4Nb_6O_{17}$ to KNb_3O_8.

Summary

Therefore, in summary, at pH 5.65 a $K_4Nb_6O_{17}$-like sample is synthesised and at pH 5.21 a KNb_3O_8 containing sample is synthesised. J. F. Liu *et al.*[197] reported a more alkaline solution is required to form K_4NbO_{17} compared to KNb_3O_8 which is consistent with what is observed in this study. This suggests the mechanism between conventional hydrothermal synthesis and hydrothermal synthesis via Lindqvist salt is similar.

In solution, the protons likely solvate the niobate ions, however a higher concentration of protons will lead to larger solvation shells and therefore larger distances between niobate ions which could cause the observed smaller particle sizes as determined by the increased damping in the XPDF (Figure 6.8). However further work is required to prove this theory.

The phase formed at pH 5.65 was studied further as it appeared to be disordered. Most of the same conditions were used, except the heating duration. Shorter heating was explored to determine whether a slightly more disordered, more phase pure sample could be obtained. $K_4Nb_6O_{17}$ has been shown to be electrochemically active and therefore is also of interest for sodium-ion anode applications.

6.3.4 Variable heating duration

Method

In addition to achieving a higher phase purity, a shorter synthesis time would also increase the rate of production and reduce heating costs which leads to greener production, if ever implemented at an industrial scale (Table 6.10).

Table 6.10: Synthesis conditions

Variable	Conditions used
Ratio of H_2O:ethanol by volume	1:2
Temperature /°C	230
Heating duration /hrs	1-12
Addition of KOH or HCl	HCl (pH 5-6)

Results

The XRD and XPDF shown in Figure 6.13 are similar to that of Figure 6.9 which was assigned to a $K_4Nb_6O_{17}$-like structure. After the short heating duration of 1 hr, there are sharp peaks in the XRD (Figure 6.13.a.) and significant intensity in the XPDF (Figure 6.13.b.). As synthesis time increases, damping in XPDF decreases indicating larger particle sizes, which is commonly observed trend in many solid state synthesis systems. The increase in crystallinity is reflected in the sharpening of Bragg peaks too (Figure 6.13.a.).

Some of the minor peaks in the 1 hr product appear to be related reflections: 1.60 Å, 3.29 Å and 6.62 Å as they are loosely, a factor of the larger values (Table 6.11). The three strongest peaks in the 1 hr product (1.67 Å, 2.74 Å and 9.75 Å in Figure 6.13.a.) could also be argued to all disappear at the same time, although due to the similarities in peak shape and relative peak intensities to the other products, it is likely peaks shifts to higher d-spacings are occurring. This indicates the distance between lattice planes are increasing. The peak at 9.75 Å is broader and could be the stacking direction.

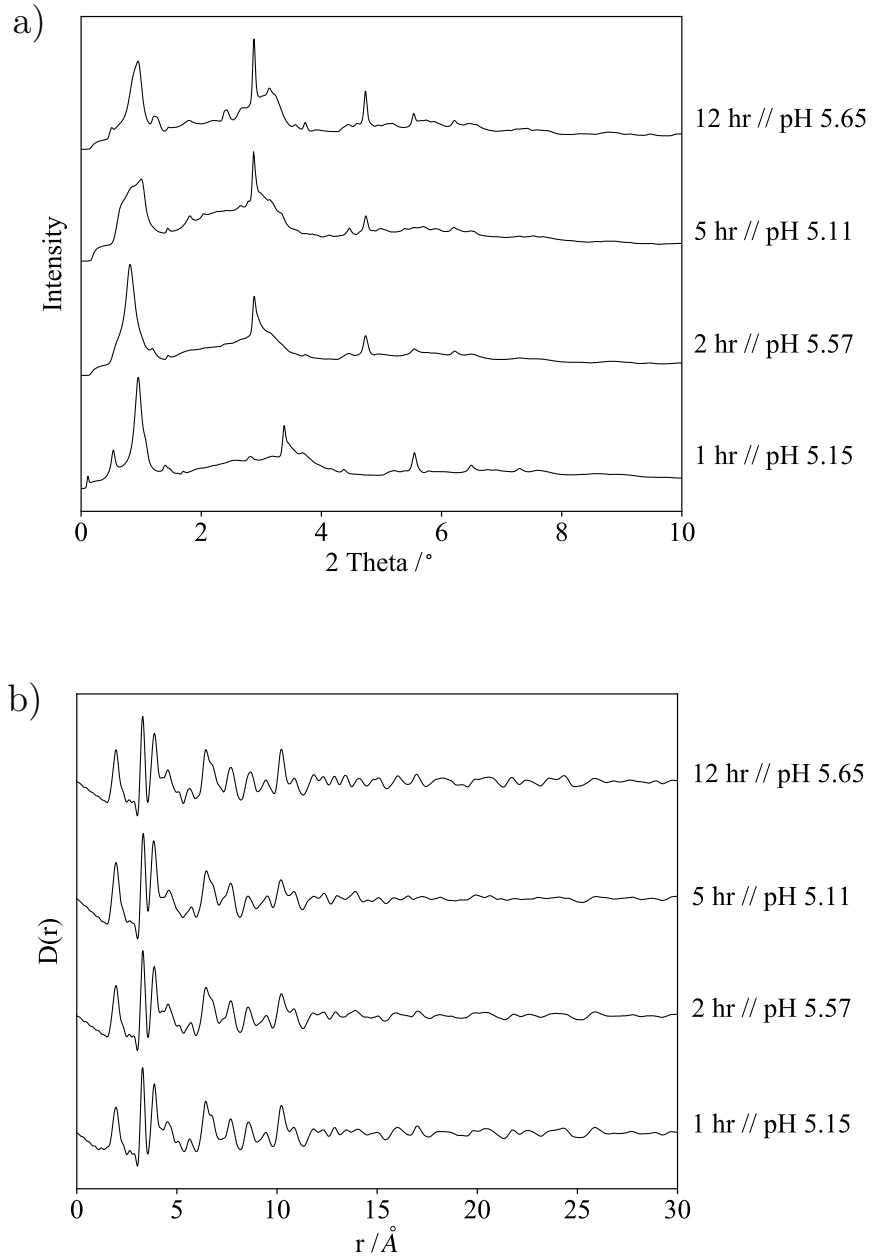


Figure 6.13: X-ray scattering data collected on I15-1 ($\lambda = 0.161669$ Å) from a range of hydrothermally synthesised products form *via* the Lindqvist intermediate which was acidified to pH 5-6 and heated for 1-12 hrs. a) XRD patterns. b) Pair distribution functions.

The sample at 2 hrs appears most phase pure as less minor peaks are observed in the XRD pattern. The other samples likely contain additional phases, and/ or are of a lower symmetry which create the additional peaks (Table 6.11).

Table 6.11: Peaks identified in the XRD pattern of samples synthesised at pH 5-6 for a varied duration given as d-spacings in units of Å. The three most intense peaks have been written in bold font.

1 hr peaks in 2θ	1 hr	2 hr	5 hr	12 hr
0.54	17.31	-	-	-
-	-	**11.30**	-	-
0.95	**9.75**	-	**9.25**	**9.75**
-	-	-	-	7.59
1.40	6.62	6.38	6.43	
-	-	-	5.12	5.12
-	-	-	-	3.83
2.62	3.29	**3.22**	**3.23**	**3.22**
3.38	**2.74**	-	-	2.96
-	-	2.48	-	2.48
4.38	2.12	-	-	-
-	-	2.08	2.07	-
-	-	**1.95**	**1.95**	**1.96**
-	-	-	1.86	-
5.55	**1.67**	1.67	-	1.67
5.79	1.60	-	1.63	-
6.50	1.43	1.49	1.49	1.49
7.29	1.27	1.27	1.23	-

The sample synthesised after 2 hrs appears to be the most pure, therefore this sample was selected for further analysis and study. Sample purity is important during cell testing as the electrochemical properties of the anode will depend on every structure present within the material. Hence, a complex mixture of structures is not desired. Therefore the phase synthesised at 2 hrs was selected for further structural characterisation (discussed in te following section) and then testing within a cell (Chapter seven).

6.3.5 Nanostructured $K_4Nb_6O_{17}$ product

Nanostructured $K_4Nb_6O_{17}$ synthesised following the exact same method used for 2 hr// pH 5.57 (Figure 6.13), in the previous section, using 1:2 ratio of water and ethanol, acidified to a pH of 5-6 and heated for 2 hours at 230 °C, and is the same sample type. The XRD pattern of nanostructured $K_4Nb_6O_{17}$ (Figure 6.17.a.) possesses a mixture of sharp and weak peaks which is similar to the restacked nanostructured material which has been successfully modelled using using a single Nb_3O_8 layer and ONb_3O_8 crystalline phase. The layered $K_4Nb_6O_{17}$. is a reported synthesis product from Lindqvist synthesis, and therefore it has been hypothesised that the nanostructured $K_4Nb_6O_{17}$ phase could be a similarly disordered, single niobate layer form of $K_4Nb_6O_{17}$ Furthermore, there is already evidence that these $K_4Nb_6O_{17}$ nanosheet layers are stable and capable of delaminating. [54,202,212,216,217]

To test this hypothesis, a simulated XRD pattern of a discrete $K_4Nb_6O_{17}$ layer is required which can be achieved by utilising the Debye equation.

Method for simulating XRD pattern of discrete layer:

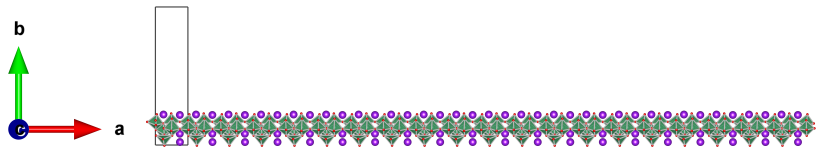


Figure 6.14: A single layer of $K_4Nb_6O_{17}$ which is 20 units long in the a and c direction, and 0.25 unit cells high in b. The [NbO_6] unit in green tetrahedra with red vertices and K ions in purple. The grey box shows the outline of one unit cell.

Using VESTA and the cif of $K_4Nb_6O_{17}$ (ICSD cif code: 35035), a single $K_4Nb_6O_{17}$ layer (Figure 6.14) was produced by modifying the unit cell boundaries. Relative to the unit cell, a and c were 20 unit cells and in b (stacking direction) it was limited to 0.25 of the unit cell which is equal to one layer. The pro-

gram *Debyer* was used to generate the XRD pattern based on the model using the code: `debyer -xray -from=5 -to=80 -step=0.01 -lambda=1.54056 -output K4Nb6O17_20_025_20.dat K4Nb6O17_20_025_20.xyz`. The resulting simulated XRD was plotted against the experimentally obtained XRD pattern (Figure 6.17.a.).

Results

There is a high degree of similarity between the simulated (Debyer) and experimental XRD (Figure 6.15), therefore the nanostructured $K_4Nb_6O_{17}$ sample resembles a single niobate layer with similar connectivity as $K_4Nb_6O_{17}$. The niobate layer is approximately 140 Å in *a* and *c* (20 unit cells long) with significant turbostatic disorder between layers.

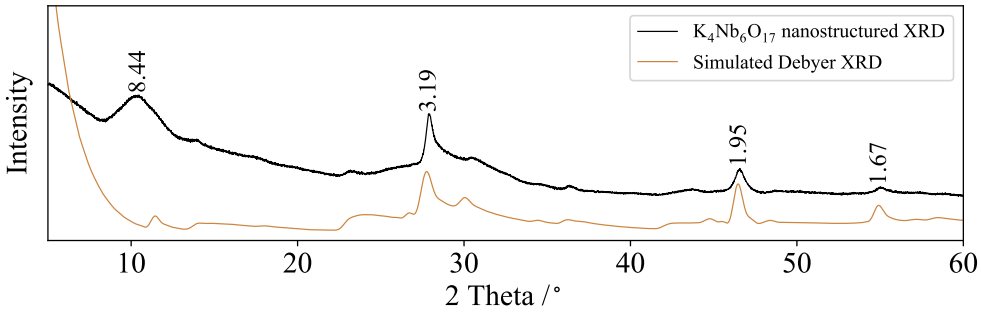


Figure 6.15: XRD pattern of nanostructured $K_4Nb_6O_{17}$ (λ= 1.54056 Å).

The peaks at 8.44 Å, 3.19 Å, 1.95 Å and 1.67 Å have been assigned to the (040), (022), (420) and (402) reflections, respectively (Figure 6.15). In the Debyer generated XRD pattern, the broad (040) peak at 8.44 Å corresponds to the average interlayer distance, and its broad peak width reveals irregularity in the interlayer distance. This interlayer distance suggests that $K_4Nb_6O_{17}$ is mostly anhydrous as M. A. Bizeto[206] studied the interlayer spacing of $K_4Nb_6O_{17}$, $K_4Nb_6O_{17} \cdot 3\,H_2O$ and $K_4Nb_6O_{17} \cdot 4.5\,H_2O$ and provided interlayer values of 8.2 Å, 9.4 Å and 10.1 Å respectively, the additional 0.22 Å compared to anhydrous $K_4Nb_6O_{17}$ can be attributed to disorder in stacking.

This is supported by the XPDF refinement (Figure 6.16) in which a good fit (r_{wp}

of 29.01 %) is achieved by modelling the phase to a single $K_4Nb_6O_{17}$ layer in a large unit cell, similarly to the refinement method used to analyse restacked niobate (Table 6.12). Although a crystalline $K_4Nb_6O_{17}$ phase was introduced at low r, the `shortrange_erf` function refined a value of 2.4 Å, thereby removing the crystalline $K_4Nb_6O_{17}$ contributions from the refinement. The reported lattice parameters for crystalline $K_4Nb_6O_{17}$ are 8.13(3) Å and 5.94(2) Å respectively, therefore the nanostructured $K_4Nb_6O_{17}$ shows a contraction in a and expansion in c by around 0.5 Å. This phenomenon was also observed when comparing restacked niobate to KNb_3O_8 but only by around 0.1 Å.

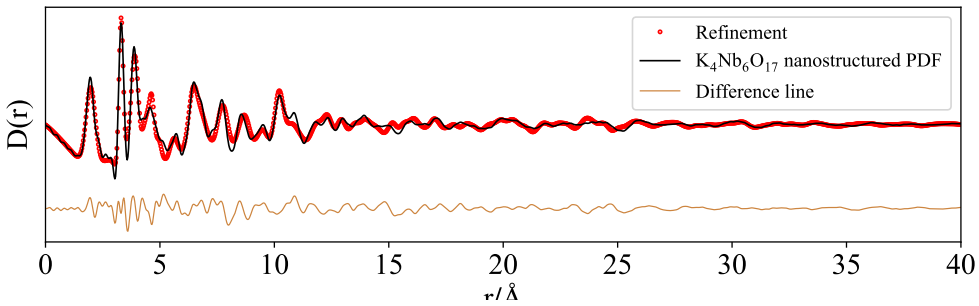


Figure 6.16: Pair distribution function with the small box refinement results of nanostructured $K_4Nb_6O_{17}$.

Table 6.12: Table summarising the results from small box refinement on the XPDF of nanostructured $K_4Nb_6O_{17}$, using a one layered model based on $K_4Nb_6O_{17}$.

Parameter	Refined value
r_{wp} / %	29.01
One layer model a / Å	7.850(4)
One layer model c / Å	6.494(4)
One layer model scale	1.252(16)
`spherical_damping`	33(1)
Nb `beq_low`	0.084(10)
Nb `beq_high`	0.10(5)
O `beq_low`	1.42(10)
O `beq_high`	10.0(5)
`radius`	32(43)

The Raman spectrum (Figure 6.17) shows a band at 642 cm^{-1} which indicates the presence of distorted niobate octahedra. The Raman spectrum of nanostructured $K_4Nb_6O_{17}$ shows similarities to the observations made by M. Maczka *et al.*[184] who studied the

Raman spectrum of $K_4Nb_6O_{17}$ (Table 6.13). Similarities are to be expected because the short range local structure is similar, however there are some discrepancies in the intensities. A significant discrepancy is the the strong band observed in this study at 880 cm^{-1} which is assigned as a weak band to the stretching vibration of short Nb=O bonds by M. Maczka. Additionally, discrepancy of the observed band at 562 cm^{-1} which is not reported by M. Maczka could be due to the difficulties in accurately identifying a wavenumber due to the broadness of the band. The strong bands of $K_4Nb_6O_{17}$ related to Nb=O short bond in the distorted octaherdra are at 905 cm^{-1} and 848 cm^{-1}. However looking more closely at Figure 6.17.c., the asymmetrical peak at 880 cm^{-1} could contain bands at 905 cm^{-1} and 848 cm^{-1}. The difference in shape of this band supports the study performed by J. Souza *et al.* which highlights the six significantly different niobate environments with significant distortion.[194]

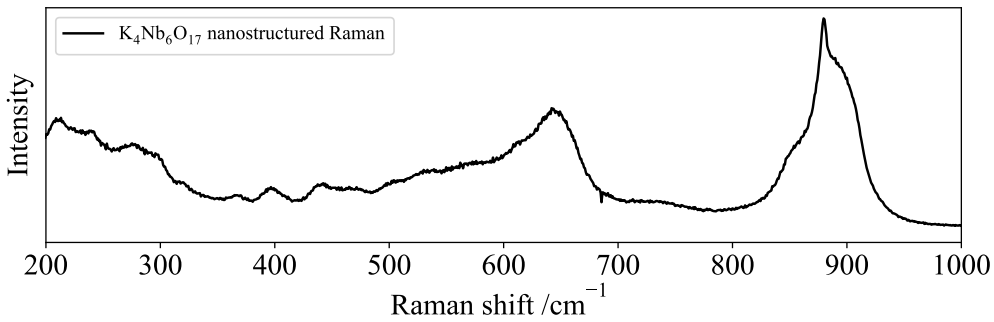


Figure 6.17: Raman spectra of nanostructured $K_4Nb_6O_{17}$.

Microscopy of the sample shows that the particles appear to lack a pre-determined form with a range of sizes (Figure 6.18). High resolution STEM shows areas with stacked layers (Figure 6.18.d.) with ordered atoms within the layer (Figure 6.18.c.). Fourier Transform of Figure 6.18.d. gives an interlayer distance of 8.77 Å which supports the interlayer distance obtained by XRD (8.44 Å).

The SAXS (Figure 6.19) is the linear region of below 10 nm^{-1} which indicates that there are no pores or particles of a consistent size and shape at sizes above 0.628 Å, similarly to the restacked niobate.

Table 6.13: Bands identified in the Raman specta for $K_4Nb_6O_{17}$ by M. Maczka *et al.*[184] compared to the Raman spectra of nanoctructured $K_4Nb_6O_{17}$ collected in this study.

This study		M. Maczka *et al.*[184]		
Band / cm^{-1}	Intensity	Band / cm^{-1}	Intensity	Assignment
213	medium	210	weak	Stretching vib. of NbO_6
275	medium	283	medium	Stretching vib. of NbO_6
397	weak	398	weak	Stretching vib. of NbO_6
442	weak	442	weak	Stretching vib. of NbO_6
562	broad	-	-	-
642	strong	644	medium	Stretching vib. of NbO_6
880	strong	880	weak	Stretching vib. of short Nb=O bonds

Not all peaks observed by M. Maczka *et al.*[184] have been included.
vib. = vibrations

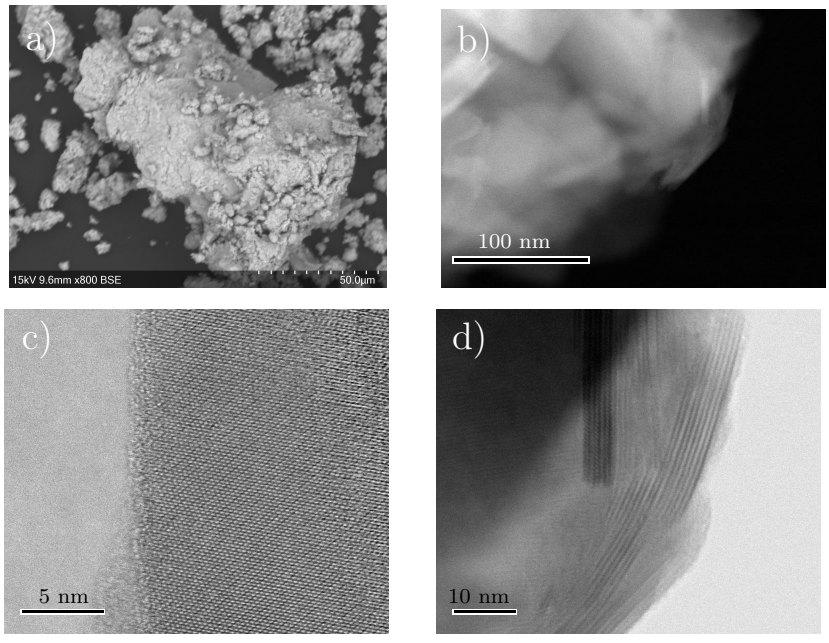


Figure 6.18: Microscopy images of nanostructured $K_4Nb_6O_{17}$ using a) Benchtop SEM b.c.d) High resolution STEM.

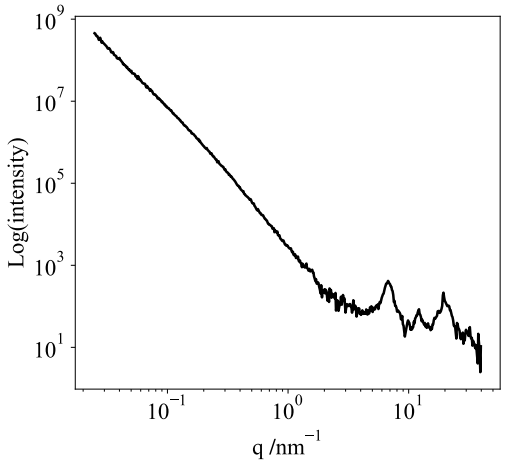


Figure 6.19: SAXS of nanostructured $K_4Nb_6O_{17}$.

6.3.6 Summary: nanostructured $K_4Nb_6O_{17}$

Nanostructured $K_4Nb_6O_{17}$ has not been synthesised before *via* the Lindqvist-ion and its XPDF and XRD pattern has not been identified elsewhere in literature. Nanostructured $K_4Nb_6O_{17}$ is based on a single $K_4Nb_6O_{17}$ niobate layer with significant turbostatic disorder as determined by XPDF using the Debye equation and also using small box refinement methods. This "bottom up" nanostructured $K_4Nb_6O_{17}$ shows a similar type of disorder as the restacked niobate, as shown by the successful modelling in the XPDF. Therefore this method of analysing disordered layered XPDF phases can be utilised on different systems.

The STEM of nanostructured $K_4Nb_6O_{17}$ and the broad (040) reflection in the XRD suggests that there is limited stacking in the *b*-direction. The average interlayer distance is 8.44 Å, with an expansion in *a* and a contraction in *c* compared to crystlline $K_4Nb_6O_{17}$.

Similarly to KNb_3O_8, $K_4Nb_6O_{17}$ has been shown to be photocatalytically active in the evolution of hydrogen from water and as also been studied for its electrochemical properties. Therefore this new type of nanostructuring could benefit those research fields.

The successful small box refinement of nanostructured $K_4Nb_6O_{17}$, indicates that disordered layerd materials of other systems can be probed successfully too. Therefore it is likely that this can also be used on other layered materials, beyond niobates, enabling a deeper understanding of disordered layered materials.

7 Electrochemistry of niobates

7.1 Introduction

7.1.1 The active materials

A range of crystalline and disordered niobates have been explored in this thesis with corresponding structural characterisation. The samples: KNb_3O_8, HNb_3O_8, restacked niobate, hydrothermally nanostructured and nanostructured $K_4Nb_6O_{17}$ have been further studied for their electrochemical properties.

The electrochemical properties of MNb_3O_8 (M = H, Na, Li, K) have been investigated by many groups for applications in a lithium-ion battery,[28,131,133], as detailed in Section 1.5. However, only one group (H. Nakayama *et al.*[143]) has studied MNb_3O_8 within sodium-ion batteries. Their study focused on crystalline HNb_3O_8 and found that not all of the potential niobium redox couples are utilised. Therefore, here we look at the effect of nanostructuring on the achievable capacity, rate capability and long-term cyclability.

7.1.2 Literature background

Under some circumstances involving KNb_3O_8 and HNb_3O_8 an increase in capacity was observed in this study, this goes against capacity fade which is typically observed. Therefore, this observed increase, sparks curiosity and could be a mechanism to maximising cell capacity, which is a constant goal in cell development. This is discussed in further detail in the results Section 7.3. Currently, additional background information is required to facilitate a well rounded discussion.

Why capacity fade is observed

Typically capacity fade occurs as the active material structure becomes less optimal as it ages, this can be due to various factors. At the electrode level, this can be due to volume changes causing electrical isolation from the conductive matrix or a degradation of the coating due to binder instability forming cracks and defects in the coating. At an atomic level within the active material, this could be due to blocked channels or pathways, or defects occurring in the active material destroying the intercalation sites. The SEI layer can also impede diffusion leading to a decrease in capacity as the SEI layer grows thicker. All these effects lead to an observed decrease in capacity as the cell ages, termed capacity fade.

Capacity increase during aging

Capacity increase was observed by B. Gyenes *et al.*[218] within NMC442/graphite cells and proposed that this was due to the cell design. Typically the anode disk is larger than the cathode disk to ensure the cathode is always opposite the anode, even if slightly misaligned, this creates an anode "overhang". In initial cycles at high state of charge, Li-ions are inserted into the overhang region of the graphite anode, followed by diffusion of Li-ions from the overhang regions in the subsequent cycling, therefore causing a slight capacity excess. However the increase in discharge and charge capacity, at 100 % SOC (state of charge) is only 1 and 2 % respectively (Figure7.1).

Table 7.1: Table reproduced from J. Guo *et al.*[219] of various reported mechanisms that could cause an observed increase in cell capacity.

Electrodes	Battery type	Capacity increase %	Mechanism	Ref
NMC/graphite	Pouch cell	1	Diffusion of Li ions from the overhang region of graphite anode	[218]
LFP/graphite	18650	0.4-1.7	Diffusion of Li ions from passive electrode areas	[220]
LFP/graphite	A123 18650	0.25	Loss of negative material change the potentials	[221]
LFP/graphite	Coin cell	1	Loss of negative electrode	[222]
LFP/graphite	100 Wh cells	20†	Non uniform Li-ion distribution is formed under shallow cycling and leads to capacity loss. It can be restored.	[223]

† recovery cycling

Other mechanisms for increasing capacity have been outlined in Table 7.1. Unfortunately all the mechanisms outlined by J. Guo *et al.*[219], show a small increase in capacity, with the exception of Y. Kobayashi*et al.*[223] However their study utilised a shallow state of charge (between 20- 60 %), which is not applicable to this study.

Unfortunately, there are very few papers which have reported an increase in capacity as the cell ages, as this is a rare phenomena. As a result, there is also a lack of understanding around this topic.

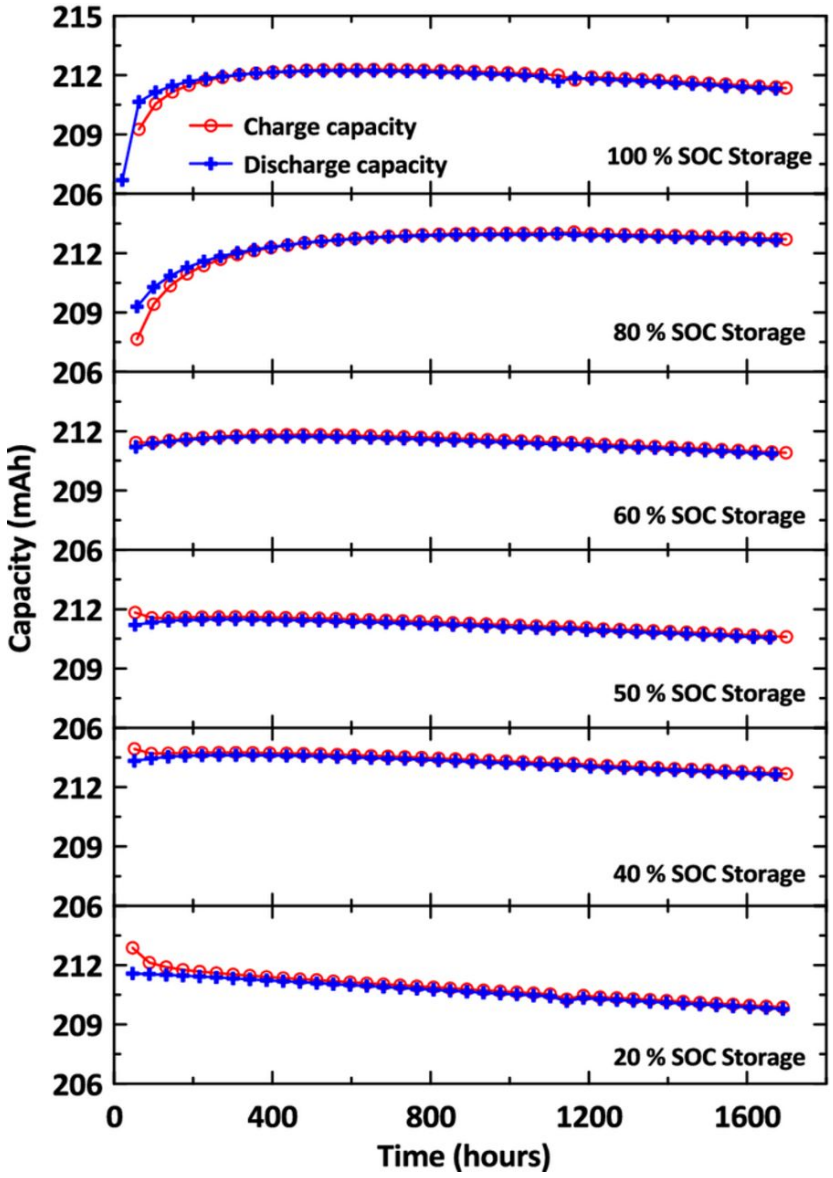


Figure 7.1: Charge and discharge capacities of aged NMC pouch cells stored open circuit for 300 hrs at various SOC in 40 °C. Diagram reproduced from open access journal, originally produced by B. Gyenes *et al.*[218]

7.2 Method

7.2.1 Anode coating

To improve the conductivity of the active material and to also minimise diffusion distances, the active material was mixed with carbon black, and then a binder was used to form a slurry which was cast on aluminium foil. Two binders were tested in this study, CMC and PVDF:

CMC binder

To the best of our knowledge, this is the first study of MNb_3O_8 based coatings made with CMC binder instead of PVDF. A polymer based binder is often used in electrode coatings as the binder enables the formation of a matrix that holds the the active material and carbon together. The dried coating cast on a current collector shows improved flexibility and stability.

Unless otherwise specified, the anode coating contained 70 % active material, 15 % carbon black and 15 % CMC cast onto aluminium at 15 μm thick using a doctor blade. Prior to coin cell assembly in a glovebox, the coating was dried in a vacuum oven at 110 °C overnight and then punched into disks and weighed.

PVDF binder

1 mL of N-Methylformamide (commonly known as NMF*) was added to 45 mg of PVDF which was then mixed with 210 mg of KNb_3O_8 and 45 mg of carbon black. The coating was cast at 15 μm thick and left to dry overnight in the fume hood, then it was dried in a vacuum oven overnight and then punched into disks and weighed.

*the abbreviation NMF is used to represent non-negative matrix factorisation in this thesis

7.2.2 Coin cell assembly

Coin cells were used for all electrochemical testing unless it was associated with an *exsitu* or an *inoperando* experiment. However all cell types utilised the same components unless otherwise specified. In a nitrogen glovebox, cell components were prepared via standard operating procedures as described:

Sodium cubes: (99.9 % trace metals basis, Sigma Aldrich) in mineral oil were washed with cyclohexane. The outer oxidised sodium was removed using a scalpel and then flattened and punched out into circular disks (1/2" diameter).
Whatman Binder-Free Glass Microfiber Prefilters: (Grade GF/D, thickness of 0.67 mm) were used as the separator. They were punched out into circular disks and then dried in a vacuum oven for a week at 110 °C prior to being bought into the glovebox for cell assembly.
Electrolyte: 1 M $NaPF_6$ in EC:DEC (1:1 v/v %) from Kishida was used as the electrolyte throughout this project.

Coin cell parts (CR2032) were manufactured by PI-KEM. Within an Ar filled glovebox, the anode disks (15 mm) was placed, foil side down, onto the center of a coin cell base. The separator was placed on top. The electrolyte (300 μL) was added using a micropippette, then the sodium disk, spacer spring and coin cell lid in that order, forming a centered stack. The coin cell was sealed using a crimping machine. Excess electrolyte was wiped and the cells were removed from the glovebox for cell testing.

7.2.3 Cell cycling

To test the cells in a controlled manner, cells were cycled using an Ivium-n-Stat alongside a uDatasecure module. The software used was IviumSoft to control the cells and collect the results. The cells were cycled between 0.005 V and 2.5 V unless otherwise specified.

Galvanostatic cell cycling

Galvanotstaic cell cycling implies the application of a constant current. The currents used in this study are calculated from the mass of the active material, more specifically mA applied per gram of active material, often written as mAg^{-1}. Rates of 3 mAg^{-1}, 10 mAg^{-1}, 20 mAg^{-1}, 40 mAg^{-1} and 100 mAg^{-1} were used in this study. A negative current was used to induce discharge (sodiation) and a positive current is used to induce charge (desodiation).

Stepped cell cycling

The cells were also sodiated and de-sodiated at rates of 10 mAg^{-1}, 20 mAg^{-1}, 100 mAg^{-1}, 200 mAg^{-1}, 500 mAg^{-1} and 1000 mAg^{-1} for 5 cycles each, sequentially in one coin cell.

Cyclic voltammetry

In this study CV was performed by sweeping voltages between 2.5 V, 0.005 V and back to 2.5 V at scan rates of 0.1 mV/s, 0.2 mV/s, 0.5 mV/s, 2.0 mV/s and 5.0 mV/s, respectively, for one full cycle using coin cells.

7.2.4 Data analysis

All electrochemical data was exported from Iviumsoft software as a text file with 3 columns: current, voltage and time. These text files were processed using specially written python scripts and then plotted for comparison.

7.3 Electrochemical testing

7.3.1 KNb_3O_8

Galvanostatic cycling plots, DCC plots and cyclic voltammetry plots for KNb_3O_8 are shown in Figure 7.2. A respectable second cycle capacity of 161 $mAhg^{-1}$ (2.68 Na^+ per formulae unit of KNb_3O_8) can be achieved by slow cycling (3 mAg^{-1}), shown in in Figure 7.2.a. This is comparable to the results published by H. Nakayama *et al.*[143] with sodiation capacities of 172 $mAhg^{-1}$. However this capacity drops once cycling at a rate of 10 mAg^{-1} to 32 $mAhg^{-1}$ (Figure 7.2.d.), with capacities further diminishing at faster rates. This significant capacity drop (below 50 mAg^{-1}) due to higher rates of charge and discharge is not ideal, especially as the theoretical capacity of KNb_3O_8 is 180 $mAhg^{-1}$ (assuming single redox couple of: Nb^{5+}/Nb^{4+}), therefore a rate of 10 mAg^{-1} is equivalent to C/18 (full charge in 18 hours), which would be considered slow charging for a mobile phone. The low capacities obtained at rates $\geq$ 10 mAg^{-1} remove the viability of these anode materials being used in real world applications.

However at slow rates of 3 $mAhg^{-1}$, the results are much more promising. The Coulombic efficiency (Figure 7.2.c.) is significantly lower for the first cycle than subsequent cycles, as expected due to SEI formation (Figure 7.2.c.). The Coulombic efficiency slowly increases with increasing cycle number, as expected, from second cycle Coulombic efficiency of 89.54 % to 97.86 % on the 14th cycle. As the cell is cycled, the second cycle capacity is 161 $mAhg^{-1}$ which then interestingly increases to 200 $mAhg^{-1}$ after 15 cycles, corresponding to a 25 % capacity increase (Figure 7.2.a.c.). This intriguing phenomena has been observed repeatedly using different batches of KNb_3O_8, coatings and coin cells. Unfortunately, this increase in cell capacity was not observed at these higher rates.

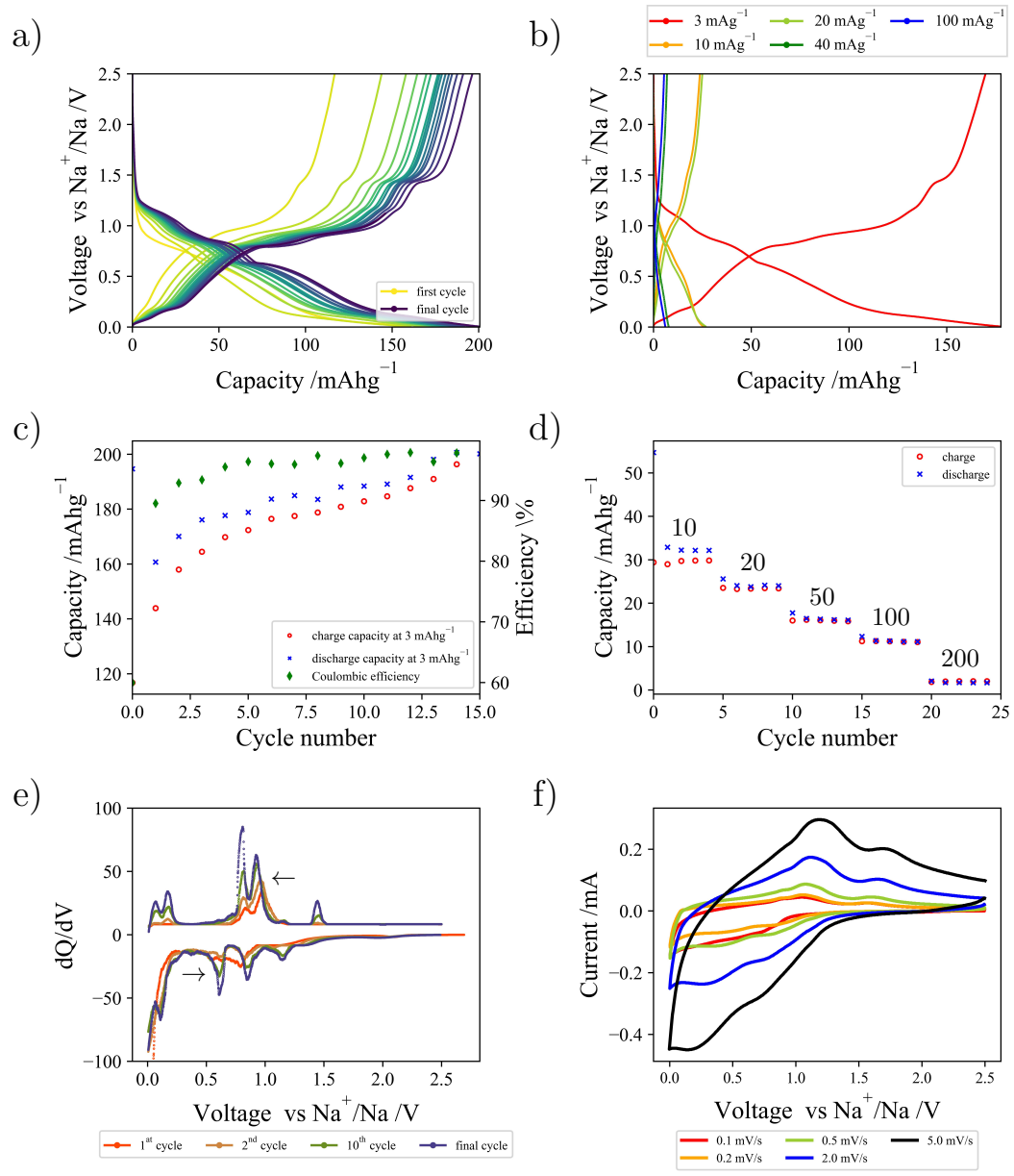


Figure 7.2: Electrochemical cell testing of KNb_3O_8. Cells cycled at 3 mAg^{-1} (left) and cells cycled at variable current or voltage (right) a) At 3 mAg^{-1} b) 5^{th} charge and discharge cycle when cycled at rates of 3 mAg^{-1}, 10 mAg^{-1}, 20 mAg^{-1}, 40 mAg^{-1} and 100 mAg^{-1}. c) Capacity of each cycle at 3 mAg^{-1} d) Cell cycled at 10 mAg^{-1}, 20 mAg^{-1}, 50 mAg^{-1}, 100 mAg^{-1} and 200 mAg^{-1} for 5 cycles each e) dQ/dV plot of cell cycled at 3 mAg^{-1} f) Cyclic voltammetry at sweep rates of 0.1 mV/s, 0.2 mV/s, 0.5 mV/s, 2.0 mV/s and 5.0 mV/s.

The shape of increasing capacity in the initial cycles in Figure 7.2.c. is similar to that observed by B. Gyenes *et al.*[218] (Figure 7.1 at 100 % SOC). However, overhang theory has not been proven to cause such a large increase in capacity, over many cycles. Therefore this is unlikely to be the cause of the observed capacity increase. Furthermore, the observed 25 % increase is significantly higher than those stated in Table 7.1 (around 1 % increase) and therefore the mechanisms proposed in Table 7.1 are most likely not the cause of the observed increase.

None of the studies into the MNb_3O_8 system have described this increase in capacity, however a different binder (PVDF or no binder) was used in their studies.[128,143] Commonly and historically PVDF is used whilst in this study we have used CMC which is a safer binder of choice as it does not require the use of toxic N-Methylformamide solvent,† and instead uses water. To test the theory that binder choice is a cause of this increased capacity, KNb_3O_8 PVDF coatings were tested and results are presented in the next section.

Figure 7.2.e., shows peaks from the sodiation and desodiation curve shifting (shown by arrows) which minimises ΔV. This shift is coupled with an increase in peak height which suggests an increase in the utilised sodium intercalation sites. The capacity increases due to a decrease in ΔV during cycle, this is due to the sodiation and desodiation voltages shifting to higher and lower potentials, respectively (Figure 7.2.a.).

The cyclic voltammetry (Figure 7.2.f.) reveals that the rate of sodiation increases almost linearly between 1.3 V- 0.005 V at low sweep rates, at faster rates, shallow peaks can be observed at 0.7 V and 0.3 V with a tendency to shift to lower V at faster rates. Desodiation occurs at 1.2 V and 1.7 V (at high sweep rates) with a peak shift to higher voltages at fast sweep rates. These peak shifts cause ΔE_p to increase as sweep rate increases which is expected.

At a slow sweep rate of 0.05 mV/s H. Nakayama *et al.*[143] reported peaks in the CV

†N-Methylformamide: Acute toxicity, Dermal (Category 4), H312 and Reproductive toxicity (Category 1B), H360D

sodiation curve at 0.9 V, 0.8 V and 0.6 V, and peaks in the desodiation curve at 0.9 V, 1.0 V and 1.5 V. At the slowest sweep rate in this study of 0.1 mV/s, the peak locations do not match this study. This could be due to their use of PVDF.

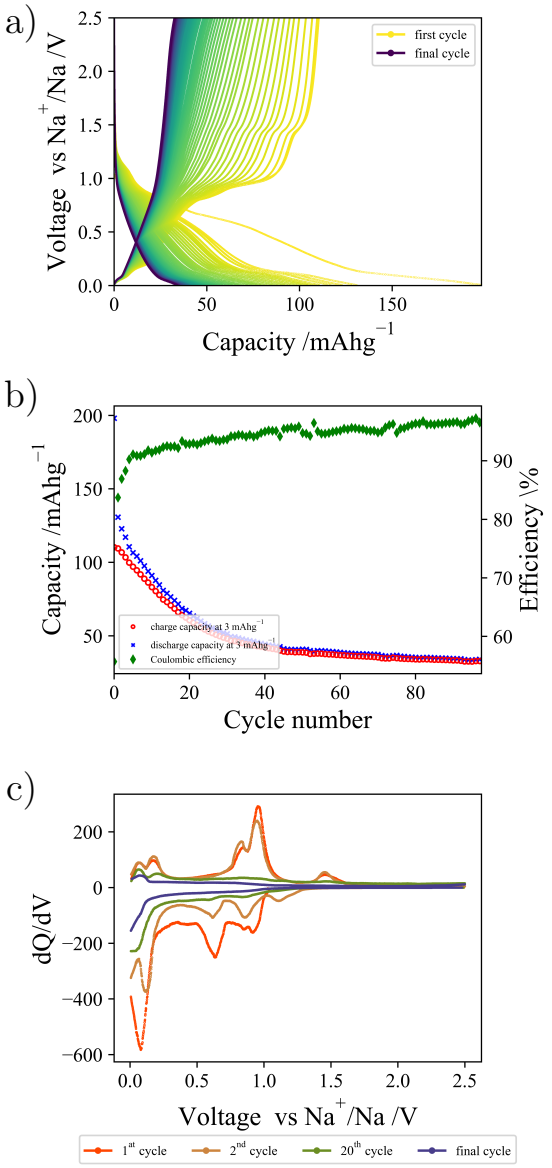


Figure 7.3: Electrochemical cell testing of KNb_3O_8 using PVDF binder cycled at 3 mAg^{-1}.

KNb_3O_8 PVDF results

Galvanostatic cycling and dQ/dV plots for KNb_3O_8 anode made using a PVDF binder are shown in Figures 7.3 and 7.4. These results can be compared to the work by H. Nakayama *et al.*[143] who also studied KNb_3O_8 PVDF sodium half cells at 3 mAg^{-1} and found a second cycle capacity of 166 $mAhg^{-1}$, whilst in this study a capacity of 163 $mAhg^{-1}$ was observed. Therefore very similar capacities were achieved. The charge and discharge curves are similar with the same noticeable change in the curvature of the charge cycle at around 1.5 V and at 1 V.

KNb_3O_8 PVDF cells cycled at 3 mAg^{-1} did not show any increase in capacity (Figure 7.3.a.b.), further supporting the hypothesis that the CMC binder plays an active role in the observed increase in capacity.

Utilising PVDF has caused the ΔV to

become static as there are no peak shifts in the DCC, only a loss of intensity implying slower rates of redox reactions (Figure 7.3.c.). This therefore leads to a decrease the cell capacity over cycles.

Comparing the capacities obtained from using PVDF and CMC directly in Figure 7.4, the first discharge capacity is similar for both PVDF and CMC (198 $mAhg^{-1}$ and 195 $mAhg^{-1}$, respectively), however the second cycle capacity is significantly lower for PVDF (163 $mAhg^{-1}$) than CMC (161 $mAhg^{-1}$), and the deviation from each other continues. Therefore there is obvious fundamental differences in the mechanism of charge storage when coatings are made with CMC or PVDF.

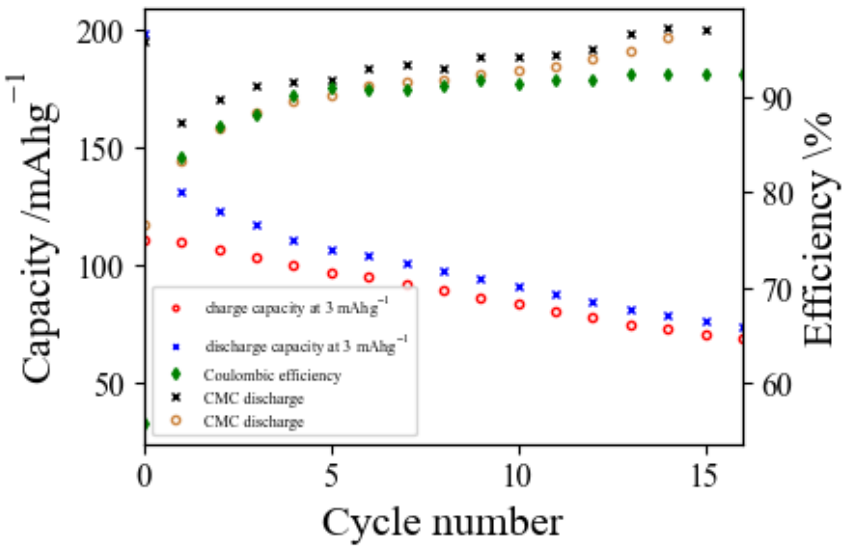


Figure 7.4: The charge and discharge capacities of KNb_3O_8 with PVDF shown in red and blue, respectively, and the Coulombic capacity in green. The charge and discharge capacities of KNb_3O_8 with CMC are shown in orange and black, respectively. Both cells cycled at a rate of 3 mAg^{-1}.

J. Guo *et al.*[219] stated CMC coatings showed a smoother surface and less cracking after cycling, when compared to PVDF. Unfortunately microscopy images of the cells after cycling were not obtained due to prolonged machine breakdown. This study hypothesises this increased in capacity is related to the reported improved binder stability of CMC over PVDF.

It was not possible to obtain long term cycling on KNb_3O_8 with CMC, due to time constraints. It would be interesting to probe whether the capacity increases indefinitely, or whether it plateaus, or even suffers from capacity fade. Further work is required to determine the mechanism behind this observed capacity increase.

7.3.2 HNb_3O_8

Cell cycling of HNb_3O_8 at 3 mAg^{-1} gave a first cycle sodiation capacity of 291 $mAhg^{-1}$ which is comparable to the capacity reported by H. Nakayama *et al.*[143] of 295 $mAhg^{-1}$. In this study HNb_3O_8 shows a high second cycle capacity (216.5 $mAhg^{-1}$) at a rate of 3 mAg^{-1}, which fades quickly to 122.0 $mAhg^{-1}$ after 20 cycles (Figure 7.5.a.c.). The capacity fade be attributed to several factors such as an increase in overpotential, as observed by the discharge curve shifting up, and charge curve shifting down (Figure 7.5.a.). Figure 7.5.e. shows a decrease in peak heights during cell cycling which can also be observed in the smoothing of the charge and discharge curves over cycles (Figure 7.5.a.). The sodiation peaks in the DCC (Figure 7.5.e.) show most of the capacity occurs at very low V, which is then lost due to increasing overpotential effects. Desodiation mostly occurs at 1.0 V, however the plateau rapidly fades with cycling, leading to the observed loss in capacity.

Secondly, capacity fade can be attributed to poor initial Coulombic efficiency (Figure 7.5.c.). The Coulombic efficiency increases from 67.8 % to 90.4 % for the first and second cycle, respectively, followed by a drop in the efficiently at the 5th cycle to 88.7 % which is due to a disproportionately large drop in the discharge capacity. Eventually the Coulombic efficiency increases to 98.7 % on the 38th cycle with a substantial capacity of 111.5 $mAhg^{-1}$.

Higher capacities can be achieved using HNb_3O_8 compared to KNb_3O_8 when using rates between 10- 40 mAg^{-1} (Figure 7.5.b.). Even at 40 mAg^{-1}, HNb_3O_8 shows a substantial 5th cycle capacity of 112 $mAhg^{-1}$ whereas the capacity of KNb_3O_8 at 40 mAg^{-1} was 7.7 $mAhg^{-1}$ (Figure 7.5.b.). However at very high rates of 100 mAg^{-1} causes dramatic capacity loss, rendering the cell useless due to low capacity (Figure 7.5.b.).

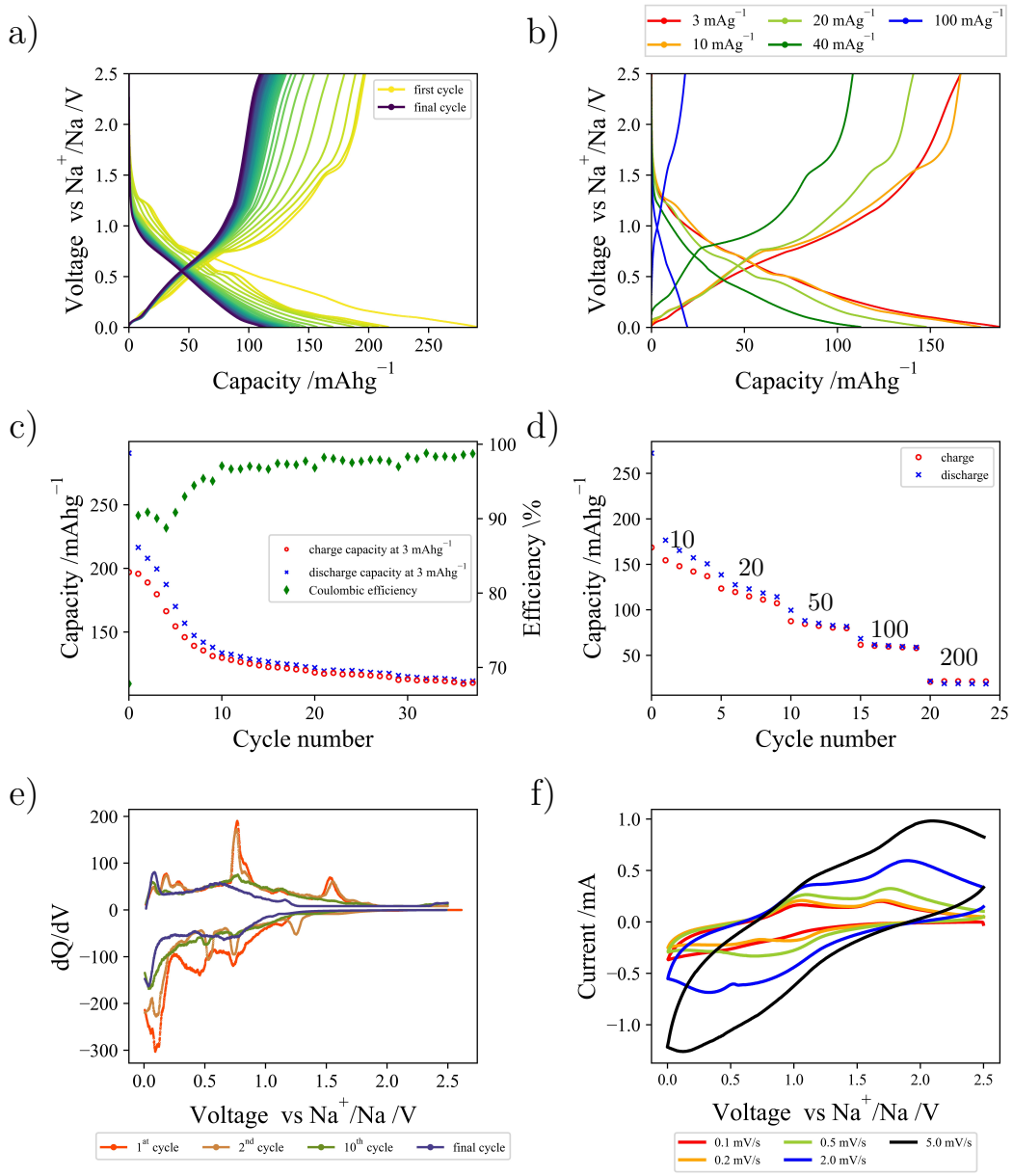


Figure 7.5: Electrochemical cell testing of HNb_3O_8. Cells cycled at 3 mAg^{-1} (left) and cells cycled at variable current or voltage (right) a) At 3 mAg^{-1} b) 5^{th} charge and discharge cycle when cycled at rates of 3 mAg^{-1}, 10 mAg^{-1}, 20 mAg^{-1}, 40 mAg^{-1} and 100 mAg^{-1}. c) Capacity of each cycle at 3 mAg^{-1} d) Cell cycled at 10 mAg^{-1}, 20 mAg^{-1}, 50 mAg^{-1}, 100 mAg^{-1} and 200 mAg^{-1} for 5 cycles each e) dQ/dV plot of cell cycled at 3 mAg^{-1} f) Cyclic voltammetry at sweep rates of 0.1 mV/s, 0.2 mV/s, 0.5 mV/s, 2.0 mV/s and 5.0 mV/s.

Although the initial capacities of HNb_3O_8 at slow charge rates are competitive with current SIB anode materials[224] such as $Na_2Ti_3O_7$ with capacities of 190 $mAhg^{-1}$, $Li_4Ti_5O_{15}$ with capacities of 200 $mAhg^{-1}$ and also TiO_2 with capacities of 220 $mAhg^{-1}$. However, the significant capacity fade and poor capcities at high charge rates of HNb_3O_8 indicates that other anodes are superior. However, the aforemntioned reported materials have been thororghly studied and optimised, unlike HNb_3O_8 and therefore, it could be possible with optmisation to become competitive or even surpass current anode capacities.

The CV (Figure 7.5.f.) shows a peak shift to lower voltages during sodiation, and a peak shift to higher V during desodiation, again increasing ΔE_p. Although in KNb_3O_8 and HNb_3O_8 both show two peaks during desodiation step, the size of the peaks are different, as KNb_3O_8 shows highest rates of activity at 1.2 V (at all sweep tested sweep rates), whilst HNb_3O_8 shows equal intensity of peaks at 1.2 V and 1.7 V at slow sweep rates, but at high sweep rates, activity at 1.7 V is significantly higher than that at 1.2 V. Therefore in HNb_3O_8 a higher threshold voltage has to be reached to induce sodiation or desodiation.

C. Huang *et al.*[128] reported the CV of HNb_3O_8 at a rate of 0.5 mV/s (between 0- 3 V) in a lithium-ion battery which shows similarities to the CV of this study, with an peak at 0.75 V corresponding to sodiation/ lithiation. However the desodiation/ delithiation curve shows significant differences, as there are two peaks observed in this study whilst there is only one peak reported by C. Huang *et al.* at 2.25 V.

HNb_3O_8 at 40 mAg^{-1}

An increase in capacity was also observed with cycling HNb_3O_8 at 40 mAg^{-1}, and therefore this is reported in more detail. The first cycle capacity is 119 $mAhg^{-1}$ which falls to 87 $mAhg^{-1}$ on the second cycle and then continues increasing until 126 $mAhg^{-1}$ on the 11th cycle, after which a linear decay of capacity is observed until the 50th cycle capacity of 79 $mAhg^{-1}$ (Figure 7.6 and 7.7). This is again a very significant capacity gain, and therefore is most likely not caused by the mechanisms reported by J. Guo *et al.*[219]

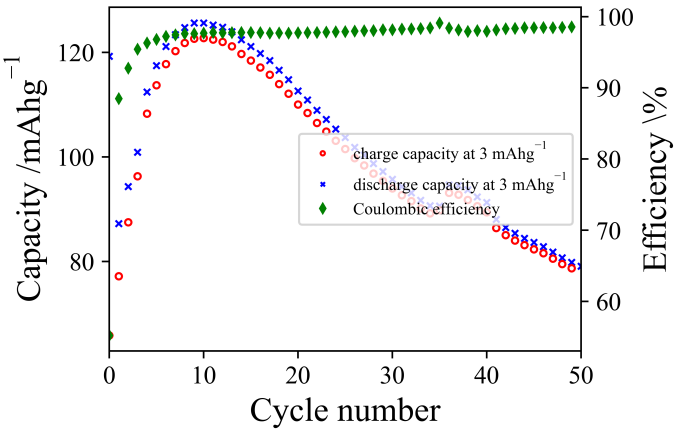


Figure 7.6: Capacity and Coulombic efficiency of each cycle for HNb_3O_8 anode coating made using CMC binder in a sodium half cell cycled at 40 mAg^{-1}.

An interesting result from HNb_3O_8 is the increase in capacity observed when cycling at the rate of 40 $mAhg^{-1}$. The capacity is observed to increase, at a faster rate than observed for KNb_3O_8. Unlike the KNb_3O_8 dataset, HNb_3O_8 shows a drop in the capacity, which could be related to the use of higher currents.

The Coulombic efficiency (Figure 7.6) begins at 55 % for the first cycle and increases to 88 % on the second cycle and continues rapidly increasing to stabilise at 97 % and 98 % Coulombic efficiency. Despite the capacity fade, Coulombic efficiency remains high. Therefore capacity fade is caused by an inability to insert the same amount of sodium-ion into the anode as the previous cycle.

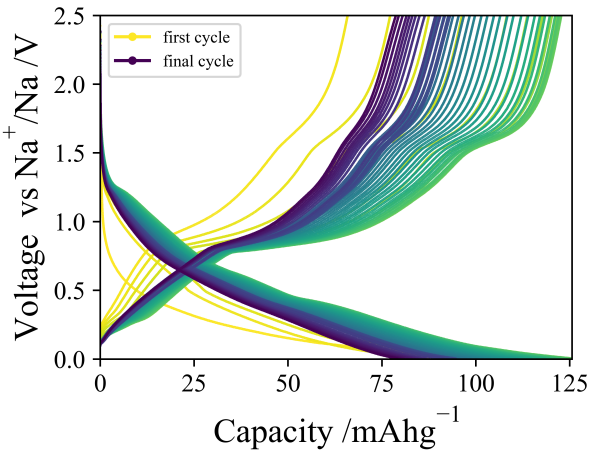


Figure 7.7: Galvonostatic curves of HNb_3O_8 anode coating made using CMC binder in a sodium half cell cycled 40 mAg^{-1}.

The area under the DCC increases initially (Figure 7.8), with more peaks and features appearing, in addition to the shifting of desodiation peaks to lower voltage, minimising ΔV, a sign of decreasing overpotential which increases capacity, similar to the observations made with KNb_3O_8, HNb_3O_8 shows desodiation peaks at 0.1 V, 1.9 V and 1.5 V, similar deosdiation peaks are observed in KNb_3O_8 with the exception that the double peaks at 0.1 V and 1 V appear as a broad singular peak instead. In both cases, desodiation occurred mainly at 1 V. Unfortunately, due to time pressures, this experiment was not repeated.

Due to the similarities in the DCC and the knowledge that KNb_3O_8 and HNb_3O_8 are related structures, it is believed that the same mechanism is at play. However it is unknown as to why this occurs at 40 mAg^{-1} for HNb_3O_8, whilst it has only been observed at rates of 3 mAg^{-1} in KNb_3O_8. This study hypothesises the rate of charge to observe this increase in capacity could be related to the diffusion speed of the alkali ion.

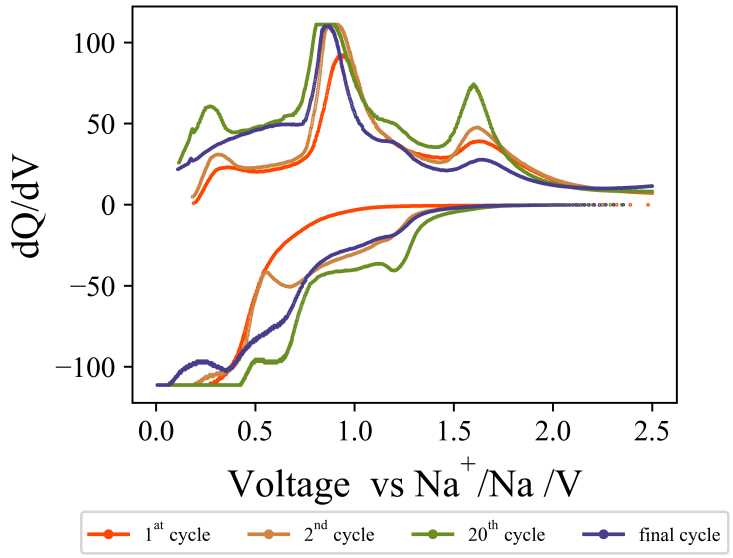


Figure 7.8: Differential capacitance curve from galvanostatic cyling of HNb_3O_8 using CMC binder cycled at 40 mAg^{-1}.

7.3.3 Restacked niobate

The galvanostatic charge discharge testing at 3 mAg^{-1} (Figure 7.9.a.) shows significant capacity fade from a first and second cycle capacities of 287 $mAhg^{-1}$ and 187 $mAhg^{-1}$, respectively, to 75 $mAhg^{-1}$ after 10 cycles. The capacity loss occurs more rapidly than KNb_3O_8 and HNb_3O_8 (Figure 7.9.c. and d.). Unlike KNb_3O_8 and HNb_3O_8, restacked niobate showed no observed increasing capacity whilst aging.

K. Akatsuka *et al.*[127] studied the electrochemical properties of exfoliated Nb_3O_8 sequentially adsorbed on an indium-tin-oxide coated glass electrode, forming a thin multilayer film. They reported a reduction/ oxidation (Nb^{4+}/Nb^{5+}) peaks at -1.2 V (vs. Ag/Ag^+) which converted to 1.87 V (vs. Na/Na^+) attributable to insertion and deintercalation of Li^+ ions. Whilst the Nb^{4+}/Nb^{5+} peaks has been reported to be 1 V vs. Na/Na^+ in bulk crystalline KNb_3O_8. However, the sloping nature of the galvanostatic curves (Figure 7.9.a.) suggests that the sodium intercalation sites are poorly defined and that sodiation occurs *via* solid-solution phase change, which is expected of a disordered material.

The Coulombic efficiency (Figure 7.9.c.) shows a similar trend to that observed in HNb_3O_8, with an initial increase, followed by a pause and then followed by a continual increase. The initial sharp increase could be due to the overhang mechanism.[225] The restacked niobate shows the lowest 6th cycle Coulombic efficiency (90.9 %) compared to HNb_3O_8 and KNb_3O_8 (93.0 % and 96.0 %, respectively). This could be due to a large quantity of SEI formation, as the process of exfoliation and restacking increases the surface area of the material, or it could be to to the disruption of diffusion pathways. By 14th cycle, the Coulombic capacity for KNb_3O_8, HNb_3O_8 and restacked niobate have all reached approximately the same value of 97.8 %, 96.99 % and 96.6 %, respectively.

It should be noted low inital Coulombic efficincy is to be expected with nanostructured materials which produce higher quanities of SEI, KNb_3O_8 nanowires[133] showing an inital Coulombic efficiency of 58 %, similar to the initial Coulombic efficiency of

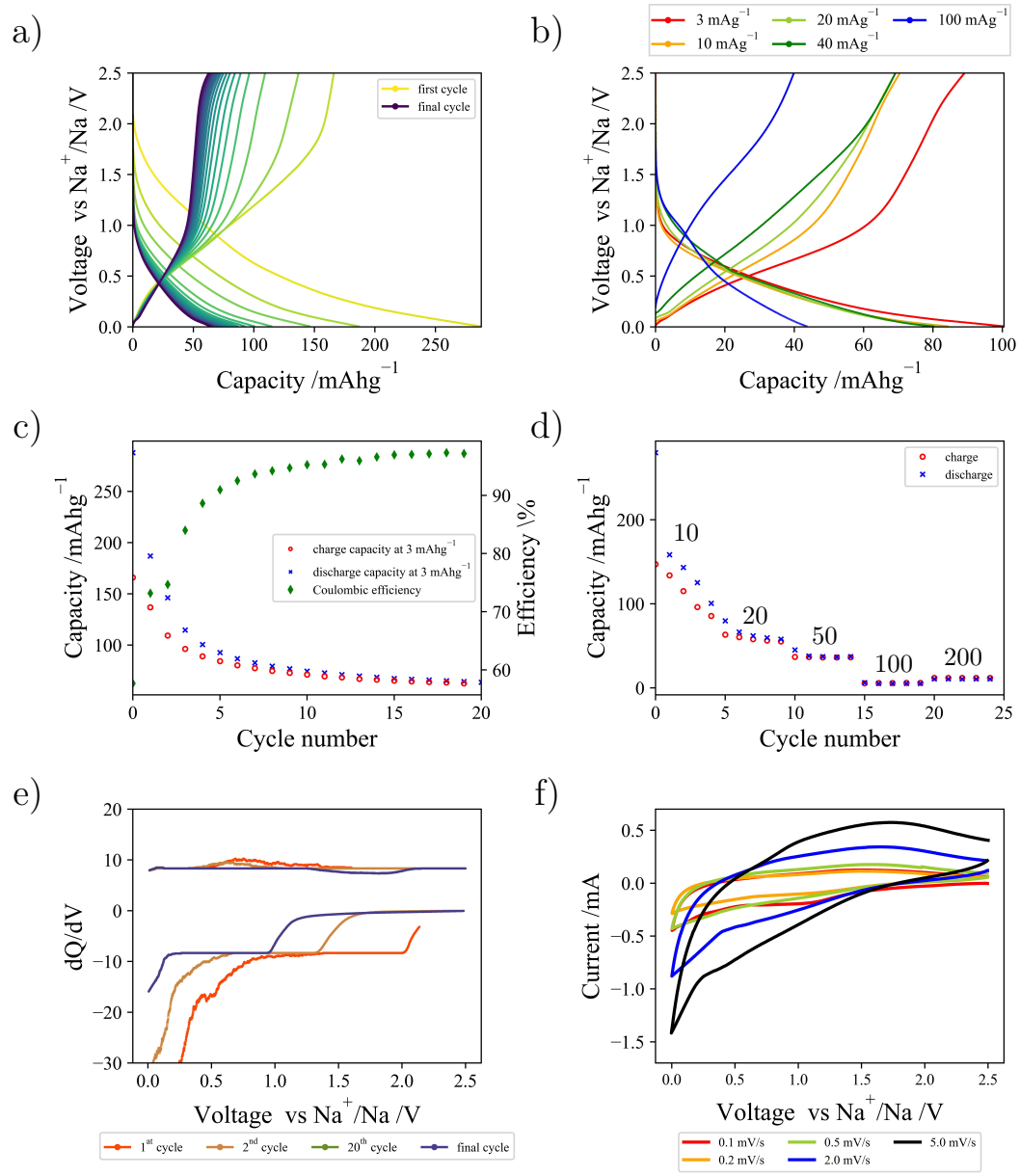


Figure 7.9: Electrochemical cell testing of restacked niobate. Cells cycled at 3 mAg^{-1} (left) and cells cycled at variable current or voltage (right) a) At 3 mAg^{-1} b) 5^{th} charge and discharge cycle when cycled at rates of 3 mAg^{-1}, 10 mAg^{-1}, 20 mAg^{-1}, 40 mAg^{-1} and 100 mAg^{-1}. c) Capacity of each cycle at 3 mAg^{-1} d) Cell cycled at 10 mAg^{-1}, 20 mAg^{-1}, 50 mAg^{-1}, 100 mAg^{-1} and 200 mAg^{-1} for 5 cycles each e) dQ/dV plot of cell cycled at 3 mAg^{-1} f) Cyclic voltammetry at sweep rates of 0.1 mV/s, 0.2 mV/s, 0.5 mV/s, 2.0 mV/s and 5.0 mV/s.

restacked niobate at 67.8 % observed in this study.

When varying the cycle rate, there is very minimal capacity loss/ change at various cycle rates until beyond 40 mAg^{-1} (Figure 7.9.b.). Therefore this material shows resilience to faster charging rates which have not been previous observed in this study. However the initial capacity is not as high as HNb_3O_8 and despite its superior capacity retention at high rates, the capacities of HNb_3O_8 are still higher (Figure 7.9.b.d. and Figure 7.5.b.d.).

Although the dQ/dV plot (Figure 7.9.e.) has been processed following the same method as previous cells, the sodiation curves contain strange plateaus, atypical of dQ/dV curves. Similar plateaus were observed for all restacked niobate cells cycled at all studied rates expect 100 mAg^{-1}, where they were simply smooth featureless curves. Unfortunately the cause of these plateaus could not be resolved, and therefore the dQ/dV sodiation curve is not interpreted.

The CV for this restacked niobate shares similarities with HNb_3O_8 (Figure 7.9.f.) at 2.0 mV/s and the sodiation curve shares a similar shape at high sweep rates with a notch at around 0.25 V. On the other hand, the desodiation curve is smoother than HNb_3O_8, which could be caused by structural disorder causing the definition of pathways and sites to be degraded, meaning the peaks at 1.5 V and 1.7 V (observed in HNb_3O_8) have merged in this sample. This smoothing of the curved has also been linked to pseudo-capacitance rather than surface reactions too.[128]

The CV curve shows the same shape as those reported by K. Akatsuka *et al.*[127] of a multilayer Nb_3O_8 nanosheets on indium-tin-oxide coated glass electrode. Therefore despite the use of sodium or lithium, there are shared kinetic characteristics between the two. However the mechanism itself is not known.

7.3.4 Hydrothermal nanostructured

The hydrothermal nanostructured material shows a higher fifth cycle capacity at rates of 10 mAg^{-1}, 20 mAg^{-1} and 40 mAg^{-1} compared to 3 mAg^{-1} (Figure 7.10.b.) which is initially unexpected, but this can be explained by higher initial first cycle capacities at these rates (Table 7.2). However after 20 cycles, the capacities are similar regardless of the rate, up to a rate of 40 mAg^{-1}. At very fast rates of 100 mAg^{-1} (Figure 7.10.d.) the capacity is significantly improved compared to that of Figure 7.10.b.

The sequential stepped cycling (Figure 7.10.d.) shows a similar result to previous phases, where the first 10 cycles shows a sloping gradient due to capacity loss, after which the capacity and Coulombic efficiency settles. The capacity achieved by hydrothermal nanostructured material cycled at 3 mAg^{-1} (shown in Figure 7.10.a. and c.) begins at 112 $mAhg^{-1}$, and steadily fades to 42 $mAhg^{-1}$ after 36 cycles. This is partly due to the slowly increasing Coulombic efficiency from 86.0 % (second cycle) and after 36 cycles, does not appear to have plateaued, unlike the previously presented samples which typically start plateauing at around the 5th cycle and reached a fairly stable point by the 20th cycle. However, strangely, the first cycle capacity is less than the second cycle by 2 $mAhg^{-1}$. On the other hand, in another cell, the expected drop in capacity between first and second cycle (330 $mAhg^{-1}$ to 140 $mAhg^{-1}$) is observed in Figure 7.10.d.

The DCC (Figure 7.10.e.) does not show any sharp features, which is to be expected in a disordered material with a lack of defined sites, this is reflected in the smooth slopes of Figure 7.10.a. The desodiaton curve of the DCC shows a peak shift to lower voltage, leading to a decrease in ΔV. Unfortunately the sodiation curve could not be interpreted due to the presence of peculiar plateaus again. However the decrease in ΔV (increase in overpotential) can be observed in Figure 7.10.a. by the shifting of the sodiation curve to lower voltage, the the shifting of desodiation curves to to higher voltage.

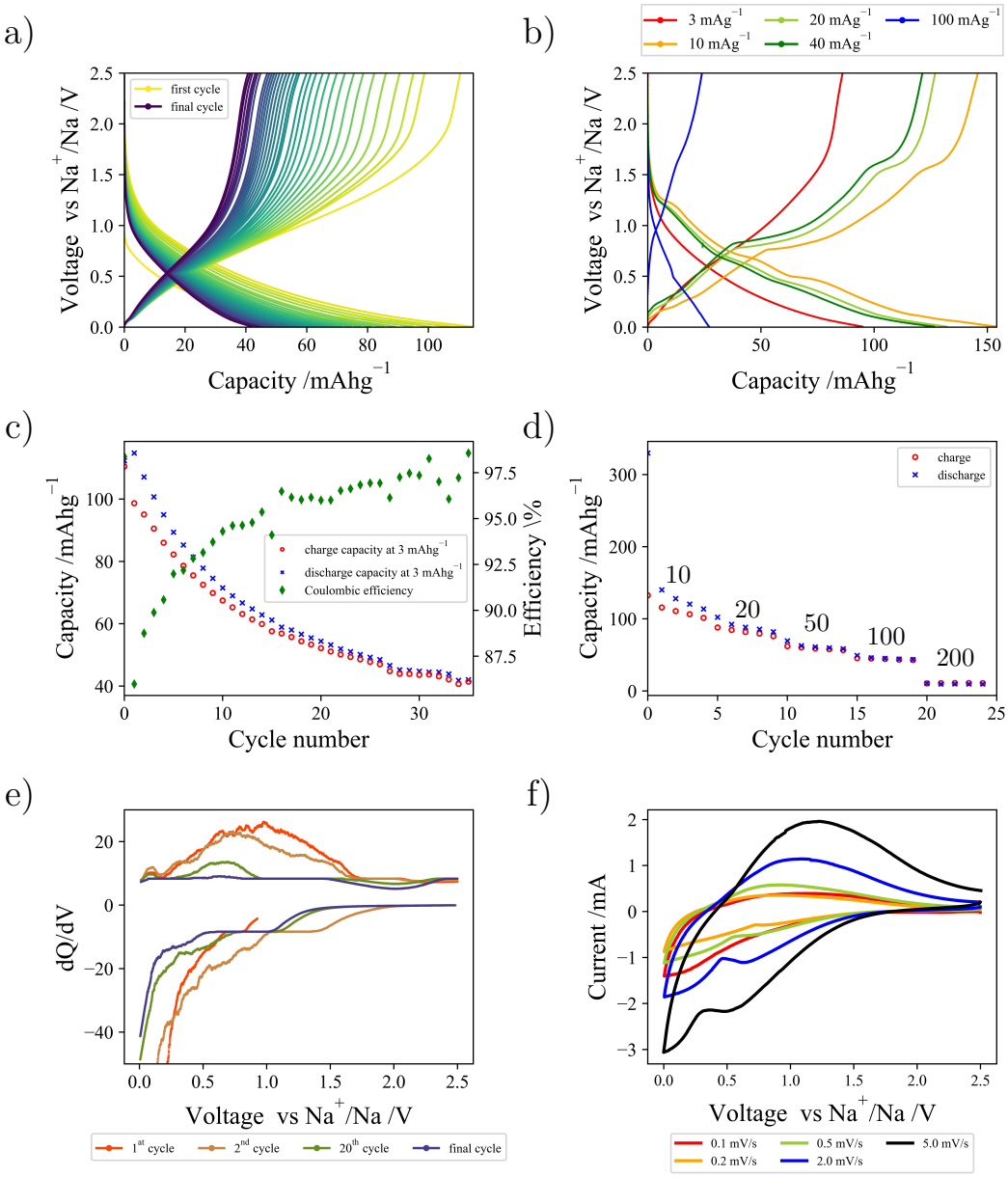


Figure 7.10: Electrochemical cell testing of hydrothermal nanostructured. Cells cycled at 3 mAg^{-1} (left) and cells cycled at variable current or voltage (right) a) At 3 mAg^{-1} b) 5^{th} charge and discharge cycle when cycled at rates of 3 mAg^{-1}, 10 mAg^{-1}, 20 mAg^{-1}, 40 mAg^{-1} and 100 $mAhg^{-1}$. c) Capacity of each cycle at 3 mAg^{-1} d) Cell cycled at 10 mAg^{-1}, 20 mAg^{-1}, 50 mAg^{-1}, 100 mAg^{-1} and 200 mAg^{-1} for 5 cycles each e) dQ/dV plot of cell cycled at 3 mAg^{-1} f) Cyclic voltammetry at sweep rates of 0.1 mV/s, 0.2 mV/s, 0.5 mV/s, 2.0 mV/s and 5.0 mV/s.

The CV (Figure 7.10.f.) shows the desodiation curve shifting to higher V as sweep rate increases (from 0.75 V to 1.25V), which is expected, whilst the same trend is observed in sodiation but with two separate peaks. The first peak originates from 0.9 V and shifts to 0.5 V whilst the second peak originates from 0.25 V and shifts to around 0 V. Although a double peak is also observed in other materials of this study (HNb_3O_8) at high sweep rates and restacked niobate), the shape these peaks are unique.

Table 7.2: Calculated capacities of each active material at the end of cycle one, two and 20th cycle capacity at various rates.

	Rate \ mAg^{-1}	Capacity \ $mAhg^{-1}$		
		1^{st} cycle	2^{nd} cycle	20^{th} cycle
Hydrothermal nanostructured	3	112	115	54
	10	243	173	69
	20	209	149	64
	40	179	136	69
	100	43	26	25

7.3.5 Nanostructured $K_4Nb_6O_{17}$

The capacity of nanostructured $K_4Nb_6O_{17}$ is a very poor anode material, even at the slow rate of 3 mAg^{-1}, the capacity is less than 15 $mAhg^{-1}$ (Figure 7.12.a.b.c.d.). The initial irreversible capacity can be attributed to SEI formation, the remaining 10 $mAhg^{-1}$ of reversible capacity could be contributions from either the sample or carbon P.

The dQ/dV curves show that there are plateaus in the galvanostatic desodiation curve (Figure 7.12.e.) at around 0.9 and 2.0 V during desodiation and around 0.2 V and 1.7 V for sodiation. The sodiation peaks rapidly decrease in intensity, this can be attributed to the SEI formation.

The dQ/dV curves (Figure 7.12.e.) shows the reduction of peak intensities as cell cycling progresses indicating fewer redox reactions. The peaks eventually smooth, to the point that they are indistinguishable. This remaining volume suggests pseudo-capacitive behaviour which is a common behaviour of niobate materials. [86,132]

The CV (Figure 7.12.f.) shows a sodiation peak originating at 0.7 V and shifts to lower V. On the other hand the desodiation shows no noticeable peaks. The possible pseudo-capacitive behaviour was investigated by applying Equation 7.1.

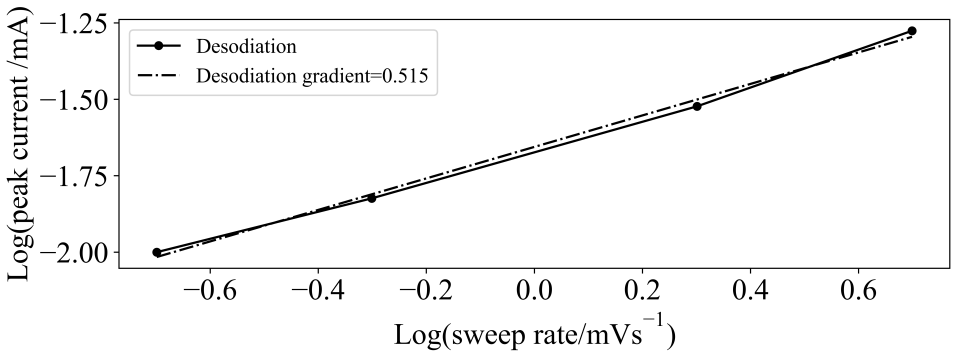


Figure 7.11: The log of peak current against the log of sweep rate for CV sweep rates between 0.2 mV/s - 5 mV/s for nanostructured $K_4Nb_6O_{17}$.

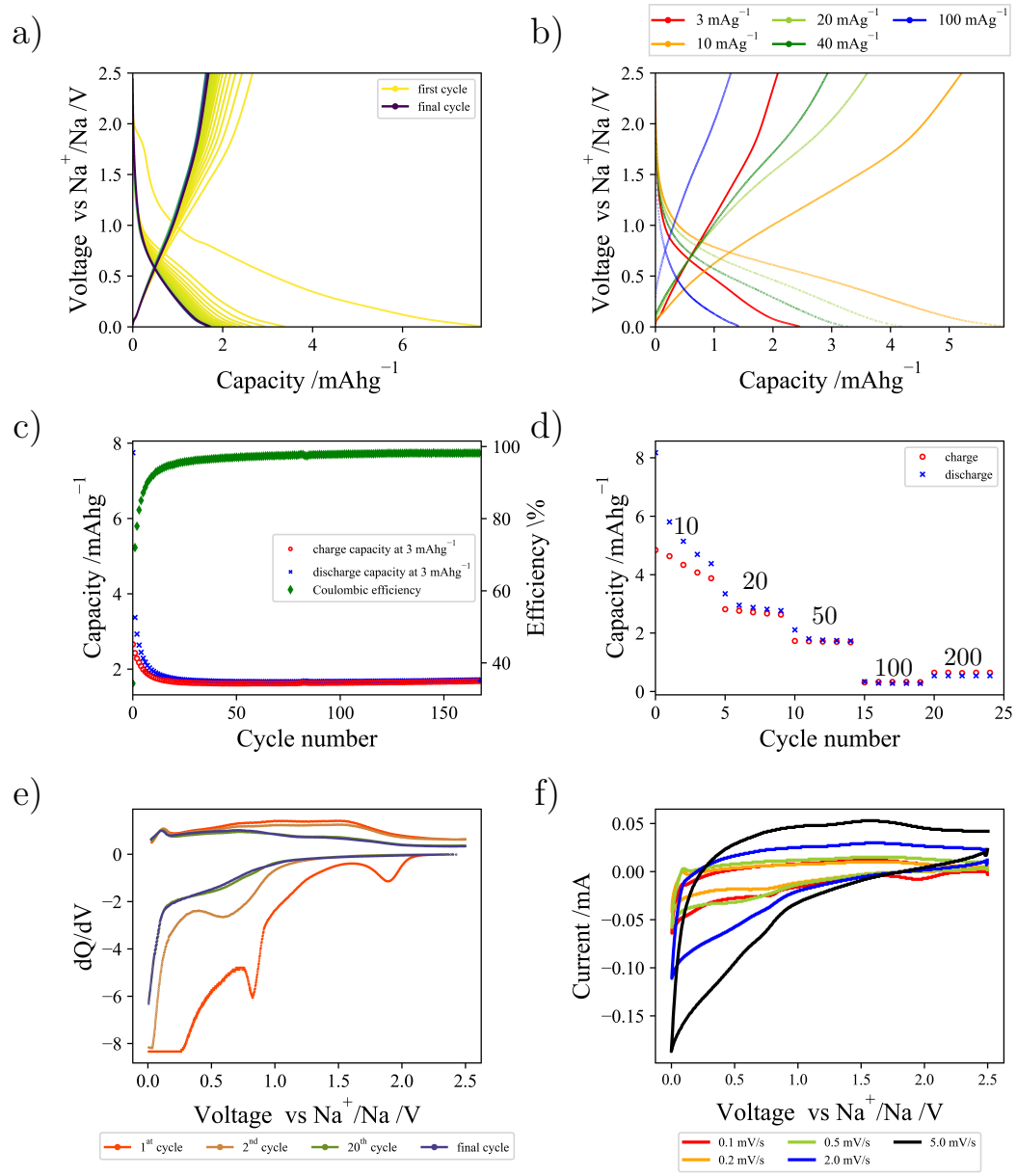


Figure 7.12: Electrochemical cell testing of nanostructured $K_4Nb_6O_{17}$. Cells cycled at 3 mAg^{-1} (left) and cells cycled at variable current or voltage (right) a) At 3 mAg^{-1} b) 5^{th} charge and discharge cycle when cycled at rates of 3 mAg^{-1}, 10 mAg^{-1}, 20 mAg^{-1}, 40 mAg^{-1} and 100 mAg^{-1}. c) Capacity of each cycle at 3 mAg^{-1} d) Cell cycled at 10 mAg^{-1}, 20 mAg^{-1}, 50 mAg^{-1}, 100 mAg^{-1} and 200 mAg^{-1} for 5 cycles each e) dQ/dV plot of cell cycled at 3 mAg^{-1} f) Cyclic voltammetry at sweep rates of 0.1 mV/s, 0.2 mV/s, 0.5 mV/s, 2.0 mV/s and 5.0 mV/s.

The relationship between the sweep rate and peak current can be understood using Equation 7.1 as previously presented. A b value of 0.5 indicates that the process is a fully reversible redox reaction, with the charge carrier freely diffusing through the active material, which is the case for nanaostructured $K_4Nb_6O_{17}$ as determined by b values equal to the gradient in Figure 7.11, Conversely, a b value of 1 would indicate capacitive behaviour.

$$i_p = av^b \tag{7.1}$$

Although typically a sodiation and a desodiation peak currents are analysed for a b value, the lack of obvious peaks in the sodiation curve leads to the analysis of only the sodiation curve. The peak at around 1.7 V was used and this provided a b value of 0.515 therefore concluding the reversible capacity is derived from redox reactions.

In summary, the nanostructured $K_4Nb_6O_{17}$ shows very poor capacity regardless of the rate of charge used and is not suitable for applications as an anode material, despite the positive reports regarding the redox behaviour of $K_4Nb_6O_{17}$. One such example includes from X. Wang *et al.*[217] whereby exfoliated and restacked $K_4Nb_6O_{17}$ achieved 381 $mAhg^{-1}$ at 0.05 Ag^{-1} when used as a lithium ion battery anode. The poor electrochemical results observed in this study are most likely due to the type of disorder induced via hydrothermal synthesis, being unsuitable for anode applications. Typically open channels and layers are optimal structures for intercalation anodes. However a 3D network of $[NbO_6]$ corner sharing octahedra, may not have any channels or layers, leading to the poor electrochemistry.

7.4 Probing the sodiated structure

7.4.1 Literature background

Unfortunately the sodium-ion intercalation sites are not known for KNb_3O_8, or any other materials tested in this study. However lithium-ion intercalation sites of $NaNb_3O_8$ site have been identified, a structure related to KNb_3O_8.

K. McColl *et al.*[131] studied the lithium-ion intercalation mechanism of $NaNb_3O_8$. 3 sites were identified for lithium intercalation into $NaNb_3O_8$ (Figure 7.13.b. and c.) denoted x, y and z (shown in cyan, yellow and neon green, respectively), alongside a migration of the interlayer Na-ions, the new Na-ion site is in blue-grey. They also proposed an intercalation pathway for Li^+ which involves the the shifting of interlayer Na^+, away from its original site into a new site (blue-grey).

A preliminary study was performed using bond valence sum (BVS) mapping to probe possible sodium sites in KNb_3O_8 (Figure 7.13). This was done done by using a python script[‡] written by Matthew Dyer (ORCiD 0000-0002-4923-3003) to build a 3D bond valence sum map (Figure 7.13.a.). Unfortunately this method of using BVS does not take into consideration the oxidation of Nb^{5+} during sodium-ion intercalation, which will have significant effect on the BVS map.

Nonetheless, the results of the BVS map is supported by the findings from K. McColl *et al.*[131], highlighting the area K. McColl *et al.* described as the new Na sites (blue-grey) and also the lithium sites y and z. Unfortunately due to the 0.5 unit cell shift for alternating niobate layers from $NaNb_3O_8$ to KNb_3O_8, it is not possible to directly convert the additional sites in $NaNb_3O_8$ into KNb_3O_8

[‡]http://pcwww.liverpool.ac.uk/m̃sd30/software/BVS_Mapping.html

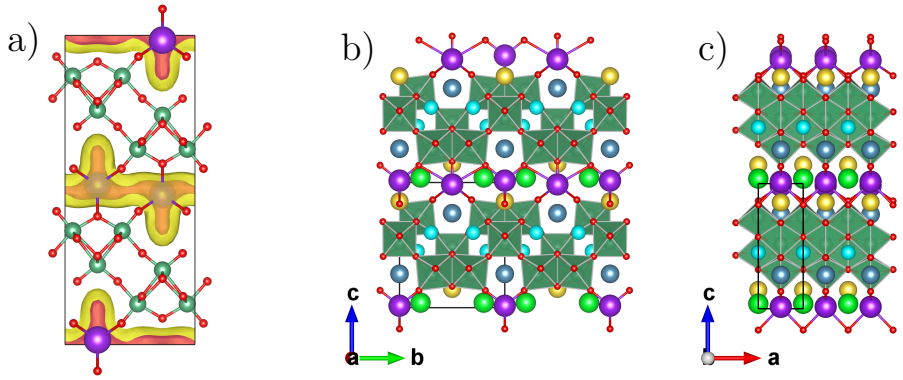


Figure 7.13: a) The result from BVS mapping of KNb_3O_8. b) and c) both show $NaNb_3O_8$ structure using green octahedra with red vertices to represent $[NbO_6]$ units with purple Na atoms. The lithium intercalation sites x, y and z (shown in cyan, yellow and neon green, respectively) and a new sodium-ion site shown in blue-grey as described by K. McColl[131] and diagram recreated in VESTA for this study. b) Along [001] axis c) Along [010] axis

7.4.2 *Inoperando* XPDF Method

It is useful to understand how the structure changes over charge cycles. Although many cells were made for this experiment, many of them cycled poorly and therefore only the results from KNb_3O_8 and restacked niobate will be presented.

Inoperando XPDF experiment was undertaken at the I15-1 beamline at Diamond Light Source using DRIX cells (Figure 7.14).[226]

A coating slurry was made using the same method as previous, however it was cast at 75 μm and allowed to dry for a few hours. At this stage it possessed some structural integrity without being too brittle, and 2.5 mm disks were punched. The coating layer was peeled off the aluminium foil and dried as free standing coating disks. This ensured there would not be aluminium peaks in the x-ray scattering data.

3 mm glass separators and 2 mm sodium disks were prepared using the same method as previously outlined with coin cells. These were assembled in the same order as previously mentioned, without a spacer or a spring, however in a DRIX cell. Fur-

thermore, in a DRIX cell, the carbon current collector was pressed against the active material disk and the metal current collector was pressed against the sodium disk.

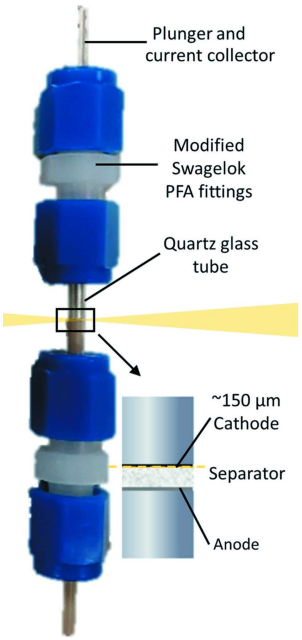


Figure 7.14: A cell specially designed for *inoperando* PDF collections on I15-1.[226]

A total of eight cells were mounted onto the beamline and each cell was connected to the Ivium-n-stat and cycled at a rate of 3 mAg^{-1}. The cells were scanned sequentially for approximately 5 mins each, therefore the diffuse scattering of each cell was recorded approximately every 40 minutes. During the experiment there was a few hours during which the x-rays were not available due to a technical fault at the synchrotron, therefore there are no scans during that period.

The data was collected and processed using PDFgetX3 to generate the XPDFs and then non-negative matrix factorisation (NMF) was used to highlight the differences in the peaks over time.

7.4.3 KNb_3O_8 results: *inoperando* XPDF

Inoperando XPDF cell cycling was use to probe the structure of KNb_3O_8 during sodaition (Figure 7.15), which were were further analysed using non-negative matrix factorization (NMF) (Figure 7.17).

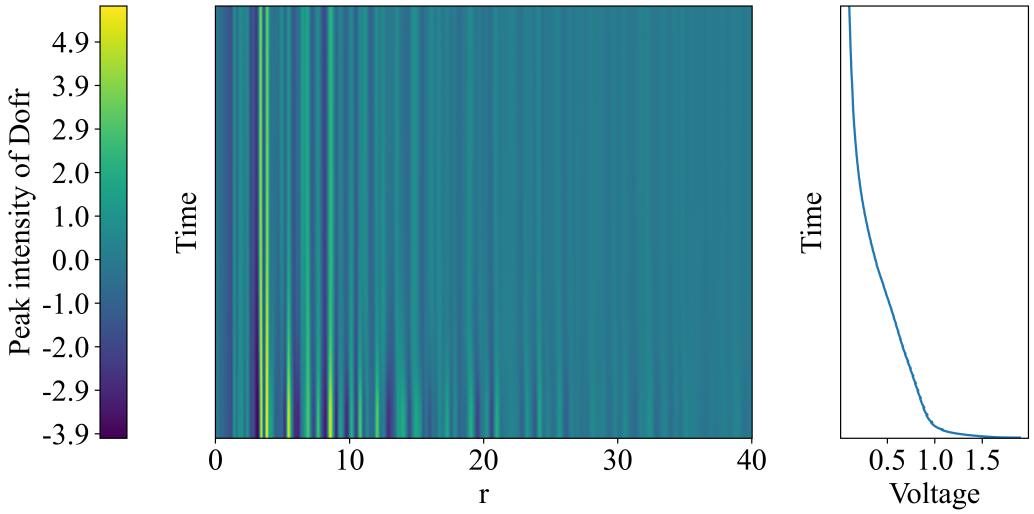


Figure 7.15: PDFs obtained during cell cycling of KNb_3O_8 plotted alongside the voltage profile.

The waterfall PDF plot (Figure 7.15) shows that during the first discharge (sodiation) cycle of KNb_3O_8 there was a loss of intensity, meaning a reduction in coherence length was observed. This is to be expected as Na^+ inserts into the structure, disturbing the local structure, causing the PDF to damp more rapidly.

The peak at 10.77 Å in the XPDF patterns (Figure 7.16.a.) corresponds to the half the unit cell (reported value of 10.749 Å between Nb2-Nb2 in the KNb_3O_8). This splits into two distances, 10.77 Å and 11.17 Å. This suggests that the interlayer distance of sodiated KNb_3O_8 phase to be 11.17 Å and indicates a two-phase mechanism.

In Figure 7.16, at higher r the peaks generally have shifted to lower r values during cycling. On the other hand, at low r, new peaks are observed (4.94 Å, 6.46 Å, 11.17 Å and 12.49 Å) with no peaks lost which supports the addition of Na in the structure.

Figure 7.17 shows the results from NMF, the PDF patterns were best modelled using two components. The weight of the two components are smoothly varying with component two being more akin to the desodiated structure KNb_3O_8 and component one being slightly more akin to the sodiated structure, mathematically (Figure 7.17.a.). Most of the structural changes occur in the first 10 scans (approximately 10 hrs). The intensity of the PDFs damp at high r, NMF has achieved this mathematically by using two components that cancel out at high r, therefore the high r NMF was not studied further (Figure 7.17.b.).

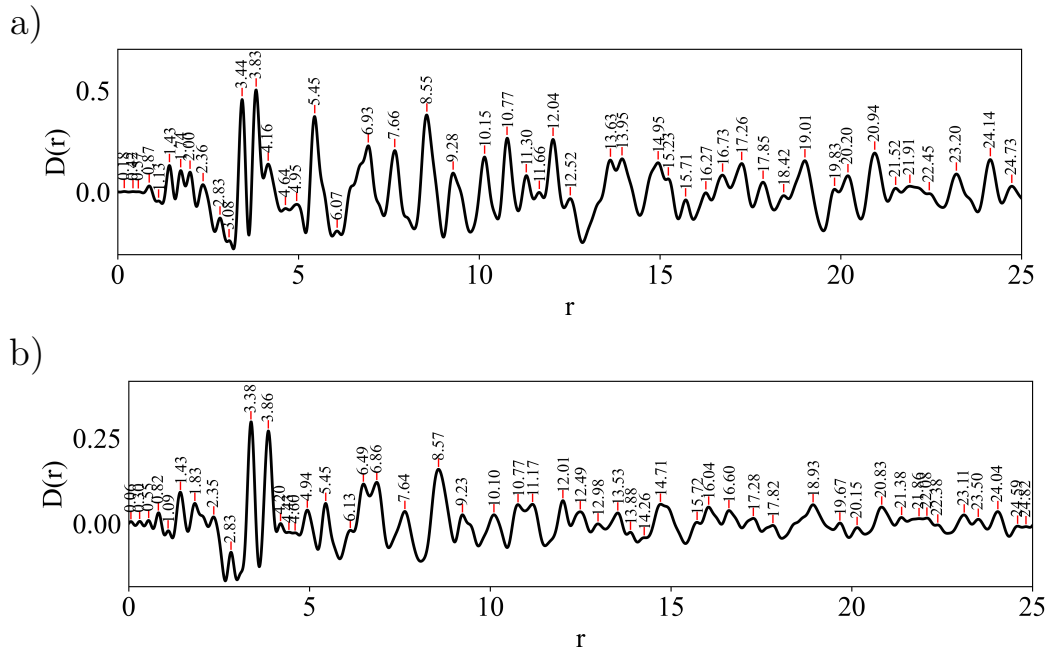


Figure 7.16: XPDF pattern from the *inoperando* study of KNb_3O_8. a) The first pattern collected. b) The last pattern collected.

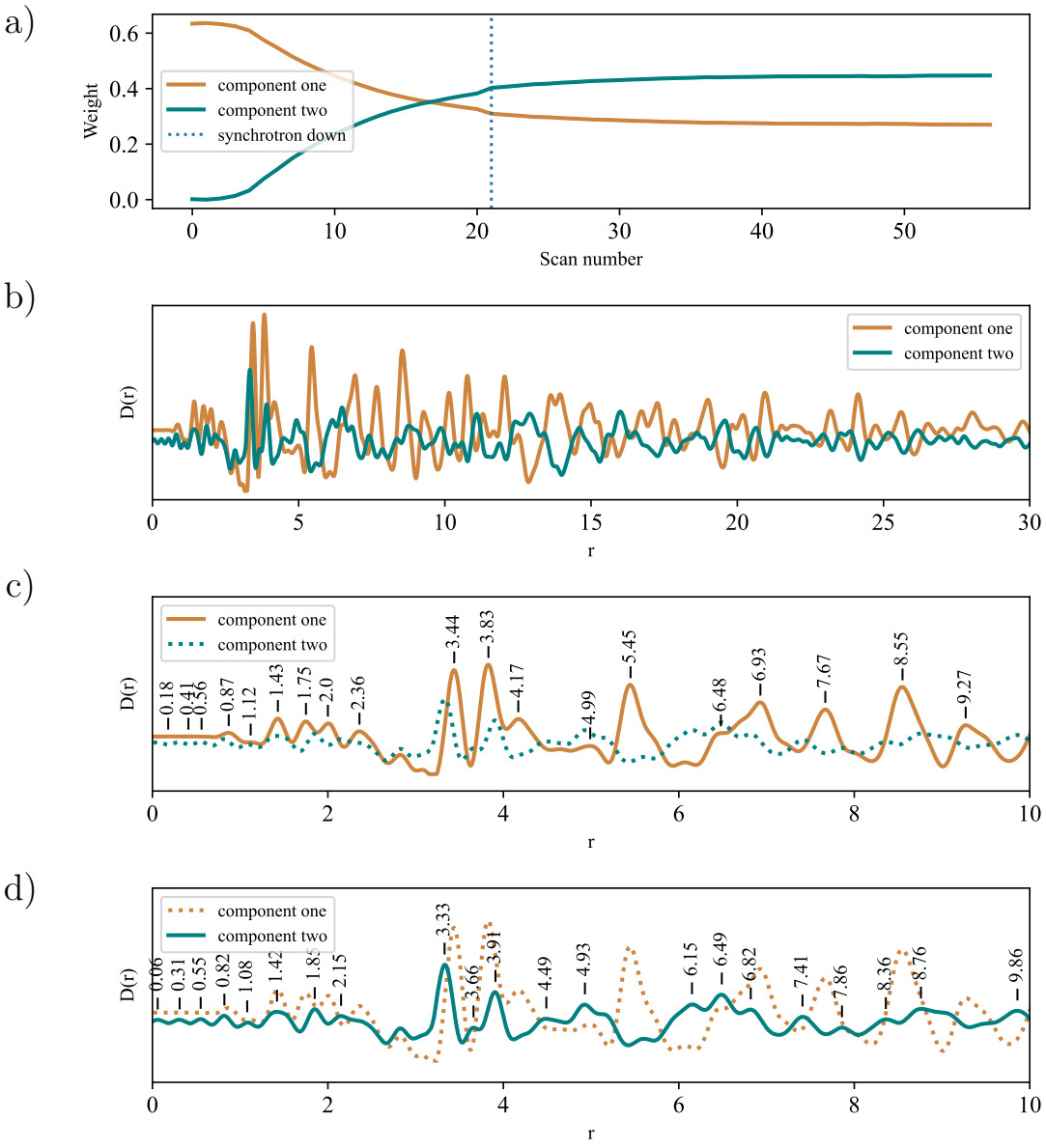


Figure 7.17: NMF results of *inoperando* XPDF cell testing of KNb_3O_8. a) Shows the change in weighting with XPDF scan number. A blue vertical dotted line indicates where two scans were removed due to a lack of x-rays at the synchrotron. b) The two components plotted between the range 0- 30 Å. c) The two components plotted between the range 0- 10 Å, with peak position labels for component one. d) The two components plotted between the range 0- 10 Å, with peak position labels for component two.

The low r region in the NMF can be studied to determine how peaks change over time, which has been as best as possible, assigned to known atomic distances using the known KNb_3O_8 structure. The peaks at 3.44 Å and 3.83 Å corresponding to edge shared and corner shared Nb to Nb distances, respectively, (Figure 7.17.c.d.) shows a peak shift to 3.35 Å and 3.89 Å, respectively. This implies that the edge sharing niobates found in a cluster of three move closer together, whilst each cluster moves further away from each other. This suggests that a possible sodium site can be found between the niobate clusters, similarly to the lithium-ion x sites described in $NaNb_3O_8$ by K. McColl *et al.*[131] in Figure 7.13.

Table 7.3: Table matching the peak locations as obtained by NMF analysis and known atomic distances of KNb_3O_8 to study *inoperando* changes to the local atomic structure.

NMF analysis results Å		Known KNb_3O_8 information Å	
Component one	Component two	Atomic distance	Atomic bond
-	1.39	-	-
1.42	1.43	-	-
1.75	-	1.74	O2-Nb1
-	1.85	1.96	Nb1-O5
2.00	-	1.99	O1-Nb1
-	2.16	-	-
2.36	-	-	-
-	3.32	3.39	Nb1-Nb1
3.44	-	3.45	Nb1-Nb2
-	3.65	3.70	Nb2-O3
3.83	-	3.84	Nb1-Nb2
-	3.92	4.02	Nb1-K1
4.17	-	4.18	O2-Nb1
-	4.49	4.50	K1-K1
4.99	4.93	5.01	Nb1-O3

7.4.4 Restacked niobate results: *inoperando* XPDF

The *inoperando* cell cycling in Figure 7.18 shows a decrease in intensity, and an increase in damping, during sodiation which is similar to the behaviour of KNb_3O_8. In this case, the damping begins at a much lower r than in KNb_3O_8, as expected of a disordered material (Figure 7.19). During the process of sodiation, peak broadening in the XPDF is observed indicating increased deviation from the ideal site. This is more likely due to defect formation/ sodium-ion intercalaction rather than changes in thermal parameters.

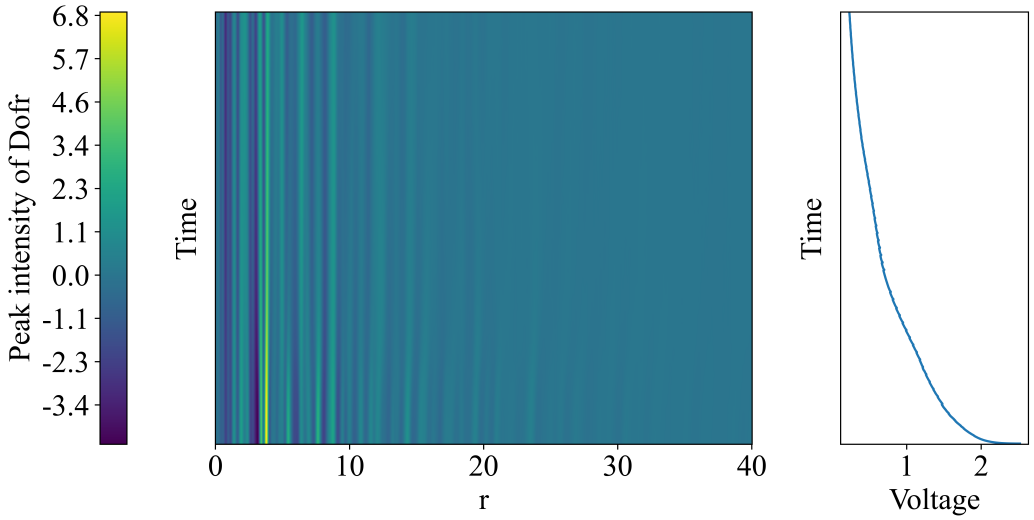


Figure 7.18: PDFs obtained during cell cycling of restacked niobate plotted alongside the voltage profile.

As the restacked nanostructured structure has been modelled as a single niobate layer, analogous to that found in KNb_3O_8, the known structure of KNb_3O_8 will be used to assign short range atomic distances (Table 7.4).

The peaks at 2.17 Å and 2.32 Å (Figure 7.19 and Table 7.4) could not be fit using the ICSD structure of KNb_3O_8, however the peaks in this range have been reported [194] in $[NbO_6]$ units of $K_4Nb_6O_{17}$, with Nb-O lengths ranging from 1.7666 Å and 2.4756 Å. It is therefore possible, that the effect of restacking and/or Na^+ has caused the distortion of $[NbO_6]$ units.

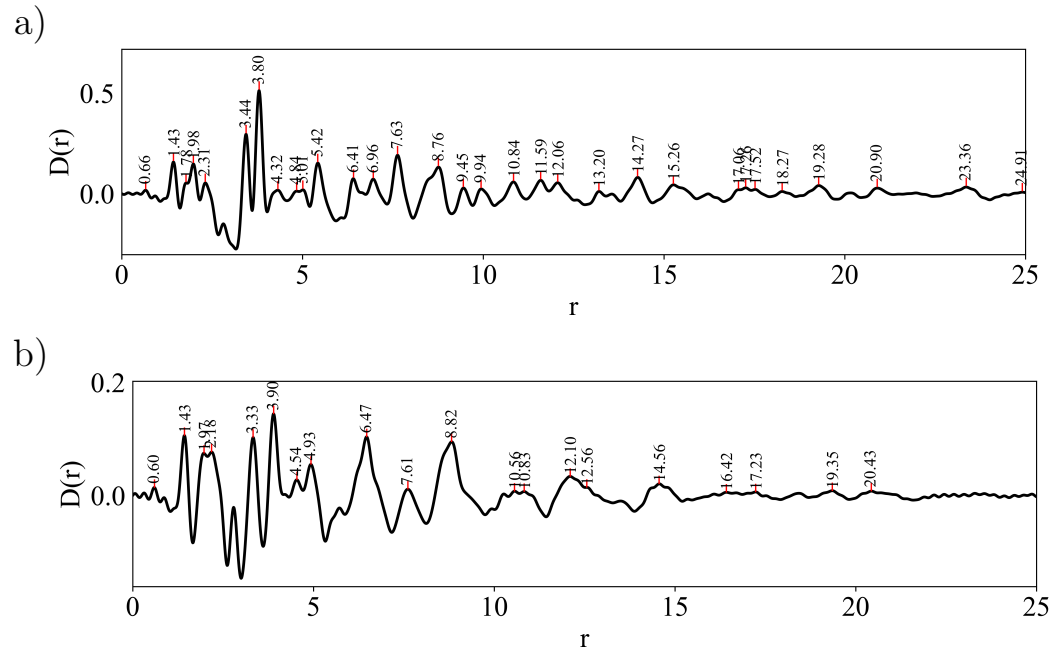


Figure 7.19: XPDF pattern from the *inoperando* study of restacked niobate. a) The first pattern collected b) The last pattern collected.

Table 7.4: Table matching the peak locations as obtained by NMF analysis and known atomic distances of restacked nanostructured to study *inoperando* changes to the local atomic structure.

NMF analysis results / Å		Known KNb_3O_8 information Å	
Component one	Component two	Atomic distance	Atomic bond
1.43	1.43	-	-
1.98	1.90	1.96	Nb1-O5
-	2.17	-	-
2.32	-	-	-
-	2.78	2.83	O2-O5
-	3.26	3.14	O2-O2
3.43	-	3.45	Nb1-Nb2
3.81	-	3.80	Nb1-Nb1
-	3.97	4.02	Nb1-K1
4.34	-	4.33	O3-Nb1
-	4.53	4.50	K1-K1
4.99	4.93	5.01	Nb1-O3

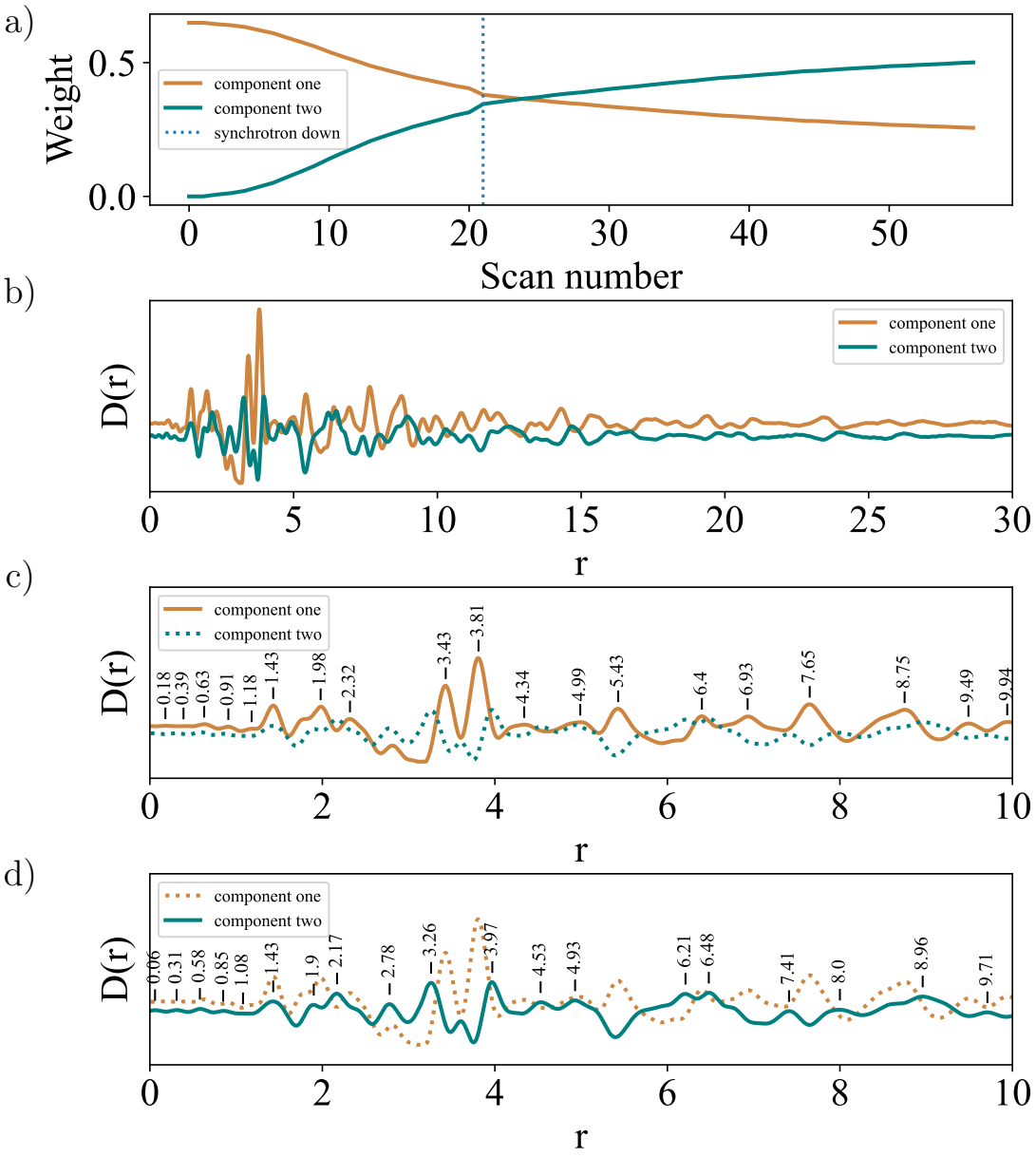


Figure 7.20: NMF results of *inoperando* XPDF cell testing of restacked niobate. a) Shows the change in weighting with XPDF scan number. A blue vertical dotted line indicates where two scans were removed due to a lack of x-rays at the synchrotron. b) The two components plotted between the range 0- 30 Å. c) The two components plotted between the range 0- 10 Å, with peak position labels for component one. d) The two components plotted between the range 0- 10 Å, with peak position labels for component two.

The peaks at 3.44 Å and 3.80 Å (Figure 7.19 and Table 7.4) again shift to lower and higher r values, to 3.33 Å and 3.90 Å, respectively (Figure 7.19), corresponding to edge shared and corner shared Nb to Nb distances, respectively. This shifting is similar to the behaviour observed in KNb_3O_8, although to a lesser degree. This could be indicative of less sodiation which is also observed in the lower capacity of the restacked material compared to KNb_3O_8. The previously suggested sites for Na^+ was found within the niobate layer, between the cluster of three niobates, and therefore expected to also be present in the restacked niobate layer.

NMF found that two components were able to highlight the changes in the PDFs during sodiation (Figure 7.20). The two components are smoothly varying in weighting with the sample showing more similarities with component one at the beginning and showing more similarities with component two at the end of sodiation (Figure 7.20.a.). The two components cancel out at high r to model the effect of damping, therefore the high r region was not further studied. Again, most of the changes occurred in the first 10 hrs of cycling. The peaks from component one and component two have been assigned to atom to atom distances in KNb_3O_8 in Table 7.4.

Figure 7.20.c. and d. highlights the loss of intensity at 5.43 Å and 7.63 Å. Both of these peaks show a rapid drop in peak intensity during cycling, at the same rate as one another. The peak at 7.63 Å can be assigned to double the unit cell length in c, reported 7.60 Å in crystalline KNb_3O_8. Whilst the peak at 5.43 Å could correspond to the known KNb_3O_8 distance from Nb1-Nb1 (5.46 Å), where they are niobium atoms of neighbouring niobate clusters. Alternatively, it could correspond to the the Nb1-Nb1 distance (5.68 Å), where each Nb is on opposite sides of interlayer. Regardless, this indicates a degradation of correlated atomic distances beyond neighbouring Nb-O-Nb distances, most likely due to irregular distortions of the niobate octahedra.

7.5 Summary: Electrochemical testing of niobates

7.5.1 Summary: Electrochemical performance

Table 7.5: Discharge capacities of each niobate-based active material at the end of cycle one, two and the 20th cycle when cycled at of 3 mAg^{-1}, 10mAg^{-1}, 20mAg^{-1}, 40 mAg^{-1} and 100 mAg^{-1} in a sodium half cell.

	Rate \ mAg^{-1}	Capacity \ $mAhg^{-1}$ 1st cycle	2nd cycle	20th cycle
KNb_3O_8 PVDF	3	198	131	65
KNb_3O_8 CMC	3	195	161	200*
	10	47	30	18
	20	40	30	22
	40	13	8	6
	100	8	6	6
HNb_3O_8	3	291	217	122
	10	257	183	86
	20	231	160	89
	40	119	87	113
	100	23	20	17
Restacked niobate	3	288	187	64
	10	272	142	48
	20	226	118	47
	40	204	101	42
	100	69	51	33
Hydrothermal nanostructured	3	112	115	54
	10	243	173	69
	20	209	149	64
	40	179	136	69
	100	43	26	25
Nanostructured $K_4Nb_6O_{17}$	3	8	3	2
	10	14	8	4
	20	10	5	3
	40	6	4	3
	100	2	2	1

* capacity after 15 cycles.

Capacities

The most interesting part of the cell cycling is the increasing capacity which appears to be related to using CMC as a binder, rather than PVDF which leads to an increase in capacity, but only at slow rates at 3 mAg^{-1} for KNb_3O_8 and also observed at 40 mAg^{-1} for HNb_3O_8. When considering all the tested rates, the highest capacities were achieved using HNb_3O_8 (Table 7.5). This could be because of the small size of H^+, a theory supported by the reported movement of Na^+ ions to new sites in $NaNb_3O_8$ to faciliated Li^+ ion diffusion within a lithium-ion half cell.

Although the nanostructured forms such as: restacked niobate, hydrothermal nanostructured and nanostructured $K_4Nb_6O_{17}$ were tested within a SIB, they generally yielded poorer gravimetric capacities than HNb_3O_8 and KNb_3O_8. The redeeming feature of restacked niobate and hydrothermal nanostructured can be observed at rates between 10 mAg^{-1} and 40 mAg^{-1} where there is minimal change in capacity, unlike the dramatic decrease in capacities at faster rates observed with KNb_3O_8 in particular, and to a lesser degree HNb_3O_8 (Table 7.5). On the other hand, nanostructured $K_4Nb_6O_{17}$ showed consistently poor redox capabilities.[217] The induced disorder may have destroyed the sodium intercaation sites leading to this observed behaviour.

Potentials

The voltages at which redox reactions occur as deduced by sodiation and desodiation peaks in the dQ/dV graphs are outlined in Table 7.6 and 7.7, respectively. All the niobates without plateaus in the dQ/dV graph have been included. In instances of shifting peaks over cycles, the potential of the highest intensity peak was used.

Firstly the sodiation and desodiation potentials (Table 7.6 and 7.7) of KNb_3O_8 regardless of binder choice shows almost exactly the same voltages, although there are differences in peak heights and differences due to peak shifting. However this suggests that the redox mechanism in both cases are similar.

Comparing KNb_3O_8 to HNb_3O_8 at 3 mAg^{-1}, the most intense sodiation peaks shift to

lower V (from 0.1 V to 0.05 V and 0.85 V to 0.75 V) in the protonated form. The most intense desodiation peaks in KNb_3O_8 around at 0.8 and 0.9 V, also shifts to lower potentials in HNb_3O_8 and therefore the absolute ΔV window of is lower than KNb_3O_8.

Table 7.6: Table of peaks observed in the dQ/dV sodiation curves for niobate samples given in units of V.

KNb_3O_8 CMC	KNb_3O_8 PVDF	HNb_3O_8 3 mAg^{-1}	HNb_3O_8 40 mAg^{-1}	nanostructured $K_4Nb_6O_{17}$ 3 mAg^{-1}
0.1	0.1	0.05	-	-
-	-	-	0.45	-
0.6	0.6	0.6	0.6	0.8†
0.85	0.85	0.75	-	
1.15	(1.1) ‡	1.65	1.2	1.9

† peak begins at 0.6 V. ‡ peak disappears after first cycle.

Table 7.7: Table of peaks observed in the dQ/dV desodiation curves for niobate samples given in units of V.

KNb_3O_8 CMC	KNb_3O_8 PVDF	HNb_3O_8 3 mAg^{-1}	HNb_3O_8 40 mAg^{-1}	hydrothermal nanostructured 3 mAg^{-1}	nanostructured $K_4Nb_6O_{17}$ 3 mAg^{-1}
0.05	0.05	0.1	-	-	0.1
0.15	0.18	0.2	-	-	-
-	-	0.3	0.3	-	-
0.8	0.8	0.75	-	0.7	-
0.9	0.95	0.85	0.85	-	-
1.45	1.45	1.05	1.10	-	1.56

The desodiation peaks peaks identified in HNb_3O_8 cycled at 40 mAg^{-1} are similar to that observed at 3 $mAhg^{-1}$ but the desodiataion peaks show little resemblance. There is a sodiaton peak at 0.45 V is unique to this study and the peak at 0.6 V is a present feature in all crystalline -Nb_3O_8 phases. Both HNb_3O_8 and KNb_3O_8 showed an increase in capacity, however their peak locations do not match, again supporting the theory that the intercalation potentials are not related to the increase in capacity.

The nanostructured materials show much broader peaks, and also fewer, although this could be the effect of several peaks merging. Peak broadening indicates more loosely defined structure which increases the likelihood of a solid-solution phase transition, rather than a two-phase transition.

7.5.2 Summary: Electrochemical performance and its structure

The increased surface area due to nanostructuring often results in more SEI formation and therefore larger capacity loss between first and second cycle which is observed for restacked nanostructured, with losses of approximately 100 $mAhg^{-1}$, due to its tissue-paper like morphology with a high surface area. However this effect is less obvious in the hydrothermal nanostructured, this is because its morphology consists of crystalline rods and amorphous which does not possess a significantly large surface area, and therefore the capacity loss due to SEI formation is similar to HNb_3O_8 (Table 7.5).

A reduction in capacity for nanostructured material is expected due to the effects of nanostructuring destroying sodium-ion intercalaction sites, which can explain the lower capacities obtained at 3 mAg^{-1} of restacked niobate and hydrothermal nanostructured (64 $mAhg^{-1}$ and 54 $mAhg^{-1}$, respectively) compared to the crystalline materials. To an extreme degree, the turbostatic disorder in nanostructured $K_4Nb_6O_{17}$ is theorised to have destroyed many of the sodium-ion intercalation sites, resulting in the very poor capacities, at all rates.

One hypothesis is that a larger interlayer distance can better facilitate the diffusion of ions,[128] following this hypothesis, restacked niobate should show the highest capacities with the largest interlayer distance at 13.08 Å (Table 7.8), however this is not observed. Instead HNb_3O_8 with an interlayer distance of 9.26 Å shows the most favourable electrochemistry. A large interlayer space does not even improve capacities at high rates, which tends to be more diffusion dependent, as the interlayer spacing of KNb_3O_8 (10.61 Å) is greater than that of hydrothermal nanostructured and HNb_3O_8 (8.52 Å and 9.26 Å, respectively) and yet KNb_3O_8 shows poor capacities at high rates.

Table 7.8: The interlayer distance for each material.

Sample name	Interlayer distance / Å
KNb_3O_8	10.61
$H_3ONb_3O_8$	11.25
HNb_3O_8	9.26
Restacked niobate	13.08
Hydrothermal nanostructured	8.52
Nanostructured $K_4Nb_6O_{17}$	8.44

The results from *inoperando* XPDF suggests a two phase sodium-intercalation process with sodium-ion intercalation sites at a similar location repoted by K. McColl *et al.*[131] and his study of KNb_3O_8 within LIBs. The similarities between the inoperando XPDF of KNb_3O_8 and restacked niobate suggests a similar mechanism is at play in both instances, which is unsprising as they are structurally related phases.

8 Conclusion

This study began with an aim to demonstrate how nanostructured materials can be effectively characterised using XPDF and to understand how various types of nanostructuring affects its electrochemical behaviour in hopes of discovering a suitable sodium-ion battery material with commercial potential.

Characterising nanostructured and disordered niobates

Firstly "top down" nanostructuring required the synthesis of crystalline reagents, KNb_3O_8 and $H_3ONb_3O_8$. KNb_3O_8 was synthesised using a modified molten salt method after varying reagent ratios, mixing methods and heating durations. $H_3ONb_3O_8$ was synthesised using a well reported method of ion-exchange with HCl. The XRD and PDF of the crystalline phases were refined against known published structures and provided a good fit.

A study on the dehydration profile of $H_3ONb_3O_8$ to form HNb_3O_8 using TGA-MS was performed because cell coatings are dried vigorously in a vaccum oven prior to cell assmbly, therefore understanding the dehydrated form of $H_3ONb_3O_8$ is crucial. Additionally, $H_3ONb_3O_8$ is often mis-reported as HNb_3O_8 leading to further misunderstandings. The TGA-MS showed dehydration occured at around 88 °C (in agreement with R. Nedjar*et al.*[124]) and coincides with a contraction of the unit cell in all directions, as determined by XRD. This study also proposes the space groups *Pnnm* and *Pnmb* for phases $H_3ONb_3O_8$ and HNb_3O_8, respectively, which were not previously established.

"Top-down" nanostructuring produced restacked niobate, formed from disordered $[Nb_3O_8]$ layers with some short range ordered stacking present. This was characterised using a novel one layer model alongside XPDF data. This demonstrated how small box refinement of XPDF can be used to probe disordered layered materials, and hope-

fully inspire other researchers to implement this methodology towards their respective fields, to advance material design and to pin point different types of disorder and their effects. Understanding this restacked niobate phase has also contributed to the field of photocatalysis, in which the activity of this material has been researched, yet little has been achieved in charactiersing its atomic structure until now.

On the other hand, "bottom-up" nanostructuring was achieved by investigating hydrothermal synthesis conditions, which had never previously been studied as disordered phases were often overlooked. Firstly using conventional hydrothermal synthesis, the hydrothermal nanostructured phase was synthesised by using 1g KOH, acidified to pH 2-3 using HCl. Unfortunately due to the lack of peaks in XPDF, XRD and in the Raman spectra, full characterisation was not possible, however, it was determined to be a corner shared niobate structure with a lack of range order.

Due to issues with dissolving Nb_2O_5, this lead to a soluble Lindqvist salt intermediate hydrothermal synthesis route was explored. Again, probing beyond the reported synthesis parameters by changing pH and also heating duration, this has lead to the synthesis of nanostructured $K_4Nb_6O_{17}$ which is formed from turbostatic niobate layers. The use of the Debye equation to simulate the XRD of a discrete $K_4Nb_6O_{17}$ layer has enabled this assignment, which has been supported by small box refinement pf XPDF data, demonstrating the applicability of the "one layer model" across various systems. The nanostructured $K_4Nb_6O_{17}$ structure is more disordered than the nanostructured niobate phase, which is unsurprising as nanostructured $K_4Nb_6O_{17}$ was synthesised *via* a bottom-up self assembly method.

Sodium-ion battery anode material

Within literature, only a few crystalline alkali niobates have been tested as an anode material in lithium half cells, and even rarer, sodium half cells. Furthermore the disordered forms have been overlooked. Therefore this study focused on expanding the horizons in regards to sodium-ion batteries and applications of nanostructured anode

materials.

Testing the crystalline KNb_3O_8 and HNb_3O_8 yielded a surprising observation, of increasing cell capacity (around 25 % increase) when cycled at slow rates, if the anode coating was produced with CMC instead of the commonly used PVDF. This highlighted an area which is often overlooked in early battery development, binder testing. The increased stability of CMC binder compared to PVDF could be the cause of the increased capacities, although this would benefit from further investigation. Hopefully more battery researchers will carefully consider their choice of binder, even in the early stages of electrode optimisation. Fully understanding the role of CMC vs PVDF in a sodium-ion battery will enable better battery coating design and formulation.

Unfortunately, the nanostructured niobates did not yield superior electrochemical properties as hoped, in particular nanostructured $K_4Nb_6O_{17}$ which showed negligible capacity. Hydrothermal nanostructured and restacked nanostructured both show promising initial capacity, however the dramatic capacity fade renders these materials unsuitable for commercial applications, at least with the current coating formulation.

Optimistically, HNb_3O_8 showed the best electrochemical performance with a discharge capacity of 122 $mAhg^{-1}$ at 3 $mAhg^{-1}$ after 20 cycles, which with further optimisation could be competitive, or surpass currently known SIB anode materials. Previously, C. Huang *et al.*[128] suggested the superior electrochemical behvaiour of protonated form of Nb_3O_8 compared to other alkali metals was due to a larger interlayer space, however after drying in a vaccum oven, $H_3ONb_3O_8$ forms HNb_3O_8 which has a smaller interlayer space than KNb_3O_8. As a result this study proposes its superior electrochemical bahvious is attributed to the smaller and mobile nature of H^+. This conclusion was drawn from results presented from K. McColl *et al.*[131] in which Na of $NaNb_3O_8$ migrated to allow Li^+ intercaltion, therefore in a similar manner, we expect H^+ ions in HNb_3O_8 to migrate during Na^+ intercalation.

From *inoperando* XPDF, the KNb_3O_8 and restacked niobate shares a similar sodiation

mechanism due to the similar peak fading observed. Additionally in both systems the edge shared Nb-Nb peaks shift to lower r whilst corner shared Nb-Nb peaks shift to higher r suggesting a contraction in the sodium "clusters". This study proposes that sodiation occurs *via* a two phase sodium-intercalation process with sodium-ion intercalation sites at an analogous site, similar location repoted by K. McColl *et al.*[131]

Summary

This project has successfully demonstrated how XPDF can be used to understand the structure of disordered layered materials using a "one layer" model. This has potential to be applied in various fields, limited only to layered materials. With this, it is hoped that solid state chemists do not overlook disordered materials and spend time analysing them as much as the crystalline counterparts.

9 Future work

Although there is an abundance of research that could stem from this study. I have identified two main areas of scientific interest.

1. Understanding the increasing capacity when CMC is used

The binder choice (CMC or PVDF) plays a fundamental role in the electrochemistry observed for KNb_3O_8 at 3 $mAhg^{-1}$. The mechanism behind this increase capacity is not known and has not been reported in niobates before. Long term cell cycling (over a year) would be ideal to further understand how the capacity changes in subsequent cycles. To study the mechanism, a multi-scale approach is required, firstly microscopy images of the coatings before and after cycling to determine any changes to particle sizes and to determine if there are any signs of cracking to the coating.

Secondly, *inoperando* XRD tomography on KNb_3O_8 with CMC and with PVDF, on the first, second and 20th cycle at 3 $mAhg^{-1}$. This would reveal the interactions between KNb_3O_8 and binder. Then at the atomic level, ^{23}Na nuclear magnetic resonance (NMR) to probe sodiation sites, XANES to probe the active redox potentials, neutron diffraction and XRD to probe sodium migration.

Piecing together the results from these experiments should reveal the sodiation mechanism of KNb_3O_8. X-ray photoelectron spectroscopy (XPS) can be used to probe the SEI and compare it to that of PVDF, a more stable SEI could be a contributing factor to this increase in capacity. Whilst further electrochemistry work such as galvanostatic intermittent titration technique (GITT) would be beneficial to determine whether surface processes are an attributing cause.

Simultaneously, it would be useful to test a range of different binders to determine

what characteristic or property of CMC leads to this behaviour. If this understanding is coupled with optimisation of the coating formulation, HNb_3O_8 anode material may show commercial potential.

2. Characterisation of niobate phases

Niobate chemistry is riddled with poor characterisation which hinders our understanding of this material and our ability to design this material for specific applications. For example, $K_2Nb_8O_{21}$ (ICSD: 00-031-1060), $K_2Nb_4O_{10}$ (ICSD: 01-083-6139) with the same XRD pattern and the multitude of phases attributed to $K_4Nb_6O_{17} \cdot xH_2O$ with a variety of unit cell parameters and space groups. It would be useful to have seminal conclusive study on the K-Nb-O system with fully characterised structures.

Further understanding of the $H_3ONb_3O_8$ and HNb_3O_8 structures would provide insights to why this material shows superior capacity to KNb_3O_8. This would most likely be achieved by neutron diffraction to probe the interlayer space, however this would require thorough deuteration of the sample. This could be achieved by the synthesis of KNb_3O_8 followed by ion-exchange with DCl. Hopefully this would produce $D_3ONb_3O_8$ which can be studied using XRD and PDF in an *insitu* variable temperature study to determine the structure of $H_3ONb_3O_8$ and HNb_3O_8. This would also benefit the photocatalytic communicty who has an interest in $H_3ONb_3O_8$.

10 Appendix: Benchmarking of cells by XRD raster scanning $LiFePO_4$ electrodes

This mini-study is separate from the study of niobates, was funded by The Faraday Institution and investigates the degree of consistency in the delithiation state of $LiFePO_4$ electrodes cycled in various cell types, as determined by XRD raster scans.

10.1 Introduction

There are various forms of a battery such as pouch, coin and cylindrical (e.g. AA) cells. Furthermore, specially designed *insitu* and *inoperando* cells enable structural studies (i.e. XRD, Raman) of the cell without dismantling the cell. *Inoperando* cells allow structural studies to be conducted whilst under operation. It is vitally important that we understand how the cell design impacts on the observed performance of the battery materials being studied if we are to separate out and understand the intrinsic properties of the materials.

10.2 Aims

Many battery researchers have designed and produced their own cells in order to perform *insitu* and *inoperando* experiments, however, there is a lack of cell standardisation. It is often assumed that the homogeneity of lithiation and delithiation is consistent within a cell and comparable across cell types. This study aims to test a small selection of different cell types in order to evaluate their homogeneity, identify whether it is scientifically justified to directly compare different types of cells, and determine which type of cell designs are best for the electrochemical studies undertaken in other chapters.

Definitions of *exsitu*, *insitu* and *inoperando*

exsitu: The sample is removed from the environment which is related to its application (i.e. removal of anode material from battery) and then analysed (i.e. using XRD, Raman etc.).

insitu : The sample to be probed remains within the environment related to its application, but is not being actively tested for its application. For example a disconnected battery being probed using XRD, this may require a specially modified cell with a kapton windown.

inoperando : This word is derived from the word "in operation", and therefore this describes situations during active testing of the materials application whilst performing additional characterisation testing simultaneously. For example, testing of a cell during cell cycling whilst collecting XRD patterns of the active material.

10.3 *Inoperando* and *Insitu* testing

Structural characterisation during *inoperando* and *insitu* electrochemical testing in generally accepted to be the best way of correlating battery performance with structure. In this work, we aim to understand the structure of battery materials, explored through powder diffraction methods (PXRD and PDF) during electrochemical cycling. Some of the benefits of *inoperando* and *insitu* testing are summarised in the following sections.

10.3.1 Air- and moisture-sensitivity

Typically one or more components of a battery are water- and/or air-sensitive. Therefore, the act of dismantling a battery, even within a glovebox, may perturb the phase of interest. The use of an *insitu* electrochemical cell which is capable of being loaded in inert conditions (such as a glove box) and sealed from air for extended periods (the days or weeks required for extended cycling) reduces the possibility of reactions with air or moisture.

10.3.2 Metastable phases

The electrochemical evolution of battery materials during (dis)charging is likley to involve metastable phases. By probing the structure *inoperando* and *insitu* it is possible to obtain information about metastable phases present at each point in the cycling. These metastable phases may break down after removing the cell from the applied current, so would not be observed by simply dismantling the cells at specific points of charge and analysing the materials *exsitu*. *inoperando* and *insitu* measurements therefore give a more complete picture of the phases present under the operating conditions.

10.3.3 Self-consistency

inoperando and *insitu* experiments analyse the progression of one cell over time during cycling, allowing a complete view of the history and evolution of the phases of interest. An equivalent *exsitu* experiment requires a large consistent batch of batteries to be cycled and dismantled at each point of interest. This is labour intensive and difficult to ensure the consistency of each cell.

10.3.4 $LiFePO_4$ cathode material

The use of $LiFePO_4$ (LFP) as a cathode material in a lithium-ion battery was discovered by A.K. Padhi, K. S. Nanjundaswamy and J. B. Goodenough[227] in 1997, and their paper has since accumulated over 8,500 citations. J. B. Goodenough went onto share the 2019 Nobel prize in Chemistry "for the development of lithium-ion batteries". $LiFePO_4$ batteries are globally commercially available. $LiFePO_4$ batteries have a high energy density and low cost.[228] Furthermore, the unit cell parameters and their evolution with electrochemical cycling are well defined, alongside a good understanding of its electrochemical properties. Therefore $LiFePO_4$ was selected for this study to compare the *insitu* performance of different cell designs.

$LiFePO_4$ possesses a reversible capacity of 120 $mAhg^{-1}$ at 3.5 V vs. Li/Li^+.[227,229,230] $LiFePO_4$ delithiathes to $FePO_4$ as outlined in Equation 10.1.[227]

$$LiFePO_4 \rightleftharpoons FePO_4 + Li^+ + e^- \tag{10.1}$$

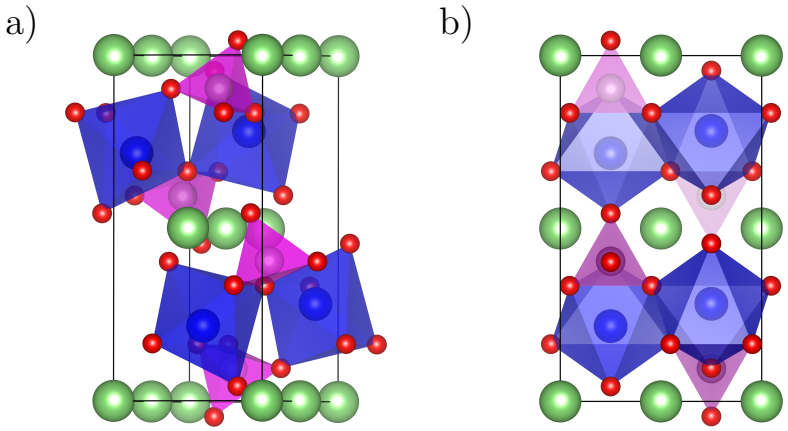


Figure 10.1: A diagram of $LiFePO_4$ unit cell. The FeO_6 units are shown in blue whilst PO_4 units are shown in pink. The oxygen atoms are shown as red sphere and the lithium atoms are shown as green spheres. a) As viewed along [021] direction. b) As viewed along the [001] direction.

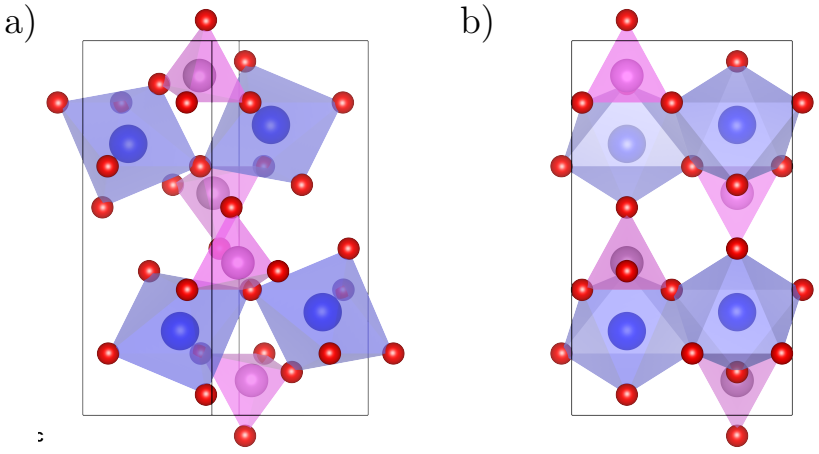


Figure 10.2: A diagram of $FePO_4$ unit cell. The FeO_6 units are shown in blue whilst PO_4 units are shown in pink. The oxygen atoms are shown as red sphere. a) As viewed along [021] direction. b) As viewed along the [001] direction.

10.4 Experimental methodology

10.4.1 Cell assembly

The LFP electrode film was supplied by MTI Corporation; this was a 68 μm thick film ($\pm$ 10 μm) formed from 91 % LFP, cast onto 15 μm thick aluminium. The aluminium cast film was punched into disks with a diameter of 3 mm and dried overnight at 110 °C. The cells were then assembled in an Ar filled glove box by P. K. Allan. The cell stack was formed from an aluminium cathode disk, 1 M $LiPF_6$ in EC/DMC (ethylene carbonate/ dimethyl carbondate) in a ratio of 1:1 by volume as the electrolyte (Sigma-Aldrich), and a pure lithium anode.

Four cell types were tested in total (Table 10.1). Three of them are based on the commonly known "Swagelock cell" design which utilises a Swagelock fitting as the main body of the cell (Figure 10.3.a). The standard Swagelock (S-Swagelock) cell was made by expanding the internal diameter of a 1/8 inch PFA Swagelok tube fitting to 3 mm, and then inserting ferrules and electrodes above and below the electrode stack (Figure 10.3.b). The Swagelock cell has been further adapted for *insitu* cell cycling (Figure 10.3.b) on beamline I15-1 at Diamond Light Source (DLS). This is achieved by narrowing the thickness of the PFA waist, where the electrode stack would sit, to produce a thin window through which x-rays can penetrate. Two forms of these *insitu* Swagelock cells were tested; one without a spring and another with a spring (labeled as "w/o Spring" and "Spring", respectively). The speing was placed above the electrode stack, next to the lithium. The fourth cell (labXRD) is a commercially available ECC-Opto-Std from EL-CELL adapted for *insitu* laboratory XRD (Figure 10.3.c). The various cell types and the abbreviations used are summarised in Table 10.1.

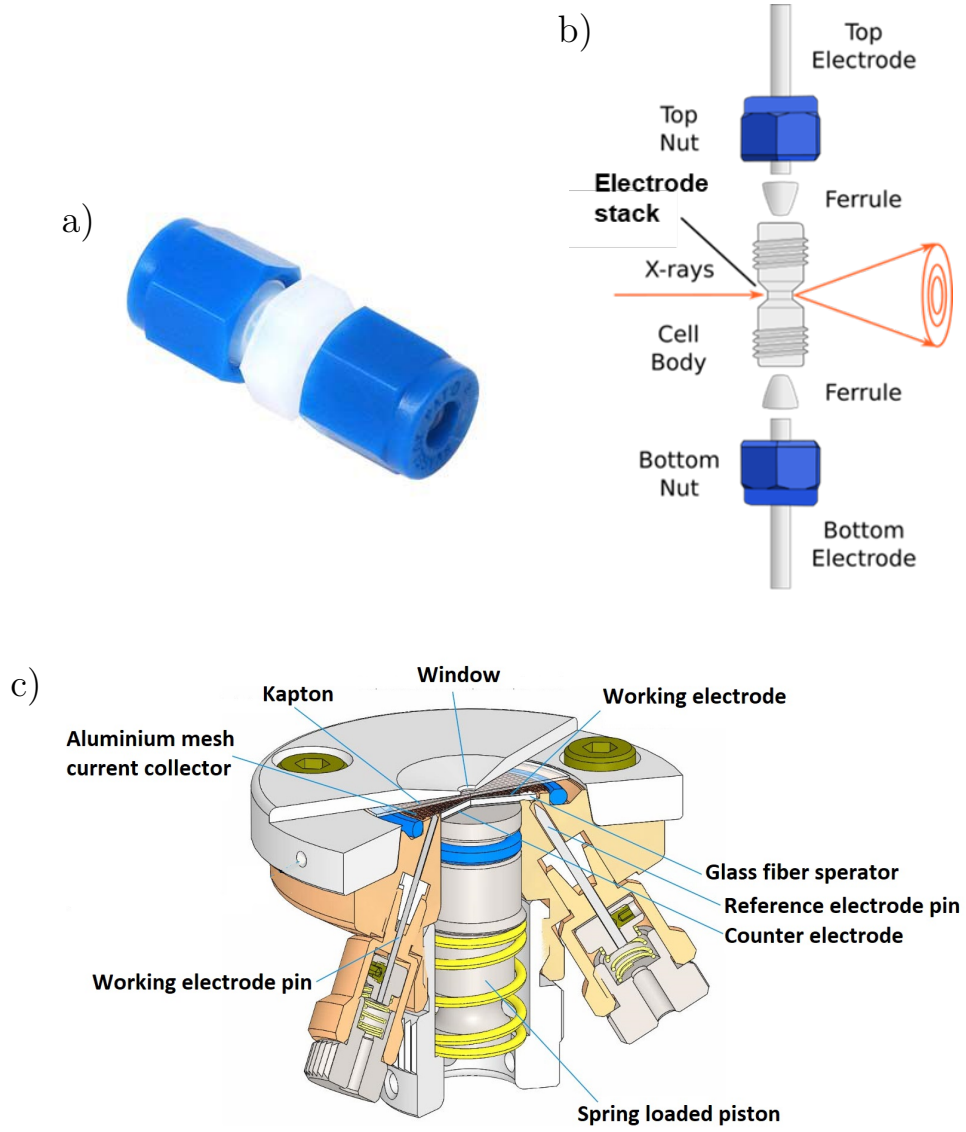


Figure 10.3: a) An image of a 1/8 inch PFA Swagelok tube fitting. b) A schematic of an *insitu* swagelock cell which is adapted for the I15-1 beamline c) The commercial cell (ECC-Opto-Std) used for *insitu* laboratory PXRD. *Images a, b and c obtained from Swagelock, P.K. Allan and EL-CELL respectively.*

Table 10.1: The four various types of cells investigated in this benchmarking study

Cell type	Abbreviation
insitu DLS swagelock cell with spring	Spring
insitu DLS swagelock cell without spring	w/o Spring
insitu laboratory XRD cell	labXRD
Standard swagelock cell	S-Swagelock

10.4.2 Cell cycling and disassembly

The cells were discharged at a rate of C/20 on an Ivium-n-Stat potentiostat by P.K. Allan. Figure 10.4 displays the discharge cycle for the labXRD cell; the other cells were discharged similarly. The cells were disassembled within an Ar glove box by P.K. Allan. Each aluminium cathode disk was sealed between two layers of Kapton tape inside an Ar glovebox prior to measurement.

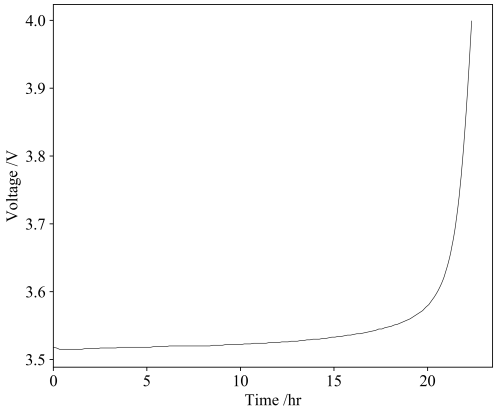


Figure 10.4: A graph to show voltage over time as the labXRD cell was discharged.

10.4.3 X-ray diffraction grid scan

The aluminium cathode disks was mounted on a kinematic sample mount on the I15 beamline at Diamond Light Source with the aid of beamline scientist, Annette Kleppe. A 50 keV, 70 μm diameter x-ray beam was used to raster scan each disk. The size of the grid scan varied for each cell (Table 10.2), most notably S-Swagelock, as the time

constraint on the allocated beamtime only allowed for 75 % of the full grid scan to be taken. P.K. Allan, D. Reed, E.C. Giles and W. C. Tang all partook in the beamtime.

Table 10.2: The dimensions of the grid scans obtained for each cathode sample

Cell number	Motor positions /mm				Grid size	
	x Position		y Position		x	y
	Start	End	Start	End		
Spring	-2.00086	1.49932	-0.34991	2.84993	36	33
w/o Spring	-2.40062	0.89950	-0.89992	2.39993	34	33
labXRD	-1.95108	1.44976	-1.19992	2.09993	35	33
S-Swagelock	-2.40086	1.19936	-1.09991	1.39993	36	26

10.4.4 Rietveld refinement and visualising the map

All subsequent XRD analysis was undertaken by W. C. Tang with the aid of P.A. Chater. The x-ray diffraction patterns underwent Rietveld refinement using TOPAS software.[151] All the scans were refined from the same set of parameters which outlined two structures for Rietveld refinement: $LiFePO_4$ and $FePO_4$ whilst Pawley fitting aluminium. Therefore the total weight percent of $LiFePO_4$ and $FePO_4$ is equal to 100 %. The weight percentage contribution from aluminium was not taken into consideration as the phase was Pawley fitted. The refinement provided calculated values such as weight percent, unit cell parameter and goodness of fit (r_{wp}).

Each individual XRD pattern was refined and its result was written into an xml file containing the results of the such as unit cell parameters, weight percent etc. The xml files generated from each cathode disk were aggregated using a python script to create a nxs which, this was then used to plot a 2D colour map, along with mean, standard deviation (std) information.

As the cathode disk is circular and the raster scan area is rectangular, there are data points in which the x-rays did not hit the cathode disk. These data points were masked to prevent misrepresentation of results when calculating mean and standard deviation values. The parameter weight percent of $LiFePO_4$ was chosen to due to the high

contrast obtained (Figure 10.5). A threshold of 60 % was set and data points/ pixels below this value was masked. The deviation from perfectly circular disks is due to damage when disassembling the cell, most notable in the top left of Figure 10.5.c.

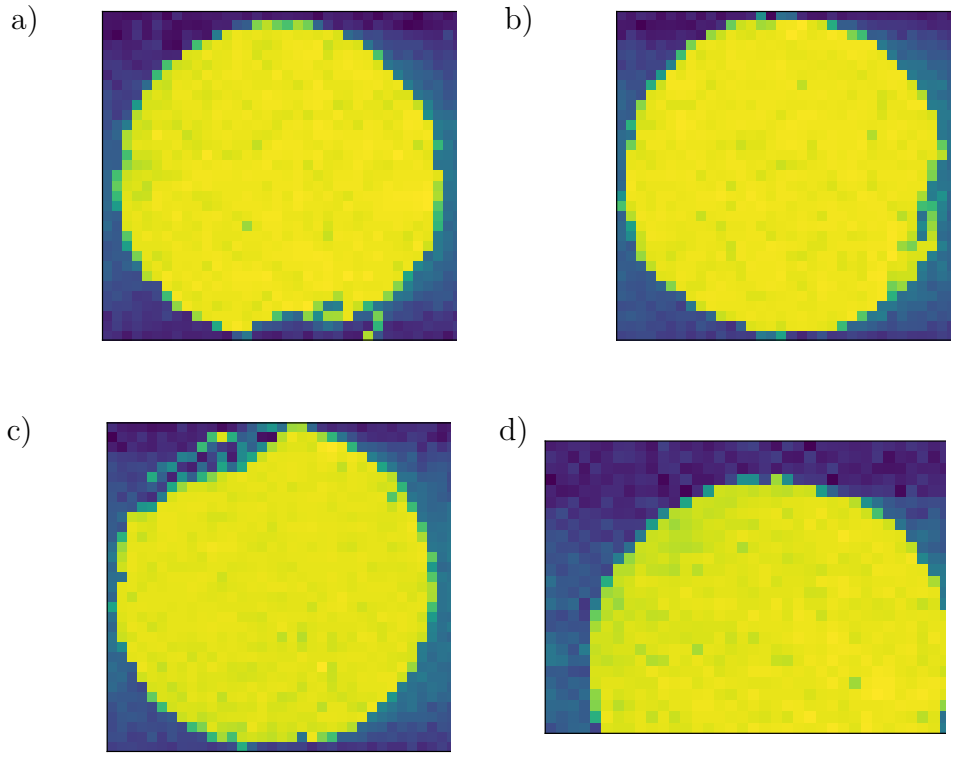


Figure 10.5: The colour map plot of the grid scans displaying the weight percent of $LiFePO_4$ which was used to generate a mask for different cells: a) Spring b) w/oSpring c) labXRD d) S-Swagelock.

10.4.5 Rietveld refinement

Each XRD pattern underwent Rietveld refined using TOPAS. The results obtained from the 620 th XRD pattern of each cathode demonstrate a high degree of agreement between calculated and experimental XRD patterns (Figure 10.6). This is further supported by the mean r_{wp} values (%) for the cells: 6.98 ± 1.26, 6.54 ± 1.12, 6.50 ± 1.15 and 5.90 ± 0.98 which corresponds to Spring, woSpring, labXRD and S-Swagelock respectively.

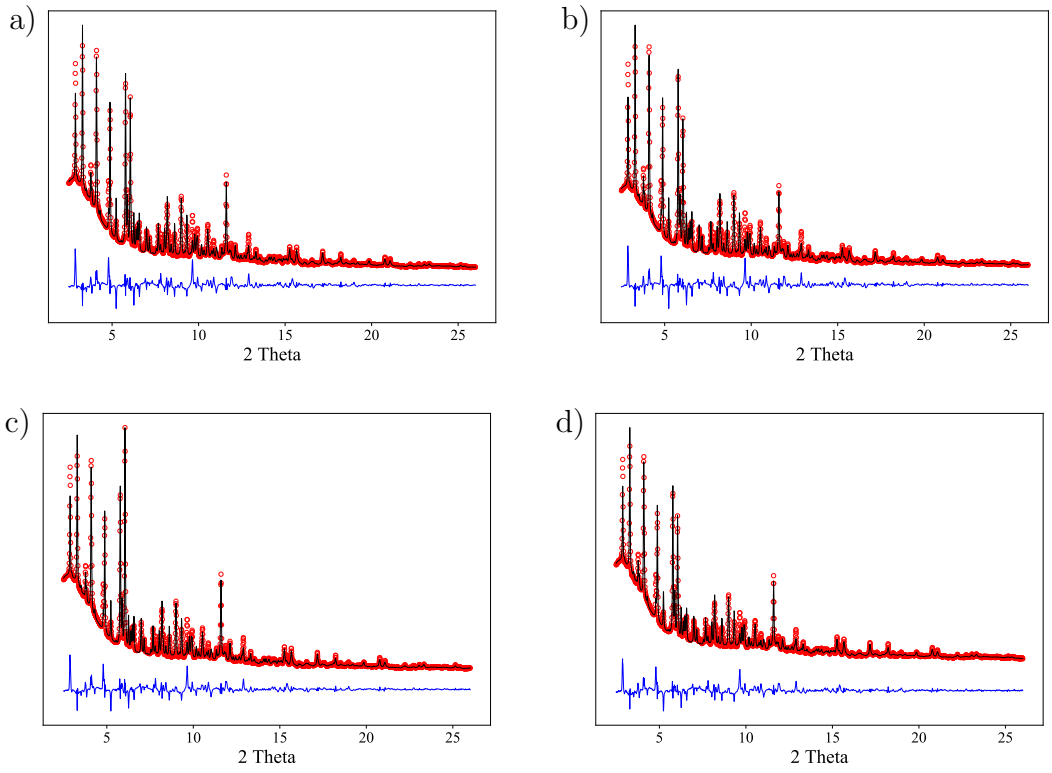


Figure 10.6: The experimental XRD pattern (black) is shown alongside the calculated XRD pattern from Rietveld refinement (red) with the different line below (blue) for the 620th data point for each sample. a) Spring b) w/oSpring c) labXRD d) S-Swagelock.

10.5 Results and discussion

10.5.1 Weight percent of $FePO_4$

The inconsistencies of delithiation between and across the cathode disks can be assessed by the calculated weight percent of $LiFePO_4$ and $FePO_4$, obtained from Rietveld refinement. Due to Equation 10.2, only the weight percent of $FePO_4$ will be presented to avoid repetition.

$$Weight\ percent\ of\ LiFePO_4 + Weight\ percent\ of\ FePO_4 = 100\% \tag{10.2}$$

In an ideal situation, the weight percent of $FePO_4$ in a completely discharged cell would be 100 % as this would indicate complete delithiation. In this study, the weight percent of $FePO_4$, calculated by TOPAS refinement across all four cells was found to similar, at around ∼92 % (Table 10.3). There is a high degree of agreement across all four cathodes, with similar min, max, mean and standard deviation values. Figure 10.7 displays homogeneous disk, with only significant variation from the mean 92 % around the edges which could be cause by the cathode only partially intersecting the x-ray beam. The error associated with weight percent, is ∼2 % which is significantly lower than the weight percent values itself and suggests a high degree of confidence in this calculated value.

The standard deviation associated to the weight percent of $FePO_4$ of each cathode disk is ∼4 %, indicating a homogeneous delithiation across the disk. The outline of the spring is not noticeable in Figure 10.7.a. The presence or lack of a spring did not appear to affect the degree of delithiation. Therefore the type of cell used does not affect the degree of delithiation.

Table 10.3: The minimum, maximum, mean and standard deviation of weight percent of $FePO_4$ values observed in the insert grid scans presented in Figure 10.7 for each cell.

Abb.	Weight percent /%			
	Min	Max	Mean	Std
Spring	60.03	95.42	92.10	4.20
w/oSpring	63.30	95.97	92.75	3.83
LabXRD	60.23	97.06	92.25	4.85
S-Standard	60.06	96.12	92.12	3.23

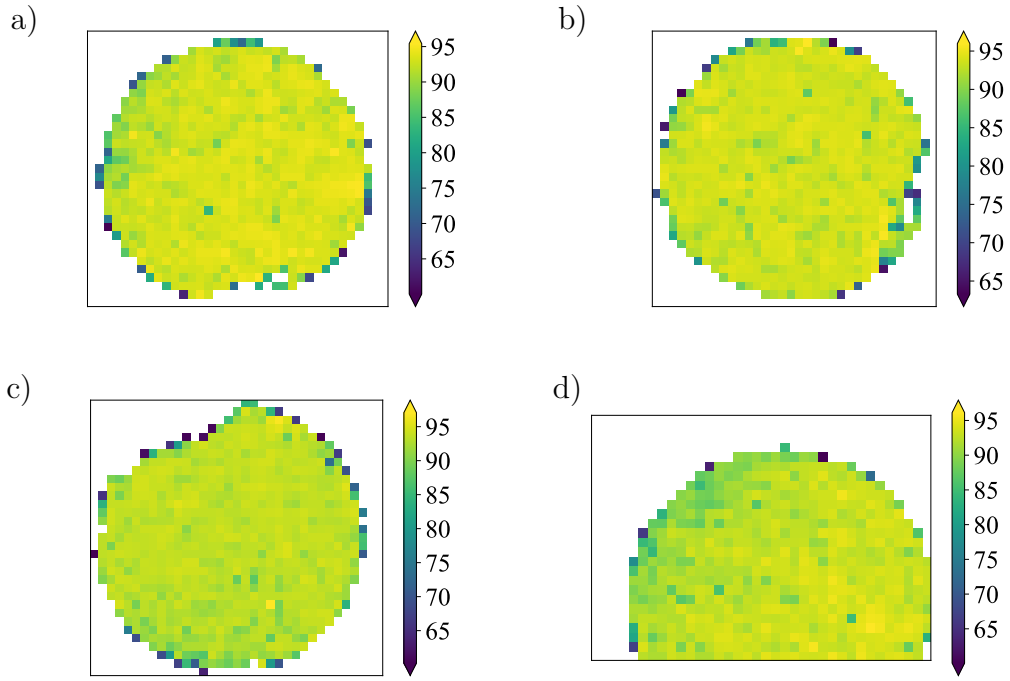


Figure 10.7: The calculated weight percent of $FePO_4$ for each cell: a) Spring b) w/oSpring c) labXRD d) S-Swagelock.

10.5.2 Unit cell parameters of $FePO_4$

The literature reported value for the unit cell volume of $FePO_4$ is 271.70 $Å^3$ (Table 10.4).[231] Across all four cells in this study, the mean volume of $FePO_4$ was calculated to be ∼272.38 $Å^3$ (Table 10.5). However, using Vegard's law, a ∼92.5 % delithiated phase (Table 10.3) would provide a cell volume of 273.6 $Å^3$ which supports the refinement obtained unit cell volume of ∼272.38 Å.

Furthermore, the mean a and b unit cell parameters obtained in this study are are ∼0.01 Å and ∼0.02 Å larger than literature (Table 10.4). The associated std is low and therefore the unit cell parameters of $FePO_4$ is consistent.

Table 10.4: The unit cell properties of $FePO_4$.[231]

Properties	$FePO_4$
Crystal systemc	Orthorhombic
Space group	*Pnma*
a / Å	9.8142
b / Å	5.7893
c / Å	4.7820
Volume / Å³	271.70
ICSD cif code	92199

Table 10.5: The minimum, maximum, mean and standard deviations of the unit cell volume of $FePO_4$.

Abb.	Volume for $FePO_4$ /$Å^3$			
	Min	Max	Mean	Std
Spring	271.95	273.22	272.37	0.10
w/oSpring	272.21	274.66	272.42	0.13
LabXRD	272.10	273.24	272.33	0.08
S-Swagelock	272.21	272.82	272.39	0.08

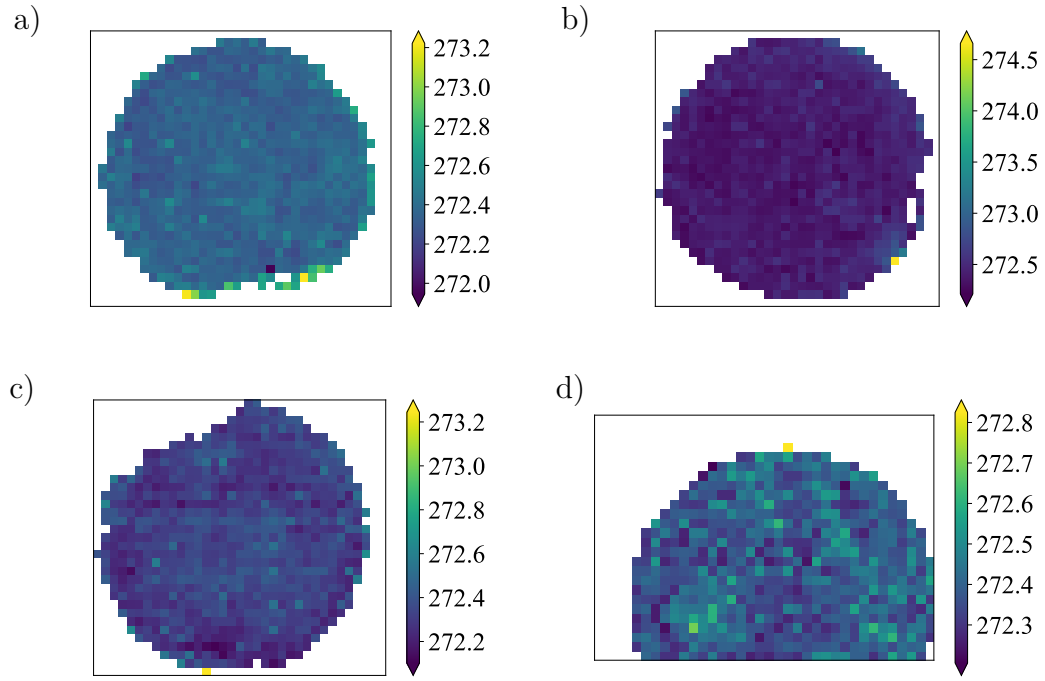


Figure 10.8: The calculated unit cell volume of $FePO_4$ in units of $Å^3$: a) Spring b) w/oSpring c) labXRD d) S-Swagelock.

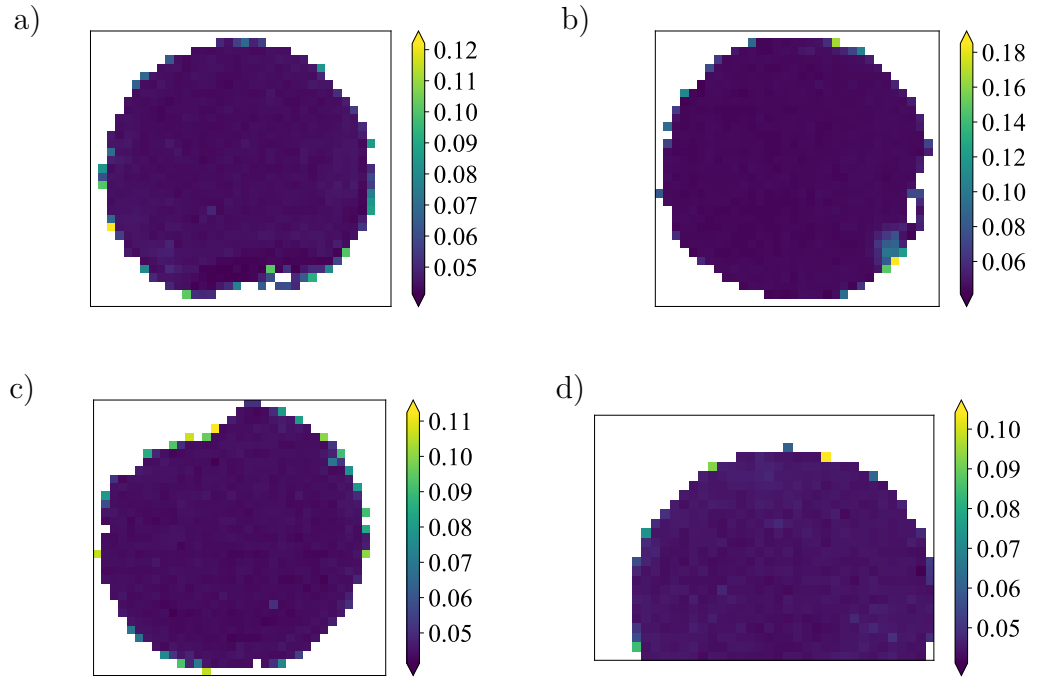


Figure 10.9: The error associated with each calculated unit cell volume of $FePO_4$: a) Spring b) w/oSpring c) labXRD d) S-Swagelock.

10.5.3 Unit cell parameters of $LiFePO_4$

In this study, the mean refined unit cell volume for $LiFePO_4$ is ∼277.62 $Å^3$, which is 6.7 % smaller than literature (Table 10.6). The mean refined a and c parameters (∼9.50 Å and ∼4.44 Å respectively) were smaller than literature whilst b was larger (∼6.58 Å). This can be explained as the the unit cell of $LiFePO_4$ after cycling is reported to adopt minor distortions: where the volume decreases by 6.81% alongside a contraction of the a and b parameters, but a small increase in the c parameter.[227] The observed decrease in unit cell volume are very similar (6.7 and 6.8 %). This is consistent with the refined unit cell parameters of $LiFePO_4$ observed in this study. The std of $LiFePO_4$ is significantly higher than $FePO_4$ as $LiFePO_4$ is the minor phase (6 % by weight) in this refinement, therefore less datapoints and leads to greater standard deviation.

Table 10.6: The unit cell properties of $LiFePO_4$.[231]

Properties	$LiFePO_4$
Crystal system	Orthorhombic
Space group	*Pnma*
a / Å	10.332
b / Å	6.010
c / Å	4.787
Volume / $Å^3$	297.25
ICSD cif code	56291

Table 10.7: The minimum, maximum, mean and standard deviations of unit cell volume of $LiFePO_4$.

Abb.	Volume for $LiFePO_4$ /$Å^3$			
	Min	Max	Mean	Std
Spring	276.08	280.67	277.72	0.61
w/oSpring	272.63	280.13	277.28	0.48
LabXRD	275.89	284.10	277.49	0.56
S-Swagelock	274.97	280.56	277.97	0.71

10.6 Conclusion

Four difference cells were charged, converting the active cathode material from $LiFePO_4$ to $FePO_4$. The degree of delithiation across each cathode was consistent across all four cathode disks (weight percentage of $FePO_4$ ∼94 %). Each disk was also evenly delithiated with a standard deviation of ∼4 % across the cathode. The degree of delithiation between disks were also consistent revealing no electrochemical benefit of using one cell type above another. Therefore, regardless of which cell type was utilised, the lithation and delithation behaviour was crystallographically comparable, displaying no significant differences. As a result, this study concludes that it would be scientifically rigorous to compare the electrode behaviour between these four cell types. This expectation can loosely be extended to other cell types too, although it would be better practice to perform further experiments to benchmark cells.

10.6.1 Acknowledgements

The scientists involved in this study are: Rachel (Wai Chi) Tang, Philip Chater (ORCiD: 0000-0002-5513-9400), Phoebe Allan (ORCiD: 0000-0001-9110-1023), Daniel Reed (ORCiD: 0000-0002-5147-6346) Emily Giles (ORCiD: 0000-0001-9880-1102) and Annette Kleppe of I15 beamline.

ORCiDs have been included where available.

10.6.2 Limitations and further work

Although this study provided insightful results into the high degree of similarity between the performance of $LiFePO_4$ cathode disks of different cell types, there are limitations within this study. A few of these limitations are:

1. Total weight percent = 100 %

This limitation causes phases other than $LiFePO_4$ and $FePO_4$ to be disregarded and ignored. This introduces errors into the weight percent obtained for $LiFePO_4$ and for $FePO_4$.

2. Lack of repeats and limited variety of cells

Due to rarity and competitive nature of beamtime, this experiment has not been repeated. Furthermore only 4 cells were tested, there is an abundance of cells designed by companies, academics and synchrotrons. This study encompasses only 4 cells. A more vigorous study is possible with a wider range of cells.

3. Limited variety of cells

Only one type of cathode material was tested, it would be interesting to chose cathode materials with different lithium diffusion coefficients and to study whether coatings with more resistance show a higher degree of inhomogeneity across the coating.

4. Lack of long term cycling

Deviations in cycling performance between cell geometries may only become apparent as the cell ages, therefore insights into the coatings after long term cycling would be insightful.

Bibliography

[1] BEIS, *Net Zero Strategy: Build Back Greener*, HM Government Technical Report October, 2021.

[2] V. Etacheri, R. Marom, R. Elazari, G. Salitra and D. Aurbach, *Energy and Environmental Science*, 2011, **4**, 3243–3262.

[3] N. Nitta, F. Wu, J. T. Lee and G. Yushin, *Materials Today*, 2015, **18**, 252–264.

[4] P. W. Gruber, P. A. Medina, G. A. Keoleian, S. E. Kesler, M. P. Everson and T. J. Wallington, *Journal of Industrial Ecology*, 2011, **15**, 760–775.

[5] C. Vaalma, D. Buchholz, M. Weil and S. Passerini, *Nature Reviews Materials*, 2018, **3**, 1–11.

[6] V. Palomares, P. Serras, I. Villaluenga, K. B. Hueso, J. Carretero-González and T. Rojo, *Energy and Environmental Science*, 2012, **5**, 5884–5901.

[7] A. M. Skundin, T. L. Kulova and A. B. Yaroslavtsev, *Russian Journal of Electrochemistry*, 2018, **54**, 113–152.

[8] J. Wang and X. Sun, *Energy and Environmental Science*, 2015, **8**, 1110–1138.

[9] M. Cary, *BBC news: Global chip shortage: US says firms' stocks have plunged*, 2022, `https://www.bbc.co.uk/news/business-60135905`.

[10] H. Goodman, *BBC news: Supermarkets set limits on sale of cooking oil*, 2022, `https://www.bbc.co.uk/news/business-61193141`.

[11] J. Swindon, *BBC news: Germany says it is no longer reliant on Russian energy*, 2023, `https://www.bbc.co.uk/news/business-64312400`.

[12] K. Chayambuka, G. Mulder, D. L. Danilov and P. H. Notten, *Advanced Energy Materials*, 2018, **8**, 1–49.

[13] R. C. Masse, E. Uchaker and G. Cao, *Science China materials*, 2015, **58**, 715–766.

[14] J. Jacobs, *Lithium, explained*, `https://www.globalxfunds.com/lithium-explained/`, https://www.globalxfunds.com/lithium-explained/, (Date accessed: 08/05/2019).

[15] J. Park, Z. L. Xu and K. Kang, *Frontiers in Chemistry*, 2020, **8**, 1–14.

[16] C. S. Johnson, Na-Ion Battery Technologies: Present Status and Update, Cancun, 2014.

[17] J. F. Peters, A. P. Cruz and M. Weil, *Batteries*, 2019, **5**, 1–15.

[18] M. H. Han, E. Gonzalo, G. Singh and T. Rojo, *Energy and Environmental Science*, 2015, **8**, 81–102.

[19] M. A. Tsiamtsouri, P. K. Allan, A. J. Pell, J. M. Stratford, G. Kim, R. N. Kerber, P. C. Magusin, D. A. Jefferson and C. P. Grey, *Chemistry of Materials*, 2018, **30**, 1505–1516.

[20] T. Yamamoto, T. Nohira, R. Hagiwara, A. Fukunaga, S. Sakai and K. Nitta, *Electrochimica Acta*, 2016, **193**, 275–283.

[21] S. Roberts and E. Kendrick, *Nanotechnology, Science and Applications*, 2018, **11**, 23–33.

[22] Y. Zhu, Y. Xu, Y. Liu, C. Luo and C. Wang, *Nanoscale*, 2013, **5**, 780–787.

[23] M. Dahbi, N. Yabuuchi, K. Kubota, K. Tokiwa and S. Komaba, *Physical Chemistry Chemical Physics*, 2014, **16**, 15007–15028.

[24] M. R. Palacín, *Chemical Society Reviews*, 2009, **38**, 2565–2575.

[25] W. Wang, W. Li, S. Wang, Z. Miao, H. K. Liu and S. Chou, *Journal of Materials Chemistry A*, 2018, **6**, 6183–6205.

[26] S. H. Yu, X. Feng, N. Zhang, J. Seok and H. D. Abruña, *Accounts of Chemical Research*, 2018, **51**, 273–281.

[27] B. L. Ellis and L. F. Nazar, *Current Opinion in Solid State and Materials Science*, 2012, **16**, 168–177.

[28] Q. Deng, M. Li, J. Wang, K. Jiang, Z. Hu and J. Chu, *Journal of Alloys and Compounds*, 2018, **749**, 803–810.

[29] C. de las Casas and W. Li, *Journal of Power Sources*, 2012, **208**, 74–85.

[30] R.-R. Li, Z. Yang, X.-X. He, X.-H. Liu, H. Zhang, Y. Gao, Y. Qiao, L. Li and S.-L. Chou, *Chem. Commun.*, 2021, **57**, 12406–12416.

[31] Y. Zhang, A. Grant, A. Carroll, U. Gulzar, M. Ferguson, A. Roy, V. Nicolosi and C. O'Dwyer, *Journal of The Electrochemical Society*, 2023, **170**, 050529.

[32] Merck, *Sodium carboxymethyl cellulose*, https://www.sigmaaldrich.com/VN/en/ substance/sodiumcarboxymethylcellulose123459004324, (Date accessed: 24/09/2023).

[33] C. Wang, L. Su, N. Wang, D. Lv, D. Wang, J. Yang and Y. Qian, *J. Mater. Chem. A*, 2022, **10**, 4060–4067.

[34] M. Dahbi, T. Nakano, N. Yabuuchi, T. Ishikawa, K. Kubota, M. Fukunishi, S. Shibahara, J. Son, Y. Cui, H. Oji and S. Komaba, *Electrochemistry Communications*, 2014, **44**, 66–69.

[35] Y. Zhang, A. Grant, A. Carroll, U. Gulzar, M. Ferguson, A. Roy, V. Nicolosi and C. O'Dwyer, *Journal of The Electrochemical Society*, 2023, **170**, 050529.

[36] E. Peled and S. Menkin, *Journal of the Electrochemical Society*, 2017, **164**, A1703–A1719.

[37] W. Liu, P. Liu and D. Mitlin, *Advanced Energy Materials*, 2020, **10**, 2002297–2002297.

[38] S. Masroor, in *Inorganic Anticorrosive Materials*, ed. C. Verma, J. Aslam and C. M. Hussain, Elsevier, 2022, pp. 85–94.

[39] S. Laurent, S. Boutry and R. Muller, in *Iron Oxide Nanoparticles for Biomedical Applications*, ed. M. Mahmoudi and S. Laurent, Elsevier, 2018, pp. 3–42.

[40] J. Hou, C. Yang, Z. Wang, W. Zhou, S. Jiao and H. Zhu, *Applied Catalysis B: Environmental*, 2013, **142-143**, 504–511.

[41] Y. Cao, F. Yuan, M. Yao, J. H. Bang and J.-H. Lee, *CrystEngComm*, 2014, **16**, 826–833.

[42] D. Su, X. Xie, P. Munroe, S. Dou and G. Wang, *Scientific Reports*, 2014, **4**, 1–8.

[43] O. Rubilar, M. Rai, G. Tortella, M. C. Diez, A. B. Seabra and N. Durán, *Biotechnology Letters*, 2013, **35**, 1365–1375.

[44] S. Laurent, D. Forge, M. Port, A. Roch, C. Robic, L. Vander Elst and R. N. Muller, *Chemical Reviews*, 2008, **108**, 2064–2110.

[45] M. Vuković, Z. Branković, D. Poleti, A. Rečnik and G. Branković, *Journal of Sol-Gel Science and Technology*, 2014, **72**, 527–533.

[46] Y. Zhu and L. Liao, *Journal of Nanoscience and Nanotechnology*, 2015, **15**, 4753–4773.

[47] A. A. Keller, S. McFerran, A. Lazareva and S. Suh, *Journal of Nanoparticle Research*, 2013, **15**, 1–17.

[48] A. B. Seabra and N. Durán, *Journal of Material Chemistry*, 2010, **20**, 1624–1637.

[49] R. W. Tarnuzzer, J. Colon, S. Patil and S. Seal, *Nano Letters*, 2005, **5**, 2573–2577.

[50] D. R. Lovley and E. J. P. Phillips, *Environmental Science & Technology*, 1992, **26**, 2228–2234.

[51] K. Prasad and A. K. Jha, *Natural Science*, 2009, **01**, 129–135.

[52] S. Sōmiya, N. Yamamoto and H. Yanagida, *Science and Technology of Zirconia III*, American Ceramic Society, 1988.

[53] V. Vidhu and D. Philip, *Spectrochimica Acta Part A: Molecular and Biomolecular Spectroscopy*, 2015, **134**, 372–379.

[54] M. A. Bizeto, A. L. Shiguihara and V. R. Constantino, *Journal of Materials Chemistry*, 2009, **19**, 2512–2525.

[55] V. Nicolosi, M. Chhowalla, M. G. Kanatzidis, M. S. Strano and J. N. Coleman, *Science*, 2013, **340**, 1420–1430.

[56] A. S. Dias, S. Lima, D. Carriazo, V. Rives, M. Pillinger and A. A. Valente, *Journal of Catalysis*, 2006, **244**, 230–237.

[57] H. Park, J. Kwon, H. Choi, T. Song and U. Paik, *Science Advances*, 2017, **3**, 1–10.

[58] J. Mei, T. Liao and Z. Sun, *Journal of Energy Chemistry*, 2018, **27**, 117–127.

[59] J. S. Ko, V. V. Doan-Nguyen, H. S. Kim, G. A. Muller, A. C. Serino, P. S. Weiss and B. S. Dunn, *ACS Applied Materials and Interfaces*, 2017, **9**, 1416–1425.

[60] X. Rui, Z. Lu, H. Yu, D. Yang, H. H. Hng, T. M. Lim and Q. Yan, *Nanoscale*, 2013, **5**, 556–560.

[61] Y. Zhu, H. Guo, Y. Wu, C. Cao, S. Tao and Z. Wu, *Journal Materials Chemistry A*, 2014, **2**, 7904–7911.

[62] Q. Zhou, L. Liu, J. Tan, Z. Yan, Z. Huang and X. Wang, *Journal of Power Sources*, 2015, **283**, 243–250.

[63] M. M. Leite, V. L. Martins, F. M. Vichi and R. M. Torresi, *Electrochimica*, 2020, **331**, 56–59.

[64] S. Zhang, Y. Li and M. Li, *Jom*, 2018, **70**, 1411–1415.

[65] A. S. Goloveshkin, I. S. Bushmarinov, N. D. Lenenko, M. I. Buzin, A. S. Golub and M. Y. Antipin, *The Journal of Physical Chemistry C*, 2013, **117**, 8509–8515.

[66] S. J. Billinge, *Philosophical Transactions of the Royal Society A: Mathematical, Physical and Engineering Sciences*, 2019, **377**, 1–200.

[67] M. W. Terban and S. J. L. Billinge, *Chemical Reviews*, 2022, **122**, 1208–1272.

[68] S. J. L. Billinge, *Zeitschrift für Kristallographie - Crystalline Materials*, 2004, **219**, 117–121.

[69] V. Petkov, S. J. L. Billinge, J. Heising and M. G. Kanatzidis, *Journal of the American Chemical Society*, 2000, **122**, 11571–11576.

[70] M. W. Terban, C. Shi, R. Silbernagel, A. Clearfield and S. J. L. Billinge, *Inorganic Chemistry*, 2017, **56**, 8837–8846.

[71] M. J. A. Leesmith, N. R. Halcovitch and X. Hua, *J. Mater. Chem. A*, 2023, **11**, 17027–17034.

[72] X. Wang, S. Tan, X.-Q. Yang and E. Hu, *Chinese Physics B*, 2020, **29**, 028802.

[73] *Chemistry of the Elements (Second Edition)*, ed. N. Greenwood and A. Earnshaw, Butterworth-Heinemann, Oxford, Second Edition edn., 1997, pp. 976–1001.

[74] N. Carey, *UK fast-charging battery startup Nyobolt raises $59 million*, 2022, `https://www.reuters.com/technology/uk-fast-charging-battery-startup-nyobolt-raises-59-mln-2022-07-15/`.

[75] C. Nico, T. Monteiro and M. Graça, *Progress in Materials Science*, 2016, **80**, 1–37.

[76] E. Kurmaev, A. Moewes, O. Bureev, I. Nekrasov, V. Cherkashenko, M. Korotin and D. Ederer, *Journal of Alloys and Compounds*, 2002, **347**, 213–218.

[77] V. Augustyn, J. Come, M. A. Lowe, J. W. Kim, P.-L. Taberna, S. H. Tolbert, H. D. Abruna, P. Simon and B. Dunn, *Nature Materials*, 2013, **12**, 518–522.

[78] R. A. Rani, A. S. Zoolfakar, A. P. O'Mullane, M. W. Austin and K. Kalantar-Zadeh, *Journal of Material Chemistry A*, 2014, **2**, 15683–15703.

[79] K. Tanabe, *Catalysis Today*, 2003, **78**, 65–77.

[80] A. L. Viet, M. V. Reddy, R. Jose, B. V. R. Chowdari and S. Ramakrishna, *The Journal of Physical Chemistry C*, 2010, **114**, 664–671.

[81] N. Kurioka, D. Watanabe, M. Haneda, T. Shimanouchi, T. Mizushima, N. Kakuta, A. Ueno, T. Hanaoka and Y. Sugi, *Catalysis Today*, 1993, **16**, 495–501.

[82] J. Marucco, *Journal of Solid State Chemistry*, 1974, **10**, 211–218.

[83] D. Bach, *Ph.D. thesis*, Laboratorium für Elektronenmikroskopie, 2009.

[84] H. T. Kreissl, M. M. Li, Y. K. Peng, K. Nakagawa, T. J. Hooper, J. V. Hanna, A. Shepherd, T. S. Wu, Y. L. Soo and S. C. Tsang, *Journal of the American Chemical Society*, 2017, **139**, 12670–12680.

[85] G. H. M. Gomes and N. D. Mohallem, *Materials Letters*, 2022, **318**, 132136.

[86] D. Cao, Z. Yao, J. Liu, J. Zhang and C. Li, *Energy Storage Materials*, 2018, **11**, 152–160.

[87] S. Liu, J. Zhou, Z. Cai, G. Fang, A. Pan and S. Liang, *Nanotechnology*, 2016, **27**, 46LT01.

[88] X. Zhang, J. Wang, X. Wang, Y. Li, Y. Zhao, Z. Bakenov and G. Li, *Applied Surface Science*, 2021, **567**, 3–12.

[89] Q. Deng and L. Yao, *Coatings*, 2022, **12**, 1–8.

[90] E. Grabowska, *Applied Catalysis B-Environmental*, 2016, **186**, 97–126.

[91] R. Comes, M. Lambert and A. Guinier, *Solid State Communications*, 1968, **6**, 715–719.

[92] L. Bai, K. Zhu, J. Qiu, H. Ji and L. Su, *Particuology*, 2010, **8**, 477–481.

[93] A. J. Paula, R. Parra, M. A. Zaghete and J. A. Varela, *Materials Letters*, 2008, **62**, 2581–2584.

[94] A. Nazeri-Eshghi, A. X. Kuang and J. D. Mackenzie, *Journal of Materials Science*, 1990, **25**, 3333–3337.

[95] Q. Xu, T. Li, H. Hao, S. Zhang, Z. Wang, M. Cao, Z. Yao and H. Liu, *Journal of the European Ceramic Society*, 2015, **35**, 545–553.

[96] G. Haiyan, H. Yudong, W. Chao, Z. Mankang and Y. Hui, *Rare Metal Materials and Engineering*, 2010, **39**, 317–319.

[97] J. W. Liu, G. Chen, Z. H. Li and Z. G. Zhang, *International Journal of Hydrogen Energy*, 2007, **32**, 2269–2272.

[98] M. Cao, W. Tian, M. Li, W. Sun, M. Hu and H. Liu, *Science in China Series E-Technological Sciences*, 2007, **50**, 658–663.

[99] G. F. Teixeira, T. R. Wright, D. C. Manfroi, E. Longo, J. A. Varela and M. A. Zaghete, *Materials Letters*, 2015, **139**, 443–446.

[100] T. Rojac, M. Kosec, B. Malic and J. Holc, *Science of Sintering*, 2005, **37**, 61–67.

[101] K. Nakashima, S. Ueno and S. Wada, *Journal of the Ceramic Society of Japan*, 2014, **122**, 547–551.

[102] K. Nakashima, Y. Toshima, Y. Kobayashi, Y. Ishikawa and M. Kakihana, *Journal of Asian Ceramic Societies*, 2019, **7**, 544–550.

[103] K. G. Zhou and M. Tokuda, *Journal of Central South University of Technology (English Edition)*, 2000, **7**, 173–174.

[104] X. Liu, W. Que and L. B. Kong, *Journal of Alloys and Compounds*, 2015, **627**, 117–122.

[105] L. Grigorjeva, D. Millers, A. Popov, E. Kotomin and E. Polzik, *Journal of Luminescence*, 1997, **72-74**, 672–674.

[106] S. Vuttivong and N. Vittayakorn, *Integrated Ferroelectrics*, 2013, **4587**, 25–31.

[107] M. Manikandan and C. Venkateswaran, Proceedings of the 58th DAE Solid State Physics Symposium 2014 (Solid State Physics), India, 2015.

[108] T. B. Wermuth, J. Venturini, W. C. Guaglianoni, A. M. Tonelli, E. Chavarriaga, S. Arcaro, M. N. Baibich and C. P. Bergmann, *Ceramics International*, 2021, **47**, 4874–4883.

[109] H. Xia, Y. Zhao, W. Li, R. Song, Y. Zhang and W. Fei, *Modern Physics Letters B*, 2020, **34**, 1–9.

[110] X. Li, Z. Zhuang, W. Li and Q. Li, *Catalysis Letters*, 2012, **142**, 901–906.

[111] H. Shi, X. Li, D. Wang, Y. Yuan, Z. Zou and J. Ye, *Catalysis Letters*, 2009, **132**, 205–212.

[112] B. Liang, N. Zhang, C. Chen, X. Liu, R. Ma, S. Tong, Z. Mei, V. A. L. Roy, H. Wang and Y. Tang, *Catal. Sci. Technol.*, 2017, **7**, 1000–1005.

[113] J. Xiong, L. Wen, F. Jiang, Y. Liu, S. Liang and L. Wu, *Journal of Materials Chemistry A*, 2015, **3**, 20627–20632.

[114] G. Zhang, F. He, X. Zou, J. Gong, H. Tu, H. Zhang, Q. Zhang and Y. Liu, *Journal of Alloys and Compounds*, 2007, **427**, 82–86.

[115] G. Zhang, J. Gong, X. Zou, F. He, H. Zhang, Q. Zhang, Y. Liu, X. Yang and B. Hu, *Chemical Engineering Journal*, 2006, **123**, 59–64.

[116] X. Li, N. Kikugawa and J. Ye, *Advanced Materials*, 2008, **20**, 3816–3820.

[117] Y. I. Kim, S. J. Atherton, E. S. Brigham and T. E. Mallouk, *The Journal of Physical Chemistry*, 1993, **97**, 11802–11810.

[118] S. Liang, L. Wen, S. Lin, J. Bi, P. Feng, X. Fu and L. Wu, *Angewandte Chemie International Edition*, 2014, **53**, 2951–2955.

[119] X. Li, H. Pan, W. Li and Z. Zhuang, *Applied Catalysis A: General*, 2012, **413-414**, 103–108.

[120] J. Xiong, Y. Liu, S. Liang, S. Zhang, Y. Li and L. Wu, *Journal of Catalysis*, 2016, **342**, 98–104.

[121] P. Zhou, Q. Li, J. He, D. Li and Z. Li, *Russian Journal of Physical Chemistry A*, 2015, **89**, 2097–2104.

[122] A. Takagaki, D. Lu, J. Kondo, M. Hara, S. Hayashi and K. Domen, *Chemsitry of Materials*, 2005, **17**, 2487–2489.

[123] T. Nakato, K. Kuroda and C. Kato, *Chemistry of Materials*, 1992, **4**, 128–132.

[124] R. Nedjar, M. Borel and B. Raveau, *Material Research Bullitin*, 1985, **20**, 1291–1296.

[125] X. Li, N. Kikugawa and J. Ye, *Chemistry-A European Journal*, 2009, **15**, 3538–3545.

[126] A. Kudo and T. Sakata, *The Journal of Physical Chemistry*, 1996, **100**, 17323–17326.

[127] K. Akatsuka, G. Takanashi, Y. Ebina, N. Sakai, M. aki Haga and T. Sasaki, *Journal of Physics and Chemistry of Solids*, 2008, **69**, 1288–1291.

[128] C. Huang, L. Hu, J. He, L. Wang, H. Cui, J. Zhu and J. Yan, *Journal of Alloys and Compounds*, 2021, **873**, 159834.

[129] F. Madaro, R. Sæterli, J. R. Tolchard, M. A. Einarsrud, R. Holmestad and T. Grande, *CrystEngComm*, 2011, **13**, 1304–1313.

[130] Z. Y. Zhan, C. Y. Xu, L. Zhen, W. S. Wang and W. Z. Shao, *Ceramics International*, 2010, **36**, 679–682.

[131] K. McColl, K. J. Griffith, R. L. Dally, R. Li, J. E. Douglas, K. R. Poeppelmeier, F. Corà, I. Levin and M. M. Butala, *Journal of Materials Chemistry A*, 2021, **9**, 20006–20023.

[132] J. Liu, I. Shakir and D. J. Kang, *Materials Letters*, 2014, **119**, 84–87.

[133] Z. Chen, X. Cheng, N. Long, H. Zhu, H. Yu, T. Liu, N. Peng, M. Shui and J. Shu, *Ceramics International*, 2018, **44**, 5699–5704.

[134] A. Waroquet, V. Demange, N. Hakmeh, J. Perrière, S. Freslon, S. Députier and M. Guilloux-Viry, *RSC Advances*, 2017, **7**, 15482–15491.

[135] R. Li, L. Liu, B. Ming, Y. Ji and R. Wang, *Applied Surface Science*, 2018, **439**, 983–990.

[136] Z. Jian, X. Lu, Z. Fang, Y.-S. Hu, J. Zhou, W. Chen and L. Chen, *Electrochemistry Communications*, 2011, **13**, 1127–1130.

[137] H. Xu, J. Shu, X. Hu, Y. Sun, W. Luo and Y. Huang, *Journal of Material Chemistry A*, 2013, **1**, 15053–15059.

[138] G. Yang, Y. Liu, W. Hou, H. Ji and Y. Li, *Journal of Applied Polymer Science*, 2009, **113**, 78–86.

[139] H. Zhai, H. Liu, H. Li, L. Zheng, C. Hu, X. Zhang, Q. Li and J. Yang, *Nanoscale Research Letters*, 2017, **12**, 36–39.

[140] H. Nakayama and J. Yoshida, *Patent Application Publication (10) Pub . No .: US 2002/0187020 A1*, 2016, https://patentimages.storage.googleapis.com/ce/0f/84/b096ce055d49a8/US20160141615A1.pdf.

[141] K. Akatsuka, G. Takanashi, Y. Ebina, N. Sakai, M.-a. Haga and T. Sasaki, *Journal of Physics and Chemistry of Solids*, 2008, **69**, 1288–1291.

[142] H. Sun, F. Niu, P. Yuan, X. He, J. Sun, Z. Liu, Q. Li and Z. Lei, *Small Structures*, 2021, **2**, 2100029.

[143] H. Nakayama, M. Nose, S. Nakanishi and H. Iba, *Journal of Power Sources*, 2015, **287**, 158–163.

[144] A. Mois Ilia, P.-M. Juan Manuel, C. Cesar, K. Eli, I. Svetoslav, M. Gotzon, K. Asen and W. Hans, *Zeitschrift für Kristallographie - Crystalline Materials*, 2006, **221**, 15–27.

[145] R. E. Dinnebier and S. J. L. Billinge, in *Powder diffraction : theory and practice*, Royal Society of Chemistry, 2008.

[146] *Fundamentals of Crystallography (Third Edition)*, ed. C. Giacovazzo, Oxford Science Publications, Oxford, Third Edition edn., 2011, p. 21.

[147] *Underneath the Bragg Peaks*, ed. T. Egami and S. J. Billinge, Pergamon, 2012, vol. 16 of Pergamon Materials Series, pp. 55–111.

[148] *Underneath the Bragg Peaks, Structural Analysis of Complex Materials*, ed. T. Egami and S. J. Billinge, Pergamon, 2003, vol. 7 of Pergamon Materials Series, pp. 25–51.

[149] Y. Liao, *Pair Distribution Function (PDF) Analysis*, http://www.globalsino.com/EM/, http://www.globalsino.com/EM/, (Date accessed: 23/03/2020).

[150] M. T. Dove and G. Li, *Nuclear Analysis*, 2022, **1**, 100037.

[151] A. A. Coelho, *Journal of Applied Crystallography*, 2018, **51**, 210–218.

[152] A. A. Coelho, P. A. Chater and A. Kern, *Journal of Applied Crystallography*, 2015, **48**, 869–875.

[153] P. W. Stephens, *Journal of Applied Crystallography*, 1999, **32**, 281–289.

[154] C. L. Farrow and S. J. L. Billinge, *Acta Crystallographica Section A*, 2009, **65**, 232–239.

[155] D. A. Keen, *Journal of Applied Crystallography*, 2001, **34**, 172–177.

[156] C. Benmore, *ISRN Materials Science*, 2012, **1**, 1–19.

[157] S. Billinge, in *Powder Diffraction: Theory and Practice*, The Royal Society of Chemistry, 2008.

[158] P. Juhás, T. Davis, C. L. Farrow and S. J. L. Billinge, *Journal of Applied Crystallography*, 2013, **46**, 560–566.

[159] T. A. Bird, A. Herlihy and M. S. Senn, *Journal of Applied Crystallography*, 2021, **54**, 1514–1520.

[160] C.-H. Liu, C. J. Wright, R. Gu, S. Bandi, A. Wustrow, P. K. Todd, D. O'Nolan, M. L. Beauvais, J. R. Neilson, P. J. Chupas, K. W. Chapman and S. J. L. Billinge, *Journal of Applied Crystallography*, 2021, **54**, 768–775.

[161] D. Sivia, *Elementary Scattering Theory: For X-ray and Neutron Users*, Oxford University Press, 2011.

[162] G. Beaucage, H. Kammler and S. Pratsinis, *Journal of Applied Crystallography*, 2004, **37**, 523–535.

[163] G. J. Smales and B. R. Pauw, *Journal of Instrumentation*, 2021, **16**, 06034.

[164] P. Evennett and C. Hammond, *Microscopy Overview*, Elsevier, Oxford, Second Edition edn., 2005, pp. 32–41.

[165] A. Bogner, P.-H. Jouneau, G. Thollet, D. Basset and C. Gauthier, *Micron*, 2007, **38**, 390–401.

[166] P. Eaton and P. West, *Atomic Force Microscopy*, Oxford University Press, 2010.

[167] P. West, *Introduction to Atomic Force Microscopy: Theory, Practice, Applications*, Pacific Nanotechnology, 2006.

[168] P. van Ekeren, in *Principles and Practice*, ed. M. E. Brown, Elsevier Science B.V., 1998, vol. 1 of Handbook of Thermal Analysis and Calorimetry, pp. 75–145.

[169] S. Ebnesajjad, in *Surface Treatment of Materials for Adhesive Bonding (Second Edition)*, ed. S. Ebnesajjad, William Andrew Publishing, Oxford, Second Edition edn., 2014, pp. 39–75.

[170] W. Borutzky, in *Bond Graph Modelling for Control, Fault Diagnosis and Failure Prognosis*, Springer International Publishing, Switzerland, 2021, pp. 195–210.

[171] N. Elgrishi, K. J. Rountree, B. D. McCarthy, E. S. Rountree, T. T. Eisenhart and J. L. Dempsey, *Journal of Chemical Education*, 2018, **95**, 197–206.

[172] Q. Deng, Y. Fu, C. Zhu and Y. Yu, *Small*, 2019, **1804884**, 1–26.

[173] M. H. K. Rubel, M. E. Hossain, M. S. Parvez, M. M. Rahaman, M. S. Islam, N. Kumada and S. Kojima, *Journal of the Australian Ceramic Society*, 2018, 1–6.

[174] J. Park and Y. W. Suh, *Korean Journal of Chemical Engineering*, 2019, **36**, 843–850.

[175] W. J. Zhang, *Journal of Power Sources*, 2011, **196**, 13–24.

[176] K.-i. KAKIMOTO, K. SUGIYAMA and I. KAGOMIYA, *Journal of the Ceramic Society of Japan*, 2010, **118**, 696–700.

[177] J. De Souza, L. Honório, J. Ferreira, S. Torres, I. Santos and A. Maia, *Ceramica*, 2018, **64**, 104–108.

[178] R. L. Lehman, J. S. Gentry and N. G. Glumac, 1998, **316**, 1–9.

[179] J. Park, J. H. Lee, Y. M. Chung and Y. W. Suh, *Advanced Powder Technology*, 2017, **28**, 2524–2531.

[180] G. Zhang, J. Gong, H. Gan and F. Lü, *Journal of Alloys and Compounds*, 2011, **509**, 9791–9797.

[181] A. Kudo and T. Sakata, *The Journal of Physical Chemistry*, 1996, **100**, 17323–17326.

[182] Y. Zhou, T. Wen, W. Kong, B. Yang and Y. Wang, *Dalton Transactions*, 2017, **46**, 13854–13861.

[183] L. Li, J. Deng, J. Chen, X. Sun, R. Yu, G. Liu and X. Xing, *Chemistry of Materials*, 2009, **21**, 1207–1213.

[184] M. Maczka, M. Ptak, A. Majchrowski and J. Hanuza, *Journal of Raman Spectroscopy*, 2011, **42**, 209–213.

[185] J. M. Jehng and I. E. Wachs, *Chemistry of Materials*, 1991, **3**, 100–107.

[186] B. Yu, B. Cao, H. Cao, X. Zhang, D. Chen, J. Qu and H. Niu, *Nanotechnology*, 2013, **24**, 085704.

[187] N. Miyamoto and T. Nakato, *Journal of Physical Chemistry B*, 2004, **108**, 6152–6159.

[188] J. Bareett, *Inorganic Chemistry in Aqueous Solution*, Royal Society of Chemistry, Cambridge, 2003, p. 35.

[189] K. Kataoka, J. Awaka, N. Kijima, H. Hayakawa, K.-i. Ohshima and J. Akimoto, *Chemistry of Materials*, 2011, **23**, 2344–2352.

[190] R. D. Shannon, *Acta Crystallographica Section A*, 1976, **32**, 751–767.

[191] M. Zarei-Chaleshtori, M. Hosseini, R. Edalatpour, S. M. Masud and R. R. Chianelli, *Microchemical Journal*, 2013, **110**, 361–368.

[192] K. Domen, Y. Ebina, S. Ikeda, A. Tanaka, J. N. Kondo and K. Maruya, *Catalysis Today*, 1996, **28**, 167–174.

[193] K. Kodama, S. Iikubo, T. Taguchi and S.-i. Shamoto, *Acta Crystallographica Section A*, 2006, **62**, 444–453.

[194] J. K. D. Souza, T. M. Duarte, I. M. G. Dos Santos, J. R. Sambrano, A. D. S. Maia and A. Dos Reis Albuquerque, *Physical Chemistry Chemical Physics*, 2020, **22**, 16562–16570.

[195] S. Uchida, Y. Inoue, Y. Fujishiro and T. Sato, *Journal of Materials Science*, 1998, **33**, 5125–5129.

[196] T. B. Wermuth, M. N. Baibich, T. M. H. Ribeiro and C. P. Bergmann, *Ceramics International*, 2018, **44**, 4758–4765.

[197] J.-F. Liu, X.-L. Li and Y.-D. Li, *Journal of Crystal Growth*, 2003, **247**, 419 – 424.

[198] L. Li, J. Deng, R. Yu, J. Chen, X. Wang and X. Xing, *Inorganic Chemistry*, 2010, **49**, 1397–1403.

[199] U. Balachahdean and N. Eror, *Journal of MAterials Science Letters*, 1982, **1**, 374–376.

[200] R. Brayner and F. Bozon-Verduraz, *Physical Chemistry Chemical Physics*, 2003, **5**, 1457–1466.

[201] H. Tong and J. Ye, *European Journal of Inorganic Chemistry*, 2010, **2010**, 1473–1480.

[202] X. Kong, D. Hu, P. Wen, T. Ishii, Y. Tanaka and Q. Feng, *Dalton Transactions*, 2013, **42**, 7699–7709.

[203] M. Nyman, T. M. Alam, F. Bonhomme, M. A. Rodriguez, C. S. Frazer and M. E. Welk, *Journal of Cluster Science*, 2006, **17**, 197–219.

[204] E. C. C. Souza, *Journal of Physical Chemistry C*, 2019, **123**, 24426–24435.

[205] A. L. Shiguihara, M. A. Bizeto and V. R. Constantino, *Journal of the Brazilian Chemical Society*, 2010, **21**, 1366–1376.

[206] M. A. Bizeto and V. R. L. Constantino, *Materials Research Bulletin*, 2004, **39**, 1729–1736.

[207] M. A. Bizeto, F. Leroux, A. L. Shiguihara, M. L. Temperini, O. Sala and V. R. Constantino, *Journal of Physics and Chemistry of Solids*, 2010, **71**, 560–564.

[208] S. Elumalai, S. Vadivel and M. Yoshimura, *Materials Advances*, 2021, **2**, 1957–1961.

[209] S. Zhang, Q. Fan, Y. Liu, S. Xi, X. Liu, Z. Wu, J. Hao, W. K. Pang, T. Zhou and Z. Guo, *Advanced Materials*, 2020, **32**, 1–10.

[210] M. Gasperin and M. T. Le Bihan, *Journal of Solid State Chemistry*, 1982, **43**, 346–353.

[211] Nassau, K, Shiever, J. W. and Bernstein, J. L., *Journal of the Electrochemical Society*, 1969, **116**, 348–353.

[212] R. B. Shinde, N. S. Padalkar, S. V. Sadavar, S. B. Kale, V. V. Magdum, Y. M. Chitare, S. P. Kulkarni, U. M. Patil, V. G. Parale, H. H. Park and J. L. Gunjakar, *Journal of Hazardous Materials*, 2022, **432**, 128734.

[213] T. M. Duarte, L. M. Honorio, A. S. Brito, J. K. Souza, E. Longo, R. L. Tranquilin, A. G. Souza, I. M. Santos and A. S. Maia, *IOP Conference Series: Materials Science and Engineering*, 2015, **97**, 435–439.

[214] O. G. Grendal, I. E. Nylund, A. B. Blichfeld, S. Tominaka, K. Ohara, S. M. Selbach, T. Grande and M. A. Einarsrud, *Chemistry - A European Journal*, 2020, **26**, 9348–9355.

[215] Y. Ma, X. Liu, Y. Li, Y. Su, Z. Chai and X. Wang, *Journal of Hazardous Materials*, 2014, **279**, 537–545.

[216] X. Kong, Q. Lu, J. Huang, L. Li, J. Zhang, X. Wang, J. Li, Y. Wang and Q. Feng, *Journal of Alloys and Compounds*, 2018, **746**, 68–76.

[217] X. Wang, Y. Zhai, C. Kuang, H. Liu and L. Li, *Materials*, 2019, **12**, 262.

[218] B. Gyenes, D. A. Stevens, V. L. Chevrier and J. R. Dahn, *Journal of The Electrochemical Society*, 2014, **162**, A278.

[219] J. Guo, Y. Li, J. Meng, K. Pedersen, L. Gurevich and D.-I. Stroe, *Journal of Energy Chemistry*, 2022, **74**, 34–44.

[220] M. Lewerenz, J. Münnix, J. Schmalstieg, S. Käbitz, M. Knips and D. U. Sauer, *Journal of Power Sources*, 2017, **345**, 254–263.

[221] K. A. Severson, P. M. Attia, N. Jin, N. Perkins, B. Jiang, Z. Yang, M. H. Chen, M. Aykol, P. K. Herring, D. Fraggedakis, M. Z. Bazant, S. J. Harris, W. C. Chueh and R. D. Braatz, *Nature Energy*, 2019, **4**, 383–391.

[222] M. Dubarry, C. Truchot and B. Y. Liaw, *Journal of Power Sources*, 2012, **219**, 204–216.

[223] Y. Kobayashi, H. Miyashiro, A. Yamazaki and Y. Mita, *Journal of Power Sources*, 2020, **449**, 227502.

[224] T. Perveen, M. Siddiq, N. Shahzad, R. Ihsan, A. Ahmad and M. I. Shahzad, *Renewable and Sustainable Energy Reviews*, 2020, **119**, 109549.

[225] S. Guo, J. Yi, Y. Sun and H. Zhou, *Energy and Environmental Science*, 2016, **9**, 2978–3006.

[226] M. Diaz-Lopez, G. L. Cutts, P. K. Allan, D. S. Keeble, A. Ross, V. Pralong, G. Spiekermann and P. A. Chater, *Journal of Synchrotron Radiation*, 2020, **27**, 1190–1199.

[227] A. K. Padhi, K. S. Nanjundaswamy and J. B. Goodenough, *Journal of The Electrochemical Society*, 1997, **144**, 1188–1194.

[228] S. Y. Chung, J. T. Bloking and Y. M. Chiang, *Nature Materials*, 2002, **1**, 123–128.

[229] A. Yamada, S. C. Chung and K. Hinokuma, *Journal of The Electrochemical Society*, 2001, **148**, A224.

[230] J. B. Goodenough and K.-S. Park, *Journal of the American Chemical Society*, 2013, **135**, 1167–1176.

[231] M. Hess, T. Sasaki, C. Villevieille and P. Novák, *Nature Communications*, 2015, **6**, 1–9.